ISSN: 2408-2384 (Online)
ISSN: 1686-5456 (Print)

Environment and Natural Resources Journal

Volume 20, Number 2, March - April 2022

Environment and Natural Resources Journal (EnNRJ)

Volume 20, Number 2, March - April 2022 ISSN: 1686-5456 (Print)
ISSN: 2408-2384 (Online)

AIMS AND SCOPE

The Environment and Natural Resources Journal is a peer-reviewed journal, which provides insight scientific knowledge into the diverse dimensions of integrated environmental and natural resource management. The journal aims to provide a platform for exchange and distribution of the knowledge and cutting-edge research in the fields of environmental science and natural resource management to academicians, scientists and researchers. The journal accepts a varied array of manuscripts on all aspects of environmental science and natural resource management. The journal scope covers the integration of multidisciplinary sciences for prevention, control, treatment, environmental clean-up and restoration. The study of the existing or emerging problems of environment and natural resources in the region of Southeast Asia and the creation of novel knowledge and/or recommendations of mitigation measures for sustainable development policies are emphasized.

The subject areas are diverse, but specific topics of interest include:

- Biodiversity
- Climate change
- Detection and monitoring of polluted sources e.g., industry, mining
- Disaster e.g., forest fire, flooding, earthquake, tsunami, or tidal wave
- Ecological/Environmental modelling
- Emerging contaminants/hazardous wastes investigation and remediation
- Environmental dynamics e.g., coastal erosion, sea level rise
- Environmental assessment tools, policy and management e.g., GIS, remote sensing, Environmental Management System (EMS)
- Environmental pollution and other novel solutions to pollution
- Remediation technology of contaminated environments
- Transboundary pollution
- Waste and wastewater treatments and disposal technology

Schedule

Environment and Natural Resources Journal (EnNRJ) is published 6 issues per year in January-February, March-April, May-June, July-August, September-October, and November-December.

Publication Fees

There is no cost of the article-processing and publication.

Ethics in publishing

EnNRJ follows closely a set of guidelines and recommendations published by Committee on Publication Ethics (COPE).

Environment and Natural Resources Journal (EnNRJ)

Volume 20, Number 2, March - April 2022

ISSN: 1686-5456 (Print)

ISSN: 2408-2384 (Online)

Editorial Office Address
Research Management and Administration Section,
Faculty of Environment and Resource Studies, Mahidol University
999, Phutthamonthon Sai 4 Road, Salaya, Phutthamonthon, Nakhon Pathom, Thailand, 73170
Phone +662 441 5000 ext. 2108 Fax. +662 441 9509-10
Website: https://ph02.tci-thaijo.org/index.php/ennrj/index
E-mail: ennrjournal@gmail.com

Environment and Natural Resources Journal (EnNRJ)
Volume 20, Number 2, March - April 2022
ISSN: 1686-5456 (Print)
ISSN: 2408-2384 (Online)

CONTENT

Assessing and Simulating Impacts of Land Use Land Cover Changes on Land Surface Temperature in Mymensingh City, Bangladesh

Tahmid Anam Chowdhury[1] and Md. Saiful Islam[2*]

[1]*Department of Geography and Environment, Shahjalal University of Science and Technology, Sylhet-3114, Bangladesh*
[2]*EQMS Consulting Limited, House 53, Road 04, Block-C, Banani, Dhaka-1213, Bangladesh*

ARTICLE INFO

Received: 18 Jun 2021
Received in revised: 30 Oct 2021
Accepted: 15 Nov 2021
Published online: 26 Nov 2021
DOI: 10.32526/ennrj/20/202100110

Keywords:
Land Use Land Cover/ Land surface temperature/ Urban growth/ Simulating LST/ Simulating LULC/ Mymensingh

*** Corresponding author:**
E-mail: mdsaiful91@gmail.com

ABSTRACT

Urban developments in the cities of Bangladesh are causing the depletion of natural land covers over the past several decades. One of the significant implications of the developments is a change in Land Surface Temperature (LST). Through LST distribution in different Land Use Land Cover (LULC) and a statistical association among LST and biophysical indices, i.e., Urban Index (UI), Bare Soil Index (BI), Normalized Difference Builtup Index (NDBI), Normalized Difference Bareness Index (NDBaI), Normalized Difference Vegetation Index (NDVI), and Modified Normalized Difference Water Index (MNDWI), this paper studied the implications of LULC change on the LST in Mymensingh city. Landsat TM and OLI/TIRS satellite images were used to study LULC through the maximum likelihood classification method and LSTs for 1989, 2004, and 2019. The accuracy of LULC classifications was 84.50, 89.50, and 91.00 for three sampling years, respectively. From 1989 to 2019, the area and average LST of the built-up category has been increased by 24.99% and 7.6°C, respectively. Compared to vegetation and water bodies, built-up and barren soil regions have a greater LST each year. A different machine learning method was applied to simulate LULC and LST in 2034. A remarkable change in both LULC and LST was found through this simulation. If the current changing rate of LULC continues, the built-up area will be 59.42% of the total area, and LST will be 30.05°C on average in 2034. The LST in 2034 will be more than 29°C and 31°C in 59.64% and 23.55% areas of the city, respectively.

1. INTRODUCTION

The extent of urbanization is growing very fast around the world, along with associated infrastructure. By 2030, it is estimated that around 60% of the world's population will be living in cities (UNHABITAT, 2016). Since population growth is a primary driving factor of urbanization, Bangladesh has a rapid increase of urbanization in line with thriving global trends (BBS, 2011). In 2017, about 4.1 billion (with 3.23% annual growth) people lived in the urban areas where it was only 1.02 billion in 1960 (UN, 2017). The world's population is predicted to grow by 2 billion in the next 30 years, from 7.7 billion today to 9.7 billion in 2050, resulting in an increased need for urban infrastructure (UN, 2019). Both vertical and horizontal expansion is happening in cities to fulfill this demand that finally causes changes to the natural landscape and environment by replacing vegetation, wetlands, and arable lands with an urban impervious surface (Bahi et al., 2016; UNHABITAT, 2016). This form of Land Use Land Cover (LULC) shift has negative consequences for the land, the ecosystem, and the urban microclimate (World Bank, 2018; McCarthy et al., 2010). The Land Surface Temperature (LST) and the formation of Urban Heat Island (UHI) are influenced by the LULC variation over time (Kikon et al., 2016; Maimaitiyiming et al., 2014). An urban heat island is where the temperature is greater than it is in the surrounding areas. It is an environmental phenomenon, which is deeply related to the LST (Trenberth, 2004; Voogt and Oke, 2003). The LST shows how the earth's surface energy changes throughout time (Kayet et al., 2016). It varies based on

Citation: Chowdhury TA, Islam MS. Assessing and simulating impacts of land use land cover changes on land surface temperature in Mymensingh City, Bangladesh. Environ. Nat. Resour. J. 2022;20(2):110-128. (https://doi.org/10.32526/ennrj/20/202100110)

LULC categories and their thermal characteristics caused by energy radiation and absorption (Ahmed et al., 2013; Kayet et al., 2016). LST, like LULC, is a significant metric for monitoring vegetation, climatic change, and changes in built-up areas. (Kayet et al., 2016). The typical LST in a UHI is equal to or more than 2ºC compared to its adjacent areas or suburbs (Lai and Cheng, 2010). Different factors, such as a linear and perpendicular expansion of concrete surfaces, open space within buildings, building materials, location of public places, highways, central business district, major and minor industrial hubs, and others, have a significant impact on the accumulation of temperature in the urban surface (Ahmed et al., 2013; Pal and Ziaul, 2017).

Many studies have been undertaken on a global scale to analyze the relationship between LULC and LST using GIS and Remote Sensing techniques, with multi-temporal satellite imageries such as Landsat and MODIS being commonly employed as data sources (e.g., Ahmed et al., 2013; Bokaie et al., 2016; Dewan and Corner, 2014a; Gazi et al., 2020; Kafy et al., 2020; Kayet et al., 2016; Maduako et al., 2016; Pal and Ziaul, 2017; Rahman et al., 2017; Rashid et al., 2021; Roy et al., 2020; Ullah et al., 2019; Vani and Prasad, 2020; Zareie et al., 2016; Zhang et al., 2016). Such imageries provide both spectral and thermal bands where the spectral band is used to detect LULC, and the thermal band is used for LST estimation. The estimation of both LULC and LST of the same position simultaneously is very efficient for this kind of analysis. The majority of these researches focused on the effects of LULC changes on LST and the link between biophysical parameters (i.e., NBDI, NDVI, etc.) and LST (e.g., Bokaie et al., 2016; Dewan and Corner, 2014a; Kayet et al., 2016; Pal and Ziaul, 2017; Rashid et al., 2021; Roy et al., 2020; Ullah et al., 2019; Vani and Prasad, 2020; Zareie et al., 2016; Zhang et al., 2016). Also, simulation has been conducted to predict LULC and LST in a few studies (e.g., Ahmed et al., 2013; Kafy et al., 2020; Maduako et al., 2016; Ullah et al., 2019). The excellent accuracy level of the Multi-Layer Perceptron-Markov Chain (MLP-MC) approach for simulating the LULC makes the predictions based on the LULC change trend of previous years more accurate (Ahmed and Ahmed, 2012; Al-sharif and Pradhan, 2014; Corner et al., 2014). Simulating continuous data, such as LST using the ANN method, on the other hand, is effective (Ahmed et al., 2013; Kafy et al., 2020; Maduako et al., 2016; Ullah et al., 2019). Previous studies on LULC and LST in urban areas have found that increasing built-up areas while decreasing natural land covers has resulted in a net rise in LST. A substantial relationship has also been discovered between LST and several indices, such as built-up/urban, vegetation, and water index.

In the context of Bangladesh, some studies have been accomplished on both LULC and LST change covering a few cities like Dhaka, Chattogram, and Rajshahi (e.g., Ahmed et al., 2013; Dewan and Corner, 2014a; Gazi et al., 2020; Kafy et al., 2020; Roy et al., 2020), but simulation has been conducted in Dhaka and Rajshahi only (e.g., Ahmed et al., 2013; Kafy et al., 2020). A study has been undertaken on vegetation and LST change in selected regions of Cox's Bazar District as a result of the Rohingya immigration, in addition to urban areas (Rashid et al., 2021). From the view of the LST derivation method, very few studies have applied a split-window algorithm for Landsat 8 in Bangladesh (Gazi et al., 2020; Roy et al., 2020), and only Gazi et al. (2020) has performed validation of LST data derived from Landsat. The rest of the studies have mainly applied both mono-window and single-channel algorithms for Landsat 5, 7, and 8 (Ahmed et al., 2013; Dewan and Corner, 2014a; Kafy et al., 2020; Rashid et al., 2021).

Mymensingh is an old city, which was recognized as a municipal in 1869. As far as it is known, no study has been conducted on this city integrating both LULC and LST change. Since the urban population of Mymensingh city has become double in 1981, the city has been experiencing significant development and degradation of natural land cover since the 1980s (Rouf and Jahan, 2007). The required Landsat satellite images are available from 1989 to study both LULC and LST of Mymensingh city. Therefore, the present study has examined the LULC and LST change from spatial and temporal dimensions using Landsat satellite images over the past thirty years (from 1989 to 2019). The Split-window algorithm for Landsat 8 was used to compute LST in this work, which has only been used in a few earlier studies in Bangladesh and LST validation. This study aims to predict LULC and LST of the year 2034 through simulation. This aim will be achieved through fulfilling these specific objectives: (i) to examine the spatial-temporal changes in LULC and LST, and (ii) to investigate relationships amongst these two variables.

2. METHODOLOGY

2.1 Study area

Mymensingh city is one of the divisional cities in Bangladesh. Geographically, it is situated on the bank of the old Brahmaputra River in Bangladesh's northern region (24 45’N latitude and 90 23’E longitude) (Alam and Haque, 2018). Akua Union surrounds it in the south, Khagdahar Union in the west, Char Ishwardia Union in the north, and Bhabkhali Union in the east. It has elevations varying from +2 to +39 m.m.s.l. (meter mean sea level). The average land height is +16.08 m.m.s.l. Mymensingh city is under the Brahmaputra-Jamuna Floodplain physiographic region and Non-Calcareous Dark Grey Floodplain soil zone (Brammer, 1996; Brammer, 2012). It has Chandina alluvium surface deposits during Holocene (Alam et al., 1990). The city was founded in 1869, and now it covers a total area of 23.16 km^2 (2,316 ha) with 21 administrative wards (Alam and Haque, 2018). It has a population of 258,040 people (male 132,123 and female 125,917) and is growing at a pace of 1.82 percent per year (BBS, 2011). The average temperature of Mymensingh is 25.62°C, with total annual rainfall ranging from 1,500 to 3,300 mm (BMD, 2019). Figure 1 depicts a city map showing the boundaries of various administrative subdivisions.

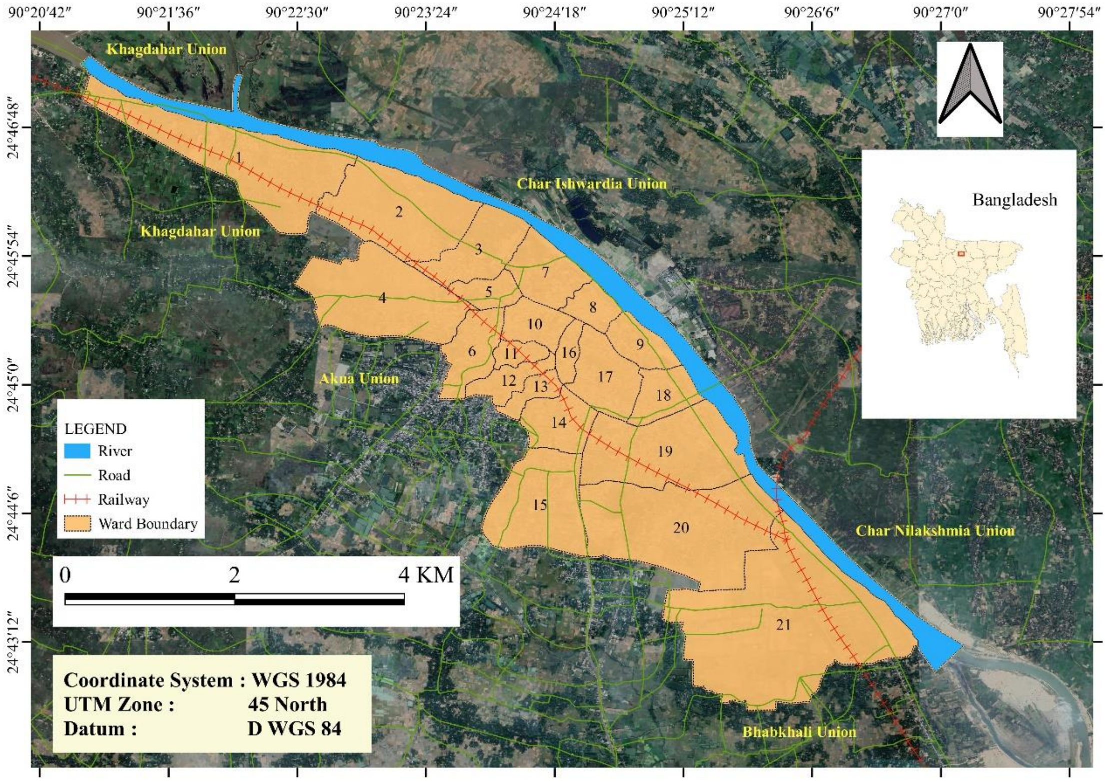

Figure 1. Map of Mymensingh City (Data source: Ward boundary is redrawn from Kabir, 2015)

2.2 Satellite image preprocessing

The necessary data was taken from Landsat satellite images (1989, 2004, and 2019) acquired from the United States Geological Survey’s (USGS) database to detect LULC and LST changes. The study area belongs to Landsat path 137 and row 43. All three images were selected from the dry season to avoid cloud cover disturbance. The images were created using the Universal Transverse Mercator (UTM) Zone 45 North projection and the World Geodetic System (WGS) 1984 datum. There is no need for additional rectification or picture correction as part of pre-processing because the images are level-one terrain-corrected (L1T) products (Ahmed et al., 2013; Bonafoni et al., 2016; USGS, 2019). The particulars of the selected images are shown in Table 1. Although Sentinel-2 data are available from 2015 with better resolution (10 m), this data has only spectral bands (for LULC), not thermal bands (required to get LST). On the other hand, Landsat data have both spectral and thermal bands. Therefore, this study used Landsat images to maintain data consistency.

Table 1. Satellite acquisition and weather information

Satellite	Date of acquisition	Spectral band resolution	Thermal band resolution	Air temperature (°C)	Rainfall (mm)	Cloud cover
Landsat 5	20 Nov 1989		120 m (resampled to 30 m)	26.33 19.81	0	0
	13 Nov 2004	30 m		27.77 18.97	0	0
Landsat 8	23 Nov 2019		100 m (resampled to 30 m)	28.96 17.30	0	3.05

Source: USGS (2019) and BMD (2019)

The images' Digital Numbers (DN) were transformed to Top of Atmospheric (TOA) radiance throughout the radiometric correction procedure using Equations (1) and (2) (Chander and Markham, 2003; USGS, 2014). For Landsat-5 TM:

$$L_\lambda = \text{Gain} * \text{DN} + \text{Bias}\ L_\lambda \qquad (1)$$
$$\text{Gain} = (L_{max} - L_{min}) / Q_{cal}$$
$$\text{Bias} = L_{min}$$

Where; L_{max} represents the spectral radiance scaled to the maximum quantized calibrated pixel value (in W/(m^2*sr*µm)), L_{min} represents the spectral radiance scaled to the minimum quantized calibrated pixel value (in W/(m^2*sr*µm)) and Q_{cal} represents the quantized and calibrated pixel DN. For Landsat-8 OLI:

$$L_\lambda = M_L\, Q_{cal} + A_L \qquad (2)$$

Here, M_L is the image metadata-derived band-specific multiplicative rescaling factor, A_L is the image metadata-derived band- specific additive rescaling factor, and Q_{cal} is the quantized and calibrated pixel DN. The photos were free of haze and cloud disruption during the atmospheric correction phase. As a result, no atmospheric adjustment was required.

2.3 LULC mapping by spectral bands

Land use refers to the functional role of humans and their environment, whereas land cover refers to the physical appearances of the earth's surface as represented in the distribution of plants, water, and soil (Kayet et al., 2016). The LULC categories were adapted from the established classification schemes (Anderson et al., 1976; Ahmed et al., 2013; Corner et al., 2014) and shown in Table 2. Firstly, all the spectral bands have been stacked or merged to classify LULC. Each band of a multispectral satellite image traces a feature. The band combination of different bands in a sequence of RGB helps distinguish different land surface features. Different band combinations proposed by Butler (2013) were used, shown in Table 3, as the adjustment of different spectral band combinations has been proved efficient to select suitable training site samples for different LULC categories (Erener, 2013). Landsat images from 1989, 2004, and 2019 were classified into four LULC classes employing supervised classification using the Maximum Likelihood Classifier (MLC) approach (Table 2). The accuracies of LULC maps were evaluated through 200 (50 for each category) ground truth points from Mymensingh Strategic Development (MSDP) base map, Toposheet, and Google Earth images (Corner et al., 2014; Kabir, 2015). These 200 points were selected using a stratified random sampling process. Finally, the confusion matrix of each year was calculated for accuracy assessment to evaluate the level of acceptance (Table 4) (Roy et al., 2015; Roy and Mahmood, 2016).

Table 2. Details of LULC categories

LULC Category	Description
Built-up	Residential, commercial and industrial services, transportation network
Vegetation	Semi-evergreen forest, homestead vegetation, mixed forest, parks and playgrounds, grassland, vegetated lands, agricultural lands, and crop fields.
Bare soil	Vacant land, open space, sand, sand bar, and landfill sites
Water body	Streams, lakes, ponds, rivers, wetlands, and reservoirs.

Source: Adapted from Anderson et al. (1976) and Ahmed et al. (2013)

Table 3. Spectral Band Combination for Landsat OLI 8 and Landsat TM 5 (modified)

Display	Spectral band combination	
	Landsat TM 5	Landsat OLI 8
Natural color	3 2 1	4 3 2
Urban	7 5 3	7 6 4
Vegetation	4 3 2	5 4 3
Agriculture	5 4 1	6 5 2
Vegetation analysis	5 4 3	6 5 4

Source: Butler (2013)

2.4 Extraction of biophysical indices

Six biophysical indices were employed to investigate a statistical relationship between LULC and LST in the study area. The indices include Urban Index (UI), Bare Soil Index (BI), Normalized Difference Builtup Index (NDBI), Normalized Difference Bareness Index (NDBaI), Normalized Difference Vegetation Index (NDVI), and Modified Normalized Difference Water Index (MNDWI) (Ahmed et al., 2013; Dewan and Corner, 2014a; Kafy et al., 2020; Maduako et al., 2016; Rahman et al., 2017; Roy et al., 2020; Ullah et al., 2019). Each index has a value ranging from -1 to +1, with a positive value indicating one land cover feature and a negative value indicating another. All these indices were calculated from the required spectral bands of the images (Table 5).

Table 4. LULC classification accuracy assessment (1989, 2004, and 2019)

Year	User's accuracy (%)				Producer's accuracy (%)				Overall classification accuracy (%)	Overall Kappa Statistics
	Built-up	Vegetation	Bare soil	Water body	Built-up	Vegetation	Bare soil	Water body		
1989	76.32	84.85	87.10	90.63	80.56	88.42	67.50	100.00	84.50	0.7709
2004	84.75	96.72	83.02	96.30	98.04	83.10	95.65	81.25	89.50	0.8569
2019	92.05	87.30	91.67	96.00	96.43	88.71	75.86	96.00	91.00	0.8685

Table 5. Different biophysical indices to relate with LST

Index	Equation	Reference
Urban Index	$\frac{(SWIR2 - NIR)}{(SWIR2 + NIR)}$	Ullah et al. (2019)
Bare Soil Index	$\frac{(SWIR1 + Red) - (NIR + Blue)}{(SWIR1 + Red) + (NIR + Blue)}$	Roy et al. (1997)
Normalized Difference Builtup Index	$\frac{(SWIR1 - NIR)}{(SWIR1 + NIR)}$	Zha et al. (2003)
Normalized Difference Bareness Index	$\frac{(SWIR1 - TIRS)}{(SWIR1 + TIRS)}$	Chen et al. (2006)
Normalized Difference Vegetation Index	$\frac{(NIR - Red)}{(NIR + Red)}$	Chen et al. (2006)
Modified Normalized Difference Water Index	$\frac{(Green - SWIR1)}{(Green + SWIR1)}$	Han-Qiu (2005)

2.5 Derivation of LST

Several techniques have been developed to estimate LST from the thermal band of a satellite image. For example, the Mono-window algorithm (Qin et al., 2001), single-channel algorithm (Sobrino et al., 2004), and split-window algorithm (Jiménez-Muñoz et al., 2014). All of these methods require land surface emissivity (LSE), which varies greatly depending on the thermal emissivity of the surface feature (Sobrino et al., 2004). This study utilized the mono-window approach to calculate LST from the Landsat-5 thermal band between 1989 and 2004. On the other hand, the split-window technique was used to obtain LST from the Landsat-8 thermal band for the year 2019. Landsat sensors record pixel data as digital numbers since the satellite image consists of many pixels for both spectral and thermal bands (DNs) (Chander et al., 2009). This section detailed the steps involved in converting DNs to LST for Landsat-5 and Landsat-8 thermal photos.

The DNs of band-6 were converted to TOA spectral radiance (L_λ) using Equation (3) to estimate LST from Landsat 5 thermal band.

$$L_\lambda = \left(\frac{LMAX_\lambda - LMIN_\lambda}{Q_{calmax} - Q_{calmin}}\right)(Q_{cal} - Q_{calmin}) + LMIN_\lambda \qquad (3)$$

Here; L_λ=Spectral Radiance at the Sensor's Aperture [W/m^2 sr μm]; Q_{cal}=Quantized Calibrated

Pixel Value; Q_{calmin}=Minimum Quantized Calibrated Pixel Value Corresponding to $LMIN_{\lambda}$ [DN]; Q_{calmax}=Maximum Quantized Calibrated Pixel Value Corresponding to $LMAX_{\lambda}$ [DN]; LMINλ=Spectral at-sensor Radiance that is Scaled to Q_{calmin}; LMAXλ=Spectral at-sensor Radiance that is Scaled to Q_{calmax} (Chander et al., 2009).

Bands 10 and 11 on Landsat 8 are two thermal bands. Each thermal band data of Landsat 8 was converted to TOA spectral radiance (L_{λ}) using Equation (4) (Zanter, 2015).

$$L_{\lambda} = M_L Q_{cal} + A_L \tag{4}$$

Here; L_{λ}=Spectral Radiance at the Sensor's Aperture [W/m^2 sr µm]; M_L=Band-specific multiplicative rescaling factor from the metadata; A_L=Band-specific additive rescaling factor from the metadata; Q_{cal}=Quantized and calibrated standard product pixel values (DN) (Zanter, 2015).

Then, the spectral radiance (L_{λ}) of both Landsat 5 and 8 were transformed to at-sensor brightness temperature (T_B) by Equation (5).

$$T_B = \frac{K_2}{\ln\left(\frac{K_1}{L_\lambda}+1\right)} \tag{5}$$

Here; K_1 and K_2 are thermal conversion constants in W/m^2 sr µm and Kelvin units (K) of the TIR band (Chander and Markham, 2003).

The difference in Land Surface Emissivity (LSE) due to surface wetness, features, roughness, and viewing angle is critical for LST derivation (Salisbury and Aria, 1994). The LSE was estimated by Equation (6) (Avdan and Jovanovska, 2016; Pal and Ziaul, 2017; Roy et al., 2014).

$$\text{LSE}\ (\varepsilon) = 0.004 * P_v + 0.986 \tag{6}$$

The NDVI threshold is the most appropriate approach of emissivity extraction among numerous options because of its ease in the estimate (Van de Griend and Owe, 1993; Sobrino and Raissouni, 2000). P_v is the Proportion of Vegetation calculated from Equation (7) (Roy et al., 2014; Yu et al., 2014).

$$P_v = \left(\frac{NDVI - NDVI_{min}}{NDVI_{max} - NDVI_{min}}\right)^2 \tag{7}$$

For Landsat-5, LST in Degree Celsius (°C) was derived by Equation (8) (Artis and Carnahan, 1982; Roy et al., 2014; Yu et al., 2014).

$$LST = \frac{T_B}{\left\{1+\left(\frac{\lambda T_B}{\rho}\right)\ln LSE\right\}} - 273.15 \tag{8}$$

Here; λ=wavelength of emitted radiance in meters (for which the peak response and the average of the limiting wavelengths, λ=1.5 µm) (Markham and Barker, 1985) is used; ρ=h*c/σ (1.438×10^{-2} mK); σ (Boltzmann constant)=1.38×10^{-23} J/K; h (Planck's constant)=6.626×10^{-34} Js and c (velocity of light) =2.998×10^{8} m/s (Roy et al., 2014; Scarano and Sobrino, 2015).

The split-window approach was used to calculate LST from Landsat-8 TIRS pictures, which is described by Equation (9) (Gazi et al., 2020; Roy et al., 2020). TIRS bands of Landsat 8 are different from the TM band of Landsat 5. Previous TM sensor is the presence of two TIR bands in the atmospheric window between 10 and 12 µm. Nevertheless, TIRS bands are narrower than the previous TM band. Here, split-window (SW) algorithms are applied to TIR bands instead of mono-window or single-channel (SC) algorithms for LST retrieval (Jiménez-Muñoz et al., 2014).

$$\begin{aligned} T_s(K) = {} & T_{10} + C_1(T_{10} - T_{11}) + C_2(T_{10} - T_{11})^2 \\ & + C_0 + (C_3 + C_4 w)(1-\varepsilon) + (C_5 + C_6 w)\Delta\varepsilon \end{aligned} \tag{9}$$

Here; T_{10} and T_{11} are at-sensor brightness temperatures of TIRS bands (in K). T_{10} and T_{11} have been calculated from Equation (3). C_0-C_6 are coefficients (Jiménez-Muñoz et al., 2014), ε represents the mean surface emissivity, Δε represents emissivity difference, and w represents the atmospheric water vapor content (in gm cm^{-2}) acquired from the Atmospheric Correction Parameter Calculator developed by NASA (2019). The values of LST of Landsat-8 were converted to Degree Celsius (ºC) unit by subtracting 273.15 from Equation (9).

2.6 Simulation of future LULC

The Multilayer Perceptron (MLP) model addresses the trend of LULC changes (e.g., growth) in developed areas by automatically producing network parameter decisions for better modeling (Veronez et al., 2006). After recognizing a pattern, it analyses the input and generates a random high-accuracy output. One appealing feature of this model is that it allows simulating many or even all of the transitions at once. The MLP neural network uses the Back Propagation (BP) technique. MLP-MC works with one or more layers between input and output through a feed-forward Neural Network (Ahmed and Ahmed, 2012; Kafy et al., 2020). This modeling is applied to simulate future LULC maps in IDRISI Selva v17 software. The model considers large and small LULC change causes and evaluates future prediction models based on their accuracy (Ahmed and Ahmed, 2012; Mishra and Rai, 2016; Kafy et al., 2020).

The change in LULC is not confined to a single component; instead, it has both natural and artificial factors and determinants. A composition of dependent and independent variables is used to predict LULC change. The study's dependent variables were DEM, slope, aspect, distance from main roads, and distance from built-up regions, while the independent variables were LULC maps in 2004 and 2019 (Figure 2(b) and 2(c)) (Kafy et al., 2020). The SRTM-DEM was used to derive elevation, slope, and aspect using QGIS v.2.8 software. The distance to main roads and built-up regions, on the other hand, was computed using vector layers from the Open Street Map (OSM) (Kafy et al., 2020).

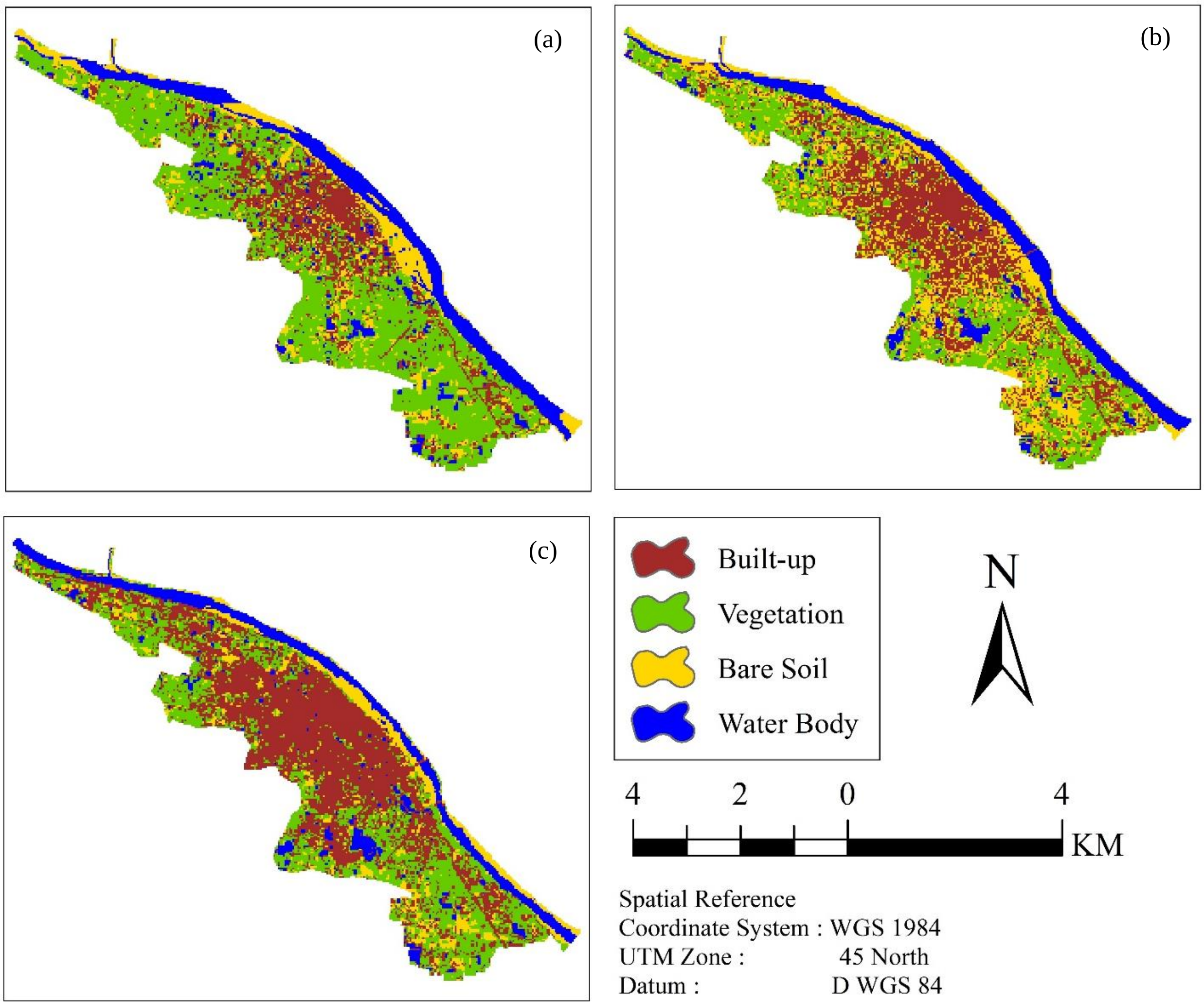

Figure 2. Land Use Land Cover maps of different years: (a) 1989, (b) 2004, and (c) 2019

All the variables mentioned above were added as processing parameters to get the potentiality of the transformation matrix. The expected matrix analysis generates the change probability of different LULC categories. After generating the potential transformation matrix, the prediction model has been run to simulate the LULC map of 2034. As a part of the model assessment, validation was performed using the existing database (Kafy et al., 2020). It was executed by cross-checking between simulated and existing LULC maps of the year 2019. As a part of the validation, some parameters (Kappa) were produced, including $K_{location}$, K_{no}, $K_{locationStrata}$, and $K_{standard}$ (Kafy et al., 2020; Mishra et al., 2018).

2.7 Simulation of future LST

The Artificial Neural Network (ANN) was proved effective for predicting LST by some previous studies (Kafy et al., 2020, Maduako et al., 2016). It is a machine learning algorithm that simulates future LST as an output layer using input, hidden layers (Li et al., 2013; Maduako et al., 2016). It was developed to predict the LST for the year 2034. The input layers were chosen based on the relation between LST and LULC since this model required input layers (Ahmed et al., 2013; Kafy et al., 2020; Rahman et al., 2017; Ullah et al., 2019). Initially, LST variations for different LULC categories were evaluated each year (1989, 2004, and 2019). Then a bivariate correlation investigation was performed between each LULC index (e.g., UI) and LST to examine the relationship strength. Here LST was regarded as a dependent variable, and indices were regarded as independent variables. Highly correlated indices were selected as input layers in the ANN model with LULC types. The ANN model was developed using the neuralnet package of R software. Accuracy assessment of the ANN model was also done using training and testing data (Kafy et al., 2020; Maduako et al., 2016). Detail description of this section is given later.

3. RESULTS

As mentioned in the methodology (in section 2), this section intends to discuss the Spatio-temporal changes in the distribution of LULC and LST and the simulation of the future LULC and LST maps.

3.1 Changes in Land Use Land Cover

Supervised classification through maximum likelihood estimation was applied using Landsat images' spectral bands to detect the change of LULC (1989-2019) patterns (Figure 2). The error matrix of this supervised classification showed an overall accuracy of 84.50, 89.50, and 91.00% in the years 1989, 2004, and 2019, respectively (Table 4).

Two trends in the changes of LULC have appeared in the findings (Figure 2 and Figure 3), such as (i) a continuous increase of built-up area and decrease of the water body; and (ii) an increase of bare soil between the first two periods, then decrease towards the third period. More specifically, built-up has become dominating land cover type in 2019, as it increased more than two times (578.50 ha) in the past 30 years (Figure 3, Table 6). The overall increase is 24.99%. Migration from rural to urban areas has resulted in population expansion, which is the main force behind the expansion in the built-up area. The built-up area's spatial growth pattern demonstrates substantial expansion in the South-East (SE) and North-West (NW) directions. In 2004, the growth towards the SE direction was 224.91 ha, which became 328.77 ha in 2019. In the case of growth towards NW direction, it was 158.58 ha in 2004 and increased to 277.02 ha in 2019 (Figure 4).

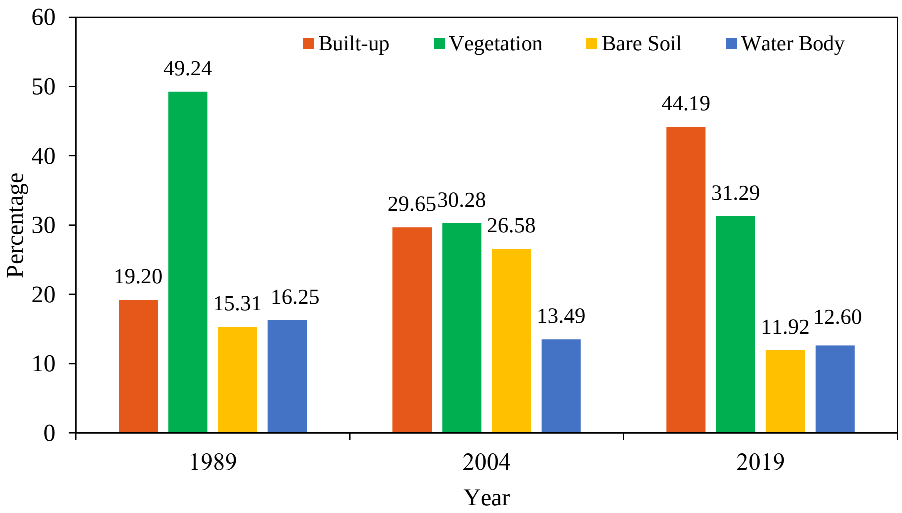

Figure 3. Percentages of LULC types in Mymensingh City (1989-2019)

The vegetation cover dominated the land cover category (1140.48 ha) in 1989, which experienced a reduction of about 415 ha by 2019. The Overall decrease in vegetation cover is 17.95% (415.80 ha) from 1989 to 2019 (Figure 3, Table 6). Bare soil was increased (261.09 ha) only up to 2004 and is decreased

339.48 ha from 2004 to 2019 (Table 6). Although bare soil fluctuated by showing both increases and decrease throughout the change, the overall decrease is 78.39 ha compared to the area in the first year to the area last year (3.38%) (Figure 3, Table 6). Among all the land cover types, the only water body has experienced a gradual decrease of 84.51 ha (3.65%) in the last three decades (Table 6).

The transition matrix is a sophisticated method to study LULC change in more detail, and it calculates the amount of inter-conversion between different forms of land cover. The results in Table 7 demonstrate that the Built-up area has gained land cover from vegetation (379.80 ha) and bare soil area (102.33 ha). Similarly, vegetation cover has also expanded by obtaining area from bare soil and water body. Besides, the bare soil has grown by gaining its maximum area from vegetation cover (91.08 ha), followed by the water body (82.98 ha). The transition matrix revealed that the vegetation and water body had been converted into bare soil, then the bare soil was quickly changed to a built-up area. In the same way, bare soil and water body have been transformed into vegetation cover. Also, significant portions of bare soil and water body are located in the adjacent river channel as sand bars and running water.

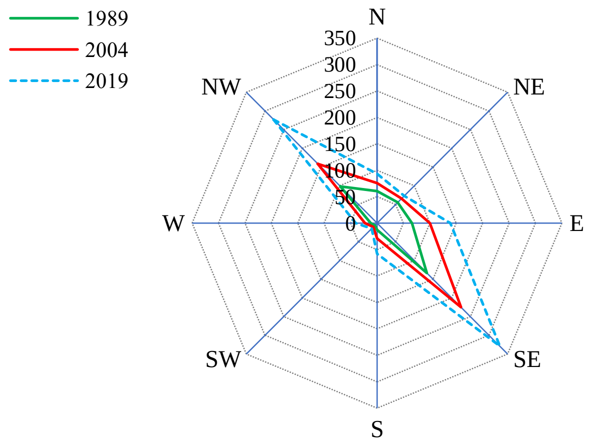

Figure 4. Spatial-temporal growth patterns of built-up area in 8 directions (in ha)

Table 6. LULC changes from 1989 to 2019

LULC Type	1989-2004		2004-2019		1989-2019	
	Area (in ha)	%	Area (in ha)	%	Area (in ha)	%
Built-up	242.10	10.45	336.60	14.53	578.70	24.99
Vegetation	-439.20	-18.96	23.40	1.01	-415.80	-17.95
Bare soil	261.09	11.27	-339.48	-14.66	-78.39	-3.38
Water body	-63.99	-2.76	-20.52	-0.89	-84.51	-3.65

Table 7. Transition matrix between LULC categories (1989-2019)

Conversion		Area (in ha)
Unchanged built-up		484.56
Vegetation	Built-up	379.80
	Unchanged	691.83
	Bare soil	91.08
	Water body	28.17
Bare soil	Built-up	102.33
	Vegetation	64.44
	Unchanged	57.24
	Water body	49.77
Water body	Built-up	22.50
	Vegetation	22.77
	Bare soil	82.98
	Unchanged	216.81

3.2 Changes in land surface temperature

The Spatio-temporal distribution of LST for 1989, 2004, and 2019 was calculated using thermal bands from Landsat data employing multiple techniques (section 2.5). The categorization of LST is helpful to get distribution in the area unit of different temperature ranges (Ahmed et al., 2013; Kafy et al., 2020). This study found that the temperature varies from 20 to 35°C, which was then classified into seven ranges (<21°C, 21°C to <23°C, 23°C to <25°C, 25°C to <27°C, 27°C to <29°C, 29°C to <31°C and ≥31°C). The spatial distribution of LST in different years is shown in Figure 5.

Different ranges of LST were found, such as 20.90°C-26.41°C, 22.52°C-29.71°C and 24.71°C-34.42°C, during the years of 1989, 2004, and 2019, respectively (Figure 5). In 1989, no regions had temperatures below 27°C, and the highest temperature coverage was below 23°C, as shown in Table 7. In 2004, the majority temperature zone shifted to 23-25°C (55.45%), which shows an overall increase of higher temperature zones. This upward trend continued in 2019, with a considerable portion of the study region (55.73%) shifting to higher temperature zones (27 to 29ºC). In 2019, no area remained in the lower temperature zones, which is noteworthy (Table 8).

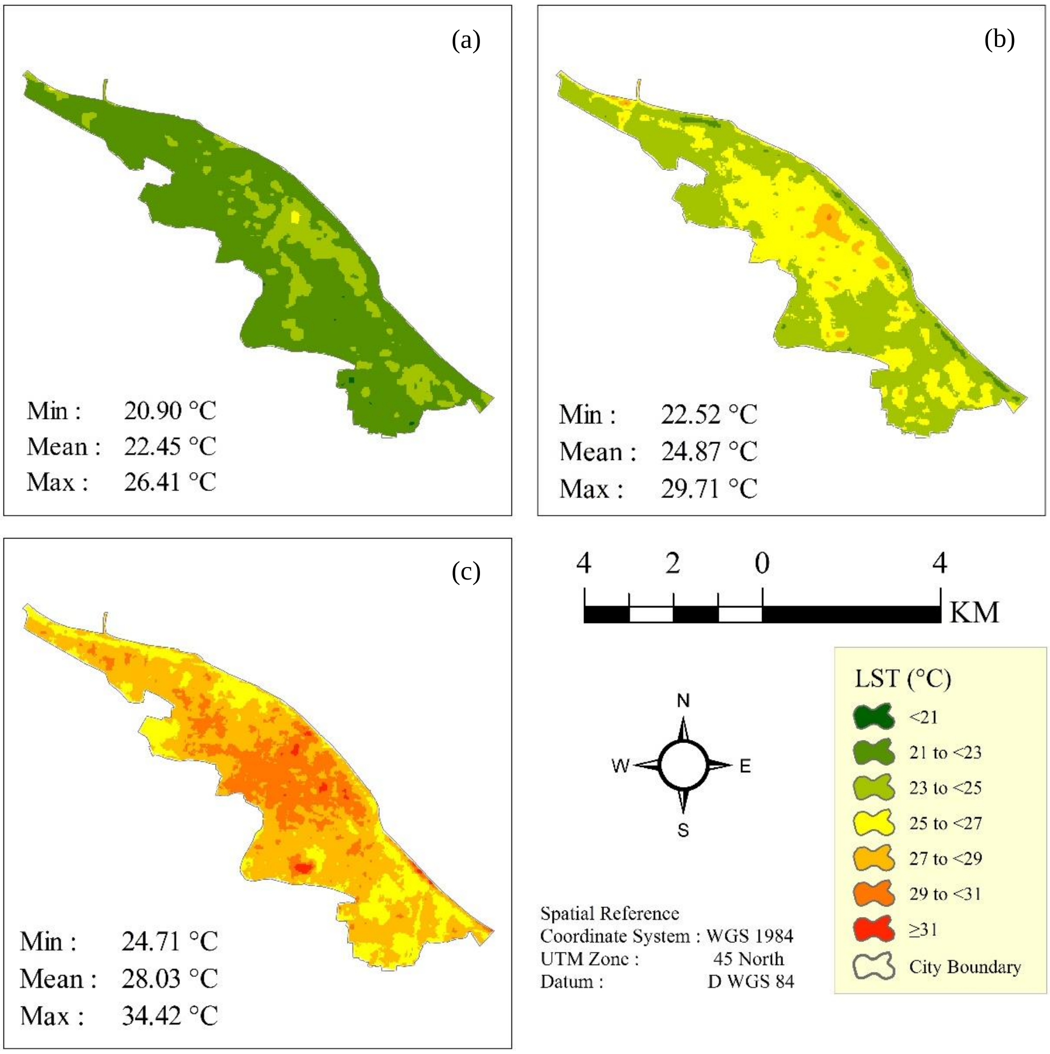

Figure 5. Spatial distribution of LST (1989-2019): (a) 1989, (b) 2004, and (c) 2019

Table 8. Distribution of LST amongst different classes (1989, 2004, and 2019)

Ranges of LST (ºC)	1989		2004		2019	
	Area	%	Area	%	Area	%
<21ºC	3.24	0.14	-	-	-	-
21 to <23ºC	1881.45	81.23	37.17	1.60	-	-
23 to <25ºC	395.55	17.08	1284.21	55.45	0.45	0.02
25 to <27ºC	5.94	0.26	887.40	38.32	484.56	20.92
27 to <29ºC	-	-	76.14	3.29	1290.78	55.73
29 to <31ºC	-	-	1.26	0.05	492.12	21.25
≥31ºC	-	-	-	-	18.27	0.79
Total	2316.06	100.00	2316.06	100.00	2316.06	100.00

3.3 Validation of LST data

Validation of calculated LST using in-situ measurements or any other satellite sensor is required to determine the correctness of LST data (Guha et al., 2019; Gazi et al., 2020). MODIS Terra data sets were used as a reference image in this research to validate LST values. The MODIS data are available from 2,000, and the MOD11A1 data with a spatial resolution of 1,000 m acquired during the same periods were used to validate the observed LST data. In order to integrate with Landsat LST, 1,000-m pixel size was resampled into 30-m pixel size (Guha et al., 2019). A total of 100 random points has been selected to correlate LST from the Landsat image with the MODIS image for 2004 and 2019. For the following reasons, there is some difference between the LST obtained from Landsat data sets and the respective MODIS data sets: (a) There is a 30 minutes interval between the Landsat sensors and MODIS sensors; (b) water vapor content; and (c) technique of resampling (Huete et al., 2010). Despite this, a moderately strong correlation has been observed between the calculated LST from Landsat data sets and MODIS data sets in 2019 and 2004 without any pre-processing (Figure 6).

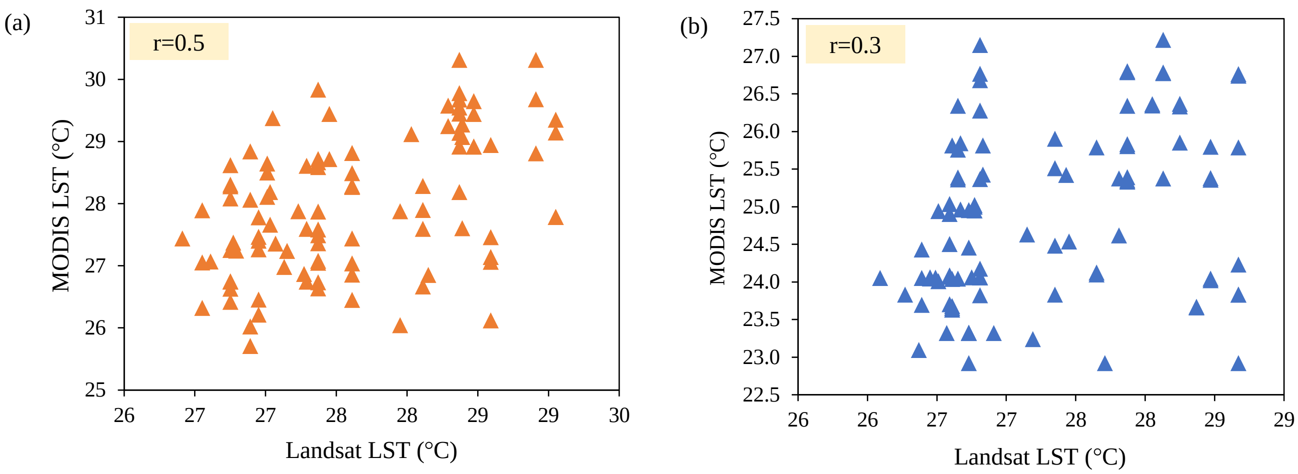

Figure 6. Validation of LST: (a) 2019 and (b) 2004

3.4 Relation between LULC and LST

Two approaches were applied to relate LULC with LST. The first one is zonal statistics between LULC categories and LST to assess variations of LST for each land cover type (Weng, 2001). Secondly, a correlation between biophysical indices and the LST of each year (Ahmed et al., 2013; Kafy et al., 2020; Rahman et al., 2017; Ullah et al., 2019).

For each land cover category, zonal statistics show the maximum, minimum, and average distribution of LST. Figure 7 shows the LST distribution with pixel numbers/frequency by LULC category of all three periods. In all three sampling periods, the built-up area has the highest LST compared to other LULC categories. The findings show that built-up regions have raised surface temperatures by replacing natural vegetation and water bodies with heat-prone, low-albedo, non-evaporating, and non-transpiring surfaces. Similarly, bare soil has higher LST in all parameters after the built-up category. On the contrary, both vegetation and water body have lower LST. For three decades, the overall LST of each land cover has been increased gradually with an average value of 5.75°C, 5.27°C, 5.31°C, and 4.91°C for built-up, vegetation, bare soil, and water body category, respectively. These data support the urban warming hypothesis; otherwise, natural LULC like plants and water bodies would not have experienced an increase in temperature. Similar urban micro-climatic warming scenarios were reported in other cities like Dhaka, Chattogram, and Rajshahi (Ahmed et al., 2013; Gazi et al., 2020; Kafy et al., 2020; Roy et al., 2020). The total LST of other surrounding land covers increased due to this gradual increase in warm land cover types, such as built-up and bare soil (Figure 7).

The correlation approach was used to quantify the strength of the associations between land cover indices and LST. The LST was correlated with each of the indices individually (Table 6). Among the indices, the UI and NDBI represent the built-up area; the BI and NDBaI belong to bare soil; and the NDVI and MNDWI represent vegetation and water body, respectively. Figure 8 shows both positive and negative correlations between biophysical indices and LST. According to the findings, the LST appears to be positively connected with UI, BI, NDBI, and NDBaI. NDVI and MNDWI, on the other hand, have a negative association. In the case of higher positive correlation, UI and BI were found suitable in each year (r>0.6) (Figure 8(a) and 8(b)). Among natural biophysical indices, the MNDWI, rather than the

NDVI, exhibited a strong negative connection (r<-0.25) with LST in each year (Ahmed et al., 2013; Kafy et al., 2020; Roy et al., 2020). In short, the UI, BI, and MNDWI values were found as significant determinants of LST as per the correlation test results. This research also revealed that the replacement of natural land cover by built-up and bare soil over long periods resulted in significant urban warming. On the other hand, the vegetation and water bodies exhibited lower LST as a natural land cover category (Figure 7 and Figure 8).

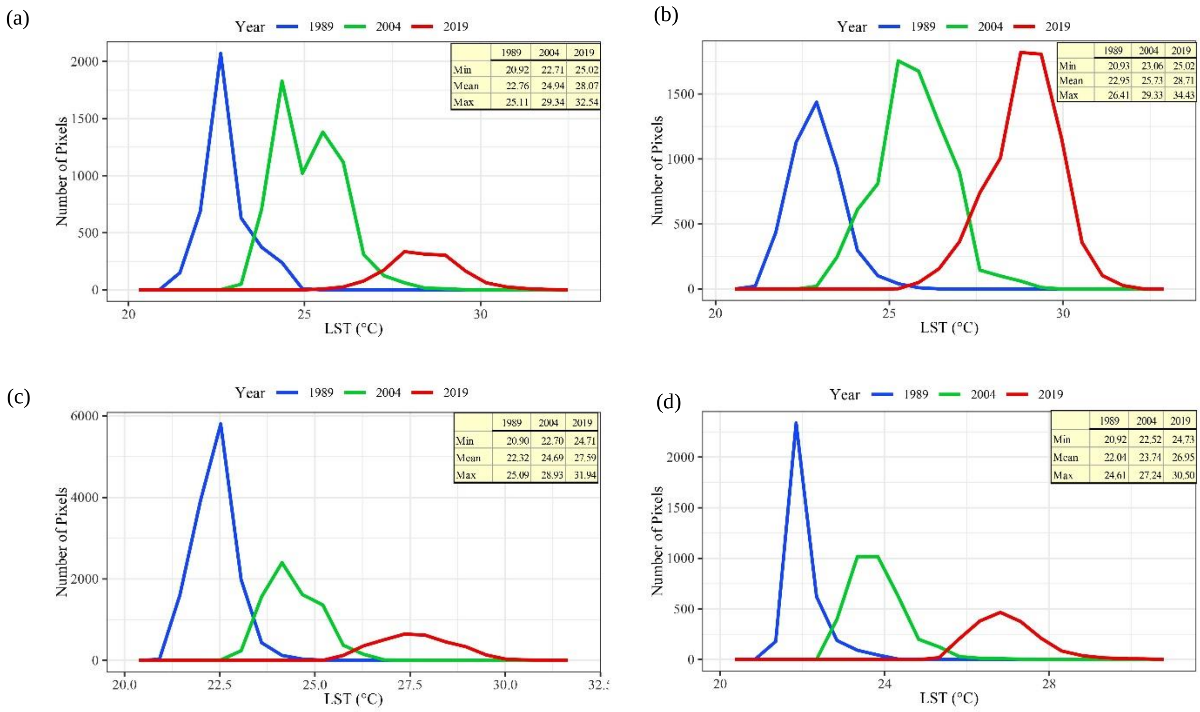

Figure 7. Variations of LST over different LULC types: (a) Bare soil, (b) Built-up, (c) Vegetation, and (d) Water body

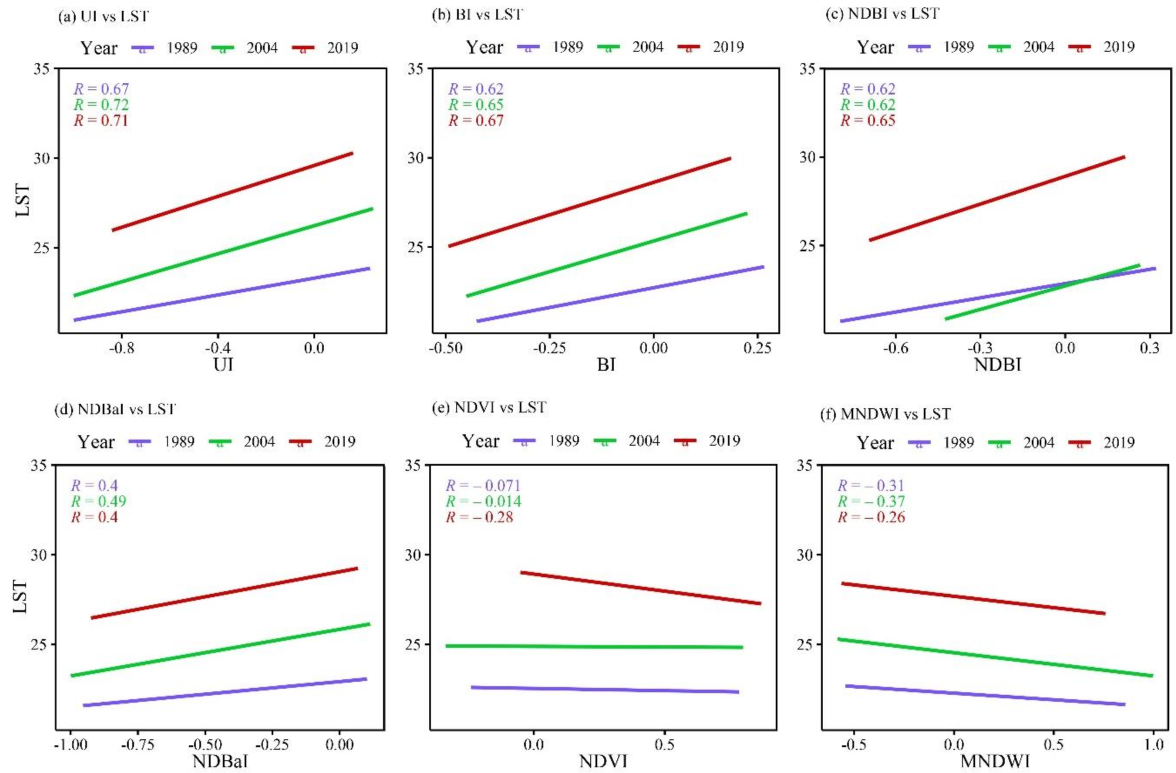

Figure 8. Correlation between biophysical indices [(a) UI, (b) BI, (c) NDBI, (d) NDBaI, (e) NDVI, and (f) MNDWI] and LST

3.5 Simulating the future LULC

The simulation of the future LULC of Mymensingh city is one of the objectives of this research. The MLP-MC Model was used to model the likely LULC scenario of 2034 using LULC maps from 2004 and 2019 (Ahmed and Ahmed, 2012; Corner et al., 2014; Kafy et al., 2020). The LULC simulation of the year 2019 was done as indicated in section 2.6 to get a valid LULC forecast for the year 2034 by MLP-MC. Kappa index statistics were used to test the correctness of the MLP-MC Model as part of the validation component. The statistics show that K_{no}, $K_{location}$, $K_{locationStrata}$, and $K_{standard}$ values were 0.8494, 0.7892, 0.7892, and 0.7240 (overall kappa), respectively. This model was utilized for LULC prediction after successful validation. A transition probability matrix was created by cross-tabulating two LULC maps from 2004 and 2019 in the MLP-MC analysis (Table 9).

According to the simulation results, in 2034, about 59.42 percent of the study area will be turned into a "built-up area" land cover type (Figure 9).

Table 10 shows the overall change statistics between observed land cover (in 1989 and 2019) and simulated land cover (in 2034). The built-up area will expand by 40.22 percent between 1989 and 2034, whereas vegetation, bare soil, and water body area will decline by 29.48 percent, 8.61 percent, and 2.13 percent, respectively. On the other hand, according to the 2019-2034 time-span, the built-up and water body category area will be increased by 15.23% and 1.52%, respectively. In contrast, the vegetation and bare soil area will be decreased by 11.53% and 5.22%, respectively. Although some portions of the water body will remain unchanged, the close or stagnant water bodies are more vulnerable to decrease than the river or running water body.

Table 9. Probability of LULC transformation change matrix (2004-2019) for 2034

	Built-up	Vegetation	Bare soil	Water body
Built-up	0.9921	0.0021	0.007	0.004
Vegetation	0.3247	0.522	0.1006	0.0527
Bare soil	0.4723	0.3264	0.1032	0.0982
Water body	0.1463	0.1627	0.2243	0.4668

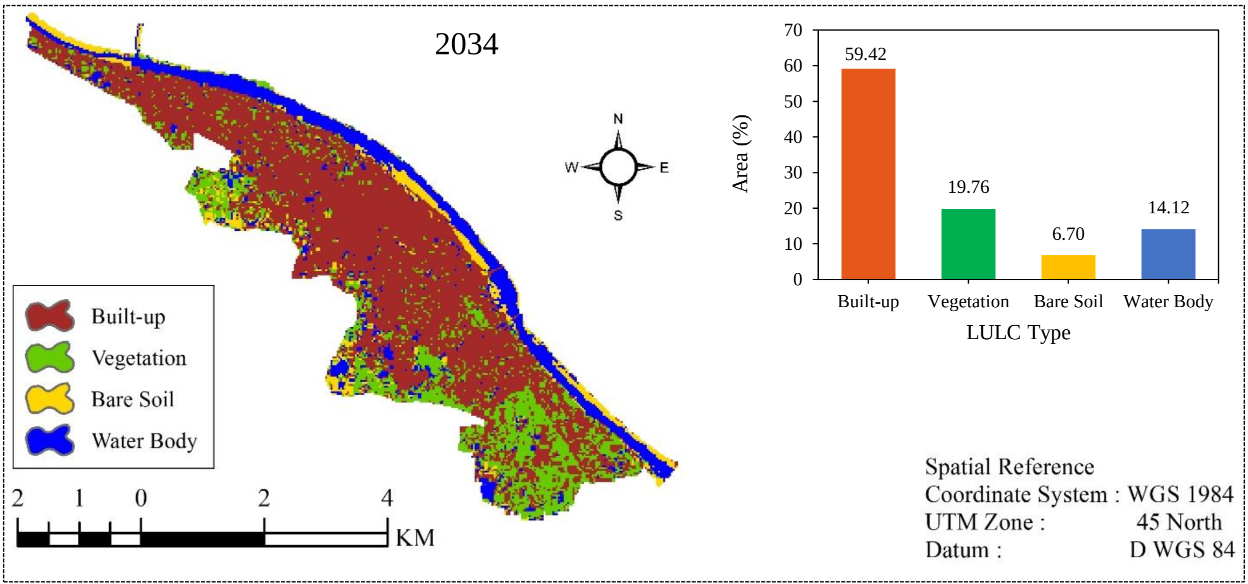

Figure 9. MLP-MC model simulated land cover map of Mymensingh city in 2034

Table 10. LULC statistics for the predicted year 2034

LULC Type	1989		2019		2034		Change (1989-2034)		Change (2019-2034)	
	Area	%	Area	%	Area	%	Area	%	Area	%
Built-up	444.69	19.20	1023.39	44.19	1376.10	59.42	931.41	40.22	352.71	15.23
Vegetation	1140.48	49.24	724.68	31.29	457.74	19.76	-682.74	-29.48	-266.94	-11.53
Bare soil	354.51	15.31	276.12	11.92	155.16	6.70	-199.35	-8.61	-120.96	-5.22
Water body	376.38	16.25	291.87	12.60	327.06	14.12	-49.32	-2.13	35.19	1.52

3.6 Simulation of LST for the year 2034

In ANN Model, the highly correlated biophysical indices like UI, BI, and MNDWI were taken as input layers with LULC types for the LST simulation process (Figure 8) (Kafy et al., 2020; Maduako et al., 2016). Since the ANN model requires training and testing data to construct a model and simulate, 2004 and 2019 were taken as training and testing data. Figure 10 shows the structure of the ANN model, having four input layers, three hidden layers, and predicted LST as the output layer.

The investigation indicated a considerable change in LST during a three-decade period, similar to the LULC change analysis. Therefore, the LST was simulated for the future year 2034. The predicted LST of 2034 shows that the LST will be increased by almost 8ºC from 1989 and 2ºC from 2019 on average (Figure 11). LST will exceed 29ºC in the majority of the city (59.64%). After that, 23.55% of the study area will have LST above 31ºC, and there will be no area below 25ºC LST.

To cross-validate, both simulated LST and LULC, the zonal statistics were calculated to assess LST variations over LULC (Figure 12(a)). The findings show that the built-up land use will have the highest LST (average, maximum) because of the increased built-up area found in the LULC prediction (Figure 12(a), Table 10). Although vegetation and water body tend to lower LST, the urban warming effect caused by increasing built-up areas will exaggerate the LST of vegetation and water body. Among all the LULC-LST distribution curves, the built-up and bare soil category will occupy a higher LST zone, whereas the water body category will be in the lower LST zone compared to the vegetation category (Figure 12(a)). Compared to all years' LST distribution curves, the simulated LST curve will move to a higher temperature zone (Figure 12(b)). As with LULC, the LST simulation model was also validated using a confusion matrix that shows the accuracy of 0.8697 and 0.9034 for training and testing data, respectively, which is a satisfactory level of accuracy for LST simulation.

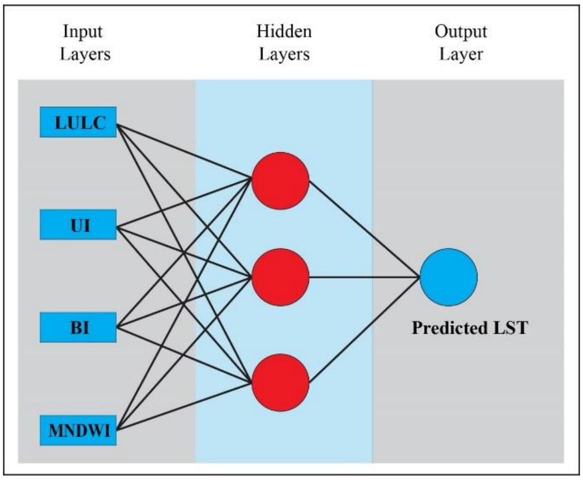

Figure 10. ANN model architecture

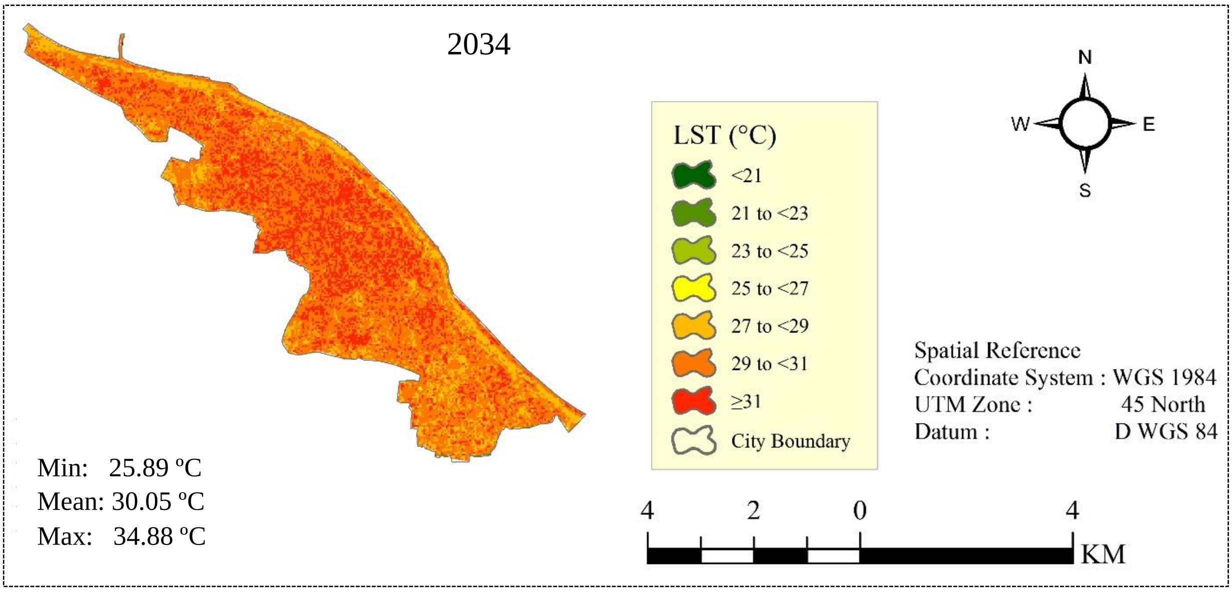

Figure 11. Simulated LST of the year 2034

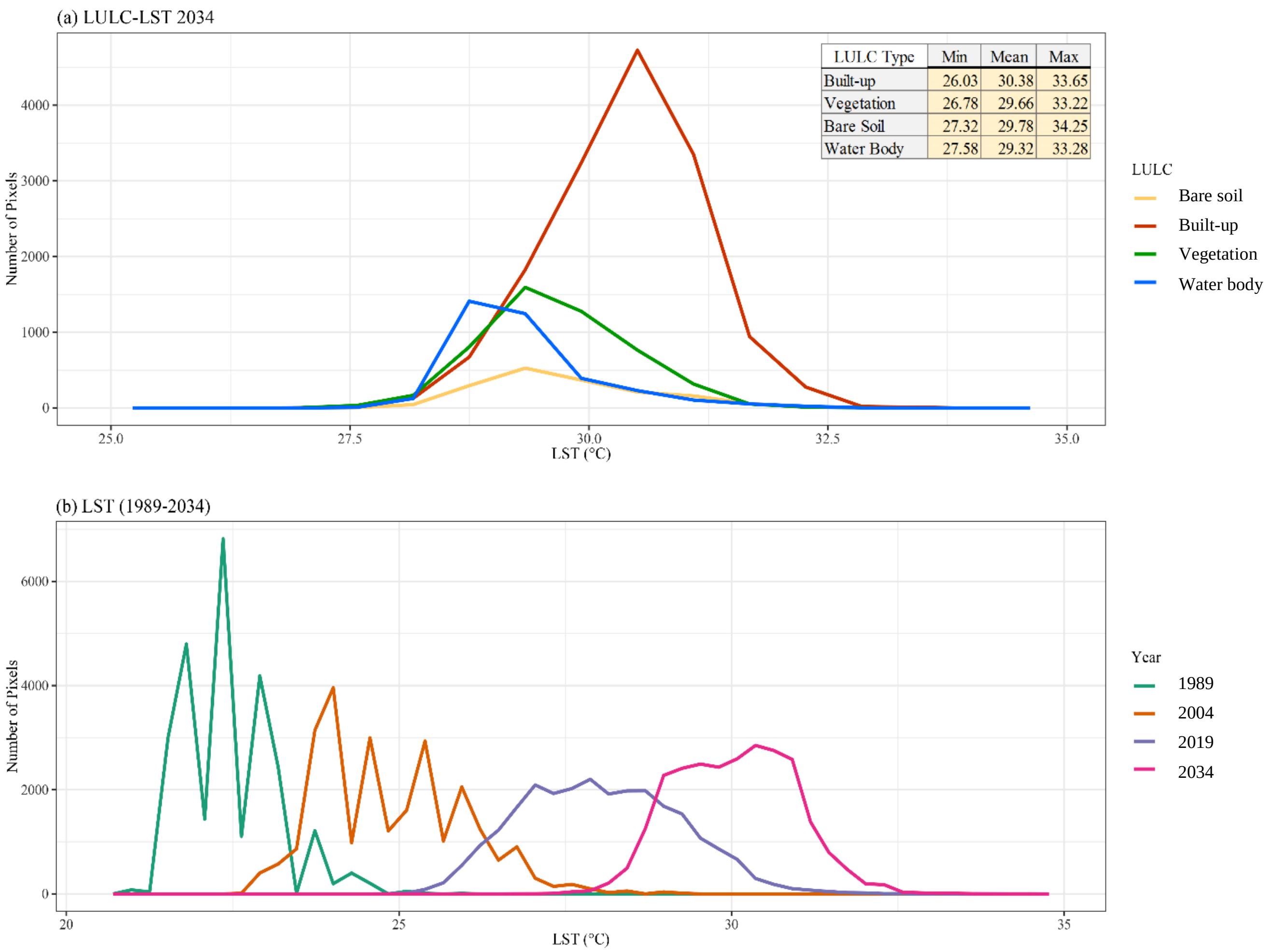

Figure 12. Simulated LST of 2034 (a) Zonal Statistics with predicted LULC 2034 and (b) variations of LST (1989-2034)

4. DISCUSSION

The effects of land cover changes on LST in the Mymensingh city region are modelled in this study for the year 2034. Several studies in Bangladesh have attempted to forecast both LULC and LST (Ahmed et al., 2013; Kafy et al., 2020). At first, both LULC and LST of Mymensingh city were studied for three different years (1989, 2004, and 2019). The MLP-MC model was used to forecast the future LULC in 2034. This study used zonal statistics and correlation to investigate the relationship between LULC and LST over three time periods to simulate LST. For all three periods, the analyzed correlations appeared to be compatible with the primary outputs indicated in the literature, such as (i) greater temperatures were found in built-up and bare soil regions, while lower temperatures were found only in vegetation and water bodies (similar results were found by Ahmed et al. (2013), Dewan and Corner (2014a), Kafy et al. (2020), and Roy et al. (2020)); (ii) correlation analysis showed a positive relation of LST with UI, BI, NDBI, NDBaI; and a negative relation of LST with other two biophysical indices (e.g., NDVI and MNDWI) considered in this study (similar results were also found by Ahmed et al. (2013), Kafy et al. (2020), and Roy et al. (2020)). Three biophysical indices (e.g., UI, BI, and MNDWI) and LULC types were chosen as input layers of the ANN model for LST prediction based on the observed association between LULC and LST. The prediction shows an increasing trend of the built-up category of LULC and temperature for LST on average, which is a sign of the rising effect of UHI in the upcoming future of Mymensingh city. In future predictions for other Bangladeshi cities, such as Dhaka and Rajshahi, a similar tendency to increase built-up area was found (Ahmed et al., 2013; Corner et al., 2014; Kafy et al., 2020). In the case of Bangladesh, rising built-up areas could be linked to both population increase and urbanization (BBS, 2011; Hasan et al., 2017). Urban sprawl caused by rapid urbanization will replace natural land covers like vegetation, bare soil, waterbody, etc., which is also found in the simulation of 2034 (Figure 9; Dewan and Corner, 2014b).

The built-up area has grown as a result of population increase and development. The vegetation cover and water body are low-cost lands that are easy to develop into an urbanized area. The trend of LULC change has been used to simulate future LULC, which revealed a drastic growth of the built-up area as a dominating LULC category. The built-up materials (i.e., solid brick) trap heat from solar radiation, causing the built-up surface to have higher LST. At the same time, anthropogenic heat like energy consumption, fossil fuel burning, etc., causes heat production. Similarly, bare soil also traps heat due to the absence of vegetation or greenery on it. On the other hand, the vegetation balances its body or surface temperature through the process of evapotranspiration (Solecki et al., 2005). The water body has a higher heat transfer capacity, which causes a lowering of its LST. A correlation between LST and biophysical indices has also validated or proved positive relation with built-up and bare soil and negative relation with vegetation and water body. The results show that the rise of the built-up area and the reduction of vegetation and water body area are critical contributors to the net increase in LST. Simulation of LST has shown an increase of LST due to the growth of the built-up area. The urban area has promoted the effect of UHI by decreasing natural land cover, including both terrestrial and aquatic (Li et al., 2012; Xu et al., 2009). The growth of UHI has detrimental consequences for humans, biodiversity, ecology, and the environment (Grimmond, 2007). Moreover, geographic location makes the Asian region face higher temperatures than the earth's average (IPCC, 2014). At the same time, due to global warming, the greenhouse effect, and changes in surface features, LST will rise even in non-urbanized places (Dereczynski et al., 2013; Kafy et al., 2020).

The impact of UHI expansion must be decreased in order to meet the SDGs 11 target of sustainable cities (Rosa, 2017). Recently, the greater Mymensingh district has been classified as a less disaster-prone zone by Bangladesh Delta Plan 2100, which is a positive sign of barrier-free development (Bangladesh Planning Commission, 2017). Therefore, sustainable urban development has to be assured through considering the issues related to LULC and LST change.

5. CONCLUSION

This study was carried out in Mymensingh City to assess changes in LULC and LST from 1989 to 2019. As per the study's objective, the prediction of LULC and LST was performed for the year 2034. The simulation of LULC shows that the vegetation, bare soil, and water body areas will decrease compared to their initial extent in 1989. Similarly, LST will be increased by 7.60°C on average. More than 29°C LST will likely be experienced by 83.2% of the total area. The built-up and bare soil LULC categories will have higher LST. It will create health, economic, and environmental problems for the city if this changing rate of LULC and LST goes upwards in the upcoming years. The findings of this study will be instructive for administrators, policymakers, and planners, who can make effective use of these study findings for sustainable development and formulation of a future master plan. Moreover, it is essential to establish rules, regulations, and strategies as a part of environmental conservation to keep LST within a reasonable level in the city. Future researchers may give attention to the microclimatic change in the city from the UHI perspective.

ACKNOWLEDGEMENTS

Authors are thankful to Md. Golam Mortoja for his cordial help in this study.

REFERENCES

Ahmed B, Ahmed R. Modeling urban land cover growth dynamics using multi-temporal satellite images: A case study of Dhaka, Bangladesh. ISPRS International Journal of Geo-Information 2012;1(1):3-31.

Ahmed B, Kamruzzaman MD, Zhu X, Rahman M, Choi K. Simulating land cover changes and their impacts on land surface temperature in Dhaka, Bangladesh. Remote Sensing 2013;5(11):5969-98.

Alam MK, Hasan AK, Khan MR, Whitney JW. Geological Map of Bangladesh [Internet]. 1990 [cited 2020 Mar 3]. Availabe from: https://pubs.usgs.gov/of/1997/ofr-97-470/OF97-470H/ofr97470H_geo.pdf.

Alam MS, Haque SM. Assessment of urban physical seismic vulnerability using the combination of AHP and TOPSIS models: A case study of residential neighborhoods of Mymensingh city, Bangladesh. Journal of Geoscience and Environment Protection 2018;6(2):165-83.

Al-sharif AA, Pradhan B. Monitoring and predicting land use change in Tripoli Metropolitan City using an integrated Markov chain and cellular automata models in GIS. Arabian Journal of Geosciences 2014;7(10):4291-301.

Anderson JR, Hardy EE, Roach JT, Witmer RE. A Land Use and Land Cover Classification System for Use with Remote Sensor Data. USGS Professional Paper 964. Sioux Falls, USA: United States Geological Survey; 1976.

Artis DA, Carnahan WH. Survey of emissivity variability in thermography of urban areas. Remote Sensing of Environment 1982;12(4):313-29.

Avdan U, Jovanovska G. Algorithm for automated mapping of land surface temperature using LANDSAT 8 satellite data. Journal of Sensors 2016;2016:Article No. 1480307.

Bahi H, Rhinane H, Bensalmia A, Fehrenbach U, Scherer D. Effects of urbanization and seasonal cycle on the surface urban heat island patterns in the coastal growing cities: A case study of Casablanca, Morocco. Remote Sensing 2016;8(10): Article No. 829.

Bangladesh Bureau of Statistics (BBS). Population and Housing Census 2011. Dhaka, Bangladesh: Ministry of Planning, Govt. of Bangladesh [Internet]. 2011 [cited 2020 Mar 3]. Available from: http://www.bbs.gov.bd/site/page/47856ad0-7e1c-4aab-bd78-892733bc06eb/Population-and-Housing-Census.

Bangladesh Meteorological Department (BMD). Climate Data Library [Internet]. 2019 [cited 2020 Mar 3]. Available from: http://datalibrary.bmd.gov.bd/maproom/Climatology /index.html.

Bangladesh Planning Commission. Bangladesh Delta Plan 2100. Dhaka, Bangladesh: Ministry of Planning, Govt. of Bangladesh [Internet]. 2017 [cited 2020 Apr 17]. Available from: http://www.plancomm.gov.bd/site/files/0adcee77-2db8-41bf-b36b-657b5ee1efb9/Bangladesh-Delta-Plan-2100.

Bokaie M, Zarkesh MK, Arasteh PD, Hosseini A. Assessment of urban heat island based on the relationship between land surface temperature and land use/land cover in Tehran. Sustainable Cities and Society 2016;23:94-104.

Bonafoni S, Anniballe R, Gioli B, Toscano P. Downscaling Landsat land surface temperature over the urban area of Florence. European Journal of Remote Sensing 2016;49(1):553-69.

Brammer H. Physical Geography of Bangladesh. Dhaka, Bangladesh: The University Press Ltd.; 2012.

Brammer H. The Geography of the Soils of Bangladesh. Dhaka, Bangladesh: The University Press Ltd.; 1996.

Butler K. Band Combinations for Landsat 8 [Internet]. 2013 [cited 2020 Feb 17]. Available from: https://blogs.esri.com /esri/arcgis/2013/07/24/band-combinations-for-landsat-8/.

Chander G, Markham B. Revised Landsat-5 TM radiometric calibration procedures and postcalibration dynamic ranges. IEEE Transactions on Geoscience and Remote Sensing 2003;41(11):2674-7.

Chander G, Markham BL, Helder DL. Summary of current radiometric calibration coefficients for Landsat MSS, TM, ETM+, and EO-1 ALI sensors. Remote Sensing of Environment 2009;113(5):893-903.

Chen XL, Zhao HM, Li PX, Yin ZY. Remote sensing image-based analysis of the relationship between urban heat island and land use/cover changes. Remote Sensing of Environment 2006;104(2):133-46.

Corner RJ, Dewan AM, Chakma S. Monitoring and prediction of land-use and land-cover (LULC) change. In: Dewan AM, Corner RJ, editors. Dhaka Megacity. Dordrecht, Netherlands: Springer; 2014. p. 75-97.

Dereczynski CP, Luiz Silva W, Marengo JA. Detection and projections of climate change in Rio de Janeiro, Brazil. American Journal of Climate Change 2013;2:25-33.

Dewan AM, Corner RJ. Impact of land use and land cover changes on urban land surface temperature. In: Dewan AM, Corner RJ, editors. Dhaka Megacity. Dordrecht, Netherlands: Springer; 2014a. p. 219-38.

Dewan AM, Corner RJ. Spatiotemporal analysis of urban growth, sprawl and structure. In: Dewan AM, Corner RJ, editors. Dhaka Megacity. Dordrecht, Netherlands: Springer; 2014b. p. 99-121.

Erener A. Classification method, spectral diversity, band combination and accuracy assessment evaluation for urban feature detection. International Journal of Applied Earth Observation and Geoinformation 2013;21:397-408.

Gazi MY, Rahman MZ, Uddin MM, Rahman FA. Spatio-temporal dynamic land cover changes and their impacts on the urban thermal environment in the Chittagong metropolitan area, Bangladesh. GeoJournal 2020;24:1-6.

Grimmond SU. Urbanization and global environmental change: Local effects of urban warming. Geographical Journal 2007;173(1):83-8.

Guha S, Govil H, Diwan P. Analytical study of seasonal variability in land surface temperature with normalized difference vegetation index, normalized difference water index, normalized difference built- up index, and normalized multiband drought index. Journal of Applied Remote Sensing 2019;13(2):Article No. 024518.

Han-Qiu XU. A study on information extraction of water body with the modified normalized difference water index (MNDWI). Journal of Remote Sensing 2005;5:589-95.

Hasan SS, Deng X, Li Z, Chen D. Projections of future land use in Bangladesh under the background of baseline, ecological protection and economic development. Sustainability 2017;9(4):Article No. 505.

Huete A, Didan K, van Leeuwen W, Miura T, Glenn E. MODIS vegetation indices. In: Ramachandran B, Justice CO, Abrams MJ, editors. Land Remote Sensing and Global Environmental Change. New York, USA: Springer; 2010. p. 579-602.

Intergovernmental Panel on Climate Change (IPCC). Climate Change 2014: Mitigation of Climate Change. In: Contribution of Working Group III to the Fifth Assessment Report of the Intergovernmental Panel on Climate Change. New York, USA: Cambridge University Press; 2014.

Jiménez-Muñoz JC, Sobrino JA, Skoković D, Mattar C, Cristóbal J. Land surface temperature retrieval methods from Landsat-8 thermal infrared sensor data. IEEE Geoscience and Remote Sensing Letters 2014;11(10):1840-3.

Kabir A. Mymensingh Strategic Development 2011-2035 [Internet]. 2015 [cited 2020 Mar 10]. Available from: http://msdp.gov.bd/reports/category/13.

Kafy AA, Rahman MS, Hasan MM, Islam M. Modelling future land use land cover changes and their impacts on land surface temperatures in Rajshahi, Bangladesh. Remote Sensing Applications: Society and Environment 2020;18: Article No. 100314.

Kayet N, Pathak K, Chakrabarty A, Sahoo S. Urban heat island explored by co-relationship between land surface temperature vs multiple vegetation indices. Spatial Information Research 2016;24(5):515-29.

Kikon N, Singh P, Singh SK, Vyas A. Assessment of urban heat islands (UHI) of Noida City, India using multi-temporal satellite data. Sustainable Cities and Society 2016;22:19-28.

Lai LW, Cheng WL. Urban heat island and air pollution: An emerging role for hospital respiratory admissions in an urban area. Journal of Environmental Health 2010;72(6):32-6.

Li YY, Zhang H, Kainz W. Monitoring patterns of urban heat islands of the fast-growing Shanghai metropolis, China: Using time-series of Landsat TM/ETM+ data. International Journal of Applied Earth Observation and Geoinformation 2012; 19:127-38.

Li ZL, Tang BH, Wu H, Ren H, Yan G, Wan Z, et al. Satellite-derived land surface temperature: Current status and perspectives. Remote Sensing of Environment 2013;131:14-37.

Maduako ID, Yun Z, Patrick B. Simulation and prediction of land surface temperature (LST) dynamics within Ikom City in Nigeria using artificial neural network (ANN). Journal of Remote Sensing and GIS 2016;5(1):1-7.

Maimaitiyiming M, Ghulam A, Tiyip T, Pla F, Latorre-Carmona P, Halik Ü, et al. Effects of green space spatial pattern on land surface temperature: Implications for sustainable urban planning and climate change adaptation. ISPRS Journal of Photogrammetry and Remote Sensing 2014;89:59-66.

Markham BL, Barker JL. Spectral characterization of the Landsat Thematic Mapper sensors. International Journal of Remote Sensing 1985;6(5):697-716.

McCarthy MP, Best MJ, Betts RA. Climate change in cities due to global warming and urban effects. Geophysical Research Letters 2010;37(9):Article No. L09705.

Mishra VN, Rai PK, Prasad R, Punia M, Nistor MM. Prediction of spatio- temporal land use/land cover dynamics in rapidly developing Varanasi District of Uttar Pradesh, India, using geospatial approach: A comparison of hybrid models. Applied Geomatics 2018;10(3):257-76.

Mishra VN, Rai PK. A remote sensing aided multi-layer perceptron-Markov chain analysis for land use and land cover change prediction in Patna District (Bihar), India. Arabian Journal of Geosciences 2016;9(4):Article No. 249.

National Aeronautics and Space Administration (NASA). NASA's Atmospheric Correction Parameter Calculator [Internet]. 2019 [cited 2020 Feb 17]. Available from: http://atmcorr.gsfc.nasa.gov/.

Pal S, Ziaul SK. Detection of land use and land cover change and land surface temperature in English Bazar urban centre. Egyptian Journal of Remote Sensing and Space Science 2017;20(1):125-45.

Qin Z, Karnieli A, Berliner P. A mono-window algorithm for retrieving land surface temperature from Landsat TM data and its application to the Israel-Egypt border region. International Journal of Remote Sensing 2001;22(18):3719-46.

Rahman MT, Aldosary AS, Mortoja M. Modeling future land cover changes and their effects on the land surface temperatures in the Saudi Arabian eastern coastal city of Dammam. Land 2017;6(2):Article No. 36.

Rashid KJ, Hoque MA, Esha TA, Rahman MA, Paul A. Spatiotemporal changes of vegetation and land surface temperature in the refugee camps and its surrounding areas of Bangladesh after the Rohingya influx from Myanmar. Environment, Development and Sustainability 2021; 23(3):3562-77.

Rosa W. Goal 11: Make cities and human settlements inclusive, safe, resilient, and sustainable. In: Rosa W, editor. A New Era in Global Health: Nursing and the United Nations 2030 Agenda for Sustainable Development. New York, USA: Springer Publishing Company; 2017. p. 339-44.

Rouf MA, Jahan S. Spatial and Temporal Patterns of Urbanization in Bangladesh. Urbanization in Bangladesh: Patterns, Issues and Approaches to Planning. Dhaka, Bangladesh: Bangladesh Institute of Planners; 2007. p. 1-24.

Roy DP, Wulder MA, Loveland TR, Woodcock CE, Allen RG, Anderson MC, et al. Landsat-8: Science and product vision for terrestrial global change research. Remote Sensing of Environment 2014;145:154-72.

Roy PS, Miyatake S, Rikimaru A. Biophysical spectral response modeling approach for forest density stratification. Proceedings of the 18th Asian Conference on Remote Sensing; 1997 Oct 20-24; Kuala Lumpur: Malaysia; 1997.

Roy S, Farzana K, Papia M, Hasan M. Monitoring and prediction of land use/land cover change using the integration of Markov chain model and cellular automation in the Southeastern Tertiary Hilly Area of Bangladesh. International Journal of Sciences: Basic and Applied Research 2015;24:125-48.

Roy S, Mahmood R. Monitoring shoreline dynamics using Landsat and hydrological data: A case study of Sandwip Island of Bangladesh. Pennsylvania Geographer 2016;54(2):20-41.

Roy S, Pandit S, Eva EA, Bagmar MS, Papia M, Banik L, et al. Examining the nexus between land surface temperature and urban growth in Chattogram Metropolitan Area of Bangladesh using long term Landsat series data. Urban Climate 2020;32:Article No. 100593.

Salisbury JW, D'Aria DM. Emissivity of terrestrial materials in the 3-5 μm atmospheric window. Remote Sensing of Environment 1994;47(3):345-61.

Scarano M, Sobrino JA. On the relationship between the sky view factor and the land surface temperature derived by Landsat-8 images in Bari, Italy. International Journal of Remote Sensing 2015;36(19-20):4820-35.

Sobrino JA, Jiménez-Muñoz JC, Paolini L. Land surface temperature retrieval from LANDSAT TM 5. Remote Sensing of Environment 2004;90(4):434-40.

Sobrino JA, Raissouni N. Toward remote sensing methods for land cover dynamic monitoring: Application to Morocco. International Journal of Remote Sensing 2000;21(2):353-66.

Solecki WD, Rosenzweig C, Parshall L, Pope G, Clark M, Cox J, et al. Mitigation of the heat island effect in urban New Jersey. Global Environmental Change Part B: Environmental Hazards 2005;6(1):39-49.

Trenberth KE. Rural land-use change and climate. Nature 2004;427(6971):Article No. 213.

Ullah S, Tahir AA, Akbar TA, Hassan QK, Dewan A, Khan AJ, et al. Remote sensing-based quantification of the relationships between land use land cover changes and surface temperature over the Lower Himalayan Region. Sustainability 2019; 11(19):Article No. 5492.

United Nations (UN). World Population Prospects 2019: Highlights. Department of Economic and Social Affairs [Internet]. 2019 [cited 2020 Mar 10]. Available from: https://www.un.org/development/desa/publications/world-population-prospects-2019-highlights.html.

United Nations (UN). World Population Prospects: The 2017 Revision, Key Findings and Advance Tables. New York, USA: The United Nations; 2017.

United Nations Human Settlement Programme (UNHABITAT). Urbanization and Development: Emerging Futures. World cities report. Nairobi, Kenya: United Nations Human Sttlements Programme; 2016.

United States Geological Survey (USGS). Changes to Thermal Infrared Sensor (TIRS) data. Landsat 8 OLI and TIRS Calibration Notices [Internet]. 2014 [cited 2020 Feb 5]. Available from: https://www.usgs.gov/land-resources/nli/landsat/landsat-8-oli-and-tirs-calibration-notices.

United States Geological Survey (USGS). Landsat 7 (L7) Data Users Handbook. South Dakota, USA: Earth Resources Observation and Science (EROS); 2019.

Van de Griend AA, OWE M. On the relationship between thermal emissivity and the normalized difference vegetation index for natural surfaces. International Journal of Remote Sensing 1993;14(6):1119-31.

Vani M, Prasad PR. Assessment of spatio-temporal changes in land use and land cover, urban sprawl, and land surface temperature in and around Vijayawada city, India. Environment, Development and Sustainability 2020; 22(4):3079-95.

Veronez MR, Thum AB, Luz AS, Da Silva DR. Artificial neural networks applied in the determination of soil surface temperature-SST. Proceedings of the 7th International Symposium on Spatial Accuracy Assessment in Natural Resources and Environmental Sciences; 2006 Jul 5-7; Portugal, New University of Lisbon: 2006. p. 889-98.

Voogt JA, Oke TR. Thermal remote sensing of urban climates. Remote Sensing of Environment 2003;86(3):370-84.

Weng Q. A remote sensing? GIS evaluation of urban expansion and its impact on surface temperature in the Zhujiang Delta, China. International Journal of Remote Sensing 2001; 22(10):1999-2014.

World Bank. World Bank staff estimates based on the United Nations Population Division's World Urbanization Prospects [Internet]. 2018 [cited 2020 Mar 10]. https://data.worldbank.org/indicator/sp.urb.totl.in.zs.

Xu H, Ding F, Wen X. Urban expansion and heat island dynamics in the Quanzhou region, China. IEEE Journal of Selected Topics in Applied Earth Observations and Remote Sensing 2009;2(2):74-9.

Yu X, Guo X, Wu Z. Land surface temperature retrieval from Landsat 8 TIRS: Comparison between radiative transfer equation-based method, split window algorithm and single channel method. Remote Sensing 2014;6(10):9829-52.

Zanter K. Landsat 8 (L8) Data Users Handbook Survey [Internet]. 2015 [cited 2020 Mar 10]. Available from: https://www.usgs.gov/core-science-systems/nli/landsat/landsat-8-data-users-handbook.

Zareie S, Khosravi H, Nasiri A, Dastorani M. Using Landsat Thematic Mapper (TM) sensor to detect change in land surface temperature in relation to land use change in Yazd, Iran. Solid Earth 2016;7(6):1551-64.

Zha Y, Gao J, Ni S. Use of normalized difference built-up index in automatically mapping urban areas from TM imagery. International Journal of Remote Sensing 2003;24(3):583-94.

Zhang F, Tiyip T, Kung H, Johnson VC, Maimaitiyiming M, Zhou M, et al. Dynamics of land surface temperature (LST) in response to land use and land cover (LULC) changes in the Weigan and Kuqa River oasis, Xinjiang, China. Arabian Journal of Geosciences 2016;9(7):1-4.

Glass Production from River Silica of Bangladesh: Converting Waste to Economically Potential Natural Resource

Mohammad Rajib[1*], Md. Fahad Hossain[2], and Mahfuza Parveen[3]

[1]*Institute of Nuclear Minerals (INM), Atomic Energy Research Establishment (AERE), Bangladesh Atomic Energy Commission (BAEC), Ganakbari, Savar, Dhaka-1349, Bangladesh*

[2]*Beach Sand Minerals Exploitation Centre (BSMEC), Bangladesh Atomic Energy Commission (BAEC), Kalatoli, GPO Box- 15, Cox's Bazar-4700, Bangladesh*

[3]*Department of Environmental Science and Disaster Management (ESDM), Daffodil International University (DIU), Daffodil Smart City, Ashulia, Dhaka-1341, Bangladesh*

ARTICLE INFO

Received: 2 Jul 2021
Received in revised: 16 Oct 2021
Accepted: 19 Nov 2021
Published online: 7 Dec 2021
DOI:10.32526/ennrj/20/202100124

Keywords:
Physical separation/ Bar sediment/ Silica/ Glass sand/ River dredging/ Gorai River/ Bangladesh

*** Corresponding author:**
E-mail:
rajib.mohammad@gmail.com

ABSTRACT

The Ganges-Brahmaputra river system at the Bengal Basin carries large amounts of sediments on the way to finally deposit at the Bay of Bengal. Those river-transported sediments form bar deposits during dry season in many areas of Bangladesh and accumulate economic mineral depositions at suitable geological environments. Dredging is a must for most of those rivers for proper navigation, as well as protecting bank erosion, which generates millions of tons of waste sand. The dredged materials from river beds are mostly composed of silicate minerals, especially quartz and feldspar along with several dark colored heavy minerals. Like the industrial processing of heavy minerals from bulk sands, various physical separation techniques can be utilized for the beneficiation of silica from those river-born silicate minerals in dredged sands. Those silica have been successfully upgraded to near-glass sand grade in the laboratory, however, they have yet to be utilized for any kind of commercial venture. The present study attempts characterization of several river sands through physical separation and laboratory analysis. The upgraded silica was successfully compared with several quality glass sands and laboratory production of glasses. This experimental production of glass from upgraded silica could potentially be economical considering its industrial application with positive environmental consequences through minimizing the dredging cost, increasing the navigability of the river and ecological balance along the flood plain.

1. INTRODUCTION

Bangladesh, the major part of the Bengal Basin, is comprised of hundreds of rivers, originating from the Himalayan mountain ranges in the north. The great Ganges-Brahmaputra-Meghna (GBM) river system carries billions of tons of sediment from Himalayan ranges into Bangladesh (Garzanti et al., 2004). Annual suspended sediment load of this river system is estimated to be 1.0-2.4 billion tons (Rahman et al., 2018). Due to flat geomorphology of the basinal area, currents deposit their bed load at the river bank areas during monsoons. In the dry season, those depositional areas become exposed in the form of numerous bars even at the middle of the river course. These bars can be as thick as 44 meters (Rahman et al., 2020) at places. Being a riverine country, Bangladesh still uses many of its river routes for communication purpose. Because of this, proper navigation of those rivers is very important for a smooth transportation system. For that purpose, dredging is a must in all major rivers which involves both cost and manpower. Every year, Bangladesh needs to spend substantial amount from its annual budget to keep the rivers running with sufficient water at its navigation routes. As a consequence, dredging is very much common in all major rivers. However, till now, the dredged materials are used for mostly earth filling and construction like conventional purposes. In many instances, dredged materials are kept in the vicinity of the river, from where they return to the same place in next monsoon.

Citation: Rajib M, Hossain MF, Parveen M. Glass production from river silica of Bangladesh: Converting waste to economically potential natural resource. Environ. Nat. Resour. J. 2022;20(2):129-136. (https://doi.org/10.32526/ennrj/20/202100124)

Which means, most parts of the dredging materials becoming wastes of large volume. Therefore, an alternate economic utilization of this waste or dredged materials would be significant findings for the country.

As stated earlier, Bangladesh has one of the largest river systems of the world. Some of the rivers are meandering, some are braided. Because of low gradients and high sediment loads, the riverbeds of most of the rivers in Bangladesh aggrades very quickly, which becomes a major environmental concern. Riverbed aggradation is so pronounced in Bangladesh that changes in riverbed level can be observed during one's lifetime. For example, the Old Brahmaputra was navigable for steamers only about 30 years ago, and is presently almost an abandoned channel. This situation is true for many other distributaries of the Ganges and Meghna, such as the Madhumati, the Bhairab, the Chitra, and the Ghorautra. The lesser water flow can also be caused by the low rainfall in the upstream area but it is reported that rainfall didn't decrease significantly during recent decades. Main causes of siltation or sedimentation in Bangladesh rivers are the control on natural water flow in the upstream area by artificial barriers, e.g., dams. The average sediment load of the Ganges-Brahmaputra river system has declined from 2.4 billion tons/year (67% delivered by the Ganges) to 1.6 billion tons/year (Milliman and Meade, 1983) since the diversion of the Ganges through the Farakka-Barrage damming project. From the border with India to the point where the Ganges meets the Brahmaputra, the riverbed has aggraded as much as 5-7 meters in recent years (Alexander, 1989). The aggradation causes several problems, such as flooding, unwanted erosion and deposition, destruction of navigation route, imbalance of ground water level, ecological hazards, decrease of fish and other resources, and saline water intrusion in coastal areas.

Only way to solve the river bed aggradation problem is to remove the excessive sediment to increase the water carrying capacity of the rivers. This can be done by dredging and re-excavation of rivers. Continuous dredging of the rivers and channels and dispersion of the dredged sediments on the delta plain will not only increase the capacity of the rivers, but also increase the elevation of the land. Understanding the importance, the Government of Bangladesh has planned to take a 15-year action plan for proper river management and dredging, called Capital Dredging, to carry out dredging in all the major rivers of Bangladesh. The spoil management from the dredged rivers is also taken into consideration in the action plan. Hence, properly planned dredging of the river beds can be of huge positive impact to the national economy, by retrieving the rivers to their natural flows as well as using industrial minerals. The natural flow of rivers will largely reduce several major environmental problems of Bangladesh.

River sediments are rich in silicate minerals. In Bangladesh, most river sediments contain around 80-85% quartz and feldspar (Jasy et al., 2010). Fresh quartz (SiO_2) is the raw material for glass production, which contains 95.0 to 99.9% quartz depending on various good quality glasses. The percentage of SiO_2 varies in different qualities of glass with varying proportion of iron, aluminum, calcium and magnesium oxides (Norton, 1957). Upgradation of silica percentages in regular river bar sands of Bangladesh by physical separation were carried out and successfully compared with a few glass sand deposits (Rajib et al., 2009; Hossain et al., 2013). Laboratory scale glass production by such upgraded silica sand was possible as well (Rafi et al., 2018). Moreover, silicon chip production from placer silicon is also reported, provided that SiO_2 percentage can be upgraded in an appropriate quantity (Marshall, 2016). In view of those potentials, the objective of the present study was to upgrade river silica by widely used density, magnetic and electric separation techniques. In addition, characterization of those upgraded silica as an alternate of glass sand to produce glass was also attempted. Possible environmental consequences were discussed based on the potential commercial extraction of river sands.

2. METHODOLOGY

Bangladesh, a small country of 144,000 km^2. located at the tip of Bay of Bengal. The country is comprising of mostly deltaic sediments coming from the GBM river system. Padma (Ganga is the name at the upstream part in India) is one of the main rivers of the country entering from west to meet with Meghna at the middle part of the country. Gorai is the tributary of the River Padma, separating at the middle of its course in the country (Figure 1).

River dredging is a must for all major rivers of Bangladesh, especially for keeping the navigation route alive. As stated earlier, dredged materials are kept within the river banks (Figure 2), therefore, requires continuous dredging for success. Sand samples were collected from several major rivers of

Bangladesh (Figure 2(a), 2(b), and 2(c)) where bar deposition is quite frequent and dredging is being done continuously. Those bars are very much temporary deposition and inundates every year during rainy season. In next monsoon, they erode by flood water, and deposits again to become exposed during summer. Such phenomena can be found in both braided and meandering rivers which eventually narrow down the natural navigability.

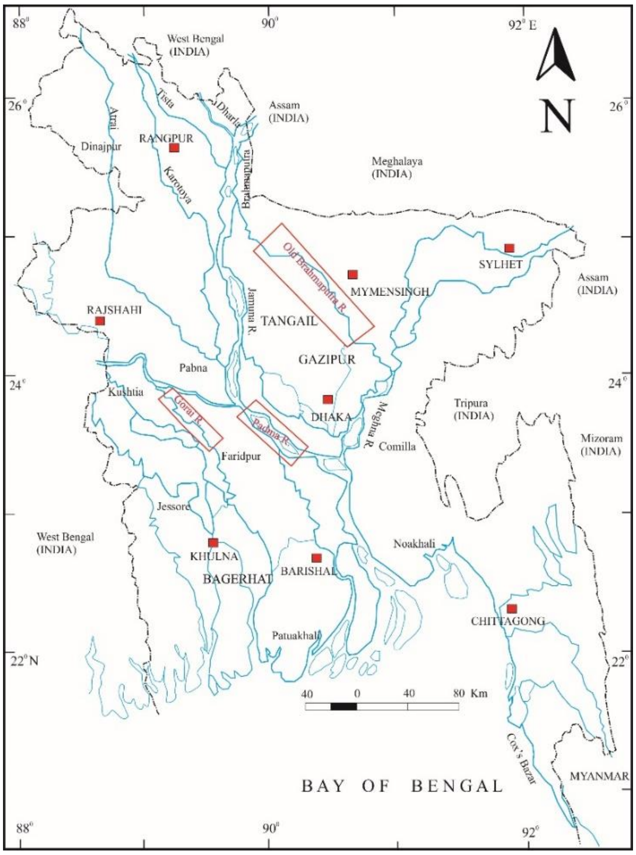

Figure 1. Location of sampling areas, as shown by red rectangles, in the context of major rivers of Bangladesh. Here, the Brahmaputra is designated as 'old' as the course is shifted during a major earthquake in 150 years ago. The current course of Brahmaputra is named as Jamuna.

Approximately 200 kilograms of raw sand samples were collected from near surface deposition, approximately within a meter by hand auger, indicating the recent most sand deposition (Figure 2(f)). The total number of samples was 10. Six samples were from Gorai River covering 14 kilometers from upstream to downstream. The other four samples were from Brahmaputra and Padma Rivers. The sand augers are of 5 feet length with a designed bottom part to collect disturbed samples as it goes down. A column of 3-5 feet sands was collected from each point, which were mixed properly to get representative samples for laboratory separation.

Samples were first washed to remove the clay materials and later sieved through 400 and 63 µm mesh size to get rid of grains other than sands. This discarded fraction includes most of the larger grains of flaky micaceous minerals. Thereafter, shaking table, induced roll magnetic separator (IRMS) and electrostatic plate separator (ESPS) were used as gravity, magnetic and electric separators, respectively, for the enrichment of silica content. Figure 3 represent the standard method of separating heavy and light minerals from placer sands which has long been used in various countries like Australia, India, Brazil, etc. A pilot plant with a quality control laboratory is set up based on this separation procedure at Beach Sand Minerals Exploitation Centre of Bangladesh Atomic Energy Commission at Cox's Bazar, the major tourist place at the coastal district of Bangladesh. The variables of the separators were adjusted according to results obtained as checked by a standard binocular microscope for the quartz percentage in the sample. Such procedure was successfully applied to upgrade silica from river sand in a previous study (Rajib et al., 2009).

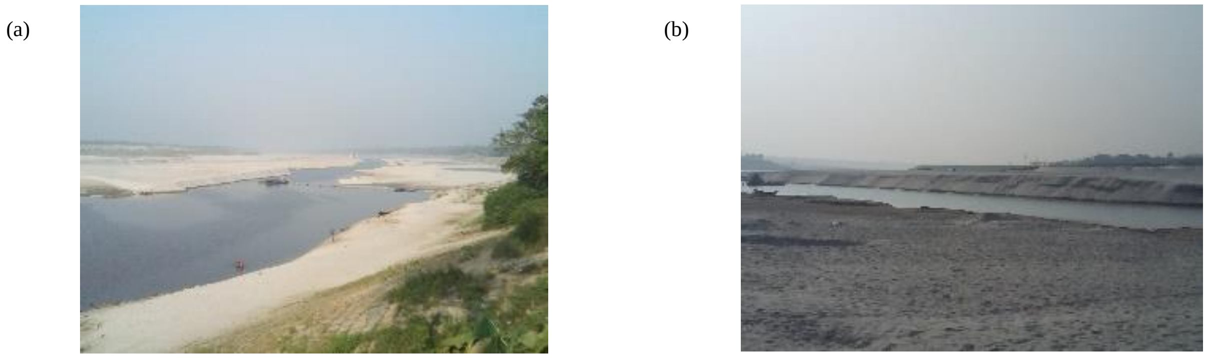

Figure 2. Bar sediments at the middle of major rivers of Bangladesh at (a, b, c) Gorai and (d) Padma rivers during summer. The pictures also represent the dredged sands are kept just beside river which returns to the dredging place in monsoon. Very bright colored sand at Gorai River (e) represents high amount of quartz or silica. Sampling with hand augers (f) is a standard method of collecting sand from shallow depth.

Figure 2. Bar sediments at the middle of major rivers of Bangladesh at (a, b, c) Gorai and (d) Padma rivers during summer. The pictures also represent the dredged sands are kept just beside river which returns to the dredging place in monsoon. Very bright colored sand at Gorai River (e) represents high amount of quartz or silica. Sampling with hand augers (f) is a standard method of collecting sand from shallow depth (cont.).

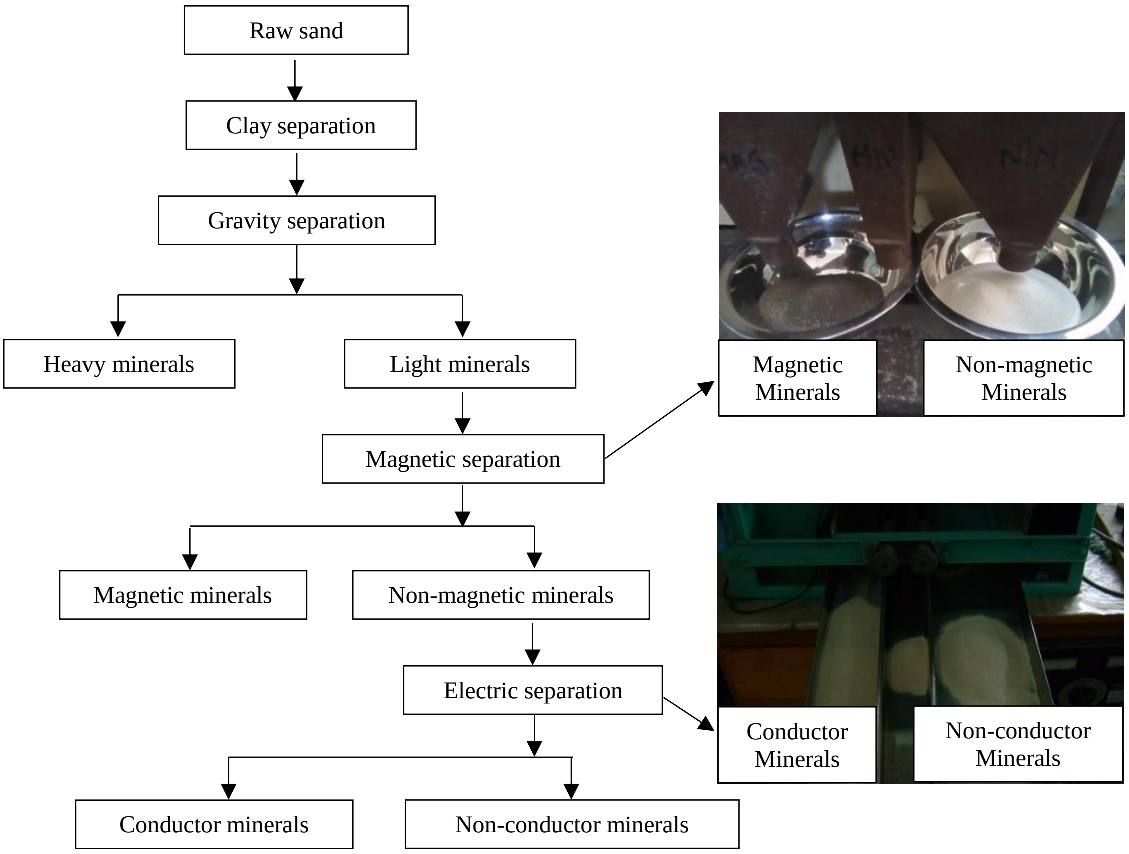

Figure 3. Generalized flow chart of the physical separation of river bar sand. The photographs show (top) white colored silica and feldspar rich part separated from dark colored magnetic minerals at magnetic separator and (bottom) white colored magnetic minerals were separated using electric separators to obtain silica-rich fractions at non-conductor part.

3. RESULTS

Silica content of river sand samples from several rivers, around 60-70%, could be enriched significantly by following a standard flow chart of physical separation procedure (Figure 3). The upgraded silica was analyzed for the grain size distribution and found to be mostly (97-98%) of more than 150 µm size (Table 1). Chemical composition (Table 2), determined by the commercial wet process revealed 86-88% SiO_2 with reasonably low percentages of oxides of K, Na, Fe, Ca, Mg, and Ti. However, alumina content was found to be significantly high (more than 7.5%). The recovery of upgraded silica from bulk sand was approximately determined as 65-70%.

Table 1. Grain size distribution of upgraded silica

Sample area	>350 mesh (%)	>150 mesh (%)	<150 mesh (%)	Total
Gorai sand	0	97.43	2.57	100.00
Padma sand	0	98.81	1.19	100.00

Table 2. Composition of upgraded silica sand by commercial wet process

Testing parameters	Gorai sand	Padma sand
SiO_2	86.68	86.96
Al_2O_3	7.65	7.58
CaO	1.78	1.58
MgO	0.29	0.34
Fe_2O_3	0.14	0.12
Na_2O	1.14	1.13
K_2O	1.23	1.22
TiO_2	0.051	0.078
Cr_2O_3	0.00124	0.00135
LOI	1.03	0.97
Total	99.99	99.98

Values in %; LOI-loss on ignition

Glass making with this upgraded silica were successfully attempted with slight modification of standard composition. The newly made glass was found to be free from bubbles and any un-melted grains which are two of the most important criteria of quality glass production (Figure 4).

4. DISCUSSION

Beneficiation of dredged materials from river sediments is not new, especially for the production of rare earth elements (REEs) containing minerals [e.g., Moscoso-Pinto and Kim (2021)]. Placer sands from the beach depositions are more common for this purpose (Kumari et al., 2015; Jordens et al., 2013). Although, utilization of light minerals, especially silica sands for any commercial purpose is not so common, except those from quartz sand or glass sand deposits (Pisutti et al., 2009).

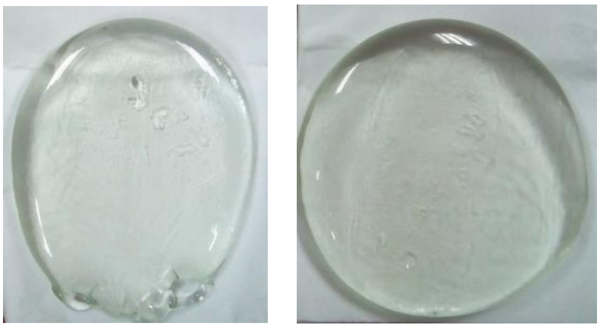

Gorai glass Padma glass

Figure 4. Laboratory production of glass from the upgraded river-born silica with various composition

The physical upgradation of silica from bar sediment was successful using various separators. After separating from bulk sands using gravity separators, light minerals are taken for further magnetic separations under electro-magnetic field suitable for dark colored minerals remaining from heavy minerals. For Bangladesh rivers, the non-magnetic part mostly composed of quartz and feldspar which needs to be further separated using electric separators under various electric field. The non-conductor part is supposed to be mostly quartz, although the conductor part also contains substantial amount of quartz grains due to their very close nature with feldspar, as shown in Figure 3 by similar color fractions at electric separation. The composition of the upgraded silica (from non-conductor minerals fraction) with the presence of very low Cr is comparable with a few quality glass producing sands of Bangladesh (Islam, 1985; Islam, 1986; Imam, 1996). Approximately 98% of the upgraded silica sand was also found to be more than 150 mesh (i.e., appx. 90 µm size) which is also within the range of a few glass producing sand grades (Rajib et al., 2009). The industrial grade glass sands generally use within the range of 100-600 µm grains, whereas, silica sands in one glass sand deposit of Bangladesh shows the size of 100-500 µm (Islam, 1985). The upgraded silica sand from Gorai River was found to be 100-300 µm in size which is even better sorted for industry operation for glass production.

As far as the chemical composition of industrial grade glass sand is concerned, the upgraded river silica is lacking in few parameters by quite a good margin. For example, the minimum quantity of SiO_2 needed for average quality glass production is around 95% (Norton, 1957). The glass sand deposits of Bangladesh from where local industries are collecting sands have more than 90% in-situ silica content. However, laboratory scale upgradation was possible from Gorai River sand previously (Rajib et al., 2009). Although glass production was not possible due to the small quantity of samples, the present attempt of utilizing larger quantity sands ended with less quantity SiO_2 content, but successful glass production. The reason for different chemical composition with less silica and high alumina content could be due to difference in measurement procedure. For example, previous work was entirely a laboratory scale analysis and therefore recycling of sample was possible due to small quantity sample. Sample recovery percentage was not considered significantly. The chemical composition was analyzed by X-ray fluorescence spectrometry. On the contrary, the present study was aimed to analyze the commercial aspects where glass production possibility with reasonable recovery percentage was considered. Therefore, samples were not recycled, which yielded less silica content. Moreover, these sands are deposited just from last year's flood, which may have changed composition from the previous study.

Although the obtained results are not suitable for the best quality of glasses, as sought by the most glass companies, however, they could be useful for producing intermediate quality glasses with high alumina content which may have economic use. For example, in typical float glass compositions, the oxides of silicon, sodium, calcium and magnesium account for around 98% of the glass [SiO_2: 72.6%, Na_2O: 13.6%, CaO: 8.6%, and MgO: 4.1%, as stated in Glass for Europe (2020)]. In that context, the studied upgraded silica is well behind in total composition, although, only silica content is well above the margin. However, a method for preparing aluminate glasses and glass-ceramic composites opens up new possibilities for generating mechanically strong structural components and high-hardness coatings (McMillan, 2004). Therefore, the present upgraded silica with high natural alumina content might have a good potentiality in glass making industry. Although, high silica content may decrease the density and phase transition temperature of the glass with minimum thermal expansion (Deshpande and Deshpande, 2009).

In addition to silica content, river sands of Bangladesh generally contain other valuable heavy minerals of significant quantity, approximately 4.5-17.0 wt% (Rahman et al., 2014, Rahman et al., 2016). During the process of industrial production of glass making silica sand, those heavy minerals could be important by-products. In Bangladesh, individual heavy mineral separation from such types of river sands has already been found successful (Rahman et al., 2015).

The deposition of bar sediments every year on both sides of the rivers makes significant morphological changes at the fluvial environment. This environment is very important for natural navigability of the river throughout the year. However, because of excessive sand deposition, most of the rivers are inaccessible for river transport, even in rainy season due to lack of water depth. As a result, each year, a huge amount of financial involvement is necessary simply for dredging to obtain minimum navigability. The Bangladesh Water Development Board has estimated that the capital dredging and river management works of the country would involve over 36 billion m^3 of dredging in 23 big rivers needing a budget of nearly BDT 1 million Crore. The government of Bangladesh is planning a 50-year mega plan of capital dredging to bring back navigability in rivers, including the Padma, the Meghna and the Jamuna, and reports that approximately BDT 31,000 would be needed which short, mid and long term phases. As stated earlier, Bangladesh's rivers carry approximately 2 billion tons of sediments in their waters every year, a significant portion of which can be utilized as mineral resource by proper planning and execution. The dredged materials are mostly composed of silicate minerals, especially quartz and feldspar along with various dark colored heavy minerals. Various physical separation techniques can be utilized for the beneficiation of both silica and heavy minerals from those river-born silicate minerals (Figure1). At the Bangladesh Atomic Energy Commission (BAEC) price of Tk. 10,000 per ton of magnetite or ilmenite to up to Tk. 60,000 per ton of zircon, those minerals in river sediments could be worth several thousand crores. For example, BAEC estimated the economic heavy minerals reserves at beach areas of Bangladesh of about 1.76 million tons which has a present market price of nearly 2,000 crore taka. Considering the volume of river dredged materials and amount of economic minerals in them, separation of minerals could be economically feasible. Besides, the ecological environment of the riverine area is also significantly changed due to the huge deposition of silts and sands.

Therefore, if such beneficiation of river silica could be commercially possible, it will facilitate the use of a huge quantity of river sands of the country. Mining of these silica sands from river beds and bars will also minimize the dredging cost which is a must in almost every major river of the country. Automatic dredging will enable the river navigation as well as maintaining the environmental balance of the flood plain. Increasing the navigability of the river would also reduce the flood risk and bank erosion which are major problems during monsoon season at several rivers. These would not only work as value addition, but also contribute to various aspects of SDGs and the Delta Plan-2100 of Bangladesh. Moreover, different other valuable heavy and light minerals, which have variety of industrial uses, can be produced as byproducts from the upgradation processes. Removal of those excess sands from river banks could have therefore significant importance for the overall socio-economic development of the country.

5. CONCLUSION

The study presents the beneficiation of a waste materials which could turn out to be a potential natural resource in the river depositions. The rivers in Bangladesh carry ample sediment for dredging and dispersion on the flood plains. These sediments are mostly sand sized and not only full of very economic mineral like quartz or silica but also include heavy minerals like ilmenite, magnetite, garnet, pyroxene, hornblende, and zircon, etc. All these minerals have familiar industrial uses. Hence, the river bars, formed by the excessive sedimentation, are full of natural resources which need to be properly studied. Upgraded silica from those river bar sediments was successfully utilized in producing glass with a small batch (less than 1,000 gm). Therefore, bench scale glass production (with approximately few tens of kg) is necessary before going for any pilot-plant scale experiment. Industrial use of such type of silica sand to produce different types of glasses will lead to the discovery of alternate glass sand deposits in Bangladesh. In addition, commercial utilization of a ‘rejected’ or waste material would boost the local industry as well as convert the enormous deposit of river sediment to a natural resource. Besides, proper solution of excessive sedimentation problem by dredging and re-excavation of rivers will benefit Bangladesh and similar countries in many other ways, e.g., reducing the severity of flood, retrieving navigation routes, natural resource recovery, reducing groundwater vulnerability risk, creating natural shield against sea level rise due to climate change, saline water intrusion, and overall ecological balance. Therefore, having an enormous source of river bar sediments in most of the major rivers in the country, Bangladesh could have potential resources of industrial grade, provided the proper management of the materials.

ACKNOWLEDGEMENTS

Authors are grateful to Bangladesh Atomic Energy Commission for allowing to carry out this research. Special acknowledgement for technical suggestions and laboratory support goes to Mr. Abdus Salam, Former Director (Operation) of Nasir Glass Industries Limited (NGIL), Bangladesh. The authors would like to thank Mr. Basudeb Kumar Malo, Former Geologist, BAEC and Mr. Sudeb Chandra Das, Scientific Officer (Geology), Institute of Nuclear Minerals, BAEC for helping in field work and preparing maps.

FUNDING

This study was carried out as part of regular research and development activities of Beach Sand Minerals Exploitation Centre of Bangladesh Atomic Energy Commission. No special funding was received for this research.

CONFLICT OF INTEREST

The authors declare that they have no conflict of interest.

REFERENCES

Alexander D. Consequences of floods in developing countries: International perspectives for disaster management. Proceedings of the International Seminar on Bangladesh Floods: Regional and Global Environmental Perspectives, 1989 Mar 4-6; Dhaka, Bangladesh; 1989.

Deshpande AM, Deshpande VK. Effect of SiO2 and Al2O3 addition on the density, Tg and CTE of mixed alkali -alkaline earth borate glass. IOP Conference Series: Materials Science and Engineering 2009;2:Article No. 012034.

Garzanti E, Vezzoli G, Ando S, France-Lanord C, Singh SK, Foster G. Sand petrology and focused erosion in collision orogens: The Brahmaputra case. Earth and Planetary Science Letters 2004;220:157-74.

Glass for Europe. From sand to flat glass: Sustainable sourcing of high-quality sand for industrial use [Internet]. 2020 [cited 2021 Nov 12] Available from: https://glassforeurope.com/from-sand-to-flat-glass/#_ftn2.

Hossain SS, Ahmed M, Islam N, Biswas PK, Rahman MA. Glass sand potentiality of bar sediments from Tista and Dharla Rivers, Bangladesh. Rajshahi University Journal of Life, Earth and Agricultural Science 2013;41:57-64.

Imam B. Mineral Resources of Bangladesh. Dhaka, Bangladesh: Bangla Academy; 1996. p. 1-159.

Islam MN. Glass Sand Deposits of the Balijuri Area, Sherpur District, Bangladesh (Volume 3, Part 4). Bangladesh: Geological Survey of Bangladesh; 1985.

Islam MN. Glass Sand Deposits of Chauddagram Area, Comilla District, Bangladesh. (Volume 4, Part 5). Bangladesh: Geological Survey of Bangladesh; 1986.

Jasy JB, Rahman MJJ, Yeasmin R. Sand petrology of the exposed bar deposits of the Brahmaputra-Jamuna River, Bangladesh: Implications for provenance. Bangladesh Geoscience Journal 2010;16:1-22.

Jordens A, Cheng YP, Waters KE. A review of the beneficiation of rare earth element bearing minerals. Minerals Engineering 2013;41:97-114.

Kumari A, Panda R, Jha MK, Kumar JR, Lee JY. Process development to recover rare earth metals from monazite mineral: A review. Minerals Engineering 2015;79:102-15.

Marshall G. From sandy beach to Kaby Lake: How sand becomes silicon [Internet]. 2016 [cited 2021 Jul 1]. Available from: www.techradar.com/news/computing-components/processors/how-sand-is-transformed-into-silicon-chips-599785.

McMillan P. Flame-broiled alumina. Nature 2004;430:Article No. 738.

Milliman JD, Meade RH. World-wide delivery of river sediment to the oceans. Journal of Geology 1983;91(1):1-21.

Moscoso-Pinto F, Kim HS. Concentration and recovery of valuable heavy minerals from dredged fine aggregate waste. Minerals 2021;11:Article No. 49.

Norton FH. Elements of Ceramics. Massachusetts, USA: Addision-Wesley Publishing Co. Inc.; 1957.

Pisutti D, Prukswan C, Pornsawat W, Narin S. Investigations on local quartz sand for application in glass industry. In: Ip W-H, Satake K. editors. Advances in Geosciences: Volume 13: Solid Earth (SE). World Scientific Publishing Co.; 2009. p. 23-9.

Rafi SMM, Tasnim UF, Rahman MS. Quantification and Qualification of silica sand extracted from Padma River sand. IOP Conference Series: Material Science and Engineering 2018;438:Article No. 012037.

Rahman M, Dustegir M, Karim R, Haque A, Nicolls RJ, Derby HE, et al. Recent sediment flux to the Ganges-Brahmaputra-Meghna delta system. Science of The Total Environment 2018;643:1054-64.

Rahman MJJ, Pownceby MI, Rana MS. Occurrence and distribution of valuable heavy minerals in sand deposits of the Jamuna River, Bangladesh. Ore Geology Reviews 2020; 116:Article No. 103273.

Rahman MA, Pownceby MI, Haque N, Bruckard WJ, Zaman MN. Characterization of titanium-rich heavy mineral concentrates from the Brahmaputra River Basin, Bangladesh. Applied Earth Science (Transactions of the Institution of Mining and Metallurgy B) 2014;123:222-33.

Rahman MA, Pownceby MI, Haque N, Bruckard WJ, Zaman MN. Valuable heavy minerals from the Brahmaputra River sands of Northern Bangladesh, Applied Earth Science (Transactions of the Institution of Mining and Metallurgy B) 2016;125:174-88.

Rahman MA, Zaman MN, Biswas PK, Sultana S, Nandy PK. Physical separation for upgradation of valuable minerals: A study on sands of the Someswari River. Bangladesh Journal of Scientific and Indusrial Research 2015;50(1):53-8.

Rajib M, Zaman MM, Kabir MZ, Deeba F, Rana SM. Physical upgradation and characterization of river silica of Bangladesh to be used as glass sand. Proceedings of International Conference on Geoscience for Global Development, 2009 Oct 26-31; Dhaka, Bangladesh; 2009. p. 192-6

Biogas Production through Co-Digestion of Olive Mill with Municipal Sewage Sludge and Cow Manure

Said Al Rabadi[1*], Kamel Al-Zboon[2], Moayyad Shawaqfah[3], Rebhi Damseh[4], and Omar Al Zoubi[5]

[1]*Chemical Engineering Department, Al-Balqa Applied University, P.O. Box 50, 21510 Huson, Jordan*
[2]*Environmental Engineering Department, Al-Balqa Applied University, P.O. Box 50, 21510 Huson, Jordan*
[3]*Civil Engineering Department, Al al-Bayt University, 25113 Mafraq, Jordan*
[4]*Mechanical Engineering Department, Al-Balqa Applied University, P.O. Box 50, 21510 Huson, Jordan*
[5]*Renewable Energy Engineering Department, Al al-Bayt University, 25113 Mafraq, Jordan*

ARTICLE INFO

Received: 16 Aug 2021
Received in revised: 14 Nov 2021
Accepted: 19 Nov 2021
Published online: 16 Dec 2021
DOI: 10.32526/ennrj/20/202100162

Keywords:
Anaerobic Methanogenic Digestion/ Olive mill/ Sewage sludge/ Cow manure/ Biogas

*** Corresponding author:**
E-mail: said.alrabadi@bau.edu.jo

ABSTRACT

The treatment of olive mill (OM) residues from agricultural facilities is a daunting challenge since tremendous amounts are disposed per annum that should be treated. One of the promising treatment methods is the anaerobic methanogenic digestion of OM residues. In current investigations, the anaerobic digestion of the OM substrate is enhanced through mixing its slurries with sewage sludge (SS) or with cow manure (C), which consists of the kernels for the digestion process. Besides feedstock, other operational parameters such as hydraulic retention time (HRT), temperature and pH have a great impact on the biogas production rate and quality. Experimental investigations were conducted by means of the anaerobic biodegradation of the substrate for OM-SS and -C using a batch reactor under mesophilic conditions and foreseen HRT for 30 days. Almost neutral pH values of 7.4-7.6 were found for the anaerobic treatment of the substrate for OM-SS, and a slightly acidic pH in the range of 4.8-5.3 was found for the anaerobic treatment of the substrate for OM-C. The results revealed that the biogas production for OM-SS and -C exceeded 0.07 and 0.31 $L_{Biogas}/(L_{Ferm}\cdot day)$, respectively. Regarding the COD reduction, its removal efficiency was obtained as 46.1 and 53.8% for OM-SS and -C respectively. For economic concerns, significant methane yields were attained as 56.8 and 115.8 $[L_{CH4}/kg_{COD}]$ for the OM-SS and -C substrates, respectively. In virtue of these remarkable merits, anaerobic methanogenic digestion should be adapted to a commercial scale for the treatment and biogas production of OM residues.

1. INTRODUCTION

The demand for fossil fuels has been dramatically increasing in the last few decades due to the acceleration for covering the population and industrial market inquiries. Maintaining the current exhaustion rates of fossil fuels would definitely cause depletion in the current renewable sources in the coming few decades. Energy and environment are rapidly growing fields of sustainability, which are meeting the needs for future energy without compromising the livelihood of the coming generations. Energy and environmental technologies refer to the knowledge of the usage skills required for energy production and integration. Consequently, one of the options is to look for alternative sources of renewable energy. The desire for new sources of sustainable energy boosts research toward the development of new strategies and technological solutions, which might be born through the treatment of biomass residues and their conversion into biofuels. Eventually, three goals are met in this context; disposal of residues through eco-friendly practices, eliciting of new energy sources, and lowering greenhouse emissions. Most countries around the world have declared strategies to switch towards renewable energy sources away from the use of the conventional fossil fuels and nuclear power. It is incumbent upon every society to implement this imperative, to preserve energy efficiency, and

Citation: Al Rabadi S, Al-Zboon K, Shawaqfah M, Damseh R, Al Zoubi O. Biogas production through co-digestion of olive mill with municipal sewage sludge and cow manure. Environ. Nat. Resour. J. 2022;20(2):137-147. (https://doi.org/10.32526/ennrj/20/202100162)

eliminate the ecological damage that occurs through pollution and emissions.

Association of Agricultural Research Institutions in the Near East and North Africa (AARINENA) countries are suitable and thriving areas for olive trees cultivation, and constitute more than 18% of the world's olive oil production (Goncalves et al., 2012; Aquilanti et al., 2014; Gholamzadeh et al., 2016; Khdair et al., 2019). Furthermore, about 36% of the cultivated areas in Jordan are planted with olive trees where more than 150,000 tons of olive fruit are harvested annually, comprising the estimations of 22,000 tons as olive oil, 75,000 tons as olive cake, and 120,000 m^3 as wastewater (Al-Zboon, 2020). However, the disposal of olive mill residues poses a heavily environmental load on water resources, air quality and soil (Al-Zboon, 2017; Khdair et al., 2019). Furthermore, research in the field of biogas production, in particular, from biodegradable resources is becoming of great interest in many countries, especially those having cultivated areas with olive trees which are producing the raw materials - as a by-product - obtained from olive oil processing facilities.

The primary effective parameter on the anaerobic digestion of olive mill residues is the temperature. There are three sorts of microbes that biologically convert the organic content of the feedstock within three ranges of the implemented temperature for the methanogenic process. Psychrophilic microbes are active within a relatively lower range of temperature 10-25°C, whereas the mesophilic microbes are active within a moderate temperature range of 25-40°C. Finally, thermophilic microbes thrive within a relatively higher temperature range of 45-60°C. Psychro- and thermophilic microbes are considered disadvantageous for the methanogenic process whereas mesophilic microbes, such as Methanosaeta, become optimal for the anaerobic bio-digestion of COD in the feedstock. This is so if the temperature is kept constant within mesophilic conditions, by reducing the heat ingress from/to the surroundings, by applying thermal insulation for the digesters (Gelegenis et al., 2007; Boukchina et al., 2007; Hartati et al., 2020). Another critical parameter is the pH value for the anaerobic digestion of the feedstock. Traditionally, the pH value within the neutral range is feasible for the methanogens' activities (Athanasoulia et al., 2012; Bouknana et al., 2014; Chiavola et al., 2014; Gholamzadeh et al., 2016, Thanos et al., 2021).

Previous investigations were performed to utilize the high-potential organic content in olive residues for enhancing alternative biogas revenues. Blika et al. (2009) have performed anaerobic digestion for olive mill (OM) wastewater, including pre-thermal operation besides the biological pretreatment with the help of fungi. It was found that solids must be removed from OM waste water to enhance the biogas yield, and hence, the stabilization of the digestion operation with HRT up to 30 days. According to Blika et al. (2009), this is attributed to the possible adsorption of long-chain phenolic compounds that are perilous to methanogens' activities, and hence, inhibit the methanization process. In the sequel, it was observed that a decrease in the biogas productivity and methane yield a biogas productivity rate below 0.4 $L/(L_{Ferm}{\cdot}day)$ with a maximal COD removal of 70%. In the study of Thanos et al. (2021), the different scenarios for the digestion process of substrates, such as poultry manure, liquid pig manure and cheese whey with OM, were investigated for optimal biogas production. Their experimental results had revealed a low biogas productivity of 0.7 $(L/L_{ferm}{\cdot}day)$ and an average COD removal in the range of 50-58% during the steady-state conditions.

Furthermore, in a previous study of Gelegenis et al. (2007), biogas productivity from OM was conducted experimentally by co-digesting with diluted poultry-manure (DPM) in continuous reactors, fed with mixtures of OM and DPM at various mesophilic conditions (temperature, pH and OM/DPM concentrations as expressed by the organic fraction of OM to the volatile solids). These experimental attempts had revealed that biogas productivity was slightly increased up to a limited OM/DPM concentration of a value of about 40%, after which the production was decreased. This is attributed to the inhibition of the methanization process due to the formation of phenolic compounds which are toxic for the methanogens' activities.

Based on these investigations, it could be deduced that few studies have been adapted to utilize the high-potential organic content in OM for enhancing alternative biogas revenues by mixing substrates of OM with OM-SS or even with OM-C, and using them as an inoculum to enhance the methanogenic digestion. The objective of the current work is to create a simple and comprehensive methodology to produce biogas from OM residues by mixing with the two substrates as waste sewage sludge and cow manure. The proposed approach was conducted under various operational parameters, including temperature, organic matter content, pH, and COD loading in OM. In the sequel, a process commercialization is foreseen which provides a high-valued engineering solution to enhance the OM digestion process, and hence, the elimination of OM residues' accumulation in the environment. On the other hand, this approach will help in achieving a target control on waste management and a site strategy, by reducing the expenses of OM waste treatment, and improving the socio-econmic infrastructure of the olive oil producing territorials.

2. METHODOLOGY

2.1 Experimental setup

The experimental setup is shown in Figure 1. The batch reactor is manufactured of stainless steel with a capacity of 100 L. It is equipped with a water jacket and electrical heater to maintain the necessary temperature of the digestion process. A water jacket is installed around the reactor to prevent heat loss. The stainless steel reactor is equipped with temperature and pressure gauges for monitoring the predefined parameters under which the digestion process is taken place. The feedstock is introduced to the reactor through an inflow port and filled up to about 70% of the total volume with OM while the balance of the volume is filled with the substrate of OM-SS or -C.

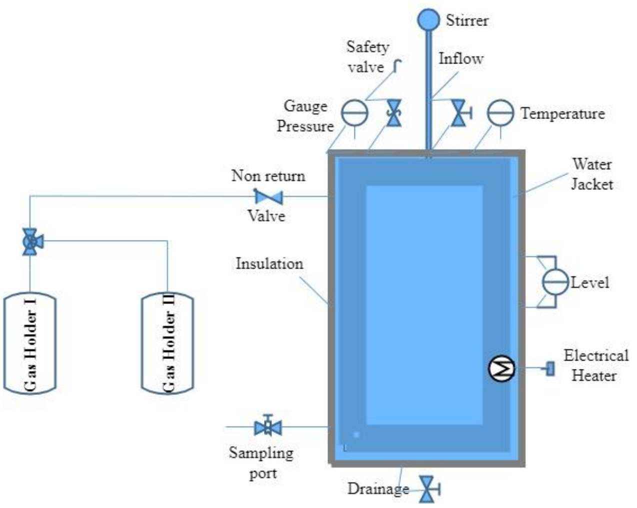

Figure 1. Experimental setup for biogas production for substrate digestion of OM-SS and -C

A tie-in is used as a sampling port for monitoring the produced biogas during the digestion process. The reactor is equipped with a safety valve to avoid the build-up pressure. The digestion process is run for a foreseen period of time of 30 days. According to the reviewed literature, this time period is believed to be sufficient for feedstock digestion and for establishing a stabilization stage consequently for the plant economics (Gelegenis et al., 2007; Blika et al., 2009). The produced gas is routed through a non-return valve to in-series connected gas holders. When the first one reaches a default pressure of 1 bar gauge, the produced gas is directed to the second gas holder.

2.2 Experimental procedure

The experimental procedure is presented as the following: the substrate of OM-SS or -C is mixed and prepared such that the reactor is filled up 70% of the total volume with OM and the balance is with SS or C. The level is regulated through a level controller. The temperature is monitored under the mesophilic conditions with an optimal value of 35±1°C while the thermal duty is regulated through the electrical heater. The water jacket ensures uniform temperature distribution through the entire batch reactor and is kept constant with the help of insulation. In order to ensure the homogeneity of the substrate mixture along the whole HRT of the digestion process, a mechanical mixer is utilized for this purpose with a constant rate of 15 times/h. Initial mixture chrematistics (pH, BOD, COD, TSS) is recorded as well as with periodical samples being withdrawn from a special sampling port and analyzed in the lab. If needed, additives such as calcium bi-carbonate are added to the reactor to maintain the pH in the applicable range, since the methanogenic digestion occurs under anaerobic conditions, which could contribute to a general acidification. The addition of such additives is repeated until a stabilization stage is established at the end of the methanogenic digestion. A percentage of 5% by volume (calcium bi-carbonate to OM mixture) was added, accordingly, an amount of 2-5 g of calcium bi-carbonate is mixed with 50 mL of OM, and then the batch reactor is buffered with the alkaline calcium bi-carbonate mixture through the inflow port. The generated gas is collected daily to determine its volume. Moreover, the substrate's temperature and pressure are measured daily. Biogas constituents are analyzed by means of gas chromatography. After the completion of each individual experimentation, the reactor is entirely drained and prepared for the upcoming investigations. The experimental data, including temperature, pH, and the gauge pressure of the reactor and the collected/accumulative gas volumes are recorded.

3. RESULTS AND DISCUSSION

3.1 Composition of the raw waste

The composition of the substrate was analyzed to get its significant constituents as shown in Table 1. Two substrates were investigated using OM-SS and -C, respectively. It is clear that the OM-C has higher concentrations of the relevant consitutents than OM-SS; this is attributed to the pretreatment of the sewage sludge in the OM-SS mixture, where the organic matter constituents TSS and TN must be dramatically reduced. The phenol content is a major concern in the methanogenic process because it is perilous when its content exceeds the limit of 4,000 PPM (Levén et al., 2012; Hartati et al., 2020), where it had been reported that phenol has a relatively faster degradation during anaerobic digestion under mesophilic conditions than the other consitutents.

3.2 pH profile

The pH value was maintained within the neutral range (7.4-7.6) for biogas production from the digestion process of OM-SS and -C as shown in Figure 2. The acidic pH values (pH≤7) are a sequel to the presence of high phenol constituents which are harmful for the methanogenic process. Obviously, the microbial growth for the benefit of methane production is only feasible in an OM-SS medium of almost neutral pH within the range of 7.4-7.6. The pH fluctuations are attributed to the variation of phenolic concentrations in the substrate, methanogenization of organic content, production of CO_2, and the formation of the acidic compounds. Regular mixing of the substrate provides sufficient homogeneity of the OM-SS medium, and consequently, the profitable dilution of phenolic compounds inside the reactor. To control the pH figures, calcium bi-carbonates are added in a scheduled manner to the reactor. This alkaline additive supports the suitable environment for better biodegradation of the perilous and long-chain phenolic compounds.

Table 1. Characterization of substrates for OM-SS and -C before anaerobic treatment

Parameter	Unit	OM-SS	OM-C
		Before	Before
pH	-	5.05	5.00
COD	PPM	47,500	97,100
BOD	PPM	31,100	47,680
TSS	PPM	17,400	21,450
TN	PPM	4,105	30,900
Phenol	PPM	4,430	5,315

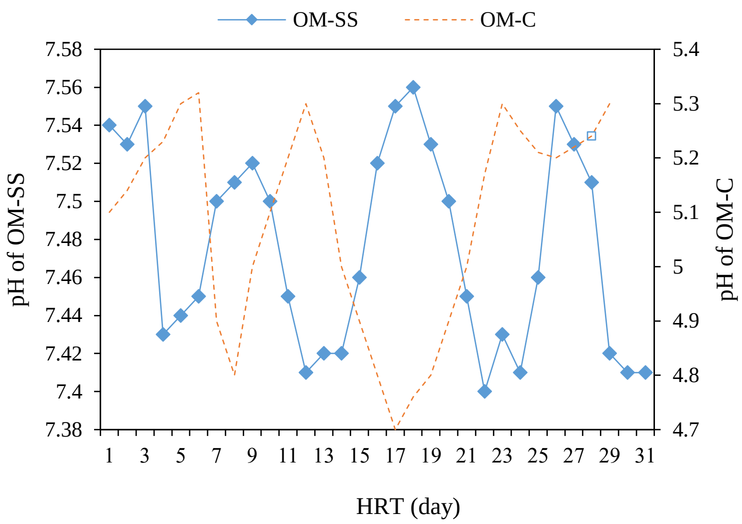

Figure 2. pH variation during digestion of substrate for OM-SS and -C

Many researchers have reported that the pH range of 5.0-6.5 is the optimum one for methane production from OM-C under an anaerobic process. In this regard, it was controlled by adding calcium bicarbonate to the substrate of OM-C (Khoufi et al., 2007; Blika et al., 2009; Goncalves et al., 2012; Boskou, 2012; El Hajjouji et al., 2013; Carlini et al., 2015; Ouazzane et al., 2017; Souilem et al., 2017; Nsair et al., 2020). During the digestion process, due to the decrease of COD and conversion of TN, the pH is subject to alternation. In this context, the pH value was maintained within the range of 4.8-5.3 during the digestion of the substrate for OM-C. Obviously, the pH reading data dropped to the lower limit synchronously with the HRTs during the first two weeks of the digestion process. The microbial growth is preferably feasible in a medium having this pH range for biogas production. This finding is attributed to the characteristics for the substrate of OM-C. The C/N ratio is in the range of 2.7-3.1, as indicated in Table 1. Hence, the ammonia product's concentration increases as higher TN content is obtained in the substrate. This would bring the pH values to slightly acidic ranges. The addition of calcium bi-carbonates raises the pH and obviously modifies the habitat for the microorganisms. Eventually, more gas production rates are foreseen.

3.3 Biogas pressure

The biogas pressure was used as an indicator of gas production in the batch reactor. The results of the biogas pressure from the digestion of the substrate of OM-SS and -C are represented in Figure 3. The pressure profile indicates that there are significant peaks in the pressure progress explicitly obtained at the end of the first two weeks of the digestion process. This is attributed due to the increasing methanogenic activity of the COD consumption and dewatering phase, resulting in the increase of carbon dioxide and hydrogen content (Khoufi et al., 2007; Athanasoulia et al., 2012). After the third week, the pressure progress is seen to have declining values, indicating that the methanogenic process is reaching the stabilization stage. The high production of gas from OM-C causes the continuous release of the produced gas to the gas holders, which affects the monitoring records of the gas pressure in such an experiment. It is noticed that the gas pressure of OM-C experiment has multiple peaks during the first two weeks. During the third week of the digestion process, the pressure progress reaches stabilization, and then the declining values are obtained due to the termination of the methanogenic process, thanks to the regular mixing of the substrate that provides sufficient homogeneity of the OM-C medium. Parallelly, the lower figures for the biogas pressure are obtained in the case of OM-SS experiments. This is attributed to the particularly lower COD, BOD, and TN contents of OM-SS, compared with the OM-C substrate (Table 1).

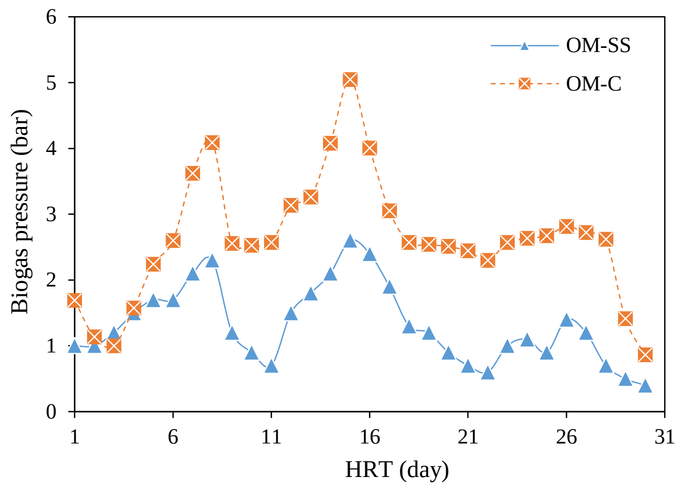

Figure 3. Biogas pressure from digestion of substrate for OM-SS and -C

3.4 Biogas productivity

The collected and accumulative biogas products from the digestion of the substrate for OM-SS are presented in Figure 4. As shown, two significant peaks in the collected biogas volume profile are obtained which are synchronous with the peaks of the biogas pressure progress in Figure 3. For the OM-SS substrate, the C/N ratio is in the range of 9-12 as indicated in Table 1. Hence, less nitrogen derivatives are accumulated in the form of an ammonia product, leading to maintain the pH reading of the substrate mainly in the neutral range. This lowers the habitat of microorganisms for COD biodegradation and eventually, the gas production is reduced.

As the pH reading is kept within an almost neutral range-the less disincentive media for the growth of the gas-producing microorganisms-less production rates are eventually achieved. An accumulative biogas volume of 210 L is obtained at the end of the digestion process of OM-SS. The average rate of the produced biogas exceeds the value of 7.0 (L_{Biogas}/day). In current investigations, the enhanced rates of biogas production are attributed to the regular mixing as well periodic pH mentoring acts, which provide the optimal conditions for the bio-degradation of COD, leading to promising biogas production rates.

The collected and accumulative biogas volumes from OM-C are depicted in Figure 5. As observed, three peaks in the collected biogas profile are obtained during the first, second and fourth weeks of the methanogenic process for the substrate of OM-C. An accumulative biogas volume of 936 L was obtained at the end of the digestion process of the substrate for OM-C. An average biogas production rate achieved the value of 31.2 (L_{Biogas}/d) for OM-C which is higher than the value obtained for OM-SS. In continuation to this, the higher recorded rates of biogas production in the current investigation could be attributed to the higher content of COD in OM-C with respect to OM-SS.

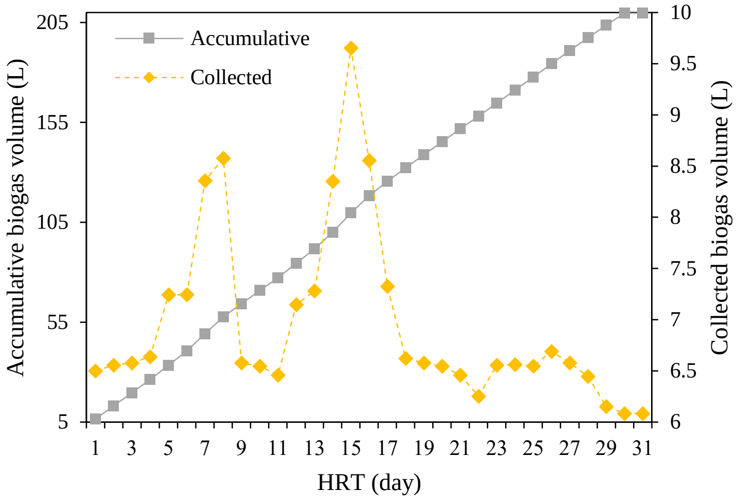

Figure 4. Accumulative and collected biogas volumes from the digestion of substrate for OM-SS

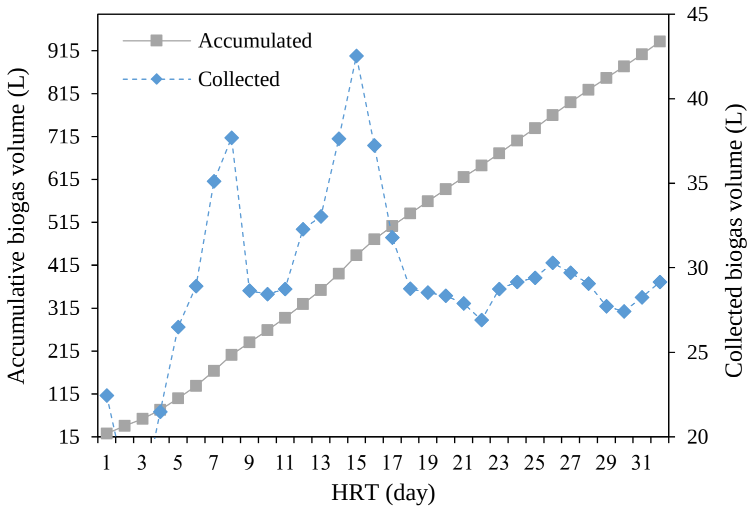

Figure 5. Collected and accumulative biogas volumes from digestion of substrate for OM-C

3.5 Substrate removal

The assessment of the biogas productivity could be elucidated by the conversion of the characteristic parameters in the stock substrates over the whole course of the digestion process. Figure 6 depicts the overall removal efficiency of the substrates for OM-SS and -C after the scheduled HRTs of 30 days and under the foreseen chrematistics of the feed mixtures. It was found that the substrate's removal efficiencies for the characteristic parameters in Table 1 are reported as following: for COD removal, it is about 46 and 52% for OM-SS and -C respectively. The BOD removal reaches close values of 40% for OM-SS and 43% for OM-C, TSS removal efficiency is 15% for OM-SS and 11% for OM-C, while 32% and 44% are attained as the TN consumption for OM-SS and -C, respectively. Neutralising the pH figures by the addition of calcium bi-carbonates had a positive effect on the bio-degradation of phenols. Obviously, the immobilization of the harmful phenol is reaching a promising percentage of 91% for OM-SS and 90% for OM-C which means that the remaining effluent phenol is below the perilous limits of the influents. Principally, the effluent substrates obtained from the digestion process could be considered eco-friendly for the environment. Besides their potential organic content, it would be suggested that these effluents are to be implemented in further ecological and economic perspectives; in agricultural applications such as soil amendments and fertilizer, livestock bedding, even in combustion after being desiccated in special molds (Niaounakis and Halvadakis, 2006; Gholamzadeh et al., 2016; Ouazzane et al., 2017; Souilem et al., 2017).

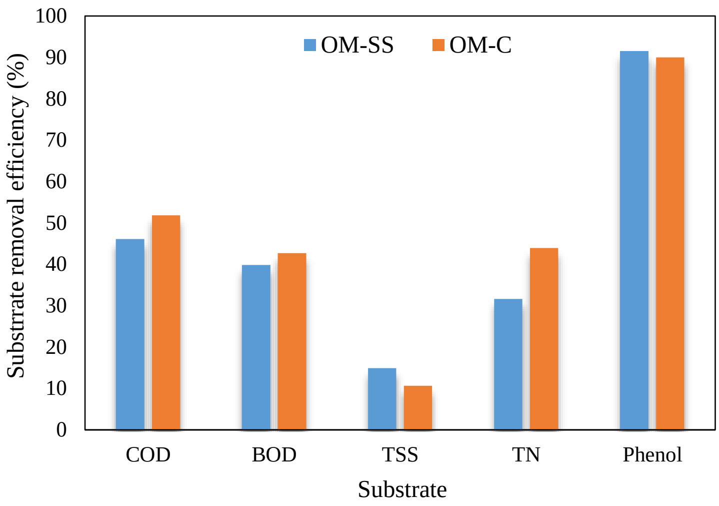

Figure 6. Substrate removal efficiency of substrates for OM-SS and -C

3.6 Biogas yield calculation

Based on the bio-degradation process, COD is eventually consumed during the microbial growth while CH_4, CO_2, and traces of other gases are produced. Due to pH fluctuations and the variation of the pressure progress inside the reactor, the production rate is dynamic and apparently relies on the dominant aerobic process during the primary HRT of the digestion process, whereas in delayed HRT it depends on the anaerobic process. This finding is confirmed by the variation of the biogas constitution with respect to CH_4 and CO_2 gases. In Figure 7, the CH_4 and CO_2 gas volume percentages are diagrammed for HRTs of 10, 20, and 30 days during the methanogenic process. COD consumption leads to co-generation of CH_4 and CO_2 and traces of other gases like H_2 and CO. During the first HRT period, the CO_2 yield is high with unpretentious CH_4 productivity. This is attributed to the dewatering/aerobic phase of the digestion process (Aquilanti et al., 2014; Bouknana et al., 2014). On the other hand, the biogas composition is getting reversed after the third HRT period of the digestion process. Hence, a reduction of COD content is performed mainly under anaerobic conditions achieving relatively better CH_4 and lower CO_2 yield, in other words, improved biogas purity is achieved. Obviously, a higher CH_4 yield for OM-C is recorded than that of the OM-SS feedstock for a HRT period of 30 days.

According to the current findings, the achieved biogas production rates from the digestion of the substrate for OM-SS and -C exceeds 0.07 and 0.31 ($L_{Biogas}/(L_{ferm} \cdot day)$) respectively as shown in Table 2. In terms of the volatile materials' removal, a COD removal is obtained as 46.1 and 51.8% for the substrates OM-SS and -C, respectively. Eventually, a promising methane yield is obtained under mesophilic conditions. The achieved methane yields, which were calculated with respect to the loaded COD, exceed the figures of 57 and 116 (L_{CH4}/kg_{COD}) for OM-SS and -C, respectively. These considerable findings would imply potential economic perspectives.

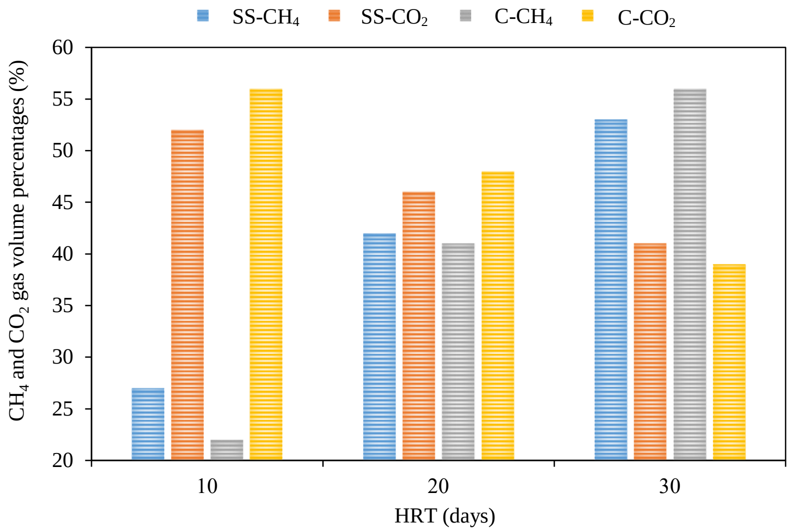

Figure 7. CH_4 and CO_2 gas content from digestion of substrate for OM-SS and -C, respectively

Table 2. Summary of biogas production rates and yields for substrates

Parameter	Unit	OM-SS	OM-C
Average biogas production rate	(L_{Biogas}/d)	6.99	31.20
Average CH_4 production rate	(L_{CH4}/d)	3.73	17.47
Biogas yield	[L_{Biogas}/(L_{ferm}.d)]	0.07	0.31
CH_4 yield	(L_{CH4}/kg_{COD})	56.84	115.80

For the determination of the gas quality of the produced biogas from the digestion of OM-SS and -C, an elemental analysis by gas chromatography of the gaseous products was performed as shown in Table 3. The analysis shows that higher methane and syngas contents were achieved from the digestion of OM-C (56.0 and 6.3% respectively), compared to those obtained for OM-SS (53.4 and 4.4%). Generally, these findings are consistent with those in the literature of Blika et al. (2009). It makes worthy to highlight that the relatively higher methane and syngas have acceptable heating values in the frame of the produced biogas' quality (Aquilanti et al., 2014; Souilem et al., 2017). More than this, the obtained biogas shows lean fractions with respect to the nitrogen content; eventually, NO_x emissions are foreseen within acceptable limits from biogas combustion. Besides that, the produced biogas is considered to be eco-friendly with respect to other harmful emissions like H_2S, considering its minor content in the traces range.

The heating value of biogas of pure methane gas is 55,200 (kJ/kg) (Niaounakis and Halvadakis, 2006; Gholamzadeh et al., 2016; Ouazzane et al., 2017). Due to the significant carbon dioxide volume fraction, the heating value of the produced biogas with 54% methane by volume is estimated to be 17,100 (kJ/kg). In Jordan, around 120,000 m^3 of OM wastewater are produced annually (Al-Zboon, 2017; Al-Zboon, 2020). Based on current findings, around 20,000 m^3 of biogas is produced annually. Biogas is principally similar to natural gas with regards to the heating value after carbon dioxide is being removed. It could be easily combusted for other heating applications as well for steam generation plants in order to produce electricity.

Table 3. Elemental analysis of produced biogas from the anaerobic digestion of OM-SS and -C

Gas compound	Formula	Gaseous content (%)	
		OM-SS	OM-C
Methane	CH_4	53.4	56.0
Carbon dioxide	CO_2	41.0	36.0
Nitrogen	N_2	1.1	1.6
Syngas	$CO+H_2$	4.4	6.3
Oxygen	O_2	0.1	0.1
Hydrogen sulfide	H_2S	Traces	Traces

3.7 Comparison with other studies

The current findings are found to be very meaningful with regards to their remarkable achievements, and upon being assessed with other relevant studies and their corresponding findings, they are summarized as shown in Table 4. According to Goncalves et al. (2012), the OM effluent was digested in a hybrid reactor to maximize the bioenergy recovery from OM. Compared to current investigations, a reported biogas production rate of 3.16 [L_{Biogas}/(L_{ferm}·day)] was achieved at a continuous COD loading rate of 7.1 [kg_{COD}/(m^3·day)]. A relatively short HRT of 7.5 days was implemented for an acidic substrate. Meanwhile, the unpretentious value for a maximum COD removal of 61% was stated. Their technique requires special arrangement for COD loading as well an OM pretreatment in order to remove coloration mainly caused by the remaining recalcitrant phenolic derivatives. Based on the investigations of Blika et al. (2009), physico-chemical and bio-treatment with fungi OM wastewater was carried out in a continuous bioreactor for various HRTs of 20 and 30 days, and 5.1 as a pH figure. Advanced figures of COD removal was 70 % and less methane gas of 0.4 [L_{CH4}/(L_{Ferm}·day)] was attained under a loading rate of 1 kg_{COD}/[L_{Ferm}·day], their HRTs are close to current investigations. This is attributed to possible adsorption of long-chain phenolic compounds that are perilous to methanogens activities, and hence, lower the inhibition of the methanization process. In the work of Carlini et al. (2015), the anaerobic digestion of OM-C and cattle slurry in a batch reactor under mesophilic conditions and a neutral medium of pH equals 7.1. The Hamble biogas productivity was 0.73 [L_{Biogas}/(L_{ferm}·day)] in spite of a relatively long HRT of 55 days. This can be attributed to a TS limitation of 14%.

Table 4. Summary of current results and those of relevant studies on the OM treatment

Substrate	COD removal (%)	CH_4 yield	Process conditions	Reference
OM-SS	46.1	56.84 (L_{CH4}/kg_{COD})	Anaerobic treatment of sewage sludge HRT 30 days, pH 7.4-7.6, 35°C	Current Study
OM-C	51.83	115.8 (L_{CH4}/kg_{COD})	Anaerobic treatment of sewage sludge HRT 30 days, pH 4.7-5.3, 35°C	Current Study
OM	51-61	3.16 [L_{CH4}/L_{ferm}·day)]	Anaerobic hybrid reactor with post-treatment to extract coloration, HRT 7.5 days and pH=4.7	Goncalves et al. (2012)
OM	70	0.4 [L_{CH4}/(L_{Ferm}·day)]	Anaerobic digestion Physico-chemical and bio-treatment with fungi in continuous bioreactor HRT (20 and 30 days), pH=5.1	Blika et al. (2009)
OM-C and cattle slurry	-	0.73 [L_{Biogas}/(L_{ferm}·day)]	Anaerobic digestion, Batch reactor with mesophilic conditions, pH=7.1, HR=55 days, TS=14%	Carlini et al. (2015)
OM	90-92	-	• Anaerobic treatment in sequencing batch reactor • Different influent organic loadings, effluent membrane separation	Chiavola et al. (2014)
OM-SS and sewage	70-85	Est. 32-34 m^3_{CH4}/m^3_{Ferm} and 0.8-1.2 [kg_{COD}/(m^3·day)]	Combined treatment of an- and aerobic digestion, HRT≥3 months, pH=7.6 and 35°C, obstacles with color and turbidity	Boukchina et al. (2007)
OM and WAS	64-72	0.6 (L_{Biogas}/kg_{COD})	2 CSTR run under mesophilic conditions, several HRTs, pH 7.12 and 4.8 for OM and WAS respectively	Athanasoulia et al. (2012)
OM and WAS	52.6	0.33 (L_{Biogas}/kg_{COD})	Electro-chemical pre-treatment in continuous reactor followed by anaerobic treatment, pH=6.5-7.2 HRT≥4 months	Khoufi et al. (2007)
OM and organic wastes	48	0.69 [L_{CH4}/(kg_{VS}·day)]	Anaerobic treatment HRT=4-7	Scaglione et al. (2008)

A combination of pre- and post-treatment membrane separation besides the anaerobic digestion process for the substrate of OM with different COD loadings was implemented, to investigate the efficiency of sequencing batch reactor, which was investigated in the study of Chiavola et al. (2014). Promising COD removal was reported in the range of 90-92%, whilst this approach is sensitive to the phenol derivatives' concentration within the domain of the current investigations. Another approach is performed by Boukchina et al. (2007) where the combined treatments of an- and aerobic digestion for the substrate of OM-SS and sewage were implemented. This approach was scheduled for an HRT longer than 3 months under neutral and mesophilic conditions. Despite the obstacles with color and turbidity, a COD removal was obtained in the range of 70-85%. Thus, a promising biogas productivity was reported in the range of 32-34 (L_{CH4}/L_{Ferm}) for the organic loading of 0.8-1.2 [$kg_{COD}/(m^3 \cdot day)$]. These figures are considered as over-estimations and apparently are unrealistic in the frame of loading CODs. In the relevant domain for the investigation of HRT, alternations were performed on the anaerobic co-digestion of the substrate of waste activated sludge (WAS) with agro-cultural OM wastewater in two-cascade continuous reactors (Athanasoulia et al., 2012). With HRT up to 20 days, moderate COD removal within 64-72% and relatively low 0.6 (L_{Biogas}/kg_{COD}) were observed. Their results could be explained due to the dilution effect by implementing the two-cascade continuous reactors due to continuous OM feeding. In the study of Khoufi et al. (2007), an electro-Fenton and chemical pretreatment were carried out in a continuous reactor followed by an anaerobic digestion stage of OM under neutral pH figures and relatively longer HRT than 4 months. COD removal was 52.6% of the organic loading rate of 10 [$kg_{COD}/(L_{Ferm} \cdot day)$] and an average methane yield of 0.33 (L_{CH4}/kg_{COD}) From an economics point of view, such techniques with long retention times and poor biogas production rates must be further promoted to be commercially adapted. On the other hand, anaerobic treatment tests were proposed by Scaglione et al. (2008) for a relatively shorter HRT within 4-7 days in a lab-scale batch reactor with various substrates of OM with low food/biomass ratio, such as thickened activated sludge, kitchen, fruit and vegetable wastes, and fresh grass. Lean COD removal was recorded with a value of 48% along with the poor biogas production rate of 0.69 [$L_{CH4}/(kg_{VS} \cdot day)$]. Obviously, this approach had stated a close CH_4/biogas quality with respect to the current findings, but it requires special processing of feedstock substrates to enhance the relevant outcomes of current investigations.

Based on these envisioned results, the biodegradation of OM with other diverse substrates and biomass, from beverage and food manufacturing facilities as well other agro-industrial wastes, merit further investigations in the batch as well continuous digestion operations. The visualization of such research portfolios in real operating facilities are highly recommended, as it which would have a great impact on the improvement of socio-economic relations/improving the infrastructure of rural areas and olive oil producing territorials.

4. CONCLUSION

Experimental investigations were conducted for the anaerobic digestion of the substrate mixtures of OM-SS and -C. The operating conditions for the anaerobic methanogenic digestion were relatively feasible; HRT of 30 days under a mesophilic temperature of 35°C. The pH readings were maintained within the neutral range for the anaerobic digestion of OM-SS, and slightly acidic for that of OM-C, through regularly adding defined amounts of calcium bi-carbonate to the reactor. By virtue of these envisioned results, the potential production rates of biogas with the promising methane quality was obtained from the anaerobic methanogenic digestion. Moreover, the digestion of OM-C was more productive with the factor of about two times than that of the OM-SS substrate, due to the considerable higher N/C ratio as well for the higher volatile organic content in the substrate of OM-C with respect to that of OM-SS. For the achievement of an optimal margin performance of digestion for the substrate of OM-SS and -C, the required chrematistics, as well other nutrients are essential for microorganisms' growth like nitrogen and Sulfur derivatives, must be ample, and specifically regulated.

The achieved OM methanogenic digestion is branded as a promising strategy to be adopted in olive oil producing territories, upon the assessment of the remarkable yielding of biogas production with a valuable methane quality. This industrial application would be helpful in enhancing the eco-friendly practices to cope with climate unpredictability due to their minimization of pollutions and greenhouse emissions which reduce the OM residues, providing technical solutions for energy demands in rural areas.

ACKNOWLEDGEMENTS

Grateful thanks for Al-Balqa Applied and Al al-Bayt Universities through the provision of the technical infrastructure for the conduction of this research.

REFERENCES

Al-Zboon K. Impact of olive cake combustion on ambient air quality using AERMOD model. Indian Journal of Engineering 2020;17(48):363-71.

Al-Zboon K. Indoor air pollution due to household use of olive cake as a source of energy. International Journal of Environment and Waste Management 2017;19(3):248-67.

Aquilanti L, Taccari M, Bruglieri D, Osimani A, Clementi F, Comitini F, et al. Integrated biological approaches for olive mill wastewater treatment and agricultural exploitation. International Biodeterioration and Biodegradation 2014;88:162-8.

Athanasoulia E, Melidis P, Aivasidis A. Anaerobic waste activated sludge co-digestion with olive mill wastewater. Water Science and Technology 2012;65(12):2251-7.

Blika PS, Stamatelatou K, Kornaros M, Lyberatos G. Anaerobic digestion of olive mill wastewater. Global NEST Journal 2009;11(3):364-72.

Boskou D. Constituents, Quality, Health Properties and Bioconversions. IntechOpen; 2012. p. 510.

Boukchina R, Choi E, Kim S, Yu YB, Cheung YJ. Strategy for olive mill wastewater treatment and reuse with a sewage plant in an arid region. Water Science and Technology 2007;55(10):71-8.

Bouknana D, Hammoutia B, Salghi R, Jodeh S, Zarrouk A, Warad I, et al. Physicochemical characterization of olive oil mill wastewaters in the eastern region of Morocco. Journal of Materials and Environmental Science 2014;5(4):1039-58.

Carlini M, Castellucci S, Moneti M. Anaerobic co-digestion of olive-mill solid waste with cattle manure and cattle slurry: Analysis of bio-methane potential. Energy Procedia 2015;81:354-67.

Chiavola A, Farabegoli G, Antonetti F. Biological treatment of olive mill wastewater in a sequencing batch reactor. Biochemical Engineering Journal 2014;85(15):71-8.

El Hajjouji H, Bailly JR, Winterton P, Merlina G, Revel JC, Hafidi M. Chemical and spectroscopic analysis of olive mill waste water during a biological treatment. Bioresource Technology 2008;99:4958-65.

Hartati E, Musodiqoh NA, Nurlina E, Permadi DA. Effect of *Hyphomicrobium* sp. in biogas formation from organic waste treated by batch mode anaerobic digestion. Environment and Natural Resources Journal 2020;18(3):257-67.

Gelegenis J, Georgakakis D, Angelidaki I, Christopoulou N, Goumenaki M. Optimization of biogas production from olive-oil mill wastewater, by co-digesting with diluted poultry manure. Applied Energy 2007;84(6):646-63.

Gholamzadeh N, Peyravi M, Jahanshahi M. Study on olive oil wastewater treatment, nanotechnology impact. Journal of Water and Environmental Nanotechnology 2016;1(2):145-61.

Goncalves MR, Freitas P, Marques IP. Bioenergy recovery from olive mill effluent in a hybrid reactor. Biomass and Bioenergy 2012;39:253-60.

Khdair AI, Abu-Rumman G, Khdair SI. Pollution estimation from olive mills wastewater in Jordan. Heliyon 2019;5(e02386):1-6.

Khoufi S, Feki F, Aloui F, Sayadi S. Pilot-plant results of the electro-Fenton treatment of olive mill wastewaters followed by anaerobic digestion. Water Science and Technology 2007;55(12):67-73.

Levén L, Nyberg K, Schnürer A. Conversion of phenols during anaerobic digestion of organic solid waste: A review of important microorganisms and impact of temperature. Journal of Environmental Management 2012;95(3):99-103.

Nsair A, Cinar SO, Alassali A, Abu Qdais H, Kuchta K. Operational parameters of biogas Plants: A review and evaluation Study. Energies 2020;13(15):Article No. 3761.

Niaounakis M, Halvadakis CP. Olive Mill Waste Management: Literature Review and Patent Survey. United Kingdom: Elsevier; 2006.

Ouazzane H, Laajine F, El Yamani M, El Hilaly J, Rharrabti Y, Amarouch MY, et al. Olive mill solid waste characterization and recycling opportunities: A review. Journal of Materials and Environmental Sciences 2017;8(8):2632-50.

Scaglione D, Caffaz S, Ficara E, Malpei F, Lubello C. A simple method to evaluate the short-term biogas yield in anaerobic co-digestion of WAS and organic wastes. Water Science and Technology 2008;58(8):1615-22.

Souilem S, Elabbassi A, Kaia H, Hafidi A, Sayadi S, Galanakis C. Olive Oil Production Sector: Environmental Effects and Sustainability Challenges. United Kingdom: Oxford; 2017. p. 1-28.

Thanos D, Maragkaki A, Venieri D, Fountoulakis M, Manios T. Enhanced biogas production in pilot digesters treating a mixture of olive mill wastewater and agro-industrial or agro-livestock by-products in Greece. Waste and Biomass Valorization 2021;12:135-43.

Lead Accumulation of Siam Weed (*Chromolaena odorata*) Grown in Hydroponics Under Drought-stressed Conditions

Chanaradee Srirueang, Nuttamon Gongseng, Sukhumaporn Saeng-ngam, and Kongkeat Jampasri*

Department of Biology, Faculty of Science, Srinakharinwirot University, Bangkok, Thailand

ARTICLE INFO

Received: 13 Sep 2021
Received in revised: 9 Nov 2021
Accepted: 22 Nov 2021
Published online: 1 Dec 2021
DOI: 10.32526/ennrj/20/202100178

Keywords:
Accumulation/ Drought/ Hydroponic/ Pb/ Siam weed

*** Corresponding author:**
E-mail: kongkeat@g.swu.ac.th

ABSTRACT

The phytoremediation potential of Siam weed (*Chromolaena odorata*) was tested in lead (Pb) contaminated nutrient media with 5% (w/v) of polyethylene glycol (PEG) 6000 induced drought stress conditions. The plant was treated with 0, 5, 10, 20, and 50 mg/L Pb for 15 days. Different concentrations of Pb or in combination with PEG had no effect on plant growth parameters. Drought reduced water content (WC) ($p<0.05$), but did not affect the reduction of chlorophyll content and photochemical efficiency in plant tissues after 15 days of treatment. Under drought conditions, plants showed the largest Pb accumulation in roots (5,503.7 mg/kg) and exhibited the highest uptake at 50 mg/L solution (18.24 g/plant), but the translocation factor values (TFs) of Pb from root to shoot were all less than 1. Under both drought and non-drought conditions, the bioconcentration factor values (BCFs) decreased with increasing Pb concentrations. According to BCFs and TFs, *C. odorata* may be promising for phytostabilization of Pb. Based on high biomass, tolerance, and Pb uptake, the result of this hydroponic study test reveals that *C. odorata* has a good potential for developing Pb phytoremediation strategies in drought-stressed conditions.

1. INTRODUCTION

Lead (Pb) is a major toxicological concern of the present day that demands immediate attention and has been listed as a hazardous heavy metal pollutant due to its high toxicity (Qi et al., 2018). Pb contamination of agricultural soils can be as a result of long-term farming or the excessive use of agrochemicals and heightens the risk of health problems (Kumar et al., 2020). Excessive Pb results in reduced soil fertility and health, affecting plant growth and leading to reduced crop production (Hassan et al., 2014). Phytoremediation has generated a great deal of interest as a cost-effective plant-based technology for the removal of toxic heavy metals from contaminated soil under natural field and greenhouse conditions (Jabeen et al., 2009). Even if the phytoremediation technique seems to be one of the best alternatives, however, abiotic factors such as drought (or water deficit) may restrict the rate of plants growth that can be affected through the use of plants for the phytoremediation process (Tangahu et al., 2011).

Drought is one of the most serious constraints to agricultural crops, causing plant growth inhibition and low productivity (Seleiman et al., 2021). Meanwhile, Pb has been released into the agricultural area from metallurgical mining activities and the long-term use of agrochemicals (Alengebawy et al., 2021). Thailand has encountered drought almost every year, and extreme droughts occur frequently during the summer season. Increasing droughts have also increasingly impacted the phytoremediation efficiency of heavy metal contamination. Due to drought stress, which causes many physiological and biochemical changes in plants, making osmotic adjustment maintenance critical and leading to a reduction in the biomass of plants (Ozturk et al., 2020). Hence, drought is an important aspect to consider when selecting suitable plants for metal extraction purposes. There are some drought-tolerant plants that show potential for accumulating heavy metals with soil remediation, such as Bermuda grass (*Cynodon dactylon*) (Sekabira et al., 2011) and Shrub Violet (*Hybanthus floribundus*) (Kachenko et al., 2011). Nevertheless, several drought-tolerant plant species have rather limited uses. This is because they each show low biomass production and slow growth

Citation: Srirueang C, Gongseng N, Saeng-ngam S, Jampasri K. Lead accumulation of siam weed (*Chromolaena odorata*) grown in hydroponics under drought-stressed conditions. Environ. Nat. Resour. J. 2022;20(2):148-156. (https://doi.org/10.32526/ennrj/20/202100178)

habit, and the responses of plant drought tolerance to drought stresses and impacts on heavy uptake have not yet been comprehensively studied. For this reason, the identification of novel plant species with high biomass yield, coupled with the ability to tolerate and accumulate multiple metals, has become an important aspect of phytoremediation research (Hemen, 2011).

At present, it is important to overcome the problem of metals toxicity and drought stress due to water shortage. *Chromolaena odorata*, known as Siam weed, is widely distributed throughout the country, especially in areas with a pronounced dry season. Studies show that it succeeds in the accumulation of multiple heavy metals (Cd, Zn, and Pb), with phytoremediation potential even in the presence of high heavy metal concentrations (Phaenark et al., 2009; Jampasri et al., 2021). Due to the ubiquity of this native species, it has a relatively high biomass with the ability to accumulate high concentrations of heavy metals (Tanhan et al., 2007; Phaenark et al., 2009; Khaokaew and Landrot, 2015). In addition, Naidoo and Naidoo (2018) indicated that *C. odorata* is a drought-avoider species. However, there are no reports on the combined effects of drought and Pb on the phytoremediation efficiency of *C. odorata*, including the ability to deal with drought. This study aims to investigate the drought tolerance and phytoremediation potential of *C. odorata* on Pb accumulation in a hydroponic experiment. The effects of drought on chlorophyll content, fluorescence parameters, and water content (WC) were also determined.

2. METHODOLOGY

2.1 Plant materials and hydroponic conditions

Chromolaena odorata used in this study was obtained from the campus of Srinakharinwirot University, Nakorn Nayok Province, Central Thailand, where there is no history of heavy metal contamination. Plants were grown from stem cuttings in a greenhouse under natural conditions for two months. The uniform plants were grown in a semi-enclosed container for one week prior to the experiment in 400 mL of 20% Hoagland solution at pH 5.5. All plants were treated with different concentrations of lead (II) nitrate [$Pb(NO_3)_2$], while drought stress was applied by adding 5% (w/v) of PEG-6000 to Hoagland solution for 15 days (Ranjbarfordoei et al., 2000). The experiment was arranged into five treatments: nutrient solutions with PEG only (T0), and 5, 10, 20, and 50 mg/L of Pb combinations with PEG (T1-T4) without both the combined effects of PEG and Pb (C0), and the same for all Pb concentrations without the addition of PEG served as control (C1-C4). Those metal concentrations were the initial range recommended by previous research for *C. odorata* screening tests in hydroponic experiments (Tanhan et al., 2007). All experiments were conducted with three replicates per treatment (each replicate consisted of one plantlet). *C. odorata* grown in the Hoagland solutions enriched with PEG-6000 (w/v-5%, 10%, and 20%) without contamination was conducted to find the effect of drought stress on chlorophyll contents, fluorescence parameters, and WC for 15 days. All experiments were conducted in a controlled environment chamber in a greenhouse under the long-day photoperiod with a temperature of 27-30ºC during the light and dark periods. All solutions were not aerated and were topped up with the original solution daily.

2.2 Determination of plant growth

The shoot heights and the root lengths for controlled and treated plants were measured using a metric ruler. Plant samples were thoroughly washed with tap water and deionized water, separated into shoots and roots, and oven-dried (65ºC for 72 h). Then, the dry weight of the shoots and roots was recorded using an analytical balance. Reduction (%) in shoot heights and the root length was calculated as a percentage of the control.

2.3 Determination of chlorophyll content, chlorophyll fluorescence parameters and water content

The leaf chlorophyll content was measured using a spectrophotometer from acetone (80% v/v) extract, and calculated using the equation of Porra et al. (1989) and Holm (1954) on the basis of mg chl/g fresh weight (FW) (Korkmaz et al., 2010):

$$\text{Chl a (mg/g FW)} = 12.25 \times A_{663.6} - 2.55 \times A_{646.6}$$

$$\text{Chl b (mg/g FW)} = 20.31 \times A_{646.6} - 4.91 \times A_{663.6}$$

$$\text{Chl a + b (mg/g FW)} = 17.76 \times A_{646.6} - 7.34 \times A_{663.6}$$

Where: Chl a=chlorophyll a; Chl b=chlorophyll b; $A_{663.6}$=absorbance at a wavelength of 663.6 nm; $A_{646.6}$=absorbance at a wavelength of 646.6 nm

The WC was measured and expressed as a percentage according to the following formula (Xu et al., 2006):

$$\text{WC (\%)} = \frac{\text{Fresh weight - Dry weight}}{\text{Fresh weight}} \times 100$$

The maximum quantum use efficiency (Fv/Fm) of photosystem II (PSII) for dark adapted leaves was calculated as $[(F_m\text{-}F_0)/F_m]$, according to the equations reviewed by Stirbet and Govindjee (2011).

The Performance Index (PI) was determined using a chlorophyll fluorometer (Pocket PEA, Hansatech Instruments Ltd, King's Lynn, Norfolk, UK). At least 30 readings from a leaf were used to get one final average reading.

2.4 Determination of Pb

The dried plants were grounded into powder and sieved through a 2 mm mesh sieve. A subsample (0.5 g) of each group's plant sample was digested in 2:1 HNO_3:$HClO_4$ (v/v) using the open tube digestion method (Simmons et al., 2005). Aqueous extracts of the plants were analyzed by a flame atomic absorption spectrometer (FAAS) (SpectrAA 55B, Varian) for Pb determination. The FAAS with a hollow cathode lamp was used. The wavelengths were set at 283.3 nm, while hollow cathode lamps were operated at 7.5 mA. Quantification was carried out with a calibration curve obtained from a series of diluted standard solutions with a coefficient of determination (r^2) higher than 0.995. The levels of detection for Pb on the FAAS were calculated by the calibration curve.

2.5 Data analysis

Bioconcentration factor (BCF): the BCF was calculated as a ratio between the Pb concentration in the plant tissue and the Pb-spiked concentration in the solution (Garg and Chandra, 1994). The calculation of BCF was expressed as shown below:

$$\text{BCF} = \frac{\text{Pb concentration in whole plant (mg/kg dry weight)}}{\text{Initial Pb concentration in solution (mg/kg dry weight)}}$$

Translocation factor (TF): the Pb translocation in these plants from root to shoot was measured using TF (Cui et al., 2007), which is given below:

$$\text{TF} = \frac{\text{Concentration of Pb in shoot (mg/kg dry weight)}}{\text{Concentration of Pb in root (mg/kg dry weight)}}$$

Where: TF>1 indicates that the plant translocated Pb effectively from the roots to the shoots (Baker and Brooks, 1989).

Pb uptake: the total uptake of Pb in plants was calculated as follows (Zhang et al., 2012):

$$\text{Pb uptake} = \frac{\text{Total Pb concentration in plant (mg/kg)} \times \text{plant dry weight (g/plant)}}{1{,}000}$$

Relative growth rate (RGR) was calculated according to Hunt's equation (1978):

$$\text{RGR} = \frac{\ln W_2 - \ln W_1}{T_2 - T_1}$$

Where: RGR is the relative growth rate (g/g/d), and W1, T1, W2, and T2 are the initial and final dry weights and times for each treatment respectively.

2.6 Statistical analysis

The mean and standard errors of the three replicates were calculated and the statistical significance evaluated using the SPSS-23.0 statistical software package (SPSS, Inc.) with the one-way analysis of variance (ANOVA). A significance level of 0.05 was used in all treatment comparisons and applied using the least significant difference (LSD).

3. RESULTS AND DISCUSSION

3.1 The combined effects of Pb and PEG on plant growth

As shown in Table 1, Pb and PEG had no significant inhibitory effects on dry plant biomass, root length, stem height, and RGR values ($p>0.05$), although T1-T4 root lengths were reduced to 87.6-93.0% of the controls (T0; 100%). Plants grown in all single Pb treatments showed a slight but non-significant reduction in stem height (90.7- 99.7%) ($p>0.05$). This 15-day hydroponic experiment confirmed the tolerance of *C. odorata* to low levels of drought stress created by adding PEG-6000 (PEG) at 5% (w/v) when combined with Pb concentrations ranging from 10 to 50 mg/L. In the case of Pb, our result was similar to that reported by Swapna et al. (2014), who performed a hydroponic experiment with the concentrations of 1 and 20 mg/L Pb for 30 days, though without drought. In the present study, nevertheless, a slight decrease (≈5-15%) in the root length of plants was observed in all treatments. This may be the result of root adaptation in the growth responses of *C. odorata* under heavy metal influence, or it may be because roots are one of the main drivers of water in the response to drought, which regulates their growth, root length, and organizational characteristics (Salazar et al., 2015; Omoregie and Ikhajiagbe, 2021).

Table 1. Dry biomass, root length, stem height, and RGR values of *C. odorata* grown in hydroponics with different concentrations of Pb combined or uncombined with PEG

Treatment	Dry biomass (g/plant)	Root length (cm)	Stem height (cm)	RGR (g/g/day)
T0: 0 mg/L Pb+PEG	2.2±0.1^{a}	12.9±1.5^{a} (100%)	56.7±1.1^{b}	0.03±0.02
C0: 0 mg/L Pb	2.6±0.8^{a}	15.6±0.7^{a} (100%)	60.2±0.9^{b} (100%)	0.05±0.01
T1: 5 mg/L Pb+PEG	2.8±0.3^{a}	11.6±1.3^{a} (89.9%)	59.1±1.4^{b}	0.05±0.01
C1: 5 mg/L Pb	3.3±0.1^{a}	13.1±0.9^{a} (84.0%)	56.2±0.3^{b} (93.4%)	0.06±0.01
T2: 10 mg/L Pb+PEG	3.1±0.4^{a}	12.0±1.7^{a} (93.0%)	58.2±1.1^{b}	0.07±0.02
C2: 10 mg/L Pb	2.4±0.3^{a}	15.2±0.9^{a} (97.4%)	60.0±2.9^{b} (99.7%)	0.04±0.01
T3: 20 mg/L Pb+PEG	2.6±0.4^{a}	11.7±1.9^{a} (90.7%)	57.7±1.4^{b}	0.06±0.03
C3: 20 mg/L Pb	3.3±0.3^{a}	14.9±1.1^{a} (95.5%)	55.8±2.1^{b} (92.7%)	0.05±0.01
T4: 50 mg/L Pb+PEG	2.9±0.4^{a}	11.3±1.9^{a} (87.6%)	56.8±0.6^{b}	0.06±0.04
C4: 50 mg/L Pb	3.4±0.3^{a}	13.9±2.9^{a} (89.1%)	54.6±1.7^{a} (90.7%)	0.06±0.05

Values are expressed as mean±SE; columns indexed by the same letter are not significantly different according to LSD ($p<0.05$).

3.2 Effects of drought stress on chlorophyll content, fluorescence parameters and WC

Polyethylene glycol (PEG-6000; w/v-5%, 10% and 20%) was used for drought stress induction in *C. odorata* for 15 days. The concentration of total chlorophyll content, chlorophyll a and chlorophyll b, changed slightly (decreased/increased by around 10%) in drought-stressed leaves of all PEG-treated plants compared to control, where the chlorophyll a content predominated chlorophyll b in all treatments, as shown in Figure 1. The 20% PEG treatment produced a marked decrease in total chlorophyll content (13.38 mg/g FW) compared to the other treatments. However results suggested that the chlorophyll content of the plants remained unaffected by PEG.

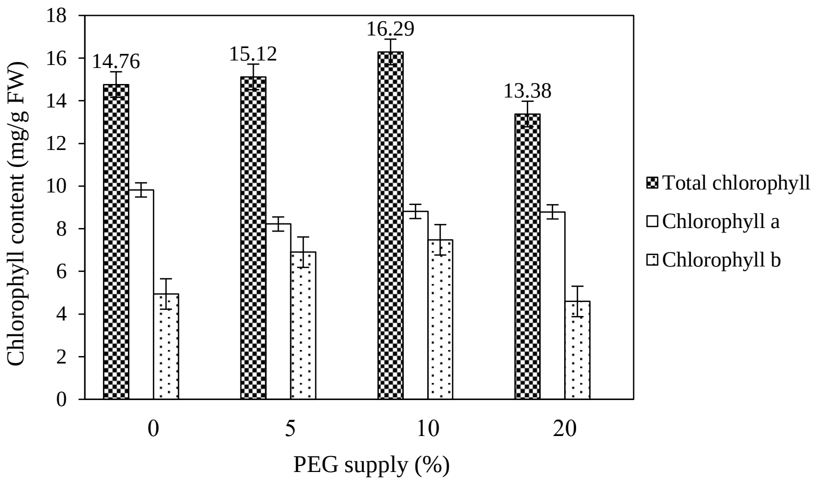

Figure 1. Effects of PEG on chlorophyll content of *C. odorata* after 15 days of treatment

Although PEG-induced drought is not severe enough to inhibit total chlorophyll content significantly after 15 days of treatment, the highest decrease was recorded with 20% PEG treatment. This was in accordance with the other species, which reported decreased or unchanged chlorophyll levels during drought stress, depending on the duration and severity of the drought (Kpyoarissis et al., 1995). On the other hand, there are many reports indicating that the application of some heavy metals substantially increases (up to 10.5% by the application of zinc (Zn)) chlorophyll content, Fv/Fm, and photosynthetic characteristics under drought conditions (Karim et al., 2012; Ma et al., 2017).

Our results indicated that the photosynthetic and fluorescence parameters of *C. odorata* were unaffected by PEG levels, but that drought stress imposed by PEG-6000 caused a decrease in the WC of the plant (Table 2). The lowest percentage of WC (71.2%) in the plant leaves was observed in the final concentration of PEG. WC was significantly ($P<0.05$) reduced in PEG-treated plants, with an increased concentration of PEG compared to the control. The results are illustrated in Table 2, which shows that the values of PI and Fv/Fm showed similar trends, with the highest values of 5.88 and 0.82 in 5% of the PEG-treated plants, respectively.

Table 2. The values of PI, Fv/Fm, and WC (%) of *C. odorata* grown under different PEG stress conditions after 15 days of treatment

PEG supply (%)	PI	Fv/Fm	WC (%)
0	4.98±0.011[a]	0.81±0.008[a]	92.3±0.293[b]
5	5.88±0.002[a]	0.82±0.004[a]	78.9±0.551[a]
10	5.11±0.009[a]	0.79±0.007[a]	76.4±0.551[a]
20	4.08±0.005[a]	0.70±0.009[a]	71.2±0.365[a]

Values are mean±SE; columns indexed by the same letter are not significantly different according to LSD ($p<0.05$).

Healthy plants with an efficient photosynthetic apparatus have typical Fv/Fm values of 0.82-0.83 (Adams and Demmig-Adams, 2004), whilst values of Fv/Fm below 0.60 are indicative of severe drought stress (Vilagrosa et al., 2010). In the present study, results in maximum quantum yield of PSII (Fv/Fm) range from 0.70 to 0.82 to indicate that the photosystems were functioning efficiently. According to Baker and Rosenqvist (2004), water stress has no major impact on the efficiency of PSII. Although *Chromolaena* sp. exhibits profuse vegetative growth when water is abundant, during drought stress, stomatal closure results in decreased leaf conductance, photosynthesis, and transpiration, which may be a sensitive response of the leaf to decreasing leaf water content, resulting in higher WC (%) reduction (Mandal and Joshi, 2014; Hailemichael et al., 2016). Based on the above criteria of Fv/Fm values, however, *C. odorata* was not affected when PEG was supplied in the range of 5-20%.

3.3 Pb accumulation in plant tissues

Lead concentrations in the roots and shoots of *C. odorata* were significantly higher ($p<0.05$) for all Pb concentrations. Moreover, the roots contained much higher concentrations, with 8-10 times more than in shoots (Figure 2 and Figure 3). Under drought conditions, both the root and shoot accumulation of Pb was significantly greater (3,173.3-5,503.7 and 441.6-786.3 mg/kg) than that in the control treatments (2,714.6-4,992.8 and 302.9-607.7 mg/kg) for all Pb solutions ($p<0.05$) except in the roots and shoots of 5 and 5-10 mg/L Pb treatment respectively. In its roots, at the highest Pb level in solution, *C. odorata* exhibited the highest accumulation (T4; 5,503.7 mg/kg) under drought stress compared to the others. The effect of PEG on Pb uptake, BCF, and TF values is shown in Table 3. Plants had a strong tolerance to PEG stress with no significant difference in Pb uptake between all nutrient solutions ($p>0.05$). Nevertheless, the BCFs of all treatments decreased and exhibited a range of 112.0-649.6 when Pb concentrations increased. In this study, all treatments had TFs<1 in all Pb solutions with a range of 0.04-0.14, and these values did not differ significantly between the single Pb treatment and that in combination with PEG. The findings of the BCF and TF tests show the ability of the plant to bioconcentrate the Pb in the root, implying that *C. odorata* is capable of Pb phytostabilization. By the end of the trial, the amount of Pb accumulation in *C. odorata* was unaffected by drought, while the translocation of Pb from the root to the shoot was affected by either single or combined stress.

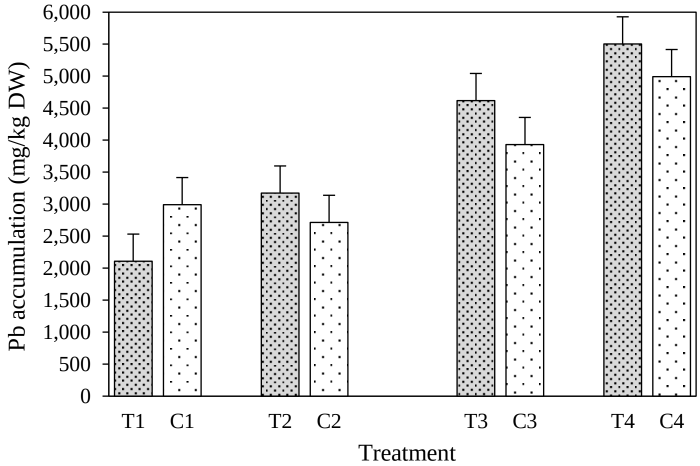

Figure 2. Pb accumulation in the roots of *C. odorata* grown for 15 days in increasing Pb concentrations with (T1-T4) and without PEG (C1-C4)

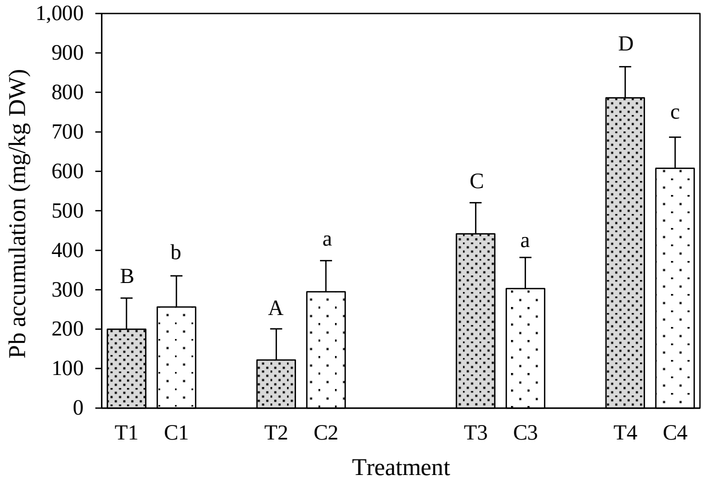

Figure 3. Pb accumulation in the shoots of *C. odorata* grown under increasing concentrations of Pb with (T1-T4) and without the addition of PEG (C1-C4) for 15 days. The same letter shows no significant differences between treatments at $p<0.05$, according to the LSD test

Table 3. The Pb uptake, TF, and BCF values of *C. odorata* grown in hydroponics under combined and uncombined with PEG

Treatments	Pb uptake (g/plant)	TF	BCF
T1: 5 mg/L Pb+PEG	6.46 ± 0.02^{a}	0.09 ± 0.04^{a}	461.7±0.1
C1: 5 mg/L Pb	10.39 ± 0.06^{a}	0.09 ± 0.03^{a}	649.6±0.2
T2: 10 mg/L Pb+PEG	10.22 ± 0.04^{a}	0.04 ± 0.08^{a}	329.5±0.1
C2: 10 mg/L Pb	7.22 ± 0.08^{a}	0.11 ± 0.11^{a}	300.9±0.0
T3: 20 mg/L Pb+PEG	13.16 ± 0.01^{b}	0.10 ± 0.01^{a}	253.0±0.3
C3: 20 mg/L Pb	13.97 ± 0.03^{b}	0.08 ± 0.52^{a}	211.7±0.0
T4: 50 mg/L Pb+PEG	18.24 ± 0.25^{c}	0.14 ± 0.12^{b}	125.8±0.0
C4: 50 mg/L Pb	19.04 ± 0.02^{c}	0.12 ± 0.60^{a}	112.0±0.1

Values are mean±SE; columns indexed by the same letter are not significantly different according to LSD ($p<0.05$).

Our results showed that *C. odorata* accumulates high root Pb concentrations, which is supported by other hydroponic studies under non-drought conditions. Tanhan et al. (2007) indicated *C. odorata* had the capacity for higher accumulations of Pb in roots (51,493-60,655 mg/kg) than in shoots, while a similar pattern can be also found in other species such as *Salix lucida* (11,535 mg/kg), *S. nigra* (14,091 mg/kg), *S. serissima* (7,036 mg/kg), and *Acacia mangium* and *Eucalyptus camaldulensis* (>40,000 mg/kg) (Zhivotovsky et al., 2011; Yongpisanphop et al., 2017). In most plants, 90% of the total Pb is accumulated in the roots (Kumar et al., 1995). It possible that the cell walls of root plants are the first barrier against Pb stress and can immobilize and accumulate some or even most Pb ions. Pb in roots is localized in the insoluble fraction of cell walls and nuclei, which is linked to the detoxification mechanism (Piechalak et al., 2002).

In order to indicate the efficiency of accumulation ability, Pb uptake and BCF values were used. Evidently, PEG added to a Pb contaminated solution did not generate significant reductions in Pb uptake of *C. odorata* when compared to uncombined PEG. On the other hand, the combined effect of Pb and PEG significantly decreased BCFs (from 461.7 to 125.8) with increased Pb concentrations, which indicates that *C. odorata* shows a relatively low bioaccumulation potential by adding Pb concentrations. In hydroponic tests, a BCF value ≥1,000 is used to identify the capacity of a plant to accumulate metals (Syuhaida et al., 2014). According to Tanhan et al. (2007), *C. odorata* was discovered to be a Pb hyperaccumulator based on a hydroponic test without drought. However, for this study, it is possible that *C. odorata* must deal with both Pb and PEG stress as a critical situation. Interestingly, in our comparison of combined and uncombined with PEG, the combined PEG treatment of 10-50 mg/L Pb solution displayed the higher BCFs, suggesting drought will cause a small increase in the ability of *C. odorata* to absorb Pb. In addition, the previous study found that the accumulation of a few heavy metals, such as copper (Cu) and zinc (Zn) in soybeans, while accumulation in French marigold (*Tagetes patula*) under drought-stress conditions was largely increased (Aziz, 2015; Kleiber et al., 2020). Unlike Cu and Zn, which are taken up by plants as essential plant nutrient elements and play an important role in a plant's metabolism, Pb is not an essential element for plants. Moreover, our results with BCFs<1,000 might be explained by the type of experiment conducted (i.e., hydroponics, greenhouse, field). In hydroponics, the number of consistent nutrient supplies might restrict the availability of Pb due to competition to limit non-essential element accumulation in plant tissues.

According to our results, all TF values less than 1 indicate that *C. odorata* is suitable for phytostabilization of Pb, as reported in other plant species grown under hydroponics such as *Avicennia marina* (Yan et al., 2010), *Sedum alfredii* (Gupta et al., 2010), *Allium sativum* (Jiang et al., 2019) and *Phyllostachys pubescens* (Liu et al., 2015). This suggests that a limited translocation of Pb occurs from the root to the other parts of the plant due to the precipitation of insoluble Pb salts in intercellular spaces, the accumulation of plasma membranes, or sequestration in the vacuoles (Yongpisanphop et al., 2017).

4. CONCLUSION

The capability of *C. odorata* to survive in a Pb-polluted solution is a clear indication of its tolerance, which is notable in its capacity for Pb uptake in the face of Pb- and PEG-induced stress. The application of PEG in nutrient solutions had no significant effect on plant growth, biomass, chlorophyll content, and fluorescence parameters. The reduction in WC (%), however, was caused by drought, while the translocation efficiency of Pb is limited by either Pb or drought. Based on the hydroponic BAFs and TF criteria, it indicates that *C. odorata* has the ability to accumulate Pb in the root and shows high Pb phytostabilization efficiency after 15 days of treatment. *C. odorata* may be considered, therefore, for Pb phytoremediation in contaminated soils under drought environmental conditions due to its tolerance to Pb and PEG combinations. In future studies, these hydroponic testing results will need to be confirmed by pot and field trial studies under drought conditions, which, considered together, significantly affect their capacity to absorb Pb.

ACKNOWLEDGEMENTS

This work was supported by the Strategic Wisdom and Research Institute from Srinakharinwirot University, Bangkok, Thailand (Grant No. 089/2562).

REFERENCES

Adams WW III, Demmig-Adams B. Chlorophyll fluorescence as a tool to monitor plant response to the environment. In: Papageorgiou GC, Govindjee G, editors. Chlorophyll A Fluorescence: A Signature of Photosynthesis, Advances in Photosynthesis and Respiration. Vol. 19. Dordrecht, Netherlands: Springer; 2004. p. 583-304.

Alengebawy A, Abdelkhalek ST, Qureshi SR, Wang MQ. Heavy metals and pesticides toxicity in agricultural soil and plants: Ecological risks and human health implications. Toxics 2021;9(3):Article No. 42.

Aziz T. A mini review on lead (Pb) toxicity in plants. Journal of Biology and Life Science 2015;6(2):91-101.

Baker AJM, Brooks RR. Terrestrial higher plants which hyperaccumulate metallic elements a review of their distribution, ecology and phytochemistry. Biorecovery 1989;1:81-126.

Baker NR, Rosenqvist E. Applications of chlorophyll fluorescence can improve crop production strategies: An examination of future possibilities. Journal of Experimental Botany 2004;55:1607-21.

Cui S, Zhou Q, Chao L. Potential hyperaccumulation of Pb, Zn, Cu and Cd in endurant plants distributed in an old smeltery, Northeast China. Environmental Geology 2007;51:1043-51.

Garg P, Chandra P. The duckweed *Wolffia globosa* as an indicator of heavy metal pollution sensitivity of Cr and Cd. Environmental Monitoring and Assessment 1994;29:89-95.

Gupta D, Huang H, Yang X, Razafindrabe B, Inouhe M. The detoxification of lead in *Sedum alfredii* H. is not related to phytochelatins but the glutathione. Journal of Hazardous Materials 2010;177(1-3):437-44.

Hailemichael G, Catalina A, González MR, Martin P. Relationships between water status, leaf chlorophyll content and photosynthetic performance in *Tempranillo vineyards*. South African Journal for Enology and Viticulture 2016; 37(2):149-56.

Hassan W, Bano R, Bashir F, David J. Comparative effectiveness of ACC-deaminase and/or nitrogen-fixing rhizobacteria in promotion of maize (*Zea mays* L.) growth under lead pollution. Environmental Science and Pollution Research International 2014;21(18):10983-96.

Hemen S. Metal hyperaccumulation in plants: A review focusing on phytoremediation technology. Journal of Environmental Science and Technology 2011;4(2):118-38.

Holm G. Chlorophyll mutations in barley. Acta Agriculturae Scandinavica 1954;4:457-61.

Hunt R. Plant Growth Analysis. London, United Kingdom: Edward Arnold; 1978.

Jabeen R, Ahmad A, Iqbal M. Phytoremediation of heavy metals: Physiological and molecular mechanisms. Botanical Review 2009;75:339-64.

Jampasri K, Saeng-ngam S, Larpkern P, Jantasorn A, Kruatrachue M. Phytoremediation potential of *Chromolaena odorata*, *Impatiens patula*, and *Gynura pseudochina* grown in cadmium-polluted soils. International Journal of Phytoremediation 2021;23(10):1061-6.

Jiang M, Liu S, Li Y, Li X, Luo Z, Song H, et al. EDTA-facilitated toxic tolerance, absorption and translocation and phytoremediation of lead by dwar bamboos. Ecotoxicology and Environmental Safety 2019;170:502-12.

Kachenko AG, Bhatia NP, Singh B. Influence of drought stress on the nickel-hyperaccumulating shrub *Hybanthus floribundus* (Lindl.) F.Muell. subsp. *Floribundus*. International Journal of Plant Sciences 2011;172(3):315-22.

Karim M, Zhang YQ, Zhao RR, Chen XP, Zhang FS, Zou CQ. Alleviation of drought stress in winter wheat by late foliar application of zinc, boron, and manganese. Journal of Plant Nutrition and Soil Science 2012;175:142-51.

Khaokaew S, Landrot G. A field-scale study of cadmium phytoremediation in a contaminated agricultural soil at Mae Sot District, Tak Province, Thailand: Determination of Cd-hyperaccumulating plants. Chemosphere 2015;138:883-7.

Kleiber T, Borowiak K, Kosiada T, Breś W, Ławniczak B. Application of selenium and silicon to alleviate short-term drought stress in French marigold (*Tagetes patula* L.) as a model plant species. Open Chemistry 2020;18(1):1468-80.

Korkmaz A, Korkmaz Y, Demirkiran AR. Enhancing chilling stress tolerance of pepper seedlings by exogenous application of 5-aminolevulinic acid. Environmental and Experimental Botany 2010;67:495-501.

Kpyoarissis A, Petropoulou Y, Manetas Y. Summer survival of leaves in a soft-leaved shrub (*Phlomis fruticosa* L., Labiatae) under Mediterranean field conditions: Avoidance of photoinhibitory damage through decreased chlorophyll contents. Journal of Experimental Botany 1995;46:1825-31.

Kumar A, Kumar A, Cabral-Pinto MMS, Chaturvedi AK, Shabnam AA, Subrahmanyam G, et al. Lead toxicity: Health hazards, influence on food chain, and sustainable remediation approaches. International Journal of Environmental Research and Public Health 2020;17:Article No. 2179.

Kumar PB, Dushenkov V, Motto H, Raskin I. Phytoextraction: The use of plants to remove heavy metals from soils. Environmental Science and Technology 1995;29(5):1232-8.

Liu D, Li S, Islam E, Chen JR, Wu JS, Ye ZQ, et al. Lead accumulation and tolerance of Moso bamboo (*Phyllostachys pubescens*) seedlings: Applications of phytoremediation. Journal of Zhejiang University Science B 2015;16(2):123-30.

Ma D, Sun D, Wang C, Ding H, Qin H, Hou J, et al. Physiological responses and yield of wheat plants in zinc-mediated alleviation of drought stress. Frontiers in Plant Science 2017;8:Article No. 860.

Mandal G, Joshi SP. Invasion establishment and habitat suitability of *Chromolaena odorata* (L.) King and Robinson over time and space in the western Himalayan forests of India. Journal of Asia-Pacific Biodiversity 2014;7:391-400.

Naidoo G, Naidoo KK. Drought stress effects on gas exchange and water relations of the invasive weed *Chromolaena odorata*. Flora 2018;248:1-9.

Omoregie G, Ikhajiagbe B. Differential morphological growth responses of *Chromolaena odorata* under heavy metal influence. Jordan Journal of Earth and Environmental Sciences 2021;12(1):50-61.

Ozturk M, Turkyilmaz Unal B, Garcia-Caparros P, Khursheed A, Gul A, Hasanuzzaman M. Osmoregulation and its actions during the drought stress in plants. Physiologia Plantarum 2020;172(2):1321-35.

Phaenark C, Pokethitiyook P, Kruatrachue M, Ngernsansaruay C. Cd and Zn accumulation in plants from the Padaeng zinc mine area. International Journal of Phytoremediation 2009;11:479-95.

Piechalak A, Tomaszewska B, Baralkiewicz D, Malecka A. Accumulation and detoxification of lead ions in legumes. Phytochemistry 2002;60(2):153-62.

Porra RJ, Thompson WA, Kriedmann PE. Determination of accurate extinction coefficients and simultaneous equations for assaying chlorophylls a and b extracted with four different solvents: Verification of the concentration of chlorophyll standards by atomic absorption spectroscopy. Biochimica et Biophysica Acta 1989;975:384-94.

Qi X, Xu X, Zhong C, Jiang T, Wei W, Song X. Removal of cadmium and lead from contaminated soils using sophorolipids from fermentation culture of *Starmerella bombicola* CGMCC 1576 fermentation. International Journal of Environmental Research and Public Health 2018;15:Article No. 2334.

Ranjbarfordoei A, Samson R, Damne PV, Lemeur R. Effects of drought stress induced by polyethylene glycol on pigment content and photosynthetic gas exchange of *Pistacia khinjuk* and *P. mutica*. Photosynthetica 2000;38(3):443-7.

Salazar C, Hernández C, Pino MT. Plant water stress: Associations between ethylene and abscisic acid response. Chilean Journal of Agricultural Research 2015;75:71-9.

Seleiman MF, Al-Shuaibani N, Ali N, Akmal M, Alotaibi M, Rafey Y, et al. Drought stress impacts on plants and different approaches to alleviate its adverse effects. Plants 2021;10(2):Article No. 259.

Sekabira KH, Oryem-Origa G, Mutumba EK, Basamba TA. Heavy metal phytoremediation by *Commelina benghalensis* (L) and *Cynodon dactylon* (L) growing in urban stream sediments. International Journal of Plant Physiology and Biochemistry 2011;3:133-42.

Simmons RW, Pongsakul P, Saiyasitpanich D, Klinphklap S. Elevated levels of cadmium and zinc in paddy soils and elevated level of cadmium in rice grain downstream of a zinc mineralized area in Thailand: Implications for public health. Environmental Geochemistry and Health 2005;27:501-11.

Stirbet A, Govindjee. On the relation between the Kautsky effect (chlorophyll a fluorescence induction) and photosystem II: Basics and applications of the OJIP fluorescence transient. Journal of Photochemistry and Photobiology B: Biology 2011;104:236-57.

Swapna KS, Shackira AM, Abdussalam AK, Nabeesa-Salim E, Puthur JT. Accumulation pattern of heavy metals in *Chromolaena odorata* (L.) King & Robins. grown in nutrient solution and soil. Journal of Stress Physiology and Biochemistry 2014;10(2):297-314.

Syuhaida AAW, Norkhadijah SIS, Praveena SM, Suriyani M. The comparison of phytoremediation abilities of water mimosa and water hyacinth. Asian Research Publishing Network Journal of Science and Technology 2014;4(12):722-31.

Tangahu BV, Abdullah SRS, Basri H, Idris M, Anuar N, Mukhlisin M. A review on heavy metals (As, Pb, and Hg) uptake by plants through phytoremediation. International Journal of Chemical Engineering 2011;2011:1-31.

Tanhan P, Kruatrachue M, Pokethitiyook P, Chaiyarat R. Uptake and accumulation of cadmium, lead and zinc by Siam weed [*Chromolaena odorata* (L.) King & Robinson]. Chemosphere 2007;68:323-9.

Vilagrosa A, Morales F, Abadía A, Bellot J, Cochard H, Gil-Pelegrin E. Are symplast tolerance to intense drought conditions and xylem vulnerability to cavitation coordinated? An integrated analysis of photosynthetic, hydraulic and leaf level processes in two Mediterranean drought-resistant species. Environmental and Experimental Botany 2010; 69:233-42.

Xu SG, Wang JH, Bao LJ. Effect of water stress on seed germination and seedling growth of wheat. Journal of Anhui Agricultural University 2006;34:5784-7.

Yan ZZ, Ke L, Tam NFY. Lead stress in seedlings of *Avicennia marina*, a common mangrove species in South China, with and without cotyledons. Aquatic Botany 2010;92(2):112-8.

Yongpisanphop J, Babel S, Kruatrachue M, Pokethitiyook P. Hydroponic screening of fast-growing tree species for lead phytoremediation potential. Bulletin of Environmental Contamination and Toxicology 2017;99(4):1-6.

Zhang Z, Rengel Z, Chang H, Meney K, Pantelic L, Tomanovic R. Phytoremediation potential of *Juncus subsecundus* in soils contaminated with cadmium and polynuclear aromatic hydrocarbon (PAHs). Geoderma 2012;1(8):175-6.

Zhivotovsky OP, Kuzovkina JA, Schulthess CP, Morris T, Pettinelli D, Ge M. Hydroponic screening of willows (*Salix* L.) for lead tolerance and accumulation. International Journal of Phytoremediation 2011;13:75-94.

Microplastic Ingestion by Fishes from Jamuna River, Bangladesh

H.M. Shahnewaz Khan* **and Shamsunnahar Setu**

Department of Environmental Science and Resource Management, Mawlana Bhashani Science and Technology University, Tangail, Bangladesh

ARTICLE INFO

Received: 23 Aug 2021
Received in revised: 19 Nov 2021
Accepted: 29 Nov 2021
Published online: 24 Jan 2022
DOI: 10.32526/ennrj/20/202100164

Keywords:
Microplastic/ Plastic pollution/ Gastrointestinal tract/ River/ Bangladesh

*** Corresponding author:**
E-mail:
Shahnewaz14037@gmail.com

ABSTRACT

Microplastics (MP) have been an evolving global concern by dint of the escalation of plastic pollution in the aquatic environment. However, few data document MP ingestion and accumulation in freshwater fauna as compared to marine organisms. This study investigates the prevalence of MPs in the gastrointestinal tracts (GIT) of 45 individuals belonging to seven commonly found Bangladeshi freshwater fish species with different feeding types (herbivore, carnivore, and omnivore). A total of 81 MP items of varying shapes were detected in 76% of individuals investigated, with an average abundance of 1.80±1.65 items/individual. Of these, fiber was identified as the most prevalent ingested MP type (70%) followed by film (14%), line (10%), fragment (4%), and foam (2%). Black-colored MPs were the most dominant (27%) followed by white (26%), blue (24%), red (17%), and green (6%). The results demonstrated a higher number of MPs in the carnivore (1.95 items/individual) and omnivore (1.85 items/individual) fish species as compared to herbivore fish species. Among carnivores, *Wallago attu* registered the highest amount of ingested MP items (3.5 items/individual), while *Anguilla bengalensis* registered the highest amount of ingested MP items (2.14 items/individual) among the omnivores. The amount of ingested MPs was significantly correlated ($P<0.05$) with body size, body weight, and gut weight, while an insignificant correlation ($P>0.05$) was found between the number of consumed MPs and trophic fractions. The results provide valuable insights into the prevalence of MPs in freshwater fish in Bangladesh and associated bioaccumulation through trophic transfer.

1. INTRODUCTION

Plastics are recognized as artificial substances composed of synthetic or semi-synthetic natural polymers manufactured from petro-based chemicals that are cost-effective, lightweight, durable, and corrosive resistant (Boucher and Friot, 2017; Denuncio et al., 2011). Plastic production has been increased about 43% over the last decade. According to data from the Association of Plastic Europe, worldwide plastic production hit 322 million tons during 2015 (Plastics Europe and EPRO, 2016), 335 million tons in 2017 (Lahens et al., 2018), and demand is presumed to increase to 1,000 million tons by 2050 (Lusher et al., 2017). Freshwater ecosystems are the primary destination of many pollutants delivered in the watershed since aquatic environments are generally situated in valleys and low-height landscapes. Plastic discarded inaccurately (e.g., roads, streets, and open landfills) are conveyed by pluvial flows to water bodies (Faure et al., 2015). Upon reaching freshwaters, plastics may get entangled by streambed structures (e.g., riverbanks, shrubs, trees, and cliffs), carry with the current to floodplains, or become entrained in adjacent sediments (Azevedo-Santos et al., 2021). In Brazil's Amazonian ecosphere, plastic comprises 15.7% of total solid waste and it is precisely estimated that 182,085 metric tons of plastic are dumped yearly, which is potentially transported by the Amazon River to the Atlantic Ocean, presently the world's second most plastic-polluted river, trailing only China's Yangtze River (Giarrizzo et al., 2019). Rivers currently dump 1.15 to 2.41 million tonnes of plastic waste each year into the ocean. The world's 20 most polluting waterways, primarily in Asia, represent

Citation: Khan HMS, Setu S. Microplastic ingestion by fishes from Jamuna River, Bangladesh. Environ. Nat. Resour. J. 2022;20(2):157-167. (https://doi.org/10.32526/ennrj/20/202100164)

67% of overall pollution (Lebreton et al., 2017). Admittedly, rivers have gotten very little consideration concerning the issue of microplastic (MP) pollution (Costa and Barletta, 2015). Plastic particles less than 5 mm are commonly known as microplastics (Hartmann et al., 2019). In the early 1970s, microplastics were documented in seawater. (Guzzetti et al., 2018). Microplastics have been marked as deriving environmental pollutants that have also procured research concern at present. The micropollutants are present in both terrestrial and aquatic environments having deleterious effects on existing ecosystems (Karim et al., 2020).

The largest densities of microplastic debris have been reported from plankton (Yu et al., 2020), water bodies (Deng et al., 2020), and sediment (Castañeda et al., 2014). Predominantly found plastic particles within the aquatic environment are: fragments, fibers, and pellets (Veiga et al., 2016). Prior studies have used various methods to detach, identify, and validate plastic pollution in fish (Boerger et al., 2010; Vendel et al., 2017). For example, plastic objects were examined in the whole gastrointestinal tract (GIT) (Liboiron, 2019). Their origin classifies microplastics. Primary microplastics are cosmetic (i.e., shower gel, lipstick, and shaving cream), cleaning products, exfoliating scrubs, and medicines. Secondary microplastics result from micro-and macro debris fragmentation, subjected to mechanical forces, oxidation, and photochemical processes (Mathalon and Hill, 2014). Plastic enters an aquatic ecosystem by river drainage, storm water, and wastewater treatment plant (WWTP) discharges (Dris et al., 2015). A range of 19 to 447 particles/L of microplastics was found in the effluent of ten of Denmark's largest tertiary WWTPs and emitted up to 1 to 30 particles/L from three secondary WWTPs (Conley et al., 2019). The most polymer confronted; specifically, microplastics are polyethylene terephthalate (PET), polypropylene (PP), polyvinylchloride (PVC), polyethylene (PE), polystyrene (PS), and polytetrafluoroethylene (PTFE) (Rocha-Santos and Duarte, 2015; Xu et al., 2020).

A broad range of marine organism ingested microplastics have been reported in fishes (Bellas et al., 2016; Jovanović, 2017), turtles (Duncan et al., 2019), sea birds (Lavers et al., 2019), and mammals (Zantis et al., 2021). Obvious consequences of microplastic ingestion by aquatic organisms are blockage of GIT, growth retardation, reproduction failure, and alteration of feeding (Cole et al., 2015; Nelms et al., 2018; Sussarellu et al., 2016). In addition, contaminants accumulating on the surface of plastic materials may have detrimental health effects on fish (Critchell and Hoogenboom, 2018; Pannetier et al., 2020). Plastic has been shown to influence DNA damage, oxidative pressure, cirrhosis, embryo-toxicity, aberrant riposte, and lipid peroxidation (Brandts et al., 2018) in fishes. The prime goal of the following study was to identify the presence of MPs in the gastrointestinal tract (GIT) of freshwater fish. Particularly, the research objectives were to 1) assess the abundance, morphotype, and color of MPs in fish gut contents, 2) compare the MPs concentration among diverse species of fishes from different feeding habitats and tropic fractions, and 3) determine the association between MPs intake rate and fish length, body weight, and gut-weight. These findings provided the early sign of microplastic contamination of Jamuna River's fishes. The findings demonstrated that fishes of Jamuna River incorporate varying amounts of microplastics in the gastrointestinal tract.

2. METHODOLOGY

2.1 Study area

This study was carried out on Jamuna River, between 24°22'41.17"N, 89°47'49.08"E (S1; close to Bangabandhu Bridge, Tangail District) and 24°11' 42.17"N, 89°46'36.74"E (S2; near Chauhali Upazila, Sirajganj District) (Figure 1). A delta plain with tributaries of the Ganges (Padma), Brahmaputra (Jamuna), and Meghna Rivers occupying 79% of the nation. Jamuna-Brahmaputra Rivers are roughly victims of industrial (pulp, paper, textiles, fertilizers, and detergent) toxic discharges, lubricants, and heavy metals. Plastic particles scattered over the branches by stream gliding or weaving and tourist spots near Jamuna Bridge could be one of the basic explanations of plastic contamination in the normal natural way of life (Hossain et al., 2019; Uddin and Jeong, 2021).

2.2 Sample collection

In total, 45 individuals representing seven species with 20.74±8.65 cm average length were collected by 5 mm mesh nets during the time period of 20th April to 5th July 2019. During sampling, divergent feeding zones (demersal, benthopelagic, and pelagic) with feeding habits were considered (herbivore, carnivore, and omnivore) (Table 1). Sample collection also relied on the conventional fish consumption nature and accessibility of fishes for that certain fishing period. Therefore, resulting in different numbers of individuals for each species. Then, samples were put into an icebox to preserve and transport, and taken to the laboratory for storage in a refrigerator at -4°C for analysis (Peters and Bratton, 2016).

2.3 Sample preparation

In the laboratory, fish were allowed to thaw for about 30 minutes at room temperature before examining total length (TL) and body weight (W). Consequently, the GIT of each fish was dissected. After weighing, samples were transferred into individual clean beakers (Figure 2).

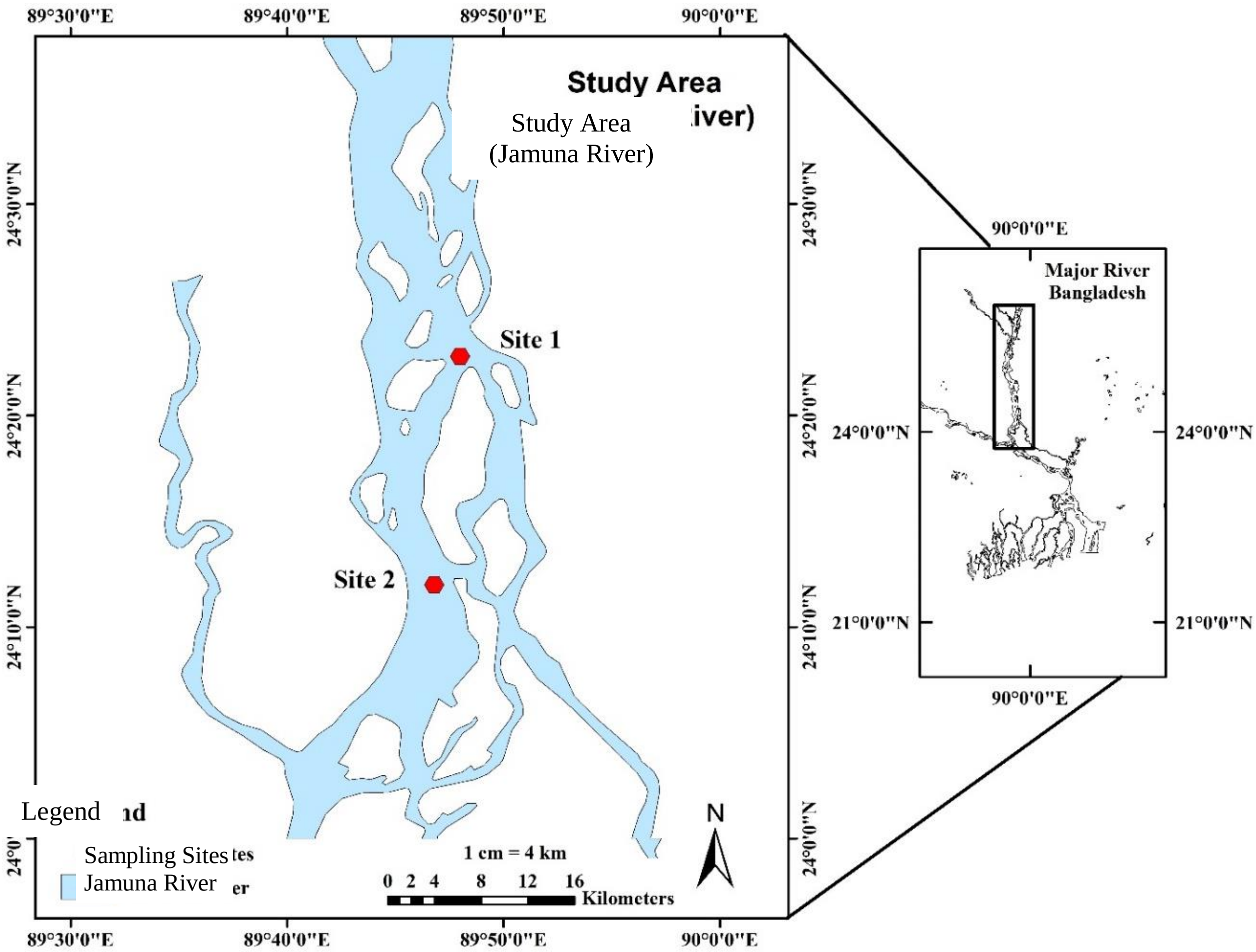

Figure 1. Map showing the study area (Jamuna River)

Table 1. Generic information about sample fishes, i.e., scientific name, local name, tropic fraction, feeding zone, and feeding group

Scientific name	Local name	Number (n)	Tropic fraction	Feeding zone	Feeding group	Total length (cm)	Total weight (g)	Gut weight (g)
Wallago attu	Boal	8	3.70±0.56	Demersal	Carnivore	31.46±3.73	142.50±50.90	3.62±0.70
Anguilla bengalensis	Biam	7	3.80±0.70	Benthopelagic	Omnivore	26.27±13.70	94.28±143.82	2.58±2.25
Labeo Calbasu	Karlbaous	8	2.00±0.00	Demersal	Omnivore	19.61±1.52	95.37±19.96	3.84±1.09
Ailia coila	Kajali	5	3.60±0.60	Pelagic	Carnivore	11.16±1.05	5.20±1.30	0.22±0.02
Cirrhinus reba	Tatkini	5	2.50±0.20	Benthopelagic	Herbivore	12.56±0.61	18.80±1.64	0.79±0.15
Ompok pabda	Pabda	7	3.80±0.60	Demersal	Carnivore	17.05±0.59	26.71±3.25	0.57±0.13
Clupisoma garua	Gaira	5	3.70±0.59	Demersal	Omnivore	20.52±1.77	50.40±12.62	2.80±1.17

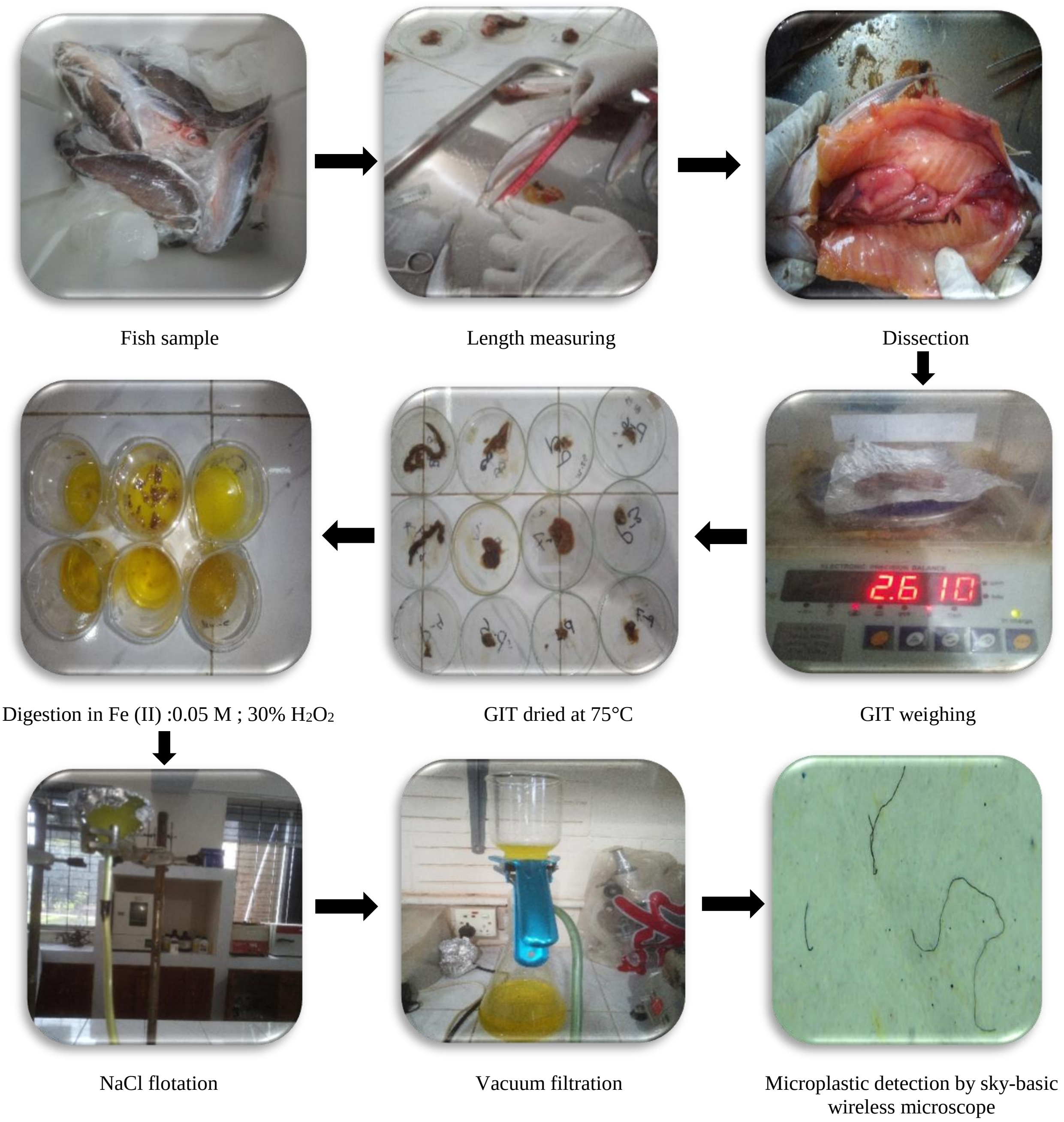

Figure 2. Preparation of samples, digestion, and analytical processes to identify microplastics in fish samples

2.4 Digestion and hydrogen peroxide (H_2O_2) treatment

The removed digestive tissue was dried a minimum of 24 h at 75°C in a hot air oven and added to 20 mL 0.05 M Fe(II) (7.5 g $FeSO_4.7H_2O$) (278.02 g/mole) in 500 mL water with 3 mL concentrated H_2SO_4) and 20 mL (H_2O_2 30%) at 75°C. The mixture was left to stand on a lab bench at room temperature for five minutes, then heated to 75°C on a hotplate. As gas bubbles affirmed, the beaker was removed from the hotplate and approximately 6 g of salt (NaCl) was added to increase the aqueous density. The mixture was heated to 75°C until the salt dissolved (McNeish et al., 2018). The developed analytical techniques have both advantages and disadvantages (Strungaru et al., 2019) for MPs detection in aquatic organisms. NaCl solution was used in this study because of its efficacy, low cost, and non-hazardous features. Instead of H_2O_2, HNO_3 (Chan et al., 2019), and NaOH (Yuan et al., 2019) was used to digest organic matter.

2.5 Density separation, floating, and vacuum filtration

The solution was transferred to the density separator (glass funnel fitted with a 50 mm segment of latex tube), putting a pinch clamp on top to control liquid flow. The beaker was rinsed with distilledwater and lined overnight by aluminum foiling to transfer all the remaining organs to the density separator. Visually inspected floating microplastics and remaining settled organs were vacuum filtered through 1.2 μm Whitman GF/Microfiber filter papers (Masura et al., 2015).

2.6 Detection of microplastics

Filters were observed under a sky-basic wireless digital microscope, and images of plastic items were taken by installing Max-See software in the android phone at 50X-100X magnifications at different resolutions (1,920×1,080, 1280×720, and 640×480). Then, visually assessed the plastic images and categorized them by color and shape (fiber, fragment, thread line, film, or foam) (Figure 3).

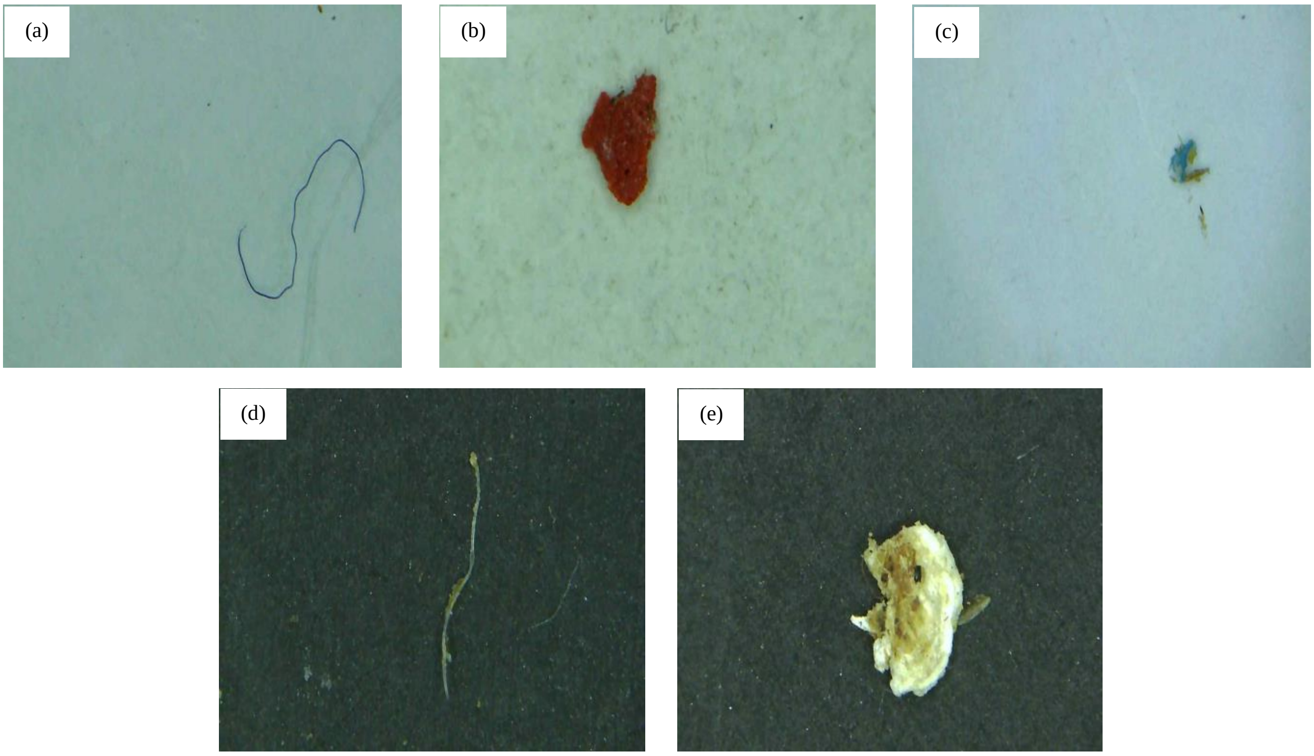

Figure 3. Example of microplastic found in fish from Jamuna River. The shapes included fiber (a), fragment (b), film (c), thread line (d), and foam (e).

3. RESULTS

3.1 Abundance of microplastic in fish

Out of seven species collected from Jamuna River, 34 of 45 individuals (76%) contained an average of 1.80±1.65 particles (SD) per total fish. Fish ranged in length from 54.3 to 10.2 cm and weight between 400 to 4 g. On average, the highest (3.50±1.93, 35%) microplastic particles per species are extracted from *Wallago attu* and the lowest MPs exhibited from *Ompok pabda* (1.00±0.58, 9%) followed by *Labeo calbasu* (2.12±1.55, 21%), *Anguilla bengalensis* (2.14±1.21, 18%), *Clupisoma garua* (1.00±1.12, 6%), *Cirrhinus reba* (1.00±1.41, 6%) and *Ailia coila* (0.80±1.30, 5%) (Figure 4(a) and 4(b)).

3.2 Morphotype and color distribution of microplastic

From the 81 particles, 57 were fiber (70%), 11 were film (14%), 8 line (10%), 3 fragment (4%), and 2 foam (2%) (Figure 4(c)). Color distribution of ingested microplastic was not homogenous. Five different colors of microplastic were found among the species. Black particles were most commonly found (27%), subsequently, white (26%), blue (24%), red (17%), and green (6%) (Figure 5(a)), which differs from Bessa et al. (2018) observed blue as most specific color (47%) led by transparent (30%) and black (11%). This study shows, the predominant fiber colors were black (39%) and blue (28%), followed by red (21%), green (9%), and white (3%) (Figure 5(b)).

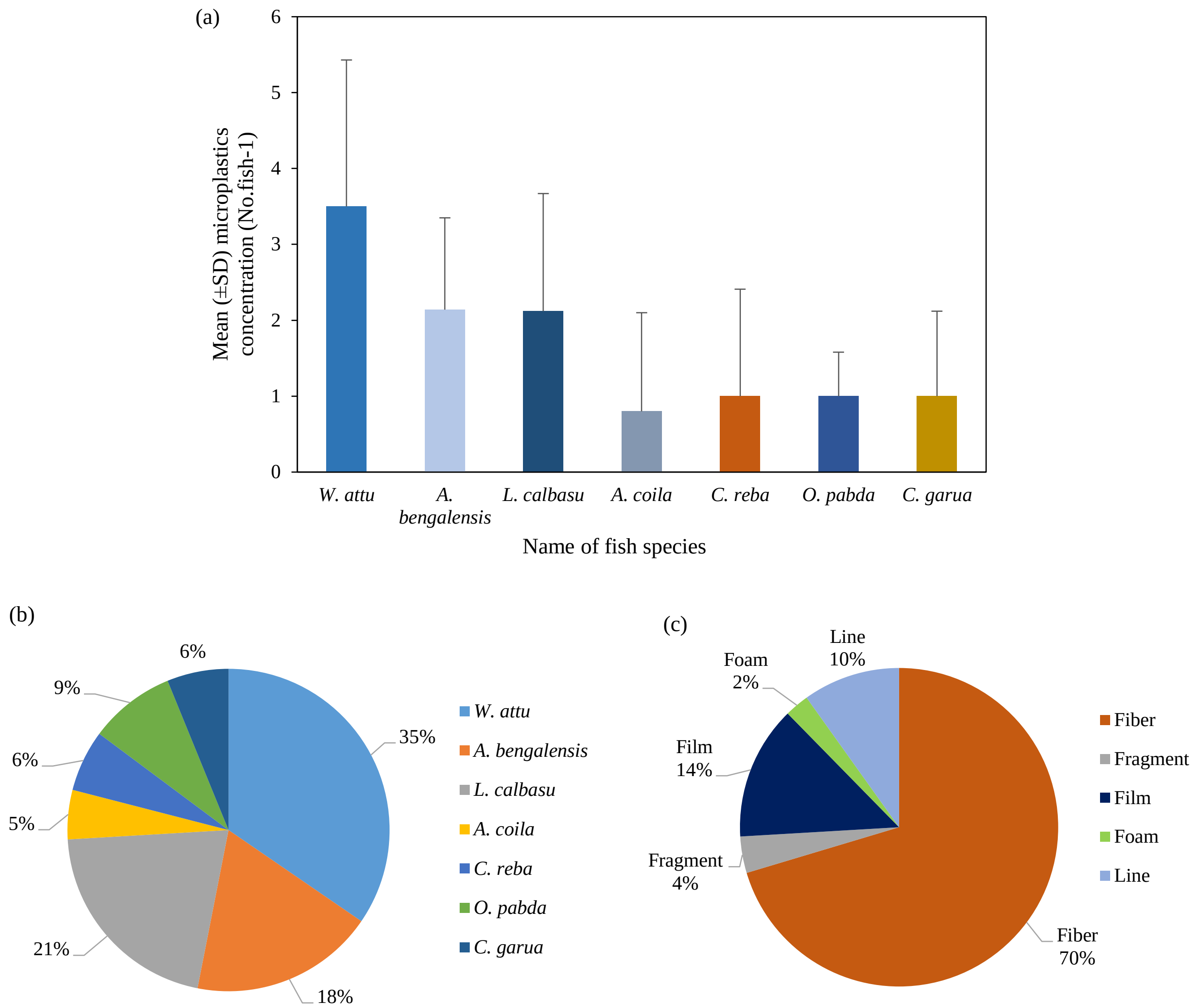

Figure 4. Average: (a) percentage (%), (b) morhotype, and (c) of microplastic in identified fishes

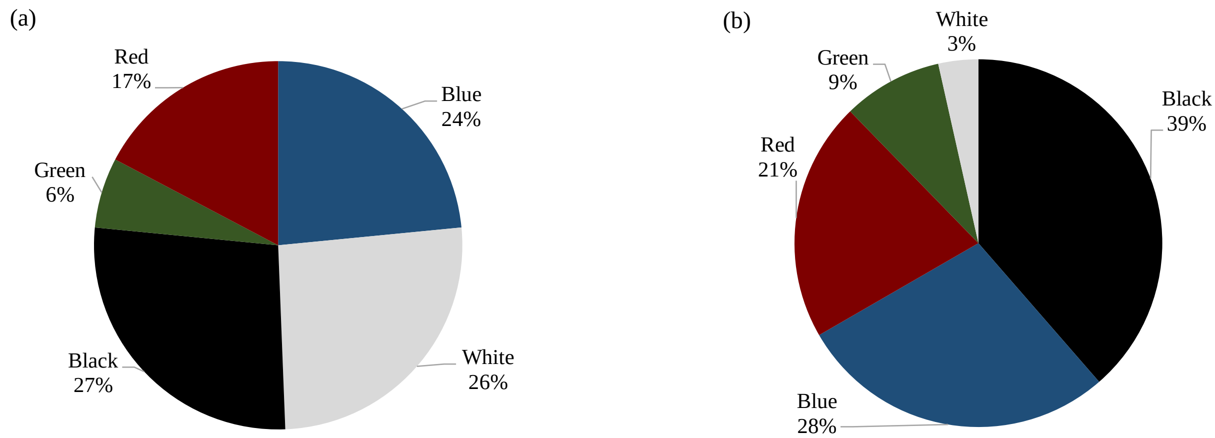

Figure 5. Percentage of MPs by color (a), frequency of fibers color (b), average of microplastic in different fish feeding zone of seven fish species (c)

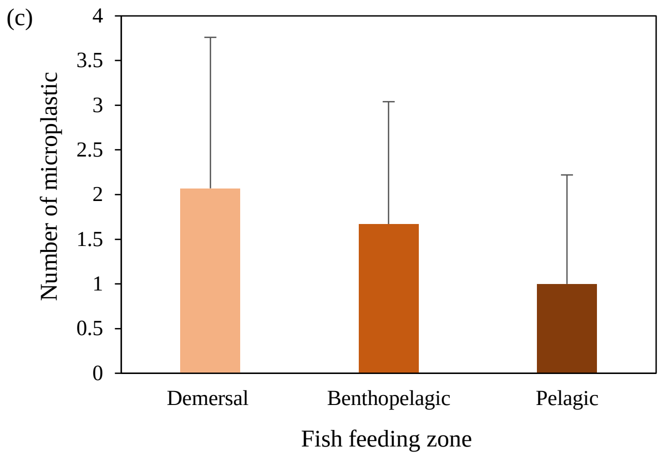

Figure 5. Percentage of MPs by color (a), frequency of fibers color (b), average of microplastic in different fish feeding zone of seven fish species (c) (cont.)

3.3 MPs abundance with fishing habitat and tropic level

A one-way ANOVA indicated that the mean microplastic particles were significantly different among the seven taxa (F=3.062, df=6, and P=0.015), but an insignificant effect of fish FFG on microplastic concentration was found (F=0.736, df=2, and P=0.485) (Table 2).

3.4 Influence of MPs absorption among fish body length, body weight, and gut weight

Fish body size (R^2=0.436, P<0.05), body weight (R^2=0.459, P<0.05) were positively correlated with the microplastic abundance in fish specimens. The relationship between the rate of microplastic intake and gut-weight was statistically significant (R^2=0.439, P<0.05) (Figure 6(a), 6(b), and 6(c)). Whereas, number of microplastics and tropic fraction showed an indistinct correlation. (Spearman's correlation, rho=0.119, P>0.05).

Table 2. Comparison of mean microplastic concentration among taxa and fishing groups, using one-way ANOVA and Kruskal-Wallis statistical analyses

Sample type	df	ANOVA		Kruskal-Wallis		
		F Value	P Value	H	X^2	P Value
Fish Taxa	6	3.062	0.015	13.331	12.591	0.038
Fish FFG	2	0.736	0.485	1.896	5.991	0.395

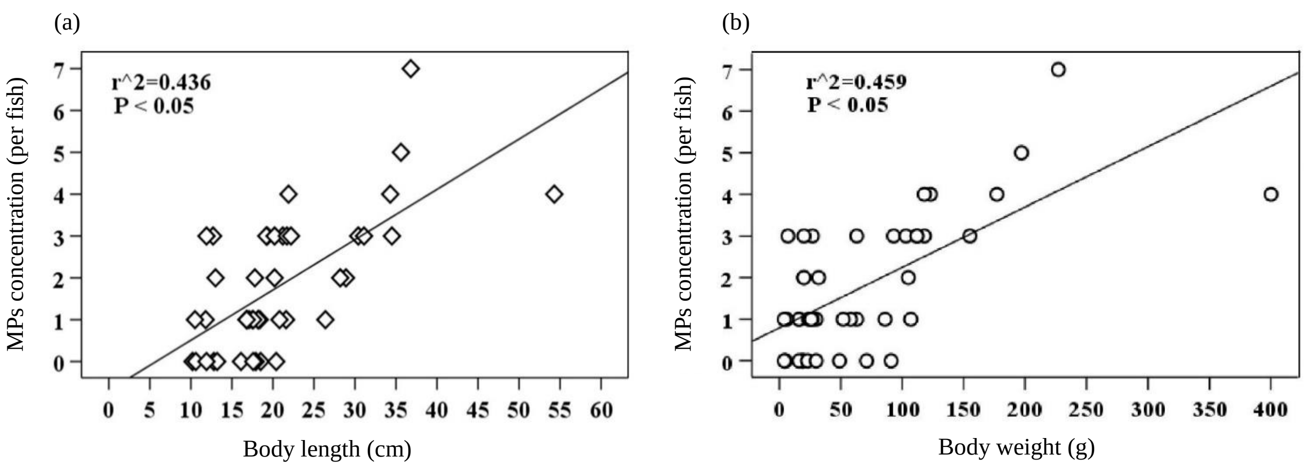

Figure 6. Linear regression analysis for number of microplastic with fish size (a), body weight (b), and gut weight (c)

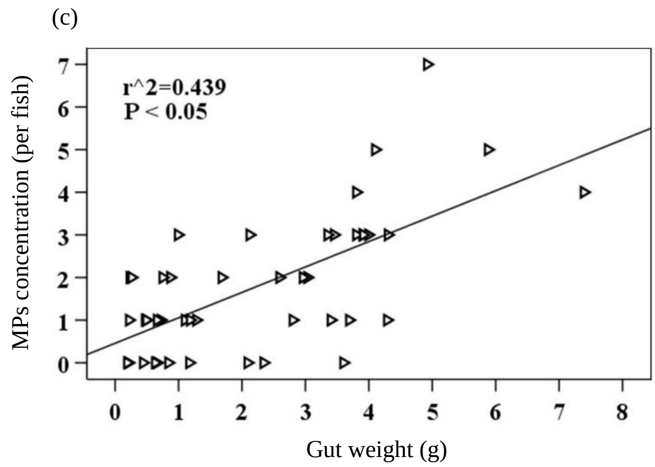

Figure 6. Linear Regression analysis for number of microplastic with fish size (a), body weight (b), and gut weight (c) (cont.)

4. DISCUSSION

In spite of the nutrient value of fish and its crucial role in the aquatic ecosystem, few studies particularly look at plastic burden in freshwater species. Our study is reputedly the first to portray ingestion of plastic by Jamuna River fishes. Bangladesh produced approximately 400 to 4,500 tons of solid debris daily which usually carries mismanaged plastic, more than half of this waste is disposed of in low-lying soil or freshwater (Arefin and Mallik, 2017). Thus, Bangladesh placed 10th over 20 improperly managed plastic generator countries around the globe. ESDO (2016) asserted Bangladesh has 7,928 billion microbeads entering its rivers, canals, and alternative water resources.

More than 250 particles were sorted from the gut contents and examined under a microscope. By characterizing the morphotype, we determined 81 particles as plastic those found in several studies (e.g., Vendel et al., 2017; Herrera et al., 2019; Arias et al., 2019). Almost all synthetic fibers are released from textile and domestic washing (Cesa et al., 2017). The line probably derives from fishing gear, nets, and sewing thread. Even so, the fragments and films come from an array of indefinite sources, from land and aquatic features. In this research, the size and nature of plastic could not be confirmed by applying FTIR spectroscopy due to the small width of plastic.

In the current study, 78% of sample fish contained microplastic with fiber (70%) most dominated. This result can be closely analogous to the findings of other research conducted in various regions. The ingestion of MPs reported in 68% in *Boops boops* from Balearic Island (Nadal et al., 2016), 95.7% in freshwater fishes from china (Jabeen et al., 2017), 85% in lake Michigan (USA) where 97-100% of all particles were fiber (McNeish et al., 2018), 8% in fishes from Mexican Gulf (Phillips and Bonner, 2015).

Sanchez et al. (2014) exposed the first proof on MPs ingestion by freshwater fish in wild gudgeons (*Gobio gobio*), about 12%. In particular, MPs were retrieved from *Wallago attu* (35% and *Labeo calbasu* (21%) in the present study. *Lepomis macrochirus* and *L. megalotis* had 45% particles that were collected from the Central River Basin of Brazos, Texas (Peters and Bratton, 2016) and ESDO (2016) found 35% microplastic in rui (*Labeo rohita*) and 2.2% in sharputi (*Puntius sarana*). MPs reported about 33%, 49%, and 18% in *H. translucens*, *H. nehereus*, and *S. gibbosa* fishes, respectively, from the coastline of northern Bay of Bengal, carried fiber mostly ascendant, while MPs differed significantly among fish species and relevant with body and GIT weight (Hossain et al., 2019). Pazos et al. (2017) reported 96% of the fiber in fish from Río de la Plata estuary, merging no correlation between MPs quantity and fish length, weight, and feeding habit. In constant, particles constituted fragments at 54% in South-western Germany (Roch et al., 2019). Pegado et al. (2018) showed the number of MPs was not correlated with weight and tropic level.

Based on feeding habits, Carnivore and omnivore guild contained 20 fishes, and the Herbivore guild had five fish. (Table 1). As a result, determining which feeding habit incorporates more MPs ingestion was difficult. According to Ismail et al. (2018), microplastic density in omnivore and carnivore fishes was lower comparing herbivore fishes from Biawak Island. Nevertheless, Garnier et al. (2019) reported herbivore fish *Siganus* spp. had the lowest MPs (0.15±0.10) and carnivore fish *Epinephelus merra* contained the highest number of MPs (0.39±0.14) per fish. Andrade et al. (2019) depicted herbivores had observed lowest percentage of plastics (13.3% for *Myloplus rubripinnis* and rose to 27.3% for *Metynnis guaporensis*). Omnivores had the greatest degree of frequency, with *Acnodon normani* accounted for 25.0% and *Myloplus rhom boidalis* making up 100%. In Carnivore stomachs, microplastic was found at a sufficient amount ranging from 14.3% in *Semasalmus manueli* to 75.0% in *Pygocentrus nattereri*. The current study found that the feeding zones have an influence on MPs assimilation by fish. The presence of MPs in demersal (2.07±1.69) fishes were higher than benthopelagic (1.67±1.37) and pelagic (1.00 ±1.22) fishes (Figure 5(c)) as demersal species are both carnivorous and omnivorous, eating a wide range of plant and animal-based foods (e.g., larvae, insects, crustaceans, mollusks, and algae).

5. CONCLUSION

Based on the study, it can be concluded that fishes from the Jamuna River are at risk of being contaminated with microplastics. Approximately 76% of processed microplastics 70% were fibers and 14% were films. We observed a significant difference in the frequency of microplastic occurrence between the different fish species. Microplastics were most abundant in carnivore species, *Wallago attu* and the lowest recorded in herbivore: *Ailia coila*. This study also showed that the number of the microplastics ingested are independent of the feeding habits but had reliant on feeding zone. Our findings include a benchmark estimate that should be considered not just in future studies aimed at describing the possible effects of microplastic in fish assemblages and potential ecological threats, as well as in studies aimed at assessing the impacts of microplastic contamination on native communities that rely on fish as food supply. Furthermore, research should be carried out within a wide variety of fish and organisms to understand the dormant effects and to clarify the MPs movement across the terrestrial-aquatic boundary on the freshwater ecosystem in Bangladesh.

ACKNOWLEDGEMENTS

For the entire study, the authors covered all expenditures on their own. The authors thank the personnel of the research lab of the ESRM Department, MBSTU for assuring all of the required equipment and nonchalant laboratory conditions for this work. We would thankfully acknowledge the editor and anonymous reviewers for their constructive feedback that improved greatly the manuscript.

REFERENCES

Andrade MC, Winemiller KO, Barbosa PS, Fortunati A, Chelazzi D, Cincinelli A, et al. First account of plastic pollution impacting freshwater fishes in the Amazon: Ingestion of plastic debris by piranhas and other serrasalmids with diverse feeding habits. Environmental Pollution 2019;244:766-73.

Arefin MA, Mallik A. Sources and causes of water pollution in Bangladesh: A technical overview. Bibechana 2017;15:97-112.

Arias AH, Ronda AC, Oliva AL, Marcovecchio JE. Evidence of microplastic ingestion by fish from the Bahía Blanca Estuary in Argentina, South America. Bulletin of Environmental Contamination and Toxicology 2019;102:750-6.

Azevedo-Santos VM, Brito MFG, Manoel PS, Perroca JF, Rodrigues-Filho JL, Paschoal LRP, et al. Plastic pollution: A focus on freshwater biodiversity. Ambio 2021;50:1313-24.

Bellas J, Martínez-Armental J, Martínez-Cámara A, Besada V, Martínez-Gómez C. Ingestion of microplastics by demersal fish from the Spanish Atlantic and Mediterranean coasts. Marine Pollution Bulletin 2016;109:55-60.

Bessa F, Barría P, Neto JM, Frias JPGL, Otero V, Sobral P, et al. Occurrence of microplastics in commercial fish from a natural estuarine environment. Marine Pollution Bulletin 2018;128: 575-84.

Boerger CM, Lattin GL, Moore SL, Moore CJ. Plastic ingestion by planktivorous fishes in the North Pacific Central Gyre. Marine Pollution Bulletin 2010;60:2275-8.

Boucher J, Friot D. Primary Microplastics in the Oceans: A Global Evaluation of Sources. Gland, Switzerland: IUCN; 2017.

Brandts I, Teles M, Tvarijonaviciute A, Pereira ML, Martins MA, Tort L, et al. Effects of polymethylmethacrylate nanoplastics on Dicentrarchus labrax. Genomics 2018;110:435-41.

Castañeda RA, Avlijas S, Simard MA, Ricciardi A. Microplastic pollution in St. Lawrence River sediments. Canadian Journal of Fisheries and Aquatic Sciences 2014;71:1767-71.

Chan HS, Dingle C, Not C. Evidence for non-selective ingestion of microplastic in demersal fish. Marine Pollution Bulletin 2019;149:Article No. 110523.

Cole M, Lindeque P, Fileman E, Halsband C, Galloway TS. The impact of polystyrene microplastics on feeding, function and fecundity in the marine copepod *Calanus helgolandicus*. Environmental Science and Technology 2015;49:1130-7.

Conley K, Clum A, Deepe J, Lane H, Beckingham B. Wastewater treatment plants as a source of microplastics to an urban estuary: Removal efficiencies and loading per capita over one year. Water Research X 2019;3:Article No. 100030.

Costa MF, Barletta M. Microplastics in coastal and marine environments of the western tropical and sub-tropical Atlantic Ocean. Environmental Sciences: Processes and Impacts 2015;17:1868-79.

Critchell K, Hoogenboom MO. Effects of microplastic exposure on the body condition and behaviour of planktivorous reef fish (*Acanthochromis polyacanthus*). PloS One 2018;13:1-19.

Deng H, Wei R, Luo W, Hu L, Li B, Di Y, et al. Microplastic pollution in water and sediment in a textile industrial area. Environmental Pollution 2020;258:Article No. 113658.

Dris R, Imhof H, Sanchez W, Gasperi CJ. Beyond the ocean: Contamination of freshwater ecosystems with (micro-) plastic particles. Environmental chemistry 2015;12:539-50.

Duncan EM, Broderick AC, Fuller WJ, Galloway TS, Godfrey MH, Hamann M, et al. Microplastic ingestion ubiquitous in marine turtles. Global Change Biology 2019;25:744-52.

Denuncio P, Bastida R, Dassis M, Giardino G, Gerpe M, Rodríguez D. Plastic ingestion in Franciscana dolphins, *Pontoporia blainvillei* (Gervais and d'Orbigny, 1844), from Argentina. Marine Pollution Bulletin 2011;62:1836-41.

Environment and Social Development Association (ESDO). Study Report Microbeads! Unfold Health Risk and Environmental Pollutant. Environment and Social Development Association; 2016.

Faure F, Demars C, Wieser O, Kunz M, De Alencastro LF. Plastic pollution in Swiss surface waters: Nature and concentrations, interaction with pollutants. Environmental Chemistry 2015; 18;12:582-91.

Garnier Y, Jacob H, Guerra AS, Bertucci F, Lecchini D. Evaluation of microplastic ingestion by tropical fish from Moorea Island, French Polynesia. Marine Pollution Bulletin 2019;140:165-70.

Giarrizzo T, Andrade MC, Schmid K, Winemiller KO, Ferreira M, Pegado T, et al. Amazonia: The new frontier for plastic pollution. Frontiers in Ecology and the Environment 2019;17:309-10.

Guzzetti E, Sureda A, Tejada S, Faggio C. Microplastic in marine organism: Environmental and toxicological effects. Environmental Toxicology and Pharmacology 2018;64:164-71.

Hartmann NB, Hüffer T, Thompson RC, Hassellöv M, Verschoor A, Daugaard AE, et al. Are we speaking the same language? Recommendations for a definition and categorization framework for plastic debris. Environmental Science and Technology 2019;53:1039-47.

Herrera A, Ŝtindlová A, Martínez I, Rapp J, Romero-Kutzner V, Samper MD, et al. Microplastic ingestion by Atlantic chub mackerel (*Scomber colias*) in the Canary Islands coast. Marine Pollution Bulletin 2019;139:127-35.

Hossain MS, Sobhan F, Uddin MN, Sharifuzzaman SM, Chowdhury SR, Sarker S, et al. Microplastics in fishes from the Northern Bay of Bengal. Science of the Total Environment 2019;690:821-30.

Ismail MR, Lewaru MW, Prihadi DJ. Microplastics Ingestion by fish in the Biawak Island. World Scientific News 2018;106: 230-7.

Jabeen K, Su L, Li J, Yang D, Tong C, Mu J, et al. Microplastics and mesoplastics in fish from coastal and fresh waters of China. Environmental Pollution 2017;221:141-9.

Jovanović, B. Ingestion of microplastics by fish and its potential consequences from a physical perspective. Integrated Environmental Assessment and Management 2017;13:510-5.

Karim ME, Sanjee SA, Mahmud S, Shaha M, Moniruzzaman M, Das KC. Microplastics pollution in Bangladesh: Current scenario and future research perspective. Chemistry and Ecology 2020;36:83-99.

Lahens L, Strady E, Kieu-le T, Dris R, Boukerma K, Rinnert E, et al. Macroplastic and microplastic contamination assessment of a tropical river (Saigon River, Vietnam) transversed by a developing megacity. Environmental Pollution 2018;236: 661-71.

Lavers JL, Stivaktakis G, Hutton I, Bond AL. Detection of ultrafine plastics ingested by seabirds using tissue digestion. Marine Pollution Bulletin 2019;142:470-4.

Lebreton LC, Van Der Zwet J, Damsteeg JW, Slat B, Andrady A, Reisser J, et al. River plastic emissions to the world's oceans. Nature Communications 2017;8:1-10.

Liboiron M. How to Investigate Fish Guts for Marine Microplastics. Civic Laboratory for Environmental Action Research; 2019.

Lusher AL, Welden NA, Sobral P, Cole M. Sampling, isolating and identifying microplastics ingested by fish and invertebrates. Analytical Methods 2017;9:1346-60.

Masura J, Baker J, Foster G, Arthur C. Laboratory Methods for the Analysis of Microplastics in the Marine Environment: Recommendations for Quantifying Synthetic Particles in Waters and Sediments. NOAA Technical Memorandum; 2015.

Mathalon A, Hill P. Microplastic fibers in the intertidal ecosystem surrounding Halifax Harbor, Nova Scotia. Marine Pollution Bulletin 2014;81:69-79.

McNeish RE, Kim LH, Barrett HA, Mason SA, Kelly JJ, Hoellein TJ. Microplastic in riverine fish is connected to species traits. Scientific Reports 2018;8:1-12.

Nadal MA, Alomar C, Deudero S. High levels of microplastic ingestion by the semipelagic fish bogue *Boops boops* (L.) around the Balearic Islands. Environmental Pollution 2016; 214:517-23.

Nelms SE, Galloway TS, Godley BJ, Jarvis DS, Lindeque PK. Investigating microplastic trophic transfer in marine top predators. Environmental Pollution 2018;238:999-1007.

Pannetier P, Morin B, Le Bihanic F, Dubreil L, Clérandeau C, Chouvellon F, et al. Environmental samples of microplastics induce significant toxic effects in fish larvae. Environment International 2020;134: Article No. 105047.

Pazos RS, Maiztegui T, Colautti DC, Paracampo AH, Gómez N. Microplastics in gut contents of coastal freshwater fish from Río de la Plata estuary. Marine Pollution Bulletin 2017; 122:85-90.

Pegado T, Schmid K, Winemiller KO, Chelazzi D, Cincinelli A, Dei L, et al. First evidence of microplastic ingestion by fishes from the Amazon River estuary. Marine Pollution Bulletin 2018;133:814-21.

Peters CA, Bratton SP. Urbanization is a major influence on microplastic ingestion by sunfish in the Brazos River Basin, Central Texas, USA. Environmental Pollution 2016;210: 380-7.

Phillips MB, Bonner TH. Occurrence and amount of microplastic ingested by fishes in watersheds of the Gulf of Mexico. Marine Pollution Bulletin 2015;100:264-9.

Plastics Europe, European association of plastic recycling and recovery organizations (EPRO). Plastics-the Facts 2016. An Analysis of European Plastics Production, Demand and Waste Data. Plastics Europe; 2016.

Roch S, Walter T, Ittner LD, Friedrich C, Brinker A. A systematic study of the microplastic burden in freshwater fishes of South-western Germany-Are we searching at the right scale? Science of the Total Environment 2019;689:1001-11.

Rocha-Santos T, Duarte AC. A critical overview of the analytical approaches to the occurrence, the fate and the behavior of microplastics in the environment. TrAC-Trends in Analytical Chemistry 2015;65:47-53.

Cesa FS, Turra A, Baruque-Ramos J. Synthetic fibers as microplastics in the marine environment: A review from textile perspective with a focus on domestic washings. Science of the Total Environment 2017;598:1116-29.

Sanchez W, Bender C, Porcher JM. Wild gudgeons (*Gobio gobio*) from French Rivers are contaminated by microplastics: Preliminary study and first evidence. Environmental Research 2014;128:98-100.

Strungaru SA, Jijie R, Nicoara M, Plavan G, Faggio C. Micro-(nano) plastics in freshwater ecosystems: Abundance, toxicological impact and quantification methodology. TrAC Trends in Analytical Chemistry 2019;110:116-28.

Sussarellu R, Suquet M, Thomas Y, Lambert C, Fabioux C, Pernet MEJ, et al. Oyster reproduction is affected by exposure to polystyrene microplastics. Proceedings of the National Academy of Sciences of the United States of America 2016;113:2430-5.

Uddin MJ, Jeong YK. Urban river pollution in Bangladesh during last 40 years: Potential public health and ecological risk, present policy, and future prospects toward smart water management. Heliyon 2021;7:e06107.

Veiga JM, Fleet D, Kinsey S, Nilsson P, Vlachogianni T, Werner S, et al. Identifying Sources of Marine Litter. JRC Technical Report; 2016.

Vendel AL, Bessa F, Alves VE, Amorim AL, Patrício J, Palma AR. Widespread microplastic ingestion by fish assemblages in tropical estuaries subjected to anthropogenic pressures. Marine Pollution Bulletin 2017;117:448-55.

Xu S, Ma J, Ji R, Pan K, Miao AJ. Microplastics in aquatic environments: Occurrence, accumulation, and biological effects. Science of the Total Environment 2020;703:Article No. 134699.

Yu H, Zhang X, Hu J, Peng J, Qu J. Ecotoxicity of polystyrene microplastics to submerged carnivorous *Utricularia vulgaris* plants in freshwater ecosystems. Environmental Pollution 2020;265:Article No. 114830.

Yuan W, Liu X, Wang W, Di M, Wang J. Microplastic abundance, distribution and composition in water, sediments, and wild fish from Poyang Lake, China. Ecotoxicology and Environmental Safety 2019;170:180-7.

Zantis L, Carroll EL, Nelms SE, Bosker T. Marine mammals and microplastics: A systematic review and call for standardization. Environmental Pollution 2021;269:Article No. 116142.

Investigation on Impact of Changes in Land Cover Patterns on Surface Runoff in Ayung Watershed, Bali, Indonesia Using Geographic Information System

I Gusti Ngurah Putu Dharmayasa, Kritsanat Surakit, Ranjna Jindal*, and Romanee Thongdara

Department of Civil and Environmental Engineering, Faculty of Engineering, Mahidol University, Salaya, Nakhon Pathom 73170, Thailand

ARTICLE INFO

Received: 14 Aug 2021
Received in revised: 27 Nov 2021
Accepted: 30 Nov 2021
Published online: 31 Jan 2022
DOI: 10.32526/ennrj/20/202100161

Keywords:
Land cover/ Runoff coefficient (C)/ Ayung watershed/ Geographic information system/ Cook's method

*** Corresponding author:**
E-mail: ranjna.jindal@gmail.com

ABSTRACT

Population growth, urbanization, and infrastructure development activities have resulted in the land conversion of forests and farmlands to residential and commercial zones. Such land conversion causes changes in the land cover, as experienced in the Ayung Watershed, in the island of Bali, Indonesia. Here, the land cover undergoes rapid changes due to the growing tourism sector, affecting the runoff coefficient. This study evaluated the changing land cover patterns and surface runoff in the Ayung Watershed between 2012 and 2019. An increase in the surface runoff during the high rainfall events may lead to flooding in the area. The identification of land change patterns in the Ayung Watershed was carried out by a manual digitizing process on Google Earth maps. The runoff coefficient was calculated by Cook's method using the four physical characteristics of the watershed: land cover, infiltration rate, land slope and drainage density; showing significant changes in the land cover in the study area. Farmlands and forests were reduced by 647.8 ha and 553.1 ha respectively, converted into fast growing grasslands or unproductive land. Such land cover changes have a negative impact by increasing the runoff coefficient in the area. During the study period, the runoff coefficient was consistently found to be more than 0.6 (high-risk category). Several sections in the city of Denpasar experienced an increase in the runoff coefficient by more than 5%. Consequently, there was a high-risk of flooding in the area because of the increasing surface runoff.

1. INTRODUCTION

Bali is an international tourist destination that had been growing gradually until the COVID-19 pandemic hit at the beginning of 2020. The number of international tourists visiting Bali increased from 3.3 million in 2013 to 5.7 million in 2017 and 6.3 million in 2019 (Directory, 2020; Woods, 2020) with an average of 4.62 million people/year from 2012-2019 (BPS, 2021a). This number exceeded the total population in Bali, which was 4.34 million in 2019 (BPS, 2021b). Large land areas have been converted into settlements to accommodate the growing population and tourism sector in Bali (Sutawa, 2012; Hua, 2017; Ayele et al., 2018; Nuarsa et al., 2018).

Surface runoff is the rainwater that is not absorbed into the soil before it reaches the waterbodies (Bellamy and Cho, 2019). The runoff coefficient (C) indicates the quantity of surface runoff and is used to determine the peak discharge during flood (Dickinson, 2017; Sudaryatno et al., 2020). Floods that occur because of high rainfall, result in an increase in the surface runoff coefficient which increases the potential for runoff; thus, the runoff coefficient is important for predicting the occurrence of surface runoff, and subsequently, flooding (Aponte, 2007; Mahmoud et al., 2014; Miardini and Susanti, 2016; Suprayogi et al., 2020).

Four factors affect the runoff coefficient: changes in the land cover, infiltration rate, slope of land and drainage density (Mahmoud et al., 2014; Lemma et al., 2018). Land cover significantly affects the infiltration ability of the soil, subsequently

Citation: Dharmayasa IGNP, Surakit K, Jindal R, Thongdara R. Investigation on impact of changes in land cover patterns on surface runoff in Ayung Watershed, Bali, Indonesia using geographic information system. Environ. Nat. Resour. J. 2022;20(2):168-178. (https://doi.org/10.32526/ennrj/20/202100161)

increasing the surface runoff (Tali and Kanth, 2011; Bellamy and Cho, 2019; Weber and Sciubba, 2019; Suprayogi et al., 2020).

The Ayung Watershed is one of the largest watersheds on the island of Bali and plays an important role in maintaining the hydrological balance on the island. It provides irrigation water for farmlands and clean water for the people inhabiting it, as well as serving as a popular tourist destination (Sumarniasih, 2015). However, the Ayung Watershed is currently experiencing problems owing to the increased surface runoff as a result of the changes in the land cover patterns. This has led to flooding in several parts of the watershed with flash floods occurring in 2016, 2017, and 2020, resulting in the loss of property and threatening human life (Sumarniasih, 2015; Berkarya, 2016; Widyaswara, 2017; Darna, 2020). A study of the runoff coefficient in some areas of the Ayung Watershed was conducted for the period ranging from 1992-2000 (Dharma et al., 2007). However, studies on the runoff coefficient and its impacts on the surface runoff of the entire Ayung Watershed have not been carried out.

The geographic information system (GIS) is a tool for analyzing the changes in the land cover and runoff coefficient, using the QGIS 3.20 software with a manual digitization method. The runoff coefficient can be calculated by Cook's method using the physical characteristics of the watershed: land cover, infiltration rate, slope of land, and drainage density (Auliyani and Nugrahanto, 2020). Obtaining the runoff coefficient by combining the physical characteristics of the watershed is a very effective method that uses limited data for mapping flood risk areas, and has yielded satisfactory results in several studies (Mahmoud et al., 2014; Asare-Kyei et al., 2015; Mousavi et al., 2019).

This study aimed to determine the patterns of land cover changes and surface runoff coefficients in the Ayung Watershed between 2012 and 2019 to evaluate the potential risk of flooding. The study was carried out for a period of only eight years owing to the limited data available and low quality of the related images available on Google Earth. Similar studies for such time durations have been conducted and reported on the significant land cover changes during the study period (Abdelaty, 2016; Dadson, 2016).

2. METHODOLOGY

2.1 Study area

The study area for this research is the Ayung Watershed on the island of Bali, Indonesia as shown in Figure 1. The watershed with an area of 271.5 km^2, is located at 8°12′26.08″S-8°39′47.38″S latitude, and 115°11′1.68″E-115°16′12.9″E longitude. The Ayung River is the main river in this watershed with a length of 68.5 km.

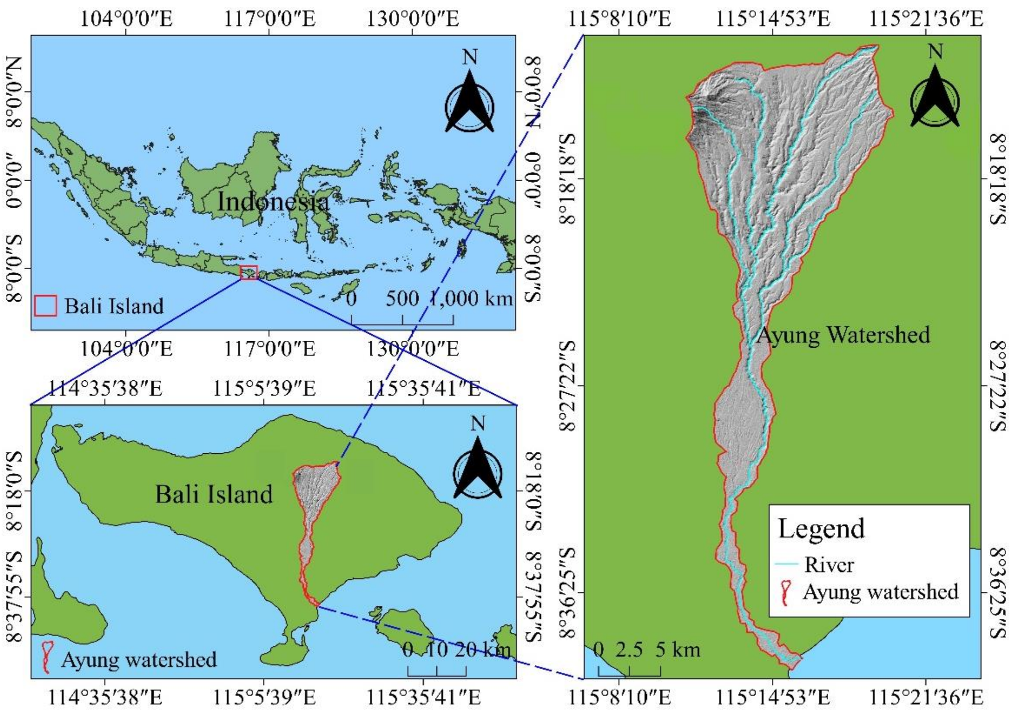

Figure 1. Maps of Indonesia, Bali Island and Ayung Watershed

2.2 Data collection

The data required to evaluate the land cover changes and runoff coefficient in the Ayung Watershed, include: the digital elevation model (DEM), land cover map, drainage density map, infiltration map, and watershed map.

The DEM for the study area had a resolution of 30 m, and was extracted from Google Earth (Rusli et al., 2013; El-Ashmawy, 2016) and interpolated using the filtering method to improve the quality and accuracy with the aim of getting it as close as possible to the actual surface pattern (Nikolakopoulos et al., 2005; Ma et al., 2020). The DEM was obtained under a resolution of 8 m through the filtering process, and was sufficient for use in hydrological modeling (Blackwell and Wells, 1999). The DEM was then used to obtain maps of the land slope and drainage density.

Google Earth provides maps with a resolution of 30 cm (Maxar Technologies, 2021) thus, the details of the objects on the Earth's surface can be seen more accurately (Cunningham, 2006; Ragheb and Ragab, 2015). Land cover maps were obtained from Google Earth maps by manual digitization at a scale of 1:20,000 for the 2012-2019 period. The land cover was divided into four categories: forest, farmland, grassland and settlement.

Soil texture maps and watershed maps were obtained from the Regional Development Planning Agency for Bali Province and the Directorate of Forest Resources Inventory and Monitoring, Republic of Indonesia, respectively.

2.3 Data analysis

The runoff coefficient was calculated by overlaying maps of the four parameters following the methods proposed by Risky et al. (2017), Auliyani and Nugrahanto (2020), and Sudaryatno et al. (2020). The data were analyzed using a quantitative descriptive research method. Each parameter, namely land cover, infiltration, slope, and drainage density, was divided into four categories and assigned with scores (Sv, Ss, St, and Sd, respectively) as shown in Table 1 and Table 2.

The scores for each category for four parameters were assigned based on the Cook's scoring system that has been widely applied to calculate the runoff coefficient (C) (Indriatmoko and Wibowo, 2007; Auliyani and Nugrahanto, 2020; Sudaryatno et al., 2020).

The drainage density was calculated using the following equation.

$$D_d = L/A_d \tag{1}$$

Where; Dd=drainage density (km/km^2), L=the total length of all channels (km); and Ad=the area of the drainage basin (km^2).

The overall runoff coefficient for each parameter was calculated using the following equation.

$$C = [\sum_{n=1}^{n=4}(Sv_n \times Av_n) + \sum_{n=1}^{n=4}(Ss_n \times As_n) + \sum_{n=1}^{n=4}(St_n \times At_n) + \sum_{n=1}^{n=4}(Sd_n \times Ad_n)] / 100 \tag{2}$$

Table 1. Scores for land cover and infiltration rate

No	Land cover	Score (S_v) (%)	Infiltration rate	Score (S_s) (%)
1	Good to excellent (approximately 50%-90% covered by trees)	5	Fast, infiltration rate is more than 2 cm/h (sandy soil)	5
2	Fair (approximately 10% to <50% covered by trees)	10	Normal, infiltration rate varies from 0.75-2.00 cm/h (sandy clay)	10
3	Poor (1% to <10% covered by trees)	15	Slow, infiltration range from 0.25-0.75 cm/h (clay loam)	15
4	No effective plant cover or only ground layer (<1%)	20	Soil with negligible infiltration (rock layers)	20

Table 2. Scores for slope and drainage density

No	Slope (%)	Score (S_t) (%)	Drainage density (km/km^2)	Score (S_d) (%)
1	Flat (<5%)	10	High (>8)	20
2	Rolling (5%-10%)	20	Normal (3.2-8.0)	15
3	Hilly (10%-30%)	30	Low (1.6 to <3.2)	10
4	Steep (>30%)	40	Very low (<1.6)	5

Where; C=overall runoff coefficient (C) for the watershed and n=order of category (1 to 4). A_v=ratio of each land cover area to the total area of watershed; A_s=ratio of infiltration rate area to the total area of watershed; A_t=ratio of slope area to the total area of watershed; A_d=ratio of drainage density area to the total area of watershed. A factor of 100 is required to convert the overall runoff coefficient value from percentage to decimal (Indriatmoko and Wibowo, 2007; Sudaryatno et al., 2020).

The runoff coefficient typically has values between 0 and 1, and is used to indicate the flood vulnerability of the area being analyzed (Dickinson, 2017; Mohamed and El-Raey, 2020).

The flood risk classification is determined using the following equation (Iswandi et al., 2016; Suhana et al., 2020).

$$I = (c-b)/k \quad (3)$$

Where; I=the class interval; c=the highest score; b=the lowest score; and k=number of the classes.

Based on the value of the runoff coefficient, the flood risk of any area is divided into five categories as shown in Table 3 (Mousavi et al., 2019).

Table 3. Runoff coefficient and flood risk category

No	Runoff coefficient (C)	Risk category
1	<0.2	Very low
2	0.2-0.4	Low
3	0.4-0.6	Moderate
4	0.6-0.8	High
5	>0.8	Very high

3. RESULTS AND DISCUSSION

3.1 Changes in the land cover

Land cover maps for the Ayung Watershed in the years 2012, 2015, and 2019, were used to represent the land cover changes during the 8-year period (Figure 2). A summary of the changes in land cover areas from 2012 to 2019 is presented in Table 4.

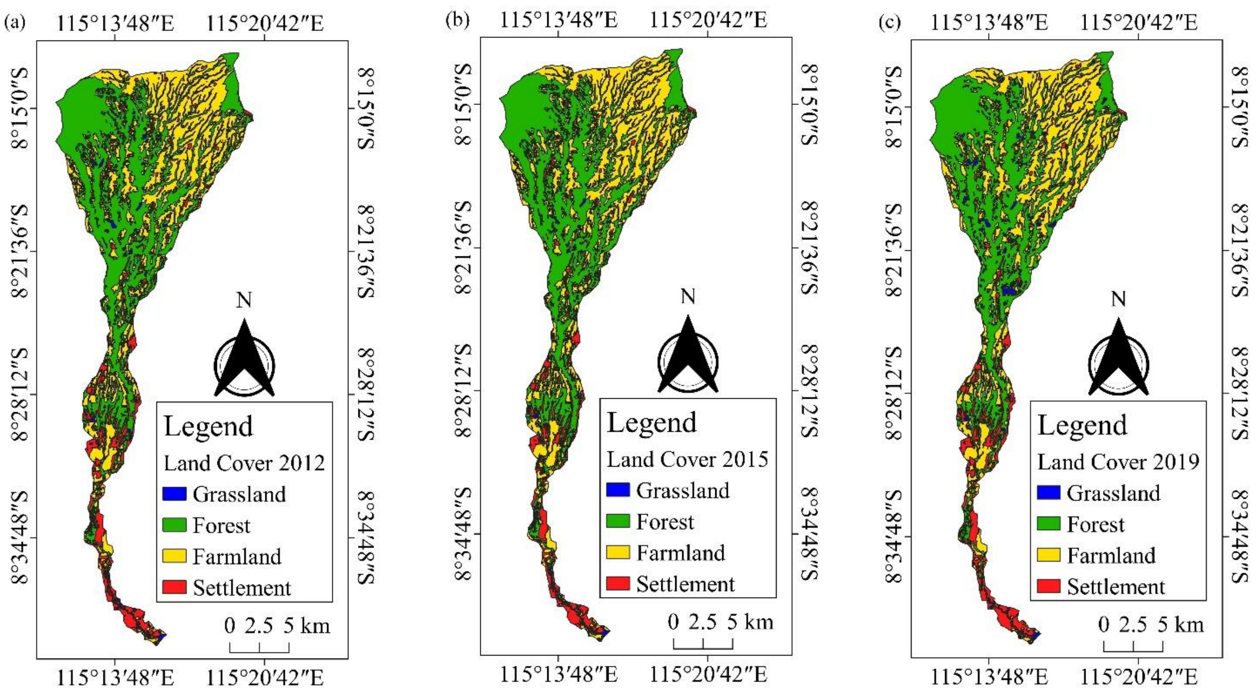

Figure 2. Land cover maps for the Ayung Watershed for years 2012, 2015, and 2019

Based on Figure 2 and Table 4, it can be seen that the highest land cover change occurred in the farmlands with a reduction in area of 647.8 ha (2.35%). Conversion of farmland to settlement also occurred in other areas of the Bali between 2012 and 2017 (Lanya et al., 2017; Rimba et al., 2019). This was also reflected by the decrease in the number of people in Bali, who were originally farmers, but opted to change their profession to work in the tourism sector (Suartika, 2005). A summary of the changes occurring in each land cover category in Ayung Watershed during 2012-2019 is shown in Figure 3 and Table 5.

Table 4. Changes in the land cover in the Ayung Watershed from 2012-2019

Year	Land cover area (ha)							
	Farmland		Forest		Grassland		Settlement	
2012	11,068.8	(40.23%)	14,232.3	(51.73%)	168.7	(0.61%)	2,040.9	(7.42%)
2013	11,013.9	(40.03%)	14,187.5	(51.57%)	198.2	(0.72 %)	2,111.1	(7.67%)
2014	10,958.0	(39.83%)	14,162.1	(51.49%)	236.8	(0.86%)	2,153.8	(7.8 %)
2015	10,841.0	(39.41%)	14,148.2	(51.43%)	297.2	(1.08%)	2,224.3	(8.09 %)
2016	10,602.8	(38.54%)	14,122.3	(51.33%)	429.5	(1.56%)	2,356.1	(8.56%)
2017	10,501.0	(38.17%)	13,921.3	(50.60%)	672.1	(2.44%)	2,417.1	(8.79%)
2018	10,449.6	(37.98%)	13,788.5	(50.12%)	815.5	(2.96%)	2,457.1	(8.93%)
2019	10,421.0	(37.88%)	13,679.2	(49.72%)	865.1	(3.14%)	2,545.3	(9.25%)
Total changes	-647.8		-553.1		696.5		504.4	

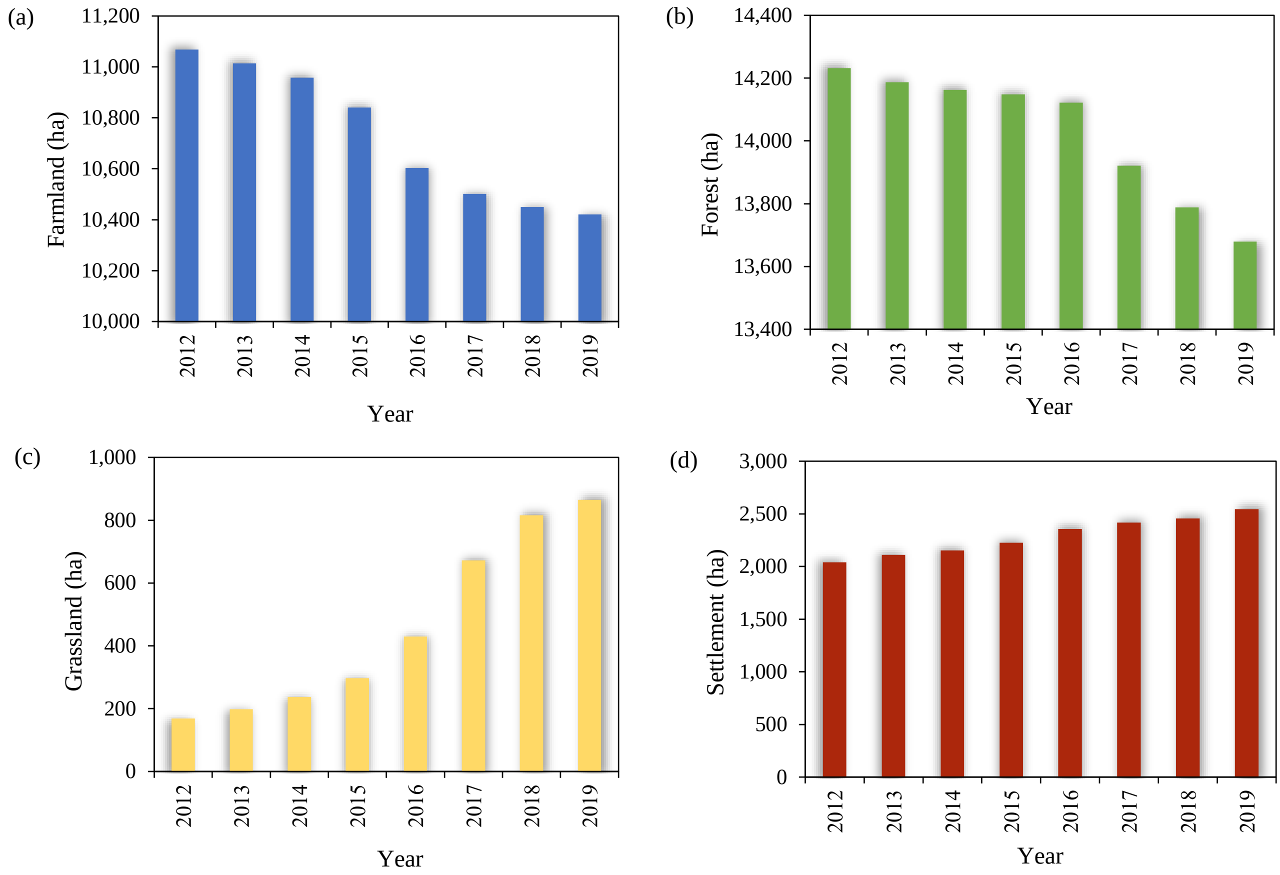

Figure 3. Summary of the changes in the land cover between 2012 and 2019 (a) Farmland, (b) Forest, (c) Grassland, and (d) Settlement

Table 5. Changes in the land cover in the Ayung Watershed between 2012 and 2019

Year	Land cover change (%)			
	Farmland	Forest	Grassland	Settlement
2012-2013	-0.20%	-0.16%	0.11%	0.25%
2013-2014	-0.20%	-0.08%	0.14%	0.16%
2014-2015	-0.42%	-0.06%	0.22%	0.26%
2015-2016	-0.87 %	-0.10%	0.48%	0.47%
2016-2017	-0.37%	-0.73%	0.88%	0.23%
2017-2018	-0.19%	-0.48%	0.52%	0.14%
2018-2019	-0.10%	-0.40%	0.18%	0.32%
Average change (%)	-0.34%	-0.29%	0.36%	0.26%

The highest average decrease occurred in the farmland (-0.34%) followed by forests (-0.29%), and the highest average increase occurred in grassland (0.36%) followed by settlement (0.26%). This is in accordance with some reported trends of the land cover changes in Bali, where there was a decrease in farmlands and an increase in grasslands (As-syakur, 2011; Adnyawati, 2019).

3.2 Slope, drainage density, and infiltration rate

The maps of the slope, drainage density and infiltration rate in the Ayung Watershed are shown in Figure 4.

As shown in Figure 4(a), most of the watershed is dominated by hilly plains with an area of 11,677.8 ha. Hilly slopes accelerate the flow and reduce water absorption thereby increasing the runoff coefficient (Duhita et al., 2020). Figure 4(b) shows that the drainage density in the Ayung watershed is very high (>8 km/km^2), especially in the upstream region that covers a substantial area of 25,526.2 ha (92.8%). Figure 4(c) shows that the soil texture in the Ayung Watershed is dominated by clay loam with an area of 22,880.8 ha (83.2%), while the rest is sandy clay with area of 4,629.9 ha (16.8%). Clay loam soil has low water infiltration ability (Pitt and Lantrip, 2000), causing a high runoff coefficient (Amatya et al., 2015). The area distributions under each category of infiltration rate, slope and drainage density, are listed in Table 6.

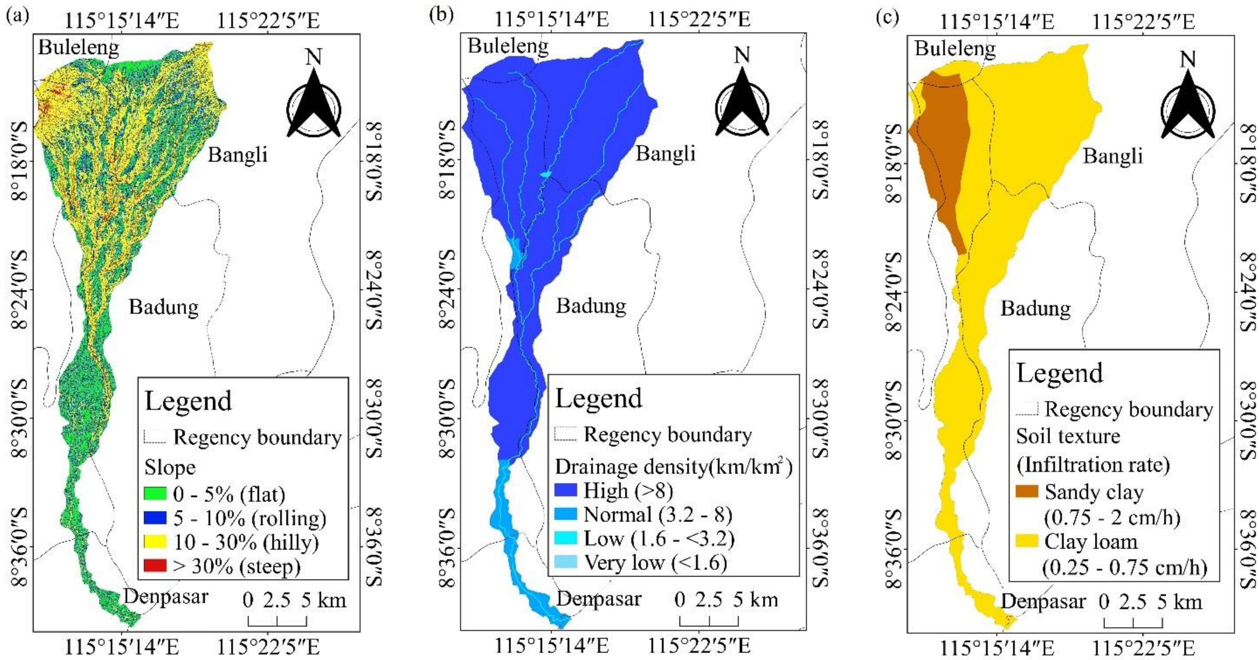

Figure 4. Ayung Watershed maps: (a) slope, (b) drainage density, and (c) infiltration rate

Table 6. Area distributions in the Ayung Watershed under each category of infiltration rate, slope and drainage density

Infiltration rate	Area (ha)		Slope (%)	Area (ha)		Drainage density (km/km^2)	Area (ha)	
Fast, infiltration rate is more than 2 cm/h (sandy soil)	-	(0.0%)	Flat (<5%)	7,256.5	(26.4%)	High (>8)	25,526.2	(92.8%)
Normal, infiltration rate varies from 0.75-2.00 cm/h (sandy clay)	4,629.9	(16.8%)	Rolling (5%-10%)	7,549.9	(27.4%)	Normal (3.2-8.0)	1,952.4	(7.1%)
Slow, infiltration range from 0.25-0.75 cm/h (clay loam)	22,880.8	(83.2%)	Hilly (10%-30%)	11,677.8	(42.5%)	Low (1.6 to <3.2)	33.0	(0.1%)
Soil with negligible infiltration (rock layers)	-	(0.0%)	Steep (>30%)	1,025.9	(3.7%)	Very low (<1.6)	-	(0.0%)

3.3 Runoff coefficient

The maps of the changes in the runoff coefficient in the Ayung watershed in 2012, 2015, and 2019 are shown in Figure 5. The areas in the Ayung watershed for different runoff coefficient (C) under the different risk of flood categories between 2012 and 2019 are shown in Table 7. Based on the runoff coefficient values, a flood risk map of the area can be created (Aponte, 2007).

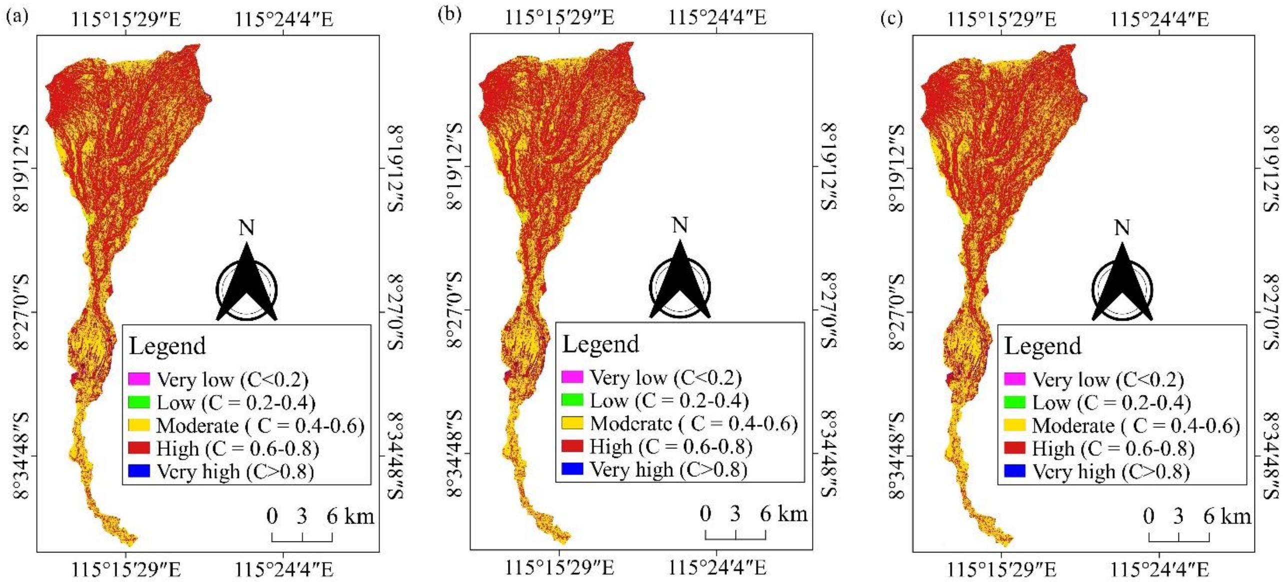

Figure 5. Runoff coefficient maps for the Ayung Watershed in (a) 2012, (b) 2015, and (c) 2019

Table 7. The areas in the Ayung Watershed with the run off coefficient (C) under the risk of different flood categories during 2012-2019.

Year	Risk category area (ha)									
	Very low (C<0.2)		Low (C=0.2-0.4)		Moderate (C=0.4-0.6)		High (C=0.6-0.8)		Very high (C>0.8)	
2012	0	(0.00%)	45.1	(0.16%)	10,176.3	(36.99%)	17,029.8	(61.90%)	259.5	(0.94%)
2013	0	(0.00%)	37.1	(0.13%)	10,139.8	(36.86%)	17,068.4	(62.04%)	265.5	(0.96%)
2014	0	(0.00%)	32.8	(0.12%)	10,129.8	(36.82%)	17,083.1	(62.10%)	265.0	(0.96%)
2015	0	(0.00%)	32.8	(0.12%)	10,079.0	(36.64%)	17,126.9	(62.26%)	272.0	(0.99%)
2016	0	(0.00%)	38.1	(0.14%)	9,996.6	(36.34%)	17,171.2	(62.42%)	304.8	(1.11%)
2017	0	(0.00%)	37.9	(0.14%)	9,919.0	(36.05%)	17,237.2	(62.66%)	316.6	(1.15%)
2018	0	(0.00%)	37.8	(0.14%)	9,786.5	(35.57%)	17,359.6	(63.10%)	326.8	(1.19%)
2019	0	(0.00%)	36.8	(0.13%)	9,704.3	(35.27%)	17,440.3	(63.39%)	329.2	(1.20%)
Total changes	0		-8.3		-472.0		410.5		69.8	

From Table 7, it can be seen that there was an increase in the high-risk category from 17,029.8 ha (61.90%) in 2012 to 17,440.3 ha (63.39%) in 2019. The total increase in the area under the high-risk category between 2012 and 2019 was 410.5 ha (1.5%). Meanwhile, the areas under the moderate risk category for flooding decreased from 10,176.3 ha (36.99%) in 2012 to 9,704.3 ha (35.27%) in 2019. Thus, the total decrease in the moderate flood risk category area between 2012 and 2019 was 472 ha (1.7%).

The overall runoff coefficient in the Ayung Watershed between 2012 and 2019 was obtained using Equation (2) and presented in Table 8.

Based on these results, the impact of changes in each type of land cover can be determined based on the runoff coefficient in the Ayung Watershed. It is clear that the decreasing farmland and forest areas, resulted in an increase in the areas of grassland and settlement, which increased the runoff coefficient.

As shown in Table 8, the overall runoff coefficient between 2012 and 2019, did not change significantly (from 0.644 in 2012 to 0.646 in 2019). However, there were several sections of Denpasar City that had a fairly high increase in the runoff coefficient, as shown in Table 9 and Figure 6. The increase in the runoff coefficient has a large impact because Denpasar is the capital city of the province of Bali with a high population density of 7,022 persons/km^2 (PU-net, 2017) leading to an increased risk of the loss of life during flooding.

Table 8. The overall runoff coefficient in the Ayung Watershed between 2012 and 2019.

Year	Runoff coefficient (C)
2012	0.644
2013	0.644
2014	0.644
2015	0.645
2016	0.645
2017	0.646
2018	0.646
2019	0.646

Table 9. Sections of Denpasar City with a fairly high increase in the runoff coefficient between 2012 and 2019

Sections	Runoff coefficient (C)								
	2012	2013	2014	2015	2016	2017	2018	2019	Total change (%)
Kesiman	0.592	0.607	0.610	0.613	0.615	0.618	0.622	0.631	6.59%
Kesiman Kertalangu	0.607	0.611	0.623	0.629	0.633	0.639	0.640	0.642	5.77%
Kesiman Petilan	0.601	0.606	0.615	0.622	0.626	0.630	0.633	0.635	5.66%
Penatih	0.605	0.611	0.620	0.633	0.634	0.638	0.640	0.646	6.78%

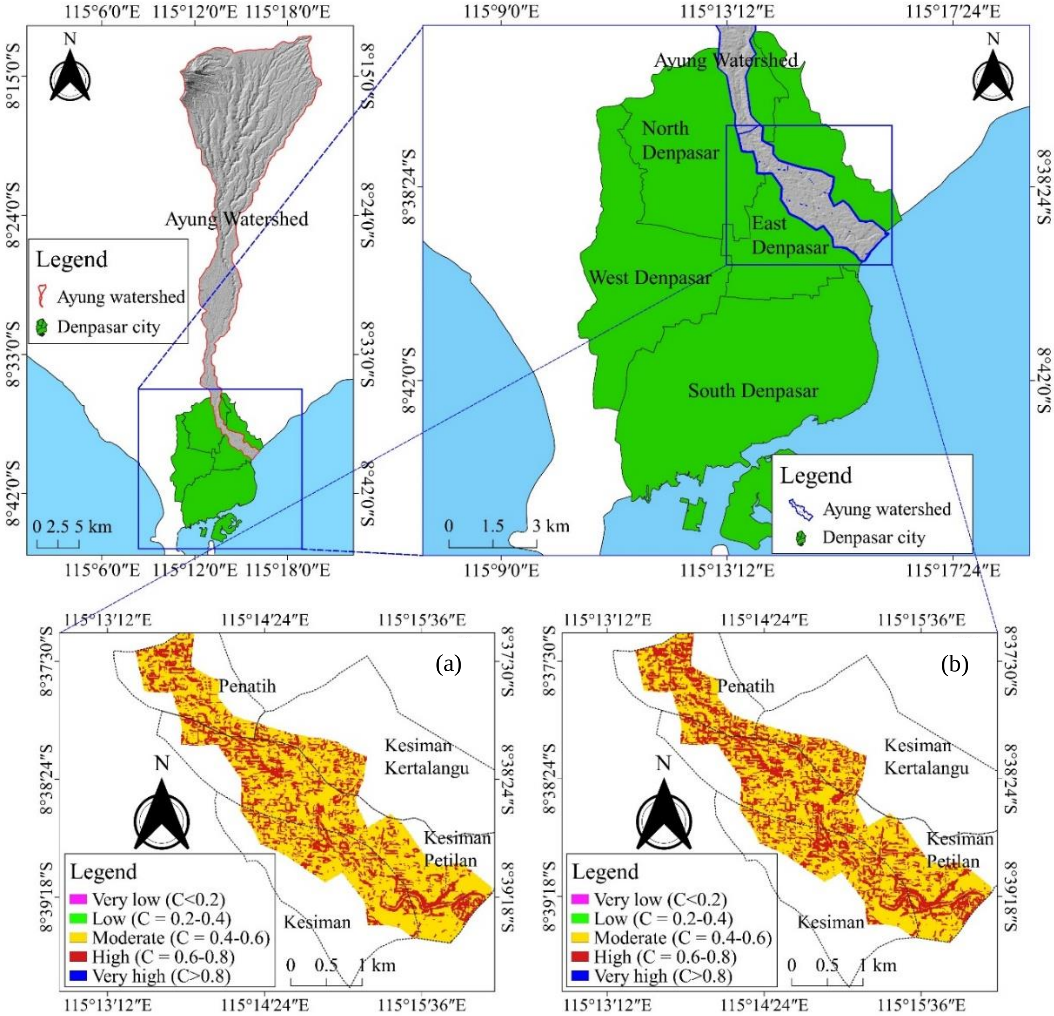

Figure 6. Maps of the flood risk areas in Denpasar City in the Ayung Watershed: (a) 2012 and (b) 2019

As shown in Table 9, several sections in the city of Denpasar experienced an increase in the runoff coefficient by more than 5% between 2012 and 2019. This is relatively high compared with that reported in several previous studies (Shi et al., 2007; Atharinafi and Wijaya, 2021). This can also be seen in Figure 6, which shows the maps of the changes in the areas under flood risk between 2012 and 2019. The higher runoff coefficient values were because of changes in the land cover, which increase the maximum flood peak discharge and thus increasing the risk of flooding (Shi et al., 2007; Suprayogi et al., 2020).

The results of this study conducted on the increased flood risk areas in the four sections of Denpasar City, are similar to a previous study that reported moderate to high flood risk in the same areas due to the increased runoff coefficient (Kusmiyarti et al., 2017). In general, the overall runoff coefficient in the Ayung Watershed between 2012 and 2019 was more than 0.6 (high flood risk category), leading to a high surface runoff that certainly increases the risk of flooding (Suprayogi et al., 2020). The results for the Ayung Watershed are similar to those in some previous studies conducted in other locations in Indonesia (Indriatmoko and Wibowo, 2007; Miardini and Susanti, 2016; Risky et al., 2017; Suprayogi et al., 2020).

4. CONCLUSION

Based on the runoff coefficient mapping of the Ayung Watershed between 2012 and 2019, it is clear that several areas are under high flood risk categories (runoff coefficient >0.6). The situation worsens with the conversion of forests and farmlands into grasslands and settlements leading to an increased runoff coefficient. Specifically, several sections in Denpasar, have experienced a significant increase in the runoff coefficient over the period 2012-2019 (>5%). The increased risk of flooding in the densely populated city of Denpasar may have a negative impact on its population.

This study provides evidence that changes in the land cover patterns have increased the potential for flooding in the Ayung Watershed. Such information could be useful for the governments of Denpasar City and Bali Province in anticipating floods to avoid losses in the future.

ACKNOWLEDGEMENTS

The authors would like to thank the Faculty of Graduate Studies, Mahidol University for providing financial support to Mr. Dharmayasa to pursue this study and to the Department of Civil and Environmental Engineering, Faculty of Engineering, Mahidol University for their support.

REFERENCES

Abdelaty EFS. Land use change detection and prediction using high spatial resolution Google Earth imagery and GIS techniques: A study on El-Beheira Governorate, Egypt. Proceedings of Fourth International Conference on Remote Sensing and Geoinformation of the Environment (RSCy2016); 2016 Apr 4-8; Paphos: Cyprus; 2016.

Adnyawati IAA. Land conversion Versus Subak: How Bali's face gradually changing throughout history. Bali Tourism Journal 2019;3(1):38-42.

Amatya D, Callahan T, Hansen W, Trettin C, Radecki-Pawlik A, Meire P. Turkey Creek: A case study of ecohydrology and integrated watershed management in the low-gradient Atlantic Coastal Plain, USA. Journal of Water Resource and Protection 2015;07(10):792-814.

Aponte AGP. Runoff coefficients using a quickbird image for mapping flood hazard in a Tropical Coastal City, Campeche, Mexico. Proceedings of the IEEE International Geoscience and Remote Sensing Symposium; 2007 Jul 23-27; Barcelona: Spain; 2007.

Asare-Kyei D, Forkuor G, Venus V. Modeling flood hazard zones at the sub-district level with the rational model integrated with GIS and remote sensing approaches. Water 2015;7(7):3531-64.

As-syakur AR. Land use changes in Bali Province. Ecotropic: Journal of Environmental Science 2011;6(1):1-7 (in Indonesian).

Atharinafi Z, Wijaya N. Land use change and its impacts on surface runoff in rural areas of the upper Citarum Watershed (Case study: Cirasea sub-watershed). Journal of Regional and City Planning 2021;32(1):36-55.

Auliyani D, Nugrahanto EB. Peak discharge in Jemelak Subwatershed, Sintang District. Jurnal Sylva Lestari 2020;8(3):273-82 (in Indonesian).

Ayele GT, Tebeje AK, Demissie SS, Belete MA, Jemberrie MA, Teshome WM, et al. Time series land cover mapping and change detection analysis using geographic information system and remote sensing, Northern Ethiopia. Air, Soil and Water Research 2018;11:1-18.

Bellamy PW, Cho HJ. A GIS-based approach for determining potential runoff coefficient and runoff depth for the Indian River Lagoon, Florida, USA. In: Lagoon Environments around the World-A Scientific Perspective. London: IntechOpen; 2019. p. 1-24.

Berkarya B. Flash flood on upstream Ayung River, Denpasar local water company stops its production until December 25, 2016 [Internet]. 2016 [cited 2021 Jun 5]. Available from: https://www.baliberkarya.com/read/201612220016/banjir-bandang-di-hulu-sungai-ayung-pdam-denpasar-stop-produksi-hingga-25-desember (in Indonesian).

Blackwell PR, Wells G. DEM resolution and improved surface representation. Proceedings of the 19th Annual ESRI International User Conference; 1999 Jul 26-30; San Diego: California; 1999.

Badan Pusat Statistik (BPS). Number of foreign visitor to Bali dan Indonesia, 1969-2020: Indonesian statistics agency [Internet].

2021a [cited 2021 Jul 21]. Available from: https://bali.bps.go.id/statictable/2018/02/09/28/jumlah-wisatawan-asing-ke-bali-dan-indonesia-1969-2019.html (in Indonesian).

Badan Pusat Statistik (BPS). Population projection of Bali Province by Gender: Indonesian statistics agency Bali Province [Internet]. 2021b [cited 2021 Jul 21]. Available from: https://bali.bps.go.id/indicator/12/28/1/proyeksi-penduduk-provinsi-bali-menurut-jenis-kelamin.html (in Indonesian).

Cunningham MA. Accuracy assessment of digitized and classified land cover data for wildlife habitat. Landscape and Urban Planning 2006;78(3):217-28.

Dadson IY. Land use and land cover change analysis along the coastal regions of Cape Coast and Sekondi. Ghana Journal of Geography 2016;8(2):108-26.

Darna IM. Due to flooding, Ayung River is Muddy, Badung Local Water Company Services Disrupted [Internet]. 2020 [cited 2021 Jul 5]. Available from: https://balitribune.co.id/content/akibat-banjir-sungai-ayung-keruh-layanan-pdam-badung-terganggu (in Indonesian).

Dharma IG, Infantri Yekti M, Indra Permana G. The effect of land use changes on flood discharge. Berkala Ilimiah Teknik Keairan 2007;13(3):1-16 (in Indonesian).

Dickinson R. Runoff coefficient in InfoSewer and InfoSWMM [Internet]. 2017 [cited 2021 Oct 17]. Available from: https://swmm5.org/2017/11/06/runoff-coefficient-in-infosewer-and-infoswmm/.

Directory BT. Bali tourism: Tourism statistics: Bali tourism directory [Internet]. 2020 [cited 2021 Oct 20]. Available from: https://www.balitourismdirectory.com/tourism-studies/bali-tourism-statistics.html.

Duhita ADP, Rahardjo AP, Hairani A. The effect of slope on the infiltration capacity and erosion of Mount Merapi Slope Materials. Journal of the Civil Engineering Forum 2020;7(1):71-84.

El-Ashmawy KLA. Investigation of the accuracy of google earth elevation data. Artificial Satellites 2016;51(3):89-97.

Hua AK. Land use land cover changes in detection of water quality: A study based on remote sensing and multivariate statistics. Journal of Environmental and Public Health 2017;2017:1-12.

Indriatmoko RH, Wibowo VE. Geographic information system application for calculating the runoff coefficient of the Ciliwung Watershed. Jurnal Air Indonesia 2007;3(2):182-90 (in Indonesian).

Iswandi U, Widiatmaka, Pramudya B, Barus B. Delineation of flood hazard zones by using a multi criteria evaluation approach in Padang West Sumatera Indonesia. Journal of Environment and Earth Science 2016;6(3):205-14.

Kusmiyarti TB, Wiguna PPK, Dewi NR. Flood risk analysis in Denpasar City, Bali, Indonesia. Proceedings of the IOP Conference Series: the 2nd Geoplanning - International Conference on Geomatics and Planning; 2017 Aug 9-10; Surakarta: Indonesia; 2017.

Lanya I, Dibia IN, Diara IW, Suarjaya DG. Analysis of Subak landuse change due to tourism accomodation development in North Kuta Sub-district, Badung Regency, Indonesia. Proceedings of the IOP Conference Series: The 5th Geoinformation Science Symposium 2017 (GSS 2017); 2017 Sep 27-28; Yogyakarta: Indonesia; 2017.

Lemma TM, Gessesse GD, Kassa AK, Edossa DC. Effect of spatial scale on runoff coefficient: Evidence from the Ethiopian highlands. International Soil and Water Conservation Research 2018;6(4):289-96.

Ma Y, Liu H, Jiang B, Meng L, Guan H, Xu M, et al. An innovative approach for improving the accuracy of digital elevation models for cultivated land. Remote Sensing 2020; 12(20):3401-20.

Mahmoud SH, Mohammad FS, Alazba AA. Determination of potential runoff coefficient for Al-Baha Region, Saudi Arabia using GIS. Arabian Journal of Geosciences 2014;7(5): 2041-57.

Maxar Technologies. Clarity and confidence: Spatial resolution [Internet]. 2021 [cited 2021 Oct 27]. Available from: https://explore.maxar.com/imagery-leadership-spatial-resolution?utm_source=marketo&utm_medium=landing-page&utm_campaign=30-cm-leadership.

Miardini A, Susanti PD. Analysis physical characteristics of land for estimated runoff coefficient as flood control effort in Comal Watershed, Central Java. Forum Geografi 2016; 30(1):58-68.

Mohamed SA, El-Raey ME. Vulnerability assessment for flash floods using GIS spatial modeling and remotely sensed data in El-Arish City, North Sinai, Egypt. Natural Hazards 2020;102(2):707-28.

Mousavi SM, Roostaei S, Rostamzadeh H. Estimation of flood land use/land cover mapping by regional modelling of flood hazard at sub-basin level case study: Marand basin. Geomatics, Natural Hazards and Risk 2019;10(1):1155-75.

Nikolakopoulos K, Vaiopoulos D, Skianis G. SRTM DTM vs. one created from 1/50.000 topographic maps: The case of Kos Island. Proceedings of SPIE Remote Sensing Volume 5980: SAR Image Analysis, Modeling, and Techniques VII; 2005 Sep 19-22; Bruges: Belgium; 2005.

Nuarsa IW, As-syakur A, Gunadi I, Sukewijaya I. Changes in gross primary production (GPP) over the past two decades due to land use conversion in a tourism city. ISPRS International Journal of Geo-Information 2018;7(2):1-20.

Pitt R, Lantrip J. Infiltration through disturbed urban soils. Journal of Water Management Modeling 2000;206(1):1-22.

PU-net. Denpasar City Profile [Internet]. 2017 [cited 2021 Aug 7]. Available from: http://perkotaan.bpiw.pu.go.id/v2/kota-besar/1 (in Indonesian).

Ragheb AE, Ragab AF. Enhancement of google earth positional accuracy. International Journal of Engineering Research and Technology 2015;4(1):627-30.

Rimba AB, Chapagain SK, Masago Y, Fukushi K, Mohan G. Investigating water Sustainability and land use/land cover change (LULC) as the impact of tourism activity in Bali, Indonesia. Proceedings of the IGARSS 2019-2019 IEEE International Geoscience and Remote Sensing Symposium; 2019 Jul 28-Aug 2; Yokohama: Japan; 2019.

Risky YS, Nurbandi W, Adiwijaya RRY, Tyas BI, Zulaikha AP, Alifiya R, et al. Using remote sensing and geographic information system (GIS) for peak discharge estimating in catchment of Way Ratai, Pesawaran District, Lampung Province. Proceedings of the IOP Conference Series: 3rd International Conference of Indonesia Society for Remote Sensing (ICOIRS 2017); 2017 Oct 31-Nov 1; Semarang: Indonesia; 2017.

Rusli N, Majid MR, Din AHM. Google Earth's derived digital elevation model: A comparative assessment with Aster and SRTM data. Proceedings of the IOP Conference Series: 8th

International Symposium of the Digital Earth (ISDE8); 2013 Aug 26-29; Kuching: Malaysia; 2013.

Shi PJ, Yuan Y, Zheng J, Wang JA, Ge Y, Qiu GY. The effect of land use/ cover change on surface runoff in Shenzhen Region, China. Catena 2007;69(1):31-5.

Suartika GAM. Vanishing Paradise: Planning and Conflict in Bali [dissertation]. Australia: University of New South Wales; 2005.

Sudaryatno, Wiratmoko B, Winanda, Saputri SY. Using hydrological mapping to evaluate the efectiveness of the Bener Dam development in reducing flood risk in Purworejo Regency, Central Java. Forum Geografi 2020;34(2):86-95.

Suhana O, Carlo N, Nofrizal AY, Rita E. Flood disaster risk and mitigation for Sumani Watershed. Proceedings of the 2nd International Conference on Environmental Sciences (ICES 2020); 2020 Dec 2-3; Padang: Indonesia; 2020.

Sumarniasih MS. Land Use Planning in the Ayung Watershed Bali Province [dissertation]. Denpasar, Indonesia: Udayana University; 2015 (in Indonesian).

Suprayogi S, Latifah R, Marfai MA. Preliminary analysis of floods induced by urban development in Yogyakarta City, Indonesia. Geographia Technica 2020;15(2):57-71.

Sutawa GK. Issues on Bali tourism development and community empowerment to support sustainable tourism development. Procedia Economics and Finance 2012;4:413-22.

Tali MPA, Kanth TA. Land Use/Land Cover Change and Its Impact on Flood Occurrence: A Case Study of Upper Jhelum Floodplain [dissertation]. Srinagar, India: University of Kashmir; 2011.

Weber H, Sciubba JD. The effect of population growth on the environment: Evidence from European Regions. European Journal of Population 2019;35(2):379-402.

Widyaswara I. Residents of Tonja Panic Ayung River Overflows While Sleeping, Houses Filled with Mud - Tribun-bali.com [Internet] 2017. [cited 2021 Oct 20]. Available from: https://bali.tribunnews.com/2017/02/11/warga-tonja-panik-sungai-ayung-meluap-saat-tidur-lelap-rumah-dipenuhi-lumpur?page=all (in Indonesian).

Woods R. A brief review of Bali Tourism in 2019 [Internet] 2020. [cited 2021 Oct 20]. Available from: http://hotelinvestmentstrategies.com/a-brief-review-of-bali-tourism-in-2019/.

Groundwater Quality Assessment Using Classification and Multi-Criteria Methods: A Case Study of Can Tho City, Vietnam

Nguyen Thanh Giao*, Huynh Thi Hong Nhien, and Phan Kim Anh

College of Environment and Natural Resources, Can Tho University, Ninh Kieu District, Can Tho City, Vietnam

ARTICLE INFO

Received: 22 Sep 2021
Received in revised: 29 Nov 2021
Accepted: 6 Dec 2021
Published online: 30 Dec 2021
DOI: 10.32526/ennrj/20/202100183

Keywords:
Coliforms/ Groundwater/ Cluster analysis/ Principal component analysis/ Groundwater quality index/ Can Tho

*** Corresponding author:**
E-mail: ntgiao@ctu.edu.vn

ABSTRACT

This study aimed to classify groundwater quality in Can Tho City, Vietnam using groundwater quality index (GWQI), principal component analysis (PCA), and cluster analysis (CA). Groundwater samples were collected in April (dry season) and October (rainy season) in 2019 and then analyzed for thirteen parameters including pH, color, total hardness, chloride, sulfate, chemical oxygen demand, magnesium, total iron, nitrate, arsenic, lead, mercury, and coliforms. The results showed that groundwater quality in Can Tho City was contaminated with coliforms in both seasons. COD and Cl^- was found exceeded the allowable limits in several wells in the dry season. The other groundwater parameters were within the permissible limits. GWQI values indicated that groundwater quality was in excellent state. The CA results revealed that groundwater quality in the dry season was more spatially varied than that in the wet season. In addition, CA revealed that groundwater monitoring sites could be reduced by 9 sites and 12 sites in the dry and wet seasons, respectively. The PCA results showed that 63.4% and 73.9% of the groundwater variation in the dry and wet seasons were explained by four PCs and three PCs, respectively. All the groundwater quality monitoring parameters were significantly and influenced by geological factors, domestic wastes, industrial and agricultural activities. Coliform should be completely treated before domestic use of groundwater in the study area. Future study should focus on investigating contribution of specific polluting sources for appropriate management measures.

1. INTRODUCTION

In Vietnam, groundwater has been exploited for different usage purposes for more than a century and has continuously expanded (Berg et al., 2007; Erban et al., 2014). Especially, in the Mekong delta, surface water has been strongly polluted by agricultural and aquaculture activities, salinity intrusion, domestic and industrial contaminants. Therefore, this water resource is unsuitable for human use and places more importance on alternative freshwater resources such as groundwater (Dao et al., 2016). However, the availability and quality of groundwater are currently affected by both natural processes and anthropogenic activities (Ha et al., 2019a). The natural processes are all related to the geology and climate of the area. Typically, arsenic is naturally released into groundwater through biological reactions or decomposition of iron oxides (Fendorf, 2010) and the solubility of fluoride-containing minerals. In addition, seasonal variation in groundwater quality and geochemical mobility of ions have been documented in previous studies (Gaikwad et al., 2020; Kadam et al., 2021a; Kadam et al., 2021b); which may limit the use of water resources during certain periods. Particularly, the Mekong Delta area has low topography, acid sulfate soil, and two distinct seasons (dry season and rainy season); therefore, groundwater quality has seasonal fluctuations and limited use in the dry season due to the impact of climate and seawater. The anthropogenic activities that could influence on groundwater quality including intensive groundwater abstraction, improper waste treatments in industrial, domestic and agricultural sectors, and excessive fertilizer application (Nguyen and Tran, 2007; Erban et al., 2014; Huang et al., 2016; Kadam et al., 2021a). According to the World Health Organization (WHO), 80% of all human diseases were

Citation: Nguyen TG, Nhien HTH, Anh PK. Groundwater quality assessment using classification and multi-criteria methods: A case study of Can Tho City, Vietnam. Environ. Nat. Resour. J. 2022;20(2):179-191. (https://doi.org/10.32526/ennrj/20/202100183)

associated with waterborne (WHO, 2017). Thus, it is necessary to assess the current groundwater quality in the study area.

Because of the complexity of the influencing factors on groundwater quality, a comprehensive assessment method is required. Recently, multivariate statistical analyses such as principal component analysis (PCA) and cluster analysis (CA), have been widely applied to recognize the key parameters in the variation of the data and to group the monitoring sites based on similar properties (Abou and Hafez, 2015; Misi et al., 2018). PCA is used to reduce the size of the dataset (i.e., physicochemical parameters) by explaining the correlation matrix and avoiding the loss of important information (Jackson, 2005). Additionally, this allows identifying the main parameters that control groundwater quality in the variation of the original dataset and determining the potential pollution sources (Nguyen et al., 2021a). Abou and Hafez (2015) studied the sources and distribution of nitrate pollution in groundwater in Damascus Oasis using PCA. The results of PCA could explain up to 84% of the cumulative variance and reveal the complication of pollutants causing groundwater pollution in Zimbabwe (Misi et al., 2018). In terms of water quality assessment, CA is also one of the effective methods in order to group samples on the basis of their similar properties (Egbueri, 2020; Nguyen et al., 2021a). For example, CA classified all groundwater monitoring sites into two clusters based on the pollution index and ecological risk index, supporting the selection of areas for groundwater treatment before use (Egbueri, 2020). In Mekong Delta, the groundwater quality index (GWQI) has been applied in previous studies to evaluate groundwater quality (Dao et al., 2016; Huynh et al., 2019). This tool can combine several different water parameters into only one index, which allows recognizing the composite impact of these parameters on groundwater in a particular area. For example, Huynh et al. (2019) and Dao et al. (2016) reported that the groundwater quality in An Giang and Ca Mau were classified as "bad water" and 50% of total samples in the good quality group based on the results of GWQI, respectively.

In the Mekong Delta Region, Can Tho is a city directly under the central government of Vietnam and also the economic and industrial center of the region. Most local economic activities strongly depend on freshwater resources including groundwater, rainwater, and surface water (DoNRE, 2009). According to Hang (2019), the total amount of groundwater being exploited in the Can Tho City has about 127,956 m^3/day at 50,673 exploited wells. In which, there are about 510 self-exploited wells with a capacity of about 75,982 m^3/day serving family activities, concentrated residential areas or producing industrial crops and vegetables, the service activities and industrial production facilities. Due to rapid industrialization and urbanization, the increasing human demand for freshwater was associated with surface water and groundwater in the city decreasing over time (Tran and Huynh, 2017; Tran et al., 2021). The research by Tran et al. (2021) reported that there was a significant decrease in groundwater levels during the period 2000-2018; especially the Upper-Pleistocence (qp_3) và Middle-Upper Pleistocene aquifers (qp_{2-3}). Lower groundwater levels in Can Tho City have been reported because of the combined effects of low recharge rates and high abstraction (Nuber et al., 2008). Therefore, it can be seen that groundwater resources play an important role in the region and are facing many threats to their quality and availability. Recently, several studies in Can Tho City and surrounding areas have also been conducted; however, these studies only focused on assessing the variability of water reserves (Tran et al., 2021) or specific pollutants (such as arsenic) in An Giang, Tien Giang, and Long An (Phan and Nguyen, 2018; Nguyen et al., 2021b). There are no comprehensive studies that assess groundwater quality using the WQI, PCA and CA in Can Tho City. Therefore, the primary purpose of this study was; (1) evaluated the seasonal groundwater variations and assess its suitability for human consumption; (2) assess the spatial distribution and groundwater quality variability of the sampling sites by using GWQI and multivariate statistical methods; (3) identify the key factors influencing groundwater quality. The results of this study provide the status and potential sources of groundwater quality variations, supporting scientific information for appropriate groundwater management strategies.

2. METHODOLOGY

2.1 Study area

This study was conducted to evaluate groundwater quality in Can Tho City belonging to the Mekong delta, Vietnam, has 1,439.2 km^2 and a population of 1,235,171 people. In terms of land use, agricultural land is dominant (79.66%), concentrated in Co Do, Vinh Thanh and Thoi Lai Districts; while non-agricultural land is representing most of the land area of Ninh Kieu and Binh Thuy Districts (Can Tho City Statistics Office, 2020). Can Tho City has a tropical monsoon climate with two seasons in the year, including the rainy season (from May to November) and the dry season (from December to April next year). The average temperature fluctuated from 26.2ºC to 29.8ºC in 2019. Total rainfall accounts for about 90% of the annual rainfall during the rainy season (1,406.6 mm/rainy season), while dry season accounts for only about 10% (179.9 mm/dry season). The terrain is relatively flat with an average height of about 1-2 m, sloping from the plains along the Hau and Can Tho Rivers and gradually lowering from the northeast to southwest (DoNRE, 2015). The geology in the city is mainly formed through the marine and alluvial Mekong River deposits. There are two main types of soil groups, including alluvial soil and acid sulfate soil. In which, alluvial soil accounts for 84% of the natural area, which is distributed along the Hau River and from 8-12 km from the river; acid sulfate soil accounts for 16% of the natural area (DoNRE, 2015). The density of rivers and canals in Can Tho City is quite large 1.8 km/km^2 with more than 158 rivers and canals (DoNRE, 2015; Nguyen, 2020). Although the network of rivers and canals is crisscrossed, only exploiting surface water for economic development and basic daily demands is not sufficient. At the same time, due to the rapid population growth, surface water quality is degraded over time because of mass domestic and industrial wastes. Therefore, groundwater has become one of the alternative water resources to serve local demands.

Can Tho City has seven water-bearing units in the order from top to bottom, namely Holocene (qh), Upper Pleistocene (qp_3), Middle-Upper Pleistocene (qp_{2-3}), Lower Pleistocene (qp_1), Upper Pliocene (n_2^2), Lower Pliocene (n_2^1), Upper Miocene aquifer (n_1^3) (Le et al., 2017). On the surface at a depth of 50 m, there are two types of sediments: Holocene (new alluvium) and Pleistocene (ancient alluvium) (DoNRE, 2015; Le et al., 2017). In which, aquifers are mainly in Pleistocene, Pliocene, Miocene at depths of 80-400 m, some places have been recorded at depths of 18-35 m. The aquifer that has the largest number of boreholes exploited and used in Can Tho City is the Pleistocene (qp_{2-3}) (Le et al., 2017).

2.2 Groundwater monitoring sites and analyses

Groundwater samples were collected from 27 monitoring locations in 2019 labeled from GW1 to GW27, shown in Figure 1. This were collected and preserved according to the national standards on guidelines for sampling and preserving groundwater of the Ministry of Science and Technology of Vietnam (2011) and Ministry of Science and Technology of Vietnam (2008). Each collected sample was analyzed for 13 parameters including pH, color, total hardness, chloride (Cl^-), sulfate (SO_4^{2-}), chemical oxygen demand (COD), magnesium (Mg), total iron (Fe), nitrate (NO_3^-), arsenic (As), lead (Pb), mercury (Hg), and coliforms. These parameters have been selected based on the characteristics of the area and national technical regulations in the assessment and monitoring of groundwater quality to guide different water use purposes (MoNRE, 2015). In addition, many previous studies have noted that As, Fe, and Pb were frequently presented in groundwater of provinces in the Mekong Delta (Huang et al., 2016; Ha et al., 2019a; Nguyen et al., 2021b). While the Ni, Cd in the Mekong River Delta exceeded (less than 1%) the WHO standards (2008) and did not have the ability to affect public health. In addition, cations were not mentioned in national technical regulation on groundwater quality in Vietnam, which is applied as the basis to guide for the different water uses (MoNRE, 2015). Therefore, these parameters are of less interest in the study area (Tran, 2019). The temporal variation of groundwater was evaluated in the dry season (April) and the rainy season (October). The pH was measured directly in the field, and other parameters were analyzed in the laboratory at the Can Tho City Environmental and Natural Resources Monitoring Center using standard methods (APHA, 1998).

2.3 Groundwater quality index (GWQI)

The groundwater quality index (GWQI) was used to evaluate overall groundwater quality. GWQI was calculated using the formula (1) (Dao et al., 2016; Li et al., 2021):

$$\mathrm{GWQI} = \sum_{n=1}^{10}(q_n \times W_n) \quad (1)$$

$$W_n = \frac{w_n}{\sum_n^{10} w_n} \quad (2)$$

Where; W_n is the relative weight of the n^{th} parameter; q_n is sub-assessment quality index corresponding to the n^{th} parameter. The q_n values was calculated by the formula (3):

$$q_n = 100 \times \frac{(V_n - V_i)}{S_n - V_i} \quad (3)$$

Where; S_n is the limit values of groundwater quality specified in the Vietnamese regulation on groundwater quality (QCVN 09-MT:2015/BTNMT) (MoNRE, 2015); V_n was the content of parameter n in the study area; V_i was ideal values (with pH=7, the rest of parameters were equal to 0). The weight factor of groundwater parameters is presented in Table 1.

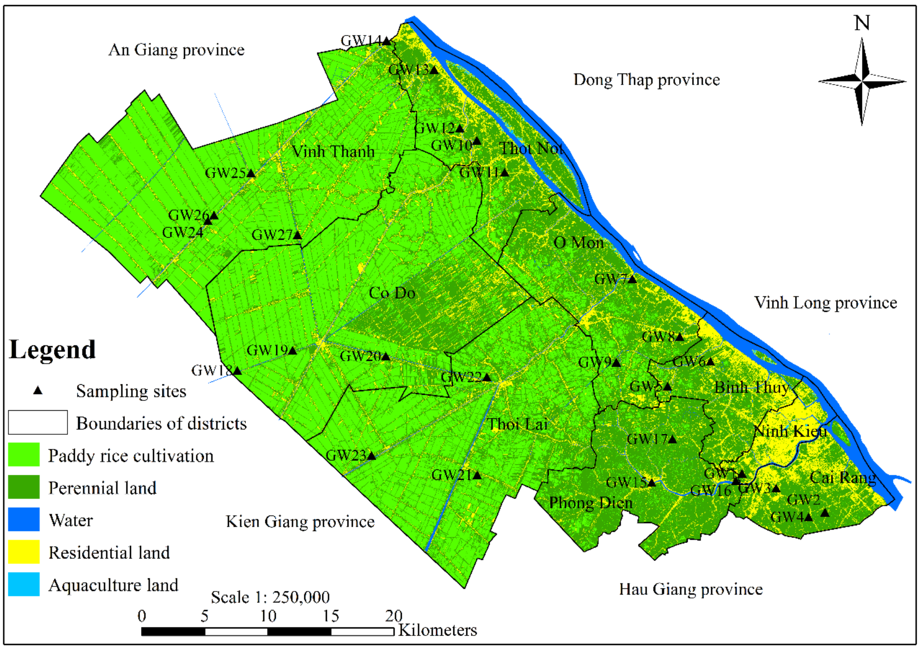

Figure 1. Location map of Can Tho City groundwater monitoring point

Table 1. The weight factor of groundwater parameters

Parameter	S_n	w_n ($1/S_n$)	W_n
pH	5.5-8.5	1.18E-01	1.05E-04
Hardness	500	2.00E-03	1.78E-06
Cl^-	250	4.00E-03	3.57E-06
SO_4^{2-}	400	2.50E-03	2.23E-06
Fe	5	2.00E-01	1.78E-04
NO_3^-	15	6.67E-02	5.95E-05
As	50	2.00E+01	1.78E-02
Pb	10	1.00E+02	8.92E-02
Hg	1	1.00E+03	8.92E-01
Coliforms	3	3.33E-01	2.97E-04

The groundwater quality is classified into 5 levels based on the computed GWQI values, as shown in Table 2. This calculated data was used to create a spatial distribution map of GWQI. The GWQI distribution map was performed using the interpolation with inverse distance weighted (IDW) method. The IDW method would estimate the GWQI values at the unsampled locations using a linear function of the sampled locations. The GWQI values of the predicted locations would decrease with the distance from the sampling site (Huynh et al., 2019; Hasan and Rai, 2020). The study used Arcgis version 10.2 software to perform the spatial interpolation. Besides that, cluster analysis (CA) and principal component analysis (PCA) were used to group the wells with similar groundwater quality and to identify key variables resulting in variation of groundwater quality (Wagh et al., 2019; Kadam et al., 2021c). CA and PCA analysis were performed using Primer 5.2 software (PRIMER-E Ltd, Plymouth, UK).

Table 2. Water quality classification based on the calculated GWQI

GWQI	<50	50-100	100-200	200-300	>300
Water quality	Excellent	Good	Poor	Very poor	Unsuitable for drinking

(Dao et al., 2016; Li et al., 2021; Huynh et al., 2019)

3. RESULTS AND DISCUSSION

3.1 Groundwater quality assessment

The seasonal changes of physicochemical properties in groundwater quality in Can Tho City are presents in Table 3. The values of the monitoring parameters were compared to the Vietnamese technical regulation on groundwater quality (QCVN09-MT:2015/BTNMT).

pH values were found to vary from 7.14-7.64 in the dry season and 6.69-8.22 in the rainy season, which are within the allowable limit (5.5-8.5). There was a little spatiotemporal variation in pH values, and alkalinity was predominant. In the dry season, the groundwater color in all monitoring sites ranged from 1 to 143 Pt-Co, with an average of 23.33±29.87 Pt-Co. This value was much lower in the rainy season which varied from 1 to 21 Pt-Co, with an average of 7.15±5.06 Pt-Co.

The results showed that there was a significant spatiotemporal variation of total hardness. The average values of total hardness at the monitoring sites were in the range of 25.20-168.50 mg/L. In the rainy season, the average hardness value was 150.19±58.69 mg/L, which was over four times higher than that in the dry season (35.50±14.77 mg/L). The reason for this fluctuation is an increase in water volume into aquifers that contain high dissolved mineral contents such as calcium and magnesium because of moving through soil and rock (Ram et al., 2021). In addition, Fe could also increase the hardness in groundwater in this study; because the study area has about 16% iron or aluminum acid soil (Hua, 2019). The detected hardness values of groundwater in the study area are within the allowable limit of the Vietnamese standard. Several studies of groundwater quality in the Mekong Delta reported that total hardness values were found in the range of 220.15 to 1,262.50 mg/L in An Giang Province (Nguyen, 2021a), 52.50 to 7,355.36 mg/L in Ca Mau peninsula (Dao et al., 2016) and 125 to 138 mg/L in Dong Thap Province (Pham, 2019). High total hardness in groundwater not only reduces the water quality for domestic and production usage but also causes adverse effects on human health (Li et al., 2021; Ram et al., 2021).

Table 3. Seasonal variation of groundwater quality

Variables	Units	Dry season	Rainy season	Vietnamese standard
pH	-	7.37±0.14	7.33±0.34	5.5-8.5
Color	Pt-Co	23.33±29.87	7.15±5.06	-
Hardness	mg $CaCO_3$/L	35.50±14.77	150.19±58.69	500
Cl^-	mg/L	138.66±118.33	24.91±25.91	250
SO_4^{2-}	mg/L	67.41±43.76	22.07±21.48	400
COD	mg/L	4.84±2.30	2.76±2.37	4
Mg	mg/L	0.12±0.08	0.20±0.36	-
Fe	mg/L	0.69±0.52	2.71±13.45	5
NO_3^-	mg N/L	0.32±0.36	0.90±3.72	15
As	µg/L	0.7±0.9	ND	50
Pb	µg/L	2.09±1.77	ND	10
Hg	µg/L	ND	ND	1
Coliforms	MPN/100 mL	8.63±6.65	4.96±3.89	3

ND: Not detected

The Cl^- concentrations in the dry and rainy seasons were found in the range of 25.20-382.30 mg/L and 15.30-146.60 mg/L, respectively. Also, there was a spatial variation of the Cl^- concentration (15.3-382.3 mg/L). Most monitoring sites had the Cl^- concentration within the permissible limit (250 mg/L), with the exception of GW2, GW3, GW4, GW7, GW15, GW16, GW17, and GW27. High Cl^- concentration could result from overexploitation of groundwater, leading the saline boundary to encroach into the aquifer

(Nguyen et al., 2017). The seasonal fluctuation of the Cl^- concentration has been reported in previous studies in which Cl^- tended to be higher in the dry season (Nguyen et al., 2017; Li et al., 2021). As a result of higher precipitation infiltration, salt concentration is diluted, which in turn reduces the Cl^- concentration in groundwater in the wet season. The presence of high Cl^- concentration is also a major concern to crop productivity and human health (Nguyen et al., 2021b; Pius et al., 2012).

Similarly, the average SO_4^{2-} concentration in the rainy season (22.07±21.48 mg/L) was lower than that in the dry season (67.41±43.76 mg/L). The spatial variation of SO_4^{2-} concentration was in the range of 2.0-181.7 mg/L, which was within the national permissible limit. SO_4^{2-} in groundwater is the result of dissolving rocks containing gypsum, iron sulfides, and other sulfur compounds (Dao et al., 2016; Ram et al., 2021). Moreover, leaching sulfate in fertilizer application in agriculture and other human activities is also responsible for SO_4^{2-} in groundwater (Al-Ahmadi, 2013).

The average value of COD in the dry season (4.84±2.30 mg/L) was found to be higher than that in the rainy season (2.76±2.37 mg/L), and the COD concentration in the monitoring sites ranged from below detection limit to 10.6 mg/L. COD at seven out of 27 monitoring sites (25% of the monitoring sites) in the rainy season exceeded the permissible limit of groundwater quality standard. Meanwhile, this ratio increased up to nearly 63% in the dry season. The seasonal variation of COD in groundwater was also reported in the previous study (Huynh et al., 2016). High COD in groundwater could be caused by anthropogenic sources such as leachates and industrial wastewater (Nguyen et al., 2019).

Mg^{2+} concentrations were ranged from below the detection limit to 0.29 mg/L in the dry season and from 0 to 2 mg/L in the rainy season (Table 3). Nguyen et al. (2017) also reported a great Mg^{2+} concentration in groundwater in Ba Ria Vung Tau, Vietnam, with the range of 0.24-118.56 mg/L in the rainy season. Higher Mg^{2+} concentrations are responsible for the higher hardness of groundwater in the rainy season, which is the result of the dissolution of magnesium-contained rocks.

The average of total Fe concentration was 0.69±0.52 mg/L in the dry season and 2.71±13.45 mg/L in the rainy season (Table 3). Total Fe concentration also considerably fluctuated among monitoring sites from 0.05 to 70.00 mg/L. While total Fe concentration found in most of the monitoring sites was within the permissible limit (5 mg/L), it was detected at very higher levels in the GW9 site which was 14-time greater than the limit. Several studies have shown a relatively lower total Fe concentration in groundwater in the Mekong Delta such as from 0.81-2.19 mg/L in Soc Trang Province (Nguyen et al., 2021b) and 0.07-2.16 mg/L in An Giang (Phan and Nguyen, 2018). When water contains higher than 0.5 mg/L of total Fe, it has an unpleasant fishy odour and yellow color, which adversely affects the quality of drinking water for domestic use and production.

The NO_3^- concentration was ranged from no detection to 1.09 mg N/L in the dry season and 19.50 mg N/L in the rainy season (Table 3). Only GW9 site in the rainy season had NO_3^- concentration exceeded the permissible limits (15 mg N/L). NO_3^--contaminated groundwater is attributed to anthropogenic sources such as fertilizer practices, domestic and industrial wastewater (Li et al., 2021; Li et al., 2016). NO_3^- concentration in groundwater was found to be varied among the study areas in the Mekong Delta. Nguyen et al. (2021b) reported that this concentration ranged from 0.008-0.047 mg/L in Soc Trang Province, while it was found over 30 mg/L in Tra Vinh Province (Nguyen and Tran, 2007). The NO_3^- groundwater contamination not only occurred in the Mekong Delta but also in other areas in Vietnam. Duong and Lam (2018) found the NO_3^- concentration greatly fluctuated from 0.09 to 95.96 mg/L in Pleiku City.

The concentration of As in groundwater was only detected in the dry season, with an average of 0.7±0.9 µg/L (Table 3). This concentration was within the permissible limit of the Vietnamese standard. As-contaminated groundwater is a major concern in the Mekong Delta because it is a carcinogenic substance (Berg et al., 2007; Huang et al., 2016). Several studies reported that As concentration in the groundwater was up to 60 µg/L in Tra Vinh Province (Nguyen and Tran, 2007) and 0.55±1.21 mg/L in An Giang Province (Phan and Nguyen, 2018). The use of As-contaminated groundwater without appropriate treatment could cause potential life time cancer risk from medium to high level (Phan and Nguyen, 2018).

The Pb concentration was only detected in the dry season with an average of 2.09±1.77 µg/L and varied from below the detection limit to 6.0 µg/L at different monitoring sites (Table 3). This is within the permissible limit of Pb in groundwater. According to Ha et al. (2019b), Pb-contaminated groundwater in Mekong delta (4 µg/L) higher than that in Can Tho

City. The presence of Pb in groundwater in Can Tho City may be due to its natural availability or runoff through agricultural areas, where there is accumulation of lead in the soil by the use of fertilizer. The accumulation of Pb in agricultural land in Thoi Lai District, Can Tho was also recorded by Nguyen (2021b). There was no detection of Hg in groundwater in the study area during the study period.

Coliforms in groundwater had a considerable spatiotemporal variation which ranged from below the detection limit to 23 MPN/100 mL (Table 3). The average density of coliforms in the dry season (8.63±6.65 MPN/100 mL) was higher than that in the rainy season (4.96±3.89 MPN/100 mL). Coliform density in most of the monitoring sites (24/27 sites) exceeded the permissible limit. The problem of coliform contamination was also previously reported in the study area in 1999-2002 (Huynh et al., 2016). This could be indicative of pollution from inadequate sanitation systems and infiltration of polluted urban runoff entering groundwater wells. Microbial contamination of groundwater in the Mekong Delta has been reported in several previous studies (Phan and Nguyen, 2018; Nguyen, 2021a). As a result of poor well protection and maintenance, microbial contaminants from septic tank leakage, agricultural runoff, wild animals, and cattle faecal matter can enter aquifers.

3.2 Groundwater quality index (GWQI)

The results of computed GWQI showed that there was a little variation between the dry season and rainy season in the study area, as presented in Figure 2. The GWQI values in the dry season were varied from 0.04 to 5.68, which was slightly higher than that in the rainy season (0.00-0.35). This difference was associated with the high concentration of Cl^-, SO_4^{2-}, COD, As, Pb, and coliforms in the dry season. In general, the groundwater quality in the study area is at an excellent level on the basis of calculated GWQI values and is potable for human consumption.

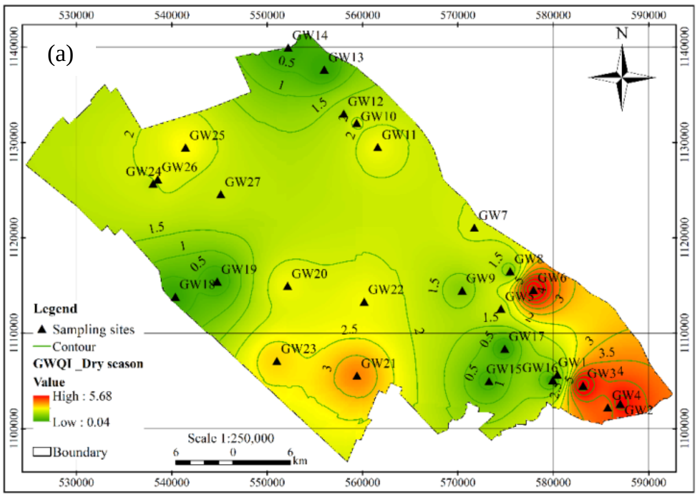

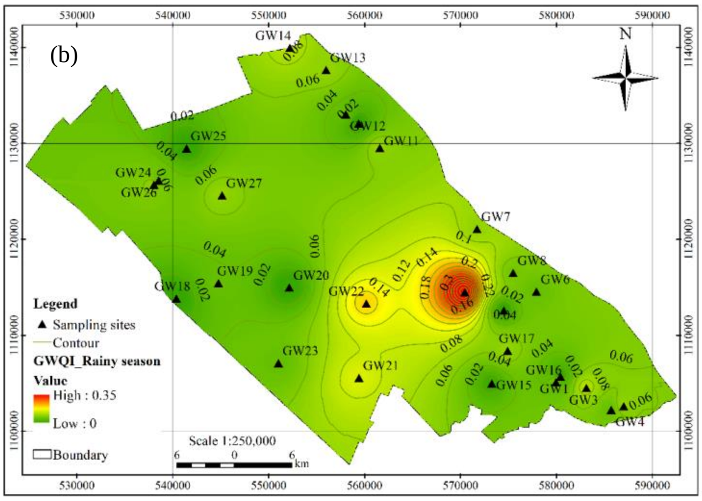

Figure 2. GWQI distribution map in (a) the dry season and (b) the rainy season

As illustrated in Figure 2, groundwater in the southeast of Can Tho City including GW2, GW3, GW4, and GW6 tended to be more polluted than the other wells in the dry season. These monitoring sites were in Ninh Kieu, Binh Thuy, and Cai Rang Districts where there are several residential areas and industrial areas as well as diverse economic activities (Vo et al., 2020). Moreover, overexploitation of groundwater in the dry season could cause the depletion of the water table and increase saline water intrusion into these areas (MoNRE, 2021). Only GW9 had slightly higher GWQI value in the study area in the rainy season because of considerable higher coliform density, NO_3^- and total Fe concentration. It means that wells in this area were not adequately protected, which caused the contamination from human sewage, livestock wastewater, or animal droppings. Thus, comminated groundwater could be the result of overexploitation, improper waste disposal or improper well maintenance in the long-term use.

3.3 Cluster analysis (CA)

Two dendrograms were created using the results of groundwater quality at different monitoring sites in the dry and rainy seasons, as showed in Figure 3. In the same distance (D_{link}/D_{max}<30), while the groundwater monitoring sites were divided into 9 clusters in the dry season, those sites were into 5 clusters in the rainy season.

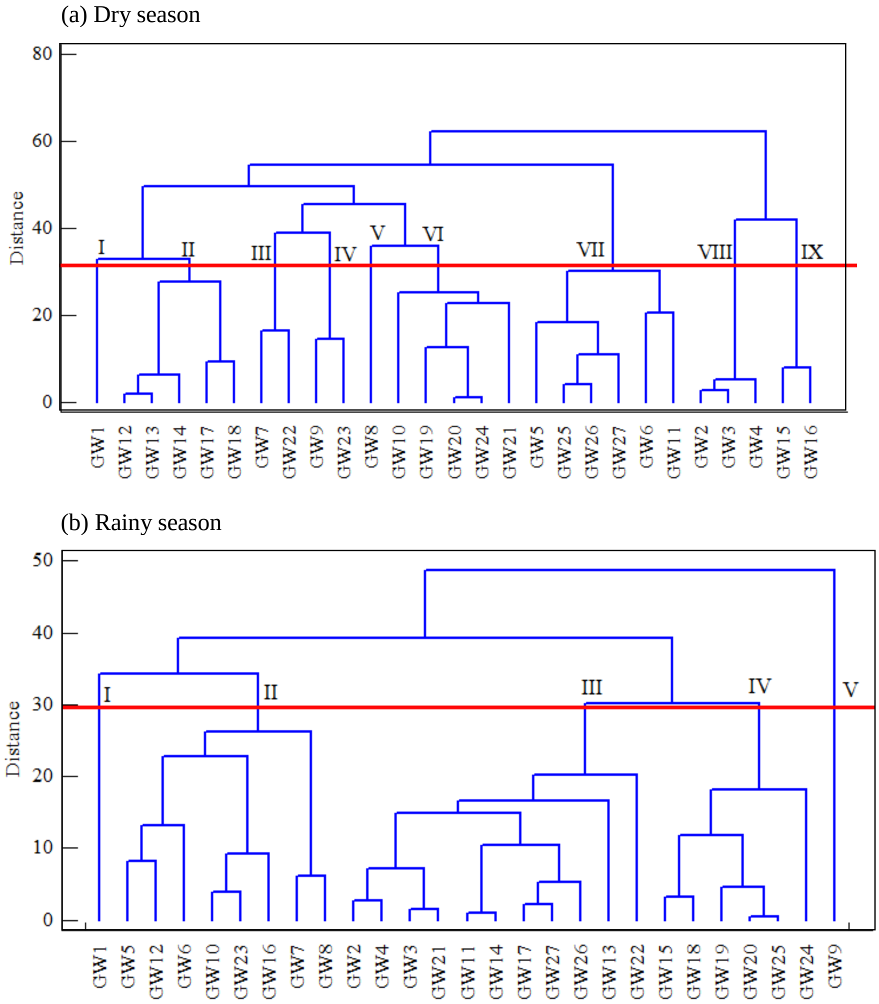

Figure 3. Water quality clustering based on seasonal parameters

The groundwater quality characteristics of each cluster are presented in Table 4. It can be seen that there was a more significant spatial variation in groundwater quality in the dry season than that in the rainy season.

In the dry season, the cluster II comprised of five monitoring sites (GW12, GW13, GW14, GW17, and GW18) located at high terrain in two districts of Co Do and Thot Not. The groundwater of these monitoring sites was polluted by coliforms, which could be the result of domestic waste leakages, animal fecal matters, and improper well protection. The monitoring sites in the cluster III, IV, and V are located in O Mon and Thoi Lai Districts, with similar economic development and land-use types. The presence of metalic compounds containing Fe, Mg, As, and Pb in these clusters could be attributed to mineral dissolution from industrial and agricultural areas into the aquifers. High Cl^- concentration was found in the cluster III, which means that saltwater intrusion strongly affects groundwater quality in GW7 and GW22. Coliform density in groundwater was extremely high the cluster IV and VI. Cluster VII included GW5, GW6, GW11, GW25, GW26, and GW27 belong to rural areas with the majority of agricultural practices and intensive fertilizer uses that resulted in high SO_4^{2-} in this cluster. The cluster VIII are located in the urban and industrial production areas facing the chloride pollution in groundwater caused by saltwater intrusion in the dry season. Very high coliform density was detected in groundwater in the cluster IX (GW15 and GW16), which belongs to the perennial crop area in Phong Dien District. The presence of coliforms in the groundwater indicated the protection and manitenance of groundwater wells are not appropriate.

Table 4. Mean values of water quality parameters for each cluster

Season	Cluster	pH	Color	Hardness	Cl^-	SO_4^{2-}	COD	Mg	Fe	NO_3^-	As	Pb	Coliform
Dry	I	7.20	10.00	57.60	62.80	36.90	2.10	0.29	0.27	0.10	0.00	1.60	4.00
	II	7.35	12.00	32.12	92.92	55.04	5.74	0.06	0.58	0.03	0.26	0.32	7.40
	III	7.52	6.50	12.00	222.20	95.45	8.50	0.20	0.96	0.00	0.00	2.35	5.50
	IV	7.60	11.00	22.90	28.05	43.30	4.25	0.22	0.56	0.63	1.65	1.95	15.00
	V	7.47	143.00	32.00	91.90	51.40	6.40	0.10	1.34	0.00	0.00	1.40	4.00
	VI	7.39	32.80	30.68	81.58	68.42	5.74	0.11	1.51	0.58	0.00	2.02	13.20
	VII	7.40	24.50	33.93	105.55	121.62	3.18	0.12	0.21	0.62	0.98	3.00	4.17
	VIII	7.14	18.33	55.87	310.63	19.93	4.97	0.11	0.43	0.13	1.33	5.07	7.33
	IX	7.24	8.00	56.90	325.50	23.70	2.65	0.06	0.48	0.06	2.15	0.00	17.00
Rainy	I	7.20	2.00	240.00	146.60	28.40	-	0.13	0.06	0.00	-	-	0.00
	II	7.39	10.00	105.00	23.00	43.29	1.33	0.13	0.12	0.09	-	-	3.38
	III	7.22	6.64	138.64	18.95	12.05	2.79	0.12	0.13	0.20	-	-	7.91
	IV	7.46	5.17	216.67	18.10	14.45	4.25	0.15	0.13	0.32	-	-	1.83
	V	-	-	-	-	2.00	7.81	2.00	70.00	19.50	-	-	9.00

Only five clusters were obtained on the basis of groundwater quality parameters in the rainy season. The cluster IV was an assemblage of monitoring sites (GW15, GW18, GW19, GW20, GW24, and GW25) located in low terrain and far from large rivers; thus, this limits the movement of pollutants from surface water into aquifers. This cluster is considered insignificant pollution in groundwater. The cluster II was comprised of eight monitoring sites (GW5, GW12, GW6, GW10, GW23, GW16, GW7, and GW8) located along the Hau River. Groundwater in this cluster was polluted by coliforms. The GW1 location was categorized into a separate cluster in both seasons, with relatively good groundwater quality but slightly contaminated with coliforms in the dry season. Nevertheless, in the rainy season, the hardness of groundwater became higher than in other clusters. Industrial waste and subsurface geological structure could be the souces calcium and magnesium that directly contributed to the hardness of groundwater.

Besides, CA analysis also showed that groundwater characteristics are similar for the districts in Can Tho City; this can be applied to reduce the number of samples to save budget and time. For example, a sampling sites may be removed when the location has the same grouping and the same district. Specifically, Cluster II included five locations in Thot Not, Phong Dien and Co Do Districts in the dry season; this cluster can be reduced to three samples in the next groundwater quality monitoring. Cluster III and cluster IV had two locations in each cluster, namely GW7 and GW22 (cluster III), GW9 and GW23 (cluster IV); however, GW7 and GW22 are located in two separate districts (O Mon and Thoi Lai Districts). Therefore, these four sampling sites will still be retained for future monitoring. The removal of samples was performed similarly for the remaining clusters. Thereby, the number of samples can be reduced from 27 to 18 (dry season) and 15 (rainy season) samples; which can save about 33.3% and 44.4% of the total budget, respectively.

3.4 Principal component analysis (PCA)

The PCA results showed that 4 PCs and 3 PCs contributed significantly to groundwater quality variation in the dry and rainy season, respectively, presented in Table 5. In the dry season, 4 PCs could explain 63.4% of total groundwater quality groundwater variation in the study area. PC1 explains 24.8% of the variance and has weak correlations with pH (-0.469), Cl^- (0.415), and As (0.309) and moderate correlation with total hardness (0.52). Groundwater hardness is associated with the dissolution of calcium or magnesium-bearing rock, industrial effluent or agricultural activities. The presence of Cl^- in groundwater could be the result of both natural and anthropogenic sources such as seawater intrusion and excessive application of inorganic fertilizers (Nguyen et al., 2017). The alkalinity of groundwater could be affected by agricultural leachate, detergents and industrial wastes (Hoko, 2008).

PC2 accounted for 17.5% of the total variation and had a weak correlation with groundwater parameters. It had a negative coefficient with COD (-0.443) and total Fe (-0.365), and a positive coefficient with Mg (0.302), NO_3^- (0.424), As (0.312), and Pb (0.335). The presence of metallic compounds in groundwater could be from mineral dissolution from industrial sites. Because as reported by Tran et al. (2021), overexploitation of groundwater has resulted in land subsidence (4.28 cm/year) as well as the release of As and possibly other heavy metals.

PC3 explained 10.7% of total variation and had weak correlations with Fe (0.352) and NO_3^- (0.430) and medium correlation with coliforms (0.678). The high positive loading coliform is due to the feces of warm-blood animals and humans; especially residential area. In addition, nitrate has shown the use of nitrogen-based fertilizers in the study area; which has been converted into nitrite and nitrate by microorganisms for the growth of plants. The contribution of nitrogen from agricultural sources has also been reported in previous studies (Wagh et al., 2019; Kadam et al., 2021c). PC4 accounted for 10.3% of total variation and was correlated with color (0.539) at medium and SO_4^{2-} (0.310) at weak.

Table 5. Key variables influencing groundwater quality in Can Tho City

Variables	Dry season				Rainy season		
	PC1	PC2	PC3	PC4	PC1	PC2	PC3
pH	**-0.469**	-0.028	-0.129	-0.244	**-0.443**	-0.041	-0.139
Color	-0.107	-0.256	0.236	**0.539**	-0.153	**0.588**	0.02
Hardness	**0.520**	-0.014	0.19	0.249	-0.231	**-0.467**	-0.06
Cl^-	**0.415**	-0.175	-0.081	0.105	-0.14	**-0.354**	**0.607**
SO_4^{2-}	-0.287	0.277	0.032	**0.31**	-0.122	**0.391**	**0.325**
COD	-0.119	**-0.443**	-0.279	**-0.317**	0.246	**-0.342**	**-0.397**
Mg	-0.108	**0.302**	-0.068	0.209	**0.449**	0.023	0.173
Fe	-0.232	**-0.365**	**0.352**	0.187	**0.451**	0.011	0.17
NO_3^-	-0.239	**0.424**	**0.43**	-0.072	**0.451**	0.002	0.165
As	**0.309**	**0.312**	0.073	**-0.349**	-	-	-
Pb	0.082	**0.335**	-0.164	0.051	-	-	-
Coliforms	0.064	-0.131	**0.678**	**-0.416**	0.154	0.197	**-0.509**
Eigenvalues	2.98	2.11	1.29	1.23	4.67	1.46	1.26
%Variation	24.8	17.5	10.7	10.3	46.7	14.6	12.6
Cum.%Variation	24.8	42.4	53.1	63.4	46.7	61.3	73.9

In the rainy season, the results of PCA could explain 73.9% of the variation in groundwater quality in the study area with 3 PCs. PC1 accounts for 46.7% of the total variation obtained with a weak correlation to groundwater parameters. It had a positive coefficient with Mg (0.449), total Fe (0.451), NO_3^- (0.451), and a negative coefficient with pH (-0.443). NO_3^- indicated the groundwater pollution sources could be from excessive application of fertilizers in the agricultural areas. Before reaching the aquifer, water can pass through limestone or gypsum and dissolve magnesium and iron, hence carrying it into groundwater. Moreover, industrial effluent and sewage can also be sources of magnesium and iron pollution. PC2 explains 14.6% of the total variation including color (0.588) with moderate correlation and weak correlation with hardness (-0.467), Cl^- (-0.354), SO_4^{2-} (0.391), and COD (-0.342). PC3 was weakly correlated with SO_4^{2-} (0.325), COD (-0.397), and correlated at medium with Cl^- (0.607) and coliforms (-0.509). Many sources can be contributed to the Cl^- and SO_4^{2-} groundwater pollution including industrial effluent, fertilizer application, and other anthropogenic activities.

It can be deduced that groundwater quality in the study area was influenced by different sources such as geological conditions (specifically the problem of serious land subsidence), agricultural activities in Thoi Lai, Co Do and Phong Dien District. While sources from industrial zones and residential areas are identified as potential sources of Binh Thuy (GW5 and GW6), Ninh Kieu (GW1), and Cai Rang (GW2-GW3) Districts. In addition, all analyzed parameters play an important role in evaluating groundwater quality and should be remained in the later monitoring program.

4. CONCLUSION

The groundwater in Can Tho City in 2019 was polluted by coliforms at all sampling sites in both seasons and by COD and Cl^- in several monitoring sites in the dry season. Groundwater quality in all monitoring sites was classified at the excellent level and groundwater in the southeast area of Can Tho tended to be more polluted in the dry season. CA results divided 27 monitoring sites into 9 clusters in the dry season and 5 clusters in the rainy season, which also confirmed more spatial variation of groundwater in the dry season. The result of CA could be used for considering reduction of the monitoring site by 9 sites (dry season) and 12 sites (rainy season). The results of PCA revealed that four PCs and three PCs could explain 63.4% in the dry season and 73.9% in the rainy season, respectively. All analyzed parameters were significantly contributed to the groundwater variations due to the influence of subsurface geological characteristics, industrial effluent, domestic waste, and agricultural practices. The findings in the current study could provide useful information for future groundwater monitoring and management.

ACKNOWLEDGEMENTS

The authors would like to express our sincere attitude toward the Department of Natural Resources and Environment Can Tho City for data provision. The scientific and personal views presented in this paper do not necessarily reflect the views of the data provider.

REFERENCES

Abou ZB, Hafez R. Hydrochemical, isotopic and statistical characteristics of groundwater nitrate pollution in Damascus Oasis (Syria). Environmental Earth Sciences 2015;74:2781-97.

Al-Ahmadi ME. Groundwater quality assessment in Wadi Fayd, Western Saudi Arabia. Arabian Journal of Geosciences 2013;6:247-58.

American Public Health Association (APHA). Standard Methods for the Examination of Water and Wastewater. 20th ed. Washington DC, USA: APHA; 1998.

Berg M, Stengel C, Trang PT, Viet PH, Sampson ML, Leng M, et al. Magnitude of arsenic pollution in the Mekong and Red River Deltas-Cambodia and Vietnam. Science of the Total Environment 2007;372:413-25.

Can Tho City Statistics Office. Can Tho City Statistics Yearbook 2019. Hanoi, Vietnam: Statistical Publishing House; 2020.

Dao HH, Nguyen KV, Tra ST, Bui VT. Assessment of groundwater quality of middle - upper pleistocene aquifer in Ca Mau peninsula. Science and Technology Development Journal 2016;19:35-44.

Deparment of Natural Resources and Environment Can Tho city (DoNRE). Report on the Environmental Status of Can Tho City for 2011 to 2015. Can Tho, Vietnam: DoNRE; 2015.

Department of Natural Resources and the Environment of Can Tho City (DoNRE). Report on Development of Environmental Quality in Can Tho City from 1999 to 2008. Can Tho, Vietnam: DoNRE; 2009.

Duong CV, Lam TH. Level of nitrate on shallow groundwater in Pleiku City, Gia Lai. The Da Nang University-Journal of Science and Technology 2018;3:116-8.

Egbueri JC. Groundwater quality assessment using pollution index of groundwater (PIG), ecological risk index (ERI) and hierarchical cluster analysis (HCA): A case study. Groundwater for Sustainable Development 2020;10:Article No. 100292.

Erban LE, Gorelick SM, Zebker HA. Groundwater extraction, land subsidence, and sea-level rise in the Mekong Delta, Vietnam. Environmental Research Letters 2014;9:Article No. 084010.

Fendorf S, Michael HA, Geen A. Spatial and temporal variations of groundwater arsenic in South and Southeast Asia. Science 2010;328:1123-7.

Gaikwad S, Gaikwad S, Meshram D, Wagh V, Kandekar A, Kadam A. Geochemical mobility of ions in groundwater from the tropical western coast of Maharashtra, India: Implication to groundwater quality. Environment, Development and Sustainability 2020;22:2591-624.

Ha QK, Choi S, Phan NL, Kim K, Phan CN, Nguyen VK, et al. Occurrence of metal-rich acidic groundwaters around the Mekong Delta (Vietnam): A phenomenon linked to well installation. Science of the Total Environment 2019b;654:1100-9.

Ha QK, Kim K, Phan NL, Phung TH, Lee J, Nguyen VK, et al. A hydrogeological and geochemical review of groundwater issues in southern Vietnam. Geosciences Journal 2019a;23:1005-23.

Hang T. Protecting underground water in urban areas of Ho Chi Minh City, Can Tho and My Tho - Lesson 2: Can Tho City - underground water is not in danger of running out [Internet]. 2019 [cited 2021 Nov 25]. Available from: https://baotainguyenmoitruong.vn/bao-ve-nuoc-duoi-dat-do-thi-tp-hcm-can-tho-va-my-tho-bai-2-do-thi-can-tho-nuoc-duoi-dat-chua-co-nguy-co-can-kiet-294492.html.

Hasan MS, Rai AK. Groundwater quality assessment in the Lower Ganga Basin using entropy information theory and GIS. Journal of Cleaner Production 2020;274:Article No. 123077.

Hoko Z. An assessment of quality of water from boreholes in Bindura District, Zimbabwe. Physics and Chemistry of the Earth 2008;33:824-8.

Hua TN. Evaluation of Changes in Groundwater Quality of Lang Son City, Lang Son Province, Period 2014-2018 [dissertation]. Hanoi, Vietnam: Vietnam National University of Forestry; 2019.

Huang Y, Miyauchi K, Endo G, Don LD, Manh NC, Inoue C. Arsenic contamination of groundwater and agricultural soil irrigated with the groundwater in Mekong Delta, Vietnam. Environmental Earth Sciences 2016;75:1-7.

Huynh VTM, Avtar R, Kumar P, Tran DQ, Ty TV, Behera HC, et al. Groundwater quality assessment using fuzzy-AHP in An Giang Province of Vietnam. Geosciences 2019;9:Article No. 330.

Huynh VTM, Duong THN, Huynh YN, Huynh VM, Tran NV, Tran VT. Assessment of groundwater level and quality: A case study in O Mon and Binh Thuy Districts, Can Tho City, Vietnam. Naresusan University Engineering Journal 2016;11:1-9.

Jackson JE. A User's Guide to Principal Components. John Wiley and Sons; 2005.

Kadam A, Wagh V, Jacobs J, Patil A, Pawar N, Umrikar B, et al. Integrated approach for the evaluation of groundwater quality through hydro geochemistry and human health risk from Shivganga River Basin, Pune, Maharashtra, India. Environmental Science and Pollution Research 2021a (article in press).

Kadam A, Wagh V, Patil S, Sankhua R. Seasonal assessment of groundwater contamination, health risk and chemometric investigation for a hard rock terrain of western India. Environmental Earth Sciences 2021c;80:1-22.

Kadam A, Wagh V, Patil S, Umrikar B, Sankhua R, Jacobs J. Seasonal variation in groundwater quality and beneficial use for drinking, irrigation, and industrial purposes from Deccan Basaltic Region, Western India. Environmental Science and Pollution Research 2021b;28:26082-104.

Le VP, Tran MT, Tran VT. The impact of the groundwater exploitation on groundwater level in Can Tho City. Journal of Science Can Tho University 2017:22-30. (in Vietnamese)

Li C, Gao Z, Chen H, Wang J, Liu J, Li C, et al. Hydrochemical analysis and quality assessment of groundwater in southeast North China Plain using hydrochemical, entropy-weight water quality index, and GIS techniques. Environmental Earth Sciences 2021;16:1-5.

Li P, Wu J, Qian H. Hydrochemical appraisal of groundwater quality for drinking and irrigation purposes and the major influencing factors: A case study in and around Hua County, China. Arabian Journal of Geosciences 2016;9:1-7.

Ministry of Natural Resources and Environment (MoNRE). National Technical Regulation on Groundwater Quality QCVN09-MT:2015/BTNMT. Vietnam: MoNRE; 2015.

Ministry of Natural Resources and Environment (MoNRE). Report on the State of the National Environment for the Period 2016 - 2020. Hanoi, Vietnam: MoNRE; 2021.

Ministry of Science and Technology of Vietnam. Water Quality - Sampling - Part 11: Guidance on Sampling of Groundwaters (TCVN 6663-11:2011). Hanoi, Vietnam: Ministry of Science and Technology of Vietnam; 2011.

Ministry of Science and Technology of Vietnam. Water Quality - Sampling - Part 3: Guidance on the Preservation and Handling of Water Samles (TCVN 6663-3:2008). Hanoi, Vietnam: Ministry of Science and Technology of Vietnam; 2008.

Misi A, Gumindoga W, Hoko Z. An assessment of groundwater potential and vulnerability in the upper Manyame Sub-Catchment of Zimbabwe. Physics and Chemistry of the Earth 2018;105:72-83.

Nguyen AH, Phan NT, Hoang TT, Phan NN. Application of multivariate statistical analysis in the assessment of groundwater quality of Tan Thanh District, Ba Ria-Vung Tau Province. Science and Technology Development Journal 2017;1:66-72.

Nguyen DGN, Goto A, Osawa K, Nguyen HT, Nguyen VCN. Assessment of groundwater quality and its suitability for domestic and irrigation use in the coastal zone of the Mekong Delta, Vietnam. Water and Power 2019;64:173-85.

Nguyen TG, Phan KA, Huynh THH. Spatiotemporal analysis of surface water quality in Dong Thap Province, Vietnam using water quality index and statistical approaches. Water 2021a;13:Article No. 336.

Nguyen TG, Le THT, Lam NTL. Survey on current status of management, exploitation, use and quality of groundwater in Vinh Chau, Soc Trang. Journal of Agriculture and Rural Development 2021b;11:162-9. (in Vietnamese)

Nguyen TG. Chemical and microbial characteristics of surface and ground water in the areas burying swine infected with African swine fever in An Giang Province, Vietnam. Journal of Energy Technology and Environment 2021a;3:1-10. (in Vietnamese)

Nguyen TG. Efficiency of land use in longan E-dor farming (*Dimocarpus longan* Lour.) in Thoi Lai District, Can Tho City, Vietnam. Journal of Science and Technology Research 2021b;3:58-71.

Nguyen TG. Surface water quality at the branches adjacent to Hau River in Can Tho City, Vietnam. Journal of Agriculture and Rural Development 2020;15:79-86.

Nguyen VVB, Tran TT. Present exploitation, utilization and quality of shallow groundwater in sand dunes in Tra Vinh Province. Journal of Science Can Tho University 2007; 8:95-104.

Nuber T, Stolpe H, Ky QV, Vu VN. Modelling the groundwater dynamics of Can Tho City - challenges, approaches, solutions. Proceedings of the International SANSED Workshop: Decentralized Water Treatment Systems and Beneficial Reuse of Generated Substrates; 15-18th Apr 2008; Can Tho University, Vietnam; 2008.

Pham THVT. Assessment of drilling water quality at Tan Thanh Commune, Thanh Binh District, Dong Thap Province. Ho Chi Minh City Open University Journal of Science - Social Sciences 2019;14:119-28.

Phan KA, Nguyen TG. Groundwater quality and human health risk assessment related to groundwater consumption in An Giang Province, Viet Nam. Journal of Vietnamese Environment 2018;10:85-91.

Pius A, Jerome C, Sharma N. Evaluation of groundwater quality in and around Peenya industrial area of Bangalore, South India using GIS techniques. Environmental Monitoring and Assessment 2012;184:4067-77.

Ram A, Tiwari SK, Pandey HK, Chaurasia AK, Singh S, Singh YV. Groundwater quality assessment using water quality index (WQI) under GIS framework. Applied Water Science 2021;11:1-20.

Tran VT, Huynh VH. Groundwater exploitation status and groundwater level declines and land subsidence relationship: A case study in Tra Vinh and Can Tho. Journal of Science Can Tho University 2017;1:128-36.

Tran VT, Huynh VTM, Ram A, Pankaj K, Huynh VH, Masaaki. Spatiotemporal variations in groundwater levels and the impact on land subsidence in Can Tho, Vietnam. Groundwater for Sustainable Development 2021;15:1-13.

Tran LL. Remarks on the current quality of groundwater in Vietnam. Environmental Science and Pollution Research 2019; 26:1163-9.

Vo QT, Pham QV, Nguyen VT. Fusion of radar and optical images to generate the land use map of Can Tho City. Journal of Science Can Tho University 2020;56:20-9.

Wagh VM, Panaskar DB, Jacobs JA, Mukate SV, Muley AM, Kadam AK. Influence of hydro-geochemical processes on groundwater quality through geostatistical techniques in Kadava River Basin, Western India. Arabian Journal of Geosciences 2019;12:1-25.

World Health Organization (WHO). Guidelines for Drinking-Water Quality, Fourth Edition, Incorporating the First Addendum. World Health Organization; 2017.

Microplastic Pollution in the Inlet and Outlet Networks of Rawa Jombor Reservoir: Accumulation in Aquatic Fauna, Interactions with Heavy Metals, and Health Risk Assessment

Rita Rahmayanti, Basith Kuncoro Adji, and Andhika Puspito Nugroho*

Faculty of Biology, Universitas Gadjah Mada, Special Region of Yogyakarta 55281, Indonesia

ARTICLE INFO

Received: 13 Oct 2021
Received in revised: 5 Dec 2021
Accepted: 9 Dec 2021
Published online: 24 Jan 2022
DOI: 10.32526/ennrj/20/202100200

Keywords:
Microplastics/ Aquatic fauna/ Metal adsorption/ Health risk assessment

*** Corresponding author:**
E-mail: andhika_pn@ugm.ac.id

ABSTRACT

Streams are regarded as a pathway for spreading microplastics from land to various aquatic systems. The contamination of streams connected to the Rawa Jombor Reservoir may increase microplastic concentrations in the reservoir. The water coming out of the reservoir carries microplastics that spread out into the stream networks around the reservoir. Heavy metals have a high affinity for microplastics, increasing metal burdens on the surface of microplastics. The transfer of microplastics along the food chain leads to the possibility of increased adverse effects on organisms, mainly top predators. This research evaluated the accumulation and characterization of microplastics in water, sediment, and aquatic fauna (zooplankton, benthos, and fish); interactions with heavy metals (Pb, Cu, Cd, and Zn); and health risk assessment. Microplastics were collected from six sampling locations. The density, type of polymers, and color of microplastics were analyzed, as well as heavy metal concentrations on the surface of microplastics and a health risk assessment. The results showed microplastic contamination at a moderate level. The accumulation of microplastics in aquatic fauna showed the same pattern as microplastics in the environment. Microplastic concentrations in aquatic fauna showed an increase through trophic transfer and indications of biomagnification. Heavy metals were adsorbed on the surface of microplastics in high concentrations. Based on the health risk assessment, microplastic contamination of fish at the inlet and outlet of the Rawa Jombor Reservoir is still safe, but further monitoring is needed because of the possible long-term health hazards that may arise.

1. INTRODUCTION

Global plastic production continues to increase and become a global threat with the accumulation of plastic waste in marine and terrestrial ecosystems (Cox et al., 2019; Park et al., 2019). Most land-based plastic disposal from urban areas, industry, and agriculture are received directly by rivers and become a vital pathway runoff to marine ecosystems (Eriksen et al., 2013; Park et al., 2019). The increase in the accumulation of plastic waste is exacerbated by poor management of plastic waste disposal (Yuan et al., 2019).

Plastic waste that enters the aquatic ecosystem will undergo mechanical processes (erosion and abrasion), chemical processes (photo-oxidation and hydrolysis), and biological processes (degradation by microorganisms) breaking down into small pieces (micro and nano), which are then transported and spread over long distances following the water flow (Fan et al., 2019; Julienne et al., 2019). Physical, chemical, and biological degradation and fragmentation processes can cause the plastic to be fragmented into plastic pieces smaller than 5 mm, such as microbeads (Godoy et al., 2019; Naqash et al., 2020).

Microplastics (MPs) less than 5 mm in size can migrate and accumulate in water and sediment, and they have the potential to be ingested by aquatic fauna (Amin et al., 2020; Barboza et al., 2020). Aquatic organisms can ingest MPs due to the small particle size

Citation: Rahmayanti R, Adji BK, Nugroho AP. Microplastic pollution in the inlet and outlet networks of Rawa Jombor Reservoir: Accumulation in aquatic fauna, interactions with heavy metals, and health risk assessment. Environ. Nat. Resour. J. 2022;20(2):192-208. (https://doi.org/10.32526/ennrj/20/202100200)

and confusion with food, which can possibly be harmful to organisms at higher trophic levels, leading to biomagnification (Akhbarizadeh et al., 2019; Barboza et al., 2019). The surface of MPs can adsorb additives and other chemicals such as heavy metals (Baalkhuyur et al., 2018; Barboza et al., 2019; Barboza et al., 2020). Association of MPs and toxic compounds may be harmful to aquatic organisms, causing respiratory disorders, nervous disorders, and damage to lipid oxidation in fish (Barboza et al., 2020; Godoy et al., 2019; Naqash et al., 2020), while in humans, it can cause anemia, hypertension, nervous system disorders, brain damage, oxidative stress, and cell damage (Campanale et al., 2020), thus requiring a quantitative assessment of the human health risks.

Rawa Jombor Reservoir (RJR) plays a vital role in the life of the local communities as it is used for irrigation and tourist destinations (Alina et al., 2015). Several studies related to pollution in RJR waters indicated that the reservoir belongs to the light to moderately polluted category (Alina et al., 2015; Atmawati, 2012; Rina et al., 2020). One study related to heavy metals in the reservoir showed cadmium accumulation in the fish *Tilapia* and sediment that exceeded the applicable regulatory quality standards (Kusumaningtyas, 2015). Meanwhile, the aquatic network system around the Rawa Jombor Reservoir is vulnerable to MP pollution due to plastic waste disposal activities around the waters, floating restaurants, and tourist activity which causes an increase in the accumulation of plastic waste that enters through the inlet through Kali Ujung (KU) and exits through the outlet of Kali Sosrodiningrat (KS). Heavy metals (HMs) can be carried on the surface of microplastics through the adsorption ability of microplastic; this condition has the potential to endanger the RJR ecosystem. In addition, it is feared that there will be long-term effects on public health due to fish consumption from the RJR waters, thus requiring a health risk assessment.

This study evaluated MP contamination in the RJR inlet and outlet water network. It was new and complemented existing research. The abundance and characteristics of MPs were identified in surface water, sediments, and aquatic fauna (zooplankton, benthos, and fish) from the inlet and outlet water networks of the RJR. The relationship between MPs accumulation in aquatic fauna and the environment at each sampling location was analyzed using Principal Component Analysis (PCA). The interaction of MPs with US EPA priority HMs (Pb, Cu, Cd, and Zn) was also studied to determine the human health risk assessment based on Estimated Daily Intake (EDI), Target Hazard Quotients (THQ), Total Target Hazard Quotients (TTHQ), and Target Cancer Risk (TR). The results of this study can also provide essential information for policymakers in environmental management and water resources conservation.

2. METHODOLOGY

2.1 Study area

This study was conducted at the RJR inlet and outlet water networks, Bayat, Klaten, Central Java, Indonesia. The RJR is surrounded by limestone hills and obtains its water source from rainwater and partly from the Ujung River (Kali Ujung), located to the west of RJR (Arumsari, 2019). Sampling was carried out in May 2021. Six sampling stations with three replications in the inlet and outlet water networks were selected based on the assumption of the level of plastic pollution visually and fishing activities around the waters of RJR (Figure 1). Sampling in the river flow that enters the reservoir (inlet) will determine the concentration of MPs in the flow and its possible contribution to MP pollution in the RJR reservoir. In addition, sampling at the outlet station is to determine whether there is microplastic contamination in the reservoir area which can lead to the spread of microplastics outside the reservoir. The selection of sampling points was based on the condition of the level of plastic pollution visually in the RJR inlet and outlet locations.

Station inlet 1 (I1) was the main inlet that Kali Ujung passes and was near the fishing line (7°45’15.9”S 110°37’10.3”E). Station inlet 2 (I2) was an inlet where fishing activities were carried out, and near a floating shop, this inlet received water from underground and was the most polluted location from initial observations (7°44’52.8”S 110°37’32.2”E). Station inlet 1 Kali Ujung (I1 KU) was a river flow, which was a water source for reservoirs located in densely populated areas (7°45’06.4”S 110°36’43.5”E). Station outlet 1 (O1) was a basin outlet with water sourced from RJR and Kali Ujung; the water condition in O1 was relatively clean compared to other stations (7°45’46.1”S 110°37’28.5”E). Station outlet (O2) was an outlet that comes from reservoir water, and this outlet location was rarely a fishing location (7°45’34.4”S 110°38’08.9”E). Station outlet 1 Kali Sosrodiningrat (O1 KS) was an underground outlet sourced from outlet 1 and was located in a densely populated area (7°46’34.7”S 110°37’18.7”E).

2.2 Sample collection

Water samples from six sampling stations in the inlet and outlet network were collected at a depth of 0-20 cm from the water surface. Samples were collected with three replications on the right, middle, and left sides of the water body under the same conditions through the sampling method described by McNeish et al. (2018). Water was sampled into a 2 L bottle from each stations. Then, the bottle was immediately closed to avoid MP contamination from the air.

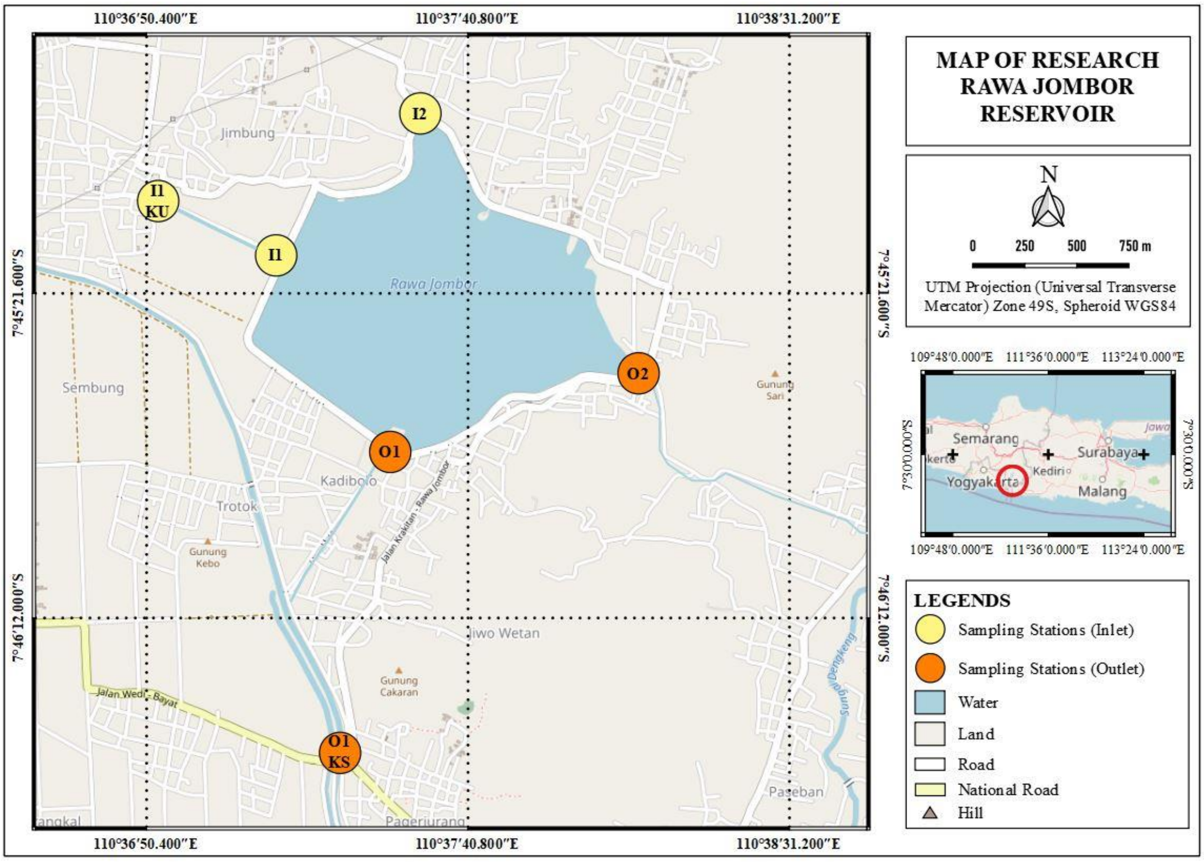

Figure 1. Location of sampling stations in the inlets and outlets of RJR

Sediment samples were taken from the surface water to a depth of 45 cm sediment layer using a 1 L Ekman dredge. In each site, three replications were randomly sampled using the grab sampling method described by Barrows et al. (2016). The filtered substrate was then dried, and density separation was carried out using NaCl to obtain MPs based on the MP particles flotation method (Wang et al., 2017).

Zooplankton samples were collected using a Wisconsin plankton net (200 µm) at a 0-20 cm water surface depth. Water containing zooplankton with a volume of 50 L was taken using a water sampler (10 L) and filtered using a plankton net for three replications at each station. The filter results were preserved with 1 mL of 4% formalin (Cole et al., 2013) and stored in a 10 mL vial.

Benthos samples were selected from the sediment sample collection at each sampling station. The benthos samples with a medium size (>5 mm) were then stored in an icebox in a labeled Ziploc container.

Fish were collected from fishermen around the stations. Several groups of fish commonly found by fishermen with a length of size include C. *batrachus* (21-31 cm), *O. marmorata* (17-26 cm), and *O. niloticus* (11-22 cm). Twenty-four fish were collected from all stations. The fish samples obtained were stored in an icebox. In the laboratory, all collected samples were stored in a freezer at -20ºC.

2.3 MPs extraction

MPs from the collected samples were extracted using the procedure according to the study of McNeish et al. (2018), Wang et al. (2017), and Hidalgo-Ruz et al. (2012), while for zooplankton samples we referred to the study of Amin et al. (2020).

The water sample was filtered using 0.45 µm filter paper (WhatmanTM, UK) to obtain MPs measuring less than 5 mm, referring to the recommendations of Sun et al. (2020). Filter papers containing MPs were stored in Petri dishes and labeled for further identification and characterization of MPs. The concentration of MPs in water samples was expressed in units of particles/L.

The sediment sample was dissolved in 2 L of concentrated NaCl (Merck, Germany), filtered through a 5 mm metal sieve, and left for 1 h to separate MPs based on density. The processed sample containing floating MPs was filtered using 0.45 µm filter paper. The papers were stored in Petri dishes for further identification of MPs. The concentrations of MPs were expressed in units of particles/kg wet weight (ww).

Zooplankton samples were identified using a light microscope to determine functional groups. In this study, copepods were found, then transferred to cavity blocks containing ten individuals each. Approximately 17-20 µL of 65% nitric acid (HNO_3) (Merck, Germany) was dripped into the cavity block (Desforges et al., 2015). The cavity block was then closed and heated at 80ºC for 30 min (Amin et al., 2020). The results of MP digestion were then counted and characterized by light microscopy (40-100X magnification). The concentrations of MPs in zooplankton were expressed in units of particles/10 individuals.

Benthos samples were measured in length and weight. In this study, *Pila ampullacea* was found at each sampling station. The contents of the benthos shell were cleaned with tweezers and transferred to a Beaker glass. We added 10% KOH (Merck, Germany) until the sample was submerged. The samples were then oven-dried at 60ºC for 24 h to dissolve the organic compounds and filtered with 0.45 µm filter paper. The filter papers were stored in a labeled petri dish for further identification. The concentrations of MPs in benthos were expressed in units of particles/individuals.

Fish were dissected and separated into the gills, GIT, and muscles. Each organ was weighed with a semi-analytical balance. For the extraction, each organ was then put into a Beaker glass and 10% KOH was added until submerged. The fish samples were then dried in an oven at 60ºC for 24 h to dissolve the organic compounds. The filtration result was filtered with 0.45 µm filter paper. The filter paper was then stored in a labelled petri dish for further identification. The concentrations of MPs in fish samples were expressed in units of particles/individuals.

The control filter paper was also analyzed to observe microplastic contamination in the laboratory, according to the study of McNeish et al. (2018). Filter paper control was carried out by filtering distilled water with 0.45 µm filter paper. In addition, to anticipate contamination in the digestion and cleaning process, a 10% KOH concentration was carried out with 0.45 µm filter paper. The control filter paper was then dried using an oven at 60ºC for 24 h. Contamination in control samples was used to compare abundances and characteristics found in laboratory samples.

2.4 MPs identification and characterization

MPs were identified using a stereomicroscope (Nikon SMZ745, Japan) and Optilab (Advance V2, Miconos, Indonesia), then characterized based on size, shape, color, and polymer type in each sample. The visual classification of MPs referred to McNeish et al. (2018) and Yuan et al. (2019). The size of MPs was classified into small (<1.5 mm), medium (1.5-3.3 mm), and large (>3.3 mm). MPs were classified into fragments, fibers, films, foams, and pellets based on the shape. Based on the color, MPs were classified into colored, white, black, and transparent.

The polymer type was identified using Fourier-transform infrared spectroscopy (FT-IR) (Nicolet Avatar 360 IR, Thermo Scientific, USA) with the reflectance mode range set at 4,000-400 cm^{-1} with a sensitivity of 50 at a collection time of 16 seconds. FT-IR test samples were taken based on the color and shape characterization of the MPs. The results of the FT-IR spectra were compared with the database in Jung et al. (2018) to determine the type of MPs polymers. Especially for zooplankton samples, the FT-IR test could not be carried out since the sample size was too small. The type of polymer was determined based on estimation by interpreting the physical characteristics of the MPs.

MPs surfaces were identified using Scanning Electron Microscope Energy-Dispersive X-ray

Spectroscopy (SEM/EDX) (Hitachi SU 3500, Japan) on randomly selected water, substrate, and fish samples. For fish samples, as a confirmatory material for heavy metals on the surface of MPs in the muscle, they were imaged using EDX at 10 keV with an SE sensor.

2.5 Heavy metal analysis

Heavy metals (HMs) Pb, Cu, Cd, and Zn were analyzed in the water, sediment, fish muscle, and on the surface of MPs found in water, sediment, and fish muscle.

The water sample in a 1 L HDPE bottle was filtered to separate out debris. The concentrations of HMs in water were determined using Atomic Absorption Spectroscopy (AAS) (Agilent 200 240FS AA Series, USA) and expressed in units of mg/L (Asare et al., 2018).

Dried sediment samples were crushed using a pestle and mortar, then sieved using a multilevel sieve to obtain fine particles (Asare et al., 2018). Sediment samples of as much as 250 g were tested for heavy metal content. The concentrations of HMs in the sediment were determined using AAS and expressed in units of µg/g.

Preparation for detecting HMs in fish muscle referred to the study of Asare et al. (2018). A 0.2 g dry weight of fish muscle was ground with a pestle and mortar and put into a 50 mL Erlenmeyer (Pyrex-Japan). Then, a total of 5 mL of concentrated H_2SO_4 (Mallinckrodt, USA) and 10 mL of concentrated HNO_3 were added to the Erlenmeyer. The sample was then heated at 130ºC for 20 min on a hotplate in a fume hood. After being cooled at room temperature, the sample was filtered with 0.45 µm filter paper to a 50 mL volumetric flask, then distilled water was added until it reached the limit. The concentrations of HMs in fish muscles were determined using AAS and expressed in units of µg/g.

The MPs from the characterization were weighed using an analytical balance and rinsed with distilled water to remove impurities. The samples were transferred into a Beaker glass. The procedure of HMs testing on the surface of MPs referred to the study of Munier and Bendell (2018). A total of 10 mL 10% HNO_3 was added and left for 2 h at 30ºC for metal decay on the surface of the MPs. The sample was then filtered with 0.45 µm filter paper in a 25 mL volumetric flask and added with distilled water until the mark. The samples were then tested for HMs (Pb, Cu, Cd, and Zn) concentration using AAS with the respective HMs limits of 0.5, 0.1, 0.1, and 0.1 mg/L. The concentrations of HMs on the MPs surface were expressed in units of µg/g.

2.6 Health risk assessment

A human health risk assessment was carried out based on an estimated consumption of fish contaminated with MPs and HM pollution. The health risk assessment of EDI referred to the study of Barboza et al. (2020) and Cox et al. (2019). The EDI of MPs was calculated using the equation (1):

$$\text{EDI of MPs} = \text{MP particles}\left(\frac{\text{particles}}{\text{g}}\right) \times \text{consumption rate (g/d/individual)} \tag{1}$$

The EDI of HMs was calculated following the study by Salam et al. (2020) using the equation (2):

$$\text{EDI of HM} = \frac{\text{HM concentration (µg/g) x consumption rate (g/d)}}{\text{body weight (kg)}} \tag{2}$$

The body weight value for Indonesian adults was assumed to be about 61.4 kg (NCD-RisC, 2020). The consumption rate of Indonesian adults was assumed to be about 130 g/d/individual (Firmansyah et al., 2019). RfD was used to evaluate the results of metal EDI calculations in fish muscle (Salam et al., 2020). RfD was the reference dose of HM referring to DeForest et al. (2007) (4.0 µg/kg/d for Pb; 40 µg/kg/d for Cu; 0.5 µg/kg/d for Cd; and 300 µg/kg/d for Zn).

The non-cancer risk assessment was calculated based on the THQ, the ratio between the estimated contaminant and reference doses (US EPA, 2000). THQ was calculated using the equation (3):

$$\text{THQ} = \frac{\text{EF x ED x FIR x C}}{\text{RfD x WAB x TA}} \times 10^{-3} \tag{3}$$

The EF value was obtained from the frequency of exposure (156 d/year) based on an estimate of eating fish about three times a week. ED was the duration of exposure (70 years), equivalent to the mean lifetime. FIR was the rate of food absorption. Based on Firmansyah et al. (2019), the FIR of Indonesian adults was 130 g/d/person. C showed the metal concentration in fish muscle (µg/g wet weight). WAB represented the average body weight of Indonesians, about 61.4 kg (NCD-RisC, 2020), and TA was the average exposure time for non-carcinogens (365 d/year×ED). As a consideration, if the THQ value was greater than 1, it was considered harmful to the health of the person who consumes the fish (Khan et al., 2008).

TTHQ was calculated using the formula from Li et al. (2013) to determine if more than one HM can cause consumers to have several non-carcinogenic effects. TTHQ was calculated using equation (4):

$$\mathrm{TTHQ} = \mathrm{THQ_{Pb}} + \mathrm{THQ_{Cu}} + \mathrm{THQ_{Cd}} + \mathrm{THQ_{Zn}} \tag{4}$$

TR, referring to the study of Liu et al. (2013) was calculated to assess the likelihood of cancer being caused by a particular carcinogen during the exposure period. TR was calculated using the equation (5):

$$\mathrm{TR} = \frac{\mathrm{EF \times ED \times FIR \times C \times CSF}}{\mathrm{WAB \times TA}} \times 10^{-3} \tag{5}$$

The CSF value was an oral carcinogenic slope factor. The CSF value for Pb was 8. 8.5×10^{-3} $(\mu g/kg/d)^{-1}$ and for Cd was 6.3 $(\mu g/kg/d)^{-1}$ (US EPA, 2015). The cumulative TR value was also calculated based on the total individual trace metal risk using the equation (6):

$$\sum \mathrm{TR} = \mathrm{TR_{Pb}} + \mathrm{TR_{Cu}} + \mathrm{TR_{Cd}} + \mathrm{TR_{Zn}} \tag{6}$$

2.7 Statistical analysis

Statistical analysis was conducted using one-way ANOVA to compare the significance of MPs concentrations in water, sediment, and aquatic fauna samples between stations. Tukey-HSD was performed for post-hoc analysis to determine the significance of each station. Principal Component Analysis (PCA) was performed to evaluate the relationship between MPs concentrations, sampling stations, and aquatic fauna.

3. RESULTS AND DISCUSSION

3.1 MPs in water and sediment

MP particles have contaminated water and sediment at all sampling stations, dominated by small (<1.5 mm) and medium (1.5-3.3 mm) sizes (Figure 2(a-b)). MP concentrations in surface water and sediment were significantly different at each station ($p<0.05$). Similar results have been reported in several studies, with MPs found predominantly less than 3 mm in size on the Brisbane River in Australia (He et al., 2020) and along the Han River in South Korea (Park et al., 2019). This finding proved that there is a process of plastic fragmentation and degradation into secondary MP particles. Plastic is decomposed into small particles due to the degradation process and chemical weathering by H_2O and CO_2 (Andrady, 2017).

The MPs observed in water were highest at station I2, about 20 particles/L (Figure 2(a)). The station was the most polluted site, a fishing spot near the floating restaurants and tourism. Fishing activities around the station may increase the concentrations of plastic waste from fishing tools (Stolte et al., 2015) and exacerbate poor plastic waste management (Yuan et al., 2019). The result was similar to the MPs found in the River Rhine, which generally detected 1-10 MP particles/L, but in the Rhine-Rhur metropolitan area, which is the most polluted area, the number of MPs exceeded 25 particles/L (Mani et al., 2015).

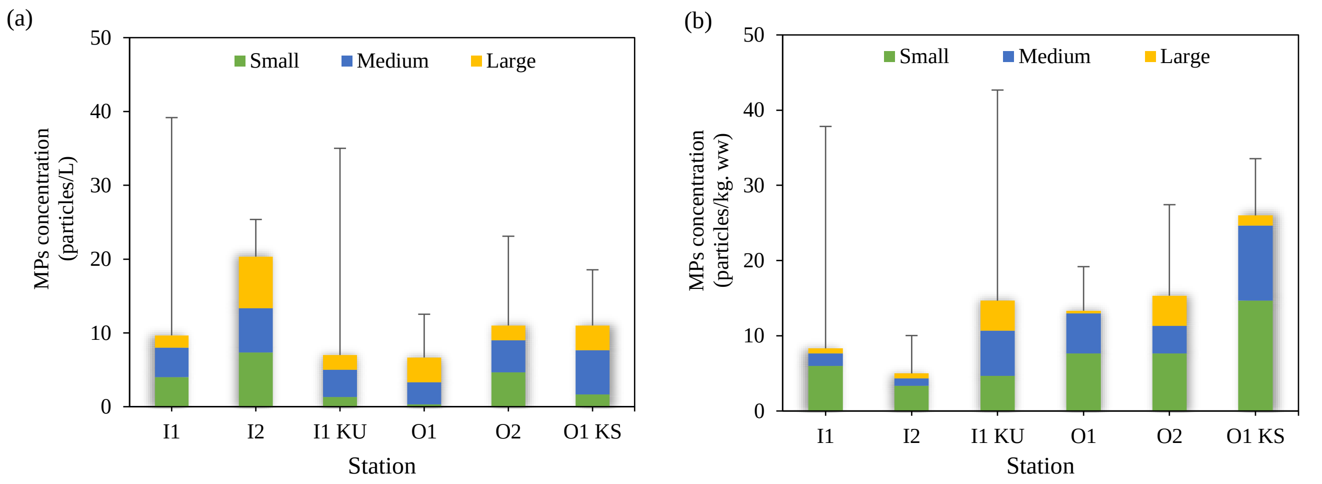

Figure 2. MP concentrations in water (a) and sediment (b) at each station. Different letters indicate significant differenced between sites at $p<0.05$.

In comparing MPs in water at the inlet and outlet area of RJR, this study showed the concentration at the inlet being lower (2.4 particles/L) than that of the outlet (4.5 particles/L), indicating microplastic pollution in the RJR. The result was also consistent with Ziajahromi et al. (2020), who reported 0.9 and 4.0 particles/L at the inlet and outlet of stormwater floating wetlands.

The concentration of MPs in water showed differentiated patterns and variables among the stations. Many factors in the water networks, such as currents, water turbulence, season, and weather, caused variations of MP concentrations in the streamflow (Bellasi et al., 2020; Mani et al., 2015). The influence of these factors is not visible, since the interactions of MPs and hydrological dynamics are very complex.

The MPs in sediment were inversely proportional to the water, lowest at station I2 (Figure 2(b)). The sedimentary structure probably affected the concentration of MPs. Gravels dominated the sediment of station I2, so that the possibility of MPs being trapped is lower than O1 KS dominated by clay and silt. He et al. (2020) reported that the concentration of MPs correlated positively with the content of clay particles. The concentration of MPs in sediments can be affected by current velocity, making it difficult to sink into the sediments (Jiang et al., 2018). Several factors, such as the retention process of MPs in sediments and sedimentation rates for certain particles, also affect the concentration (Mani et al., 2015).

The MPs in the water and sediment indicated that stream ecosystems require great attention to MPs pollution due to the possibility of aquatic fauna ingesting MPs directly from their habitat (water or sediment) or indirectly through trophic transfer.

Identification of polymer types by FT-IR showed that polyethylene (PE) and polypropylene (PP) were common polymer types of MPs (Figure 3(a)). The proportion of polymer PP and PE in water was about 68% and 32%, in sediment 32% and 53%, respectively. The MP pollution of inlet and outlet networks Rawa Jombor Reservoir may result from local input of plastic materials, such as fishery materials and household waste as secondary MPs. PP and PE are the most common polymers in plastic products, such as single-use packaging (Bordós et al., 2019). It is known that the two polymers have a lower density than water, so they are more commonly found on the surface of the water (Amelia et al., 2021; Andrady, 2011). When PP and PE interact with additives and attach to biofilms from the environment, it can increase their density (Pinheiro et al., 2020). Therefore, PP and PE can sink and be found in the sediment; benthic organisms can ingest them (Chubarenko et al., 2016).

In water, the most dominant MP shapes were film (33%) and fiber (28%). In sediment, the film was the most common MP (49%). All of them were dominantly colored MPs (Figure 3(b)-(c)). Similar results were reported by Fan et al. (2019) that the types of film, fiber, and fragment were the most dominant in Pearl River, China. It shows that plastics are degraded and fragmented into smaller sizes with different shapes based on the sources. Furthermore, management and mitigation of MP pollution are essential to reduce MP contamination to aquatic fauna.

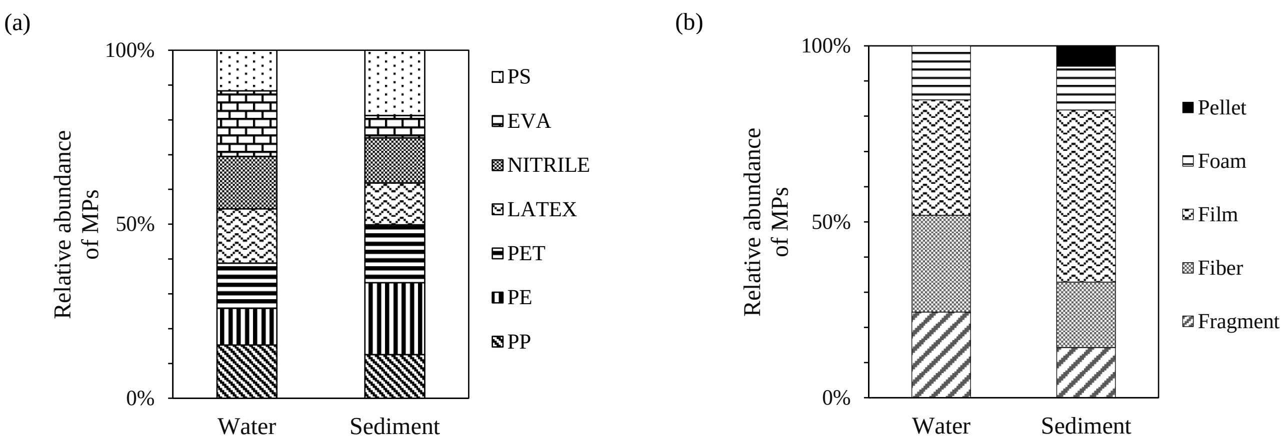

Figure 3. Relative abundance of polymer type (a), shape (b), and color (c) of MPs in water and sediment of Rawa Jombor Reservoir

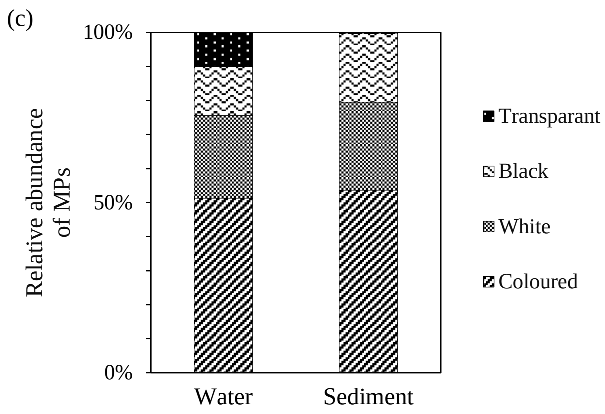

Figure 3. Relative abundance of polymer type (a), shape (b), and color (c) of MPs in water and sediment of Rawa Jombor Reservoir (cont.)

3.2 MPs in aquatic fauna

This study highlights the potential of MPs to be ingested by the food chain. Small MPs dominated the concentration of MPs in copepods (<1.5 mm), since the observed zooplankton sizes ranged from 0.5 to 2.0 mm. The ingestion of MPs is mainly due to the particle size of the MPs and the trophic position of the zooplankton in the water column (Desforges et al., 2015). MP concentration in zooplankton was highest at station I2 (Figure 4). These findings indicate that MPs in copepods tend to be associated with the concentration of MPs in water, the highest MPs in water being at station I2 (Figure 2(a)). In this study, MP concentration in copepods was not significantly different (NS) at each stations ($p<0.05$).

Several studies have reported that copepods are highly susceptible to MP exposure (Costa et al., 2020; Sun et al., 2018). However, studies of zooplankton in lotic waters are very limited. The concentration of MPs ingested by zooplankton was variable and inconsistent. It may be influenced by the region's abundance of MPs and zooplankton (Amin et al., 2020).

Similar to zooplankton, MPs were also found in benthic organisms, except in the O1 KS station. The most common benthic organism found was P. ampullacea. The MP concentrations in the benthos were more variable in size, with the medium MPs (1.5-3.3 mm) predominantly found (Figure 5). Benthic organisms compared to fish are more susceptible to ingesting MPs and have wide distribution, while current velocity can affect the ability of MPs to settle in sediment. Thus, it has been proposed to be used as a potential bioindicator of MP pollution (Li et al., 2020; Wang et al., 2019). The average MP concentration in benthos between stations was not significantly different (NS) at each station ($p<0.05$).

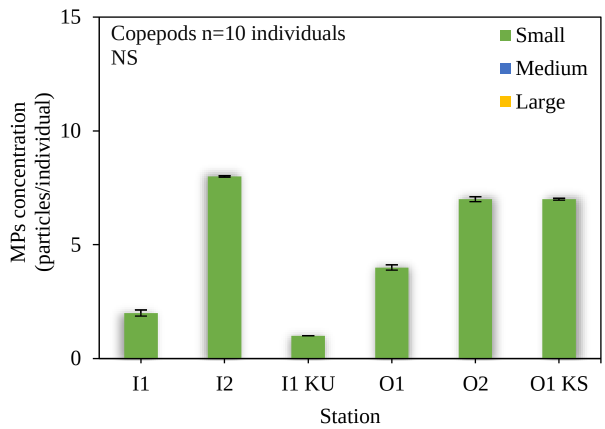

Figure 4. MP concentrations in Copepods at each station

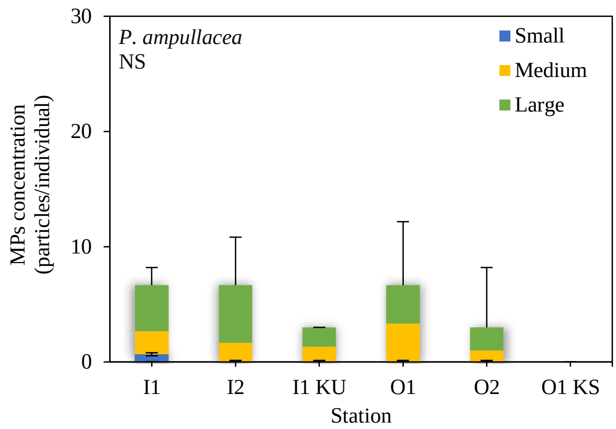

Figure 5. MP concentrations in *P. ampullacea* at each station

Zooplankton and benthos have an essential role in the food chain, affecting the accumulation of MPs at higher trophic levels. Zooplankton and benthos are susceptible to predation, so they can be the main route for transferring MPs from one trophic to another higher, such as fish.

MPs were found in the gills, GIT, and muscle of fish at each station, small MPs (<1.5 mm) being the most commonly found (Figure 6(a)-(c)). This finding was in line with the study of Park et al. (2019), who found MPs with a size of <0.6 mm were dominant in the gills of *C. batrachus* and other fish. In this present study, MPs were found mainly in the gills. It may be related to direct interaction between the gills and the surrounding environment, MPs being easily trapped in the gills. As a comparison, in the research of Park et al. (2019), who reported MPs in catfish and other species from the Han River, South Korea, MPs in the gills ranged from 1 to 16 particles/fish, and in GIT ranging from 4 to 48 particles/fish, while in muscle no MPs were found. Inversely, this study observed that MPs tended to be lower in GIT. In addition, the average of MP concentration in fish between stations was not significantly different (NS) at each station ($p<0.05$).

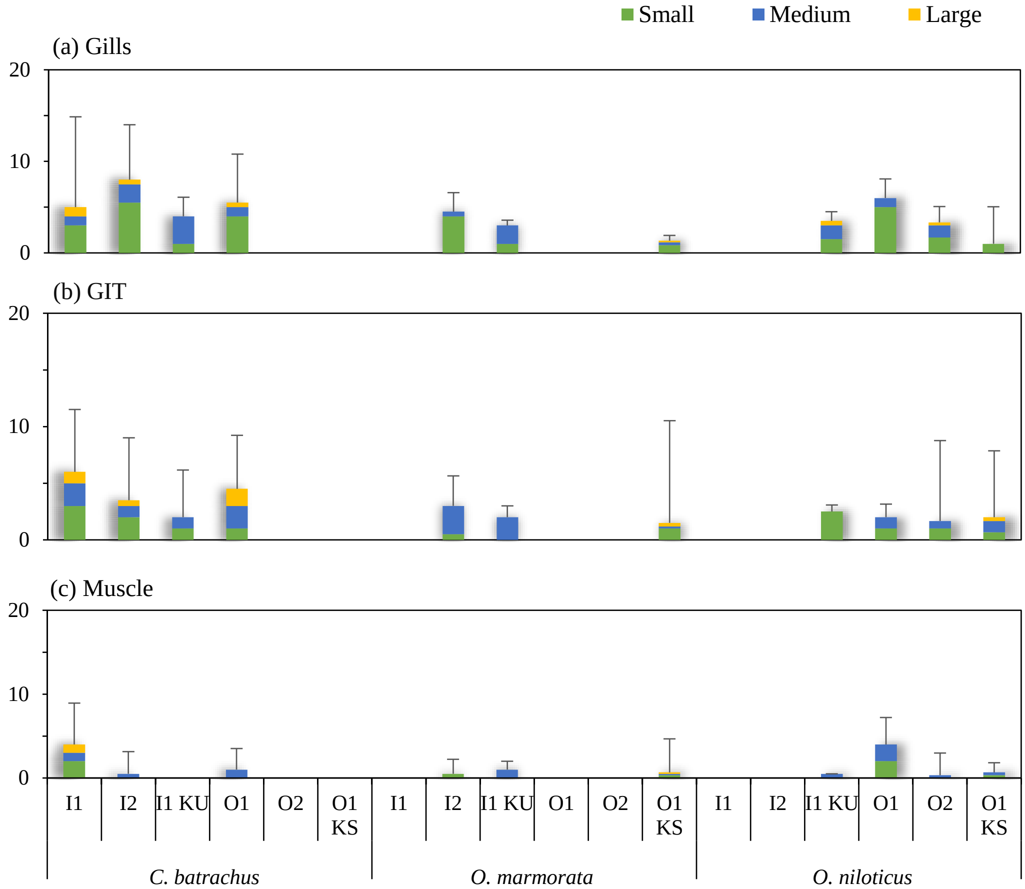

Figure 6. MP concentrations in fish gills (a), GIT (b), and muscle (c)

MPs in the gills resulted from retention during water filtration. It is also influenced by the size of the MP, morphology, and efficiency of the filtering apparatus (Barboza et al., 2020; Collard et al., 2017). MPs may have been ingested by fish directly from the water stream passively (e.g., gills) and actively (i.e., ingested by confusion with prey). The ingestion causes the accumulation of MP in fish organs (Barboza et al., 2020; Lusher et al., 2013). It is also possible that the fish ingested the plastic from the fishing tools used to catch the fish (Lusher et al., 2013). The buildup of MPs in the gills can cause fish to experience hypoxia and decreased respiratory efficiency, causing fish death in severe conditions (Barboza et al., 2020; Jabeen et al., 2018). The difference in the concentration of MPs was also influenced by several factors, such as several ecological characteristics (time spent in MP contaminated areas), physiological differences (e.g., water filtration rate and elimination process) in fish (Barboza et al., 2020), and eating habits (Baalkhuyur et al., 2018).

Some of the risks of plastic consumption depend on a variety of factors, including particle size, abundance, and plastic deposition in the environment (i.e., similarity to prey), as well as the mode of feeding and the anatomy of the consumer's feeding/digestive organs (Desforges et al., 2015; Kaposi et al., 2014).

Polymer PP and PE, which are floating plastic polymers, showed the highest abundance in zooplankton (Figure 7(a)). This is confirmed by the study of Frias et al. (2014), which also found PE and PP as major polymers used in the last decade. In contrast to zooplankton, the types in benthic organisms were nitrile and EVA. Hoellein et al. (2017) and Hurley et al. (2021) reported that nitrile and EVA polymer types were commonly abundant in benthic organisms. This study also revealed that the dominant polymer type of MPs in fish was nitrile and EVA (Figure 7(a)). This is confirmed by the study of Ferreira et al. (2020), EVA is one of the most common polymers in fish organs.

The majority of MPs ingested by zooplankton was fibers and fragments (Figure 7(b)). This result was consistent with other studies that showed fibers and fragments are the common MP types in zooplankton (Amin et al., 2020; Payton et al., 2020). In benthic organisms, a higher amount of MP was found in the film form, followed by fibers and fragments. As expected, the film was the common type of MP in sediment. Benthic organisms generally ingest MPs, especially fibers, fragments, and some pellets (Li et al., 2016; Lusher et al., 2013; Wang et al., 2019). In fish organs, the colored fiber was also the common type of MP (Figure 7(b)-(c)). In addition, color plays an important role since the colored MPs are more likely to be ingested by fish due to confusion with prey and the color of the MP (Barboza et al., 2020).

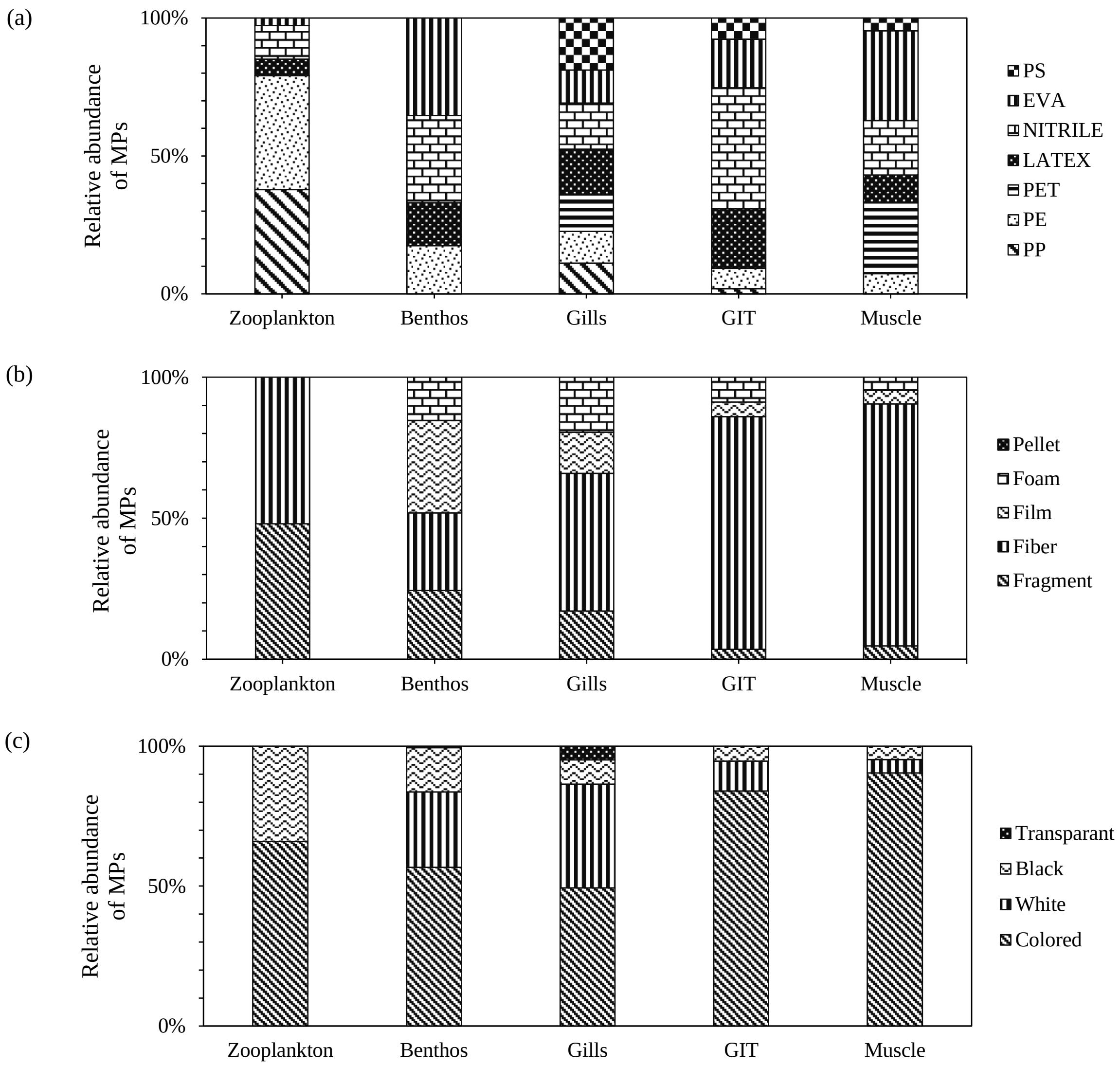

Figure 7. Relative abundance of polymer type (a), shape (b), and color (c) of MP in aquatic fauna of Rawa Jombor Reservoir

MPs found in aquatic fauna are similar to MPs found in water and sediments, with MPs being predominantly small and medium in size. This indicates that the smaller the MPs in the environment, the more likely they are to be ingested by aquatic fauna due to incorrect food preferences or inadvertently ingested by water currents (Barboza et al., 2020; Yuan et al., 2019). In addition, the accumulation of MPs can increase from one trophic to higher trophic levels as a potential for biomagnification and may affect human health risks due to additives adsorbed by MPs (Akhbarizadeh et al., 2019; Kumar et al., 2020).

SEM results showed that the surface of MPs tended to be rough, cracked, and had signs of deformation (Figure 8(a)-(c)). A rough surface can increase the surface area of the MPs and the possibility of metal residing on the plastic surface (Godoy et al., 2019; Wang et al., 2019). The degradation process from physical abrasion and hydraulic friction allows plastic particles to become smaller; this can also increase the potential for ingestion by aquatic fauna (Barboza et al., 2020). Thus, weathered MPs have toxicological effects on ingested aquatic organisms. These patterns of MP weathering were also found in the study conducted in the Pearl River, China (Yan et al., 2019) and in the Atoyac River basin, Mexico (Shruti et al., 2019).

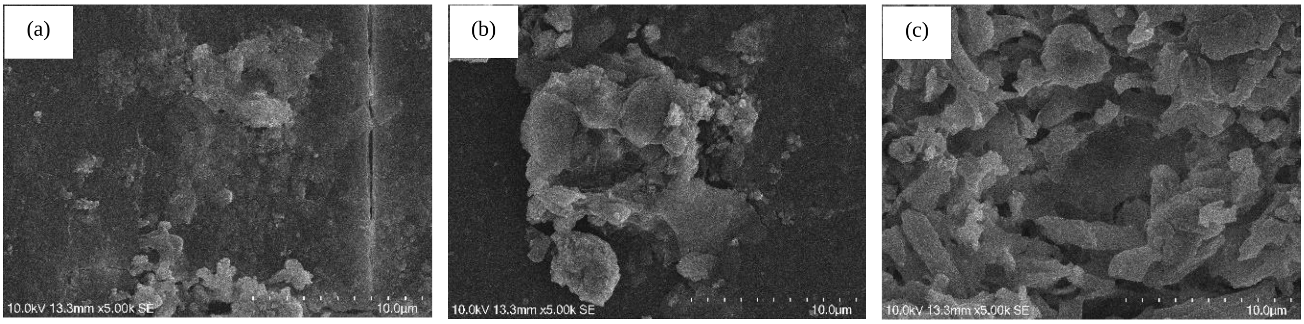

Figure 8. Mechanical weathering of surface MP in water (a), sediment (b), and fish muscle (c) from selected MPs

3.3 PCA Analysis

The analysis of PCA was conducted to identify correlations between the variables that contributed to explain the MPs concentration at each station. PCA results show that of the 13 active variables, there is a spatial distribution at the sampling stations in the four quadrants of the coordinate plane (Figure 9). The PCA biplot revealed an apparent clustering of MPs concentrations with PC1 and PC2, explaining >71.84% variation of the total variance. Station I2, with the condition of the water column being contaminated with MPs had a significant effect on the accumulation of MPs in zooplankton, benthos, and *C. batrachus* (gills). The highest MP contaminated sediment was found at the O1 KS station, and *O. niloticus* (GIT and muscle) accumulated many MPs. The MP concentration variable did not correlate with several stations such as the O1 and O2 station, which were quite clean from MP pollution.

3.4 MP interaction with heavy metal

HMs Pb, Cu, Cd, and Zn, were detected in water, sediment, fish muscle, and the surface of MPs of all samples. The concentration of heavy metals in the water and sediment among the stations varied (Table 1). This study explained that some heavy metals in water and sediment exceeded the permissible limits referring to the US EPA (2002) and WHO (2011).

The HMs were detected in fish muscle, with varying values (Table 2). According to the US EPA (2002) and WHO (2011), some exceeded the allowed limits. Accumulation of heavy metals in fish can vary due to fish size and mass, sex, and ability to bind heavy metals (Ozmen et al., 2008; Salam et al., 2020). Zn metal accumulation was detected higher than other metals. Zn metal was left in fish muscle since it binds to metallothionein proteins, which is an important component of fish muscle cells (Salam et al., 2020). In contrast, Cu was detected at very low levels. However, the long-term possibility is hazardous, such as Wilson disease and other disturbances of copper homeostasis (WHO, 2011).

Human activities are a significant contributor to heavy metal concentrations in the environment, such as agricultural and industrial residues carried into

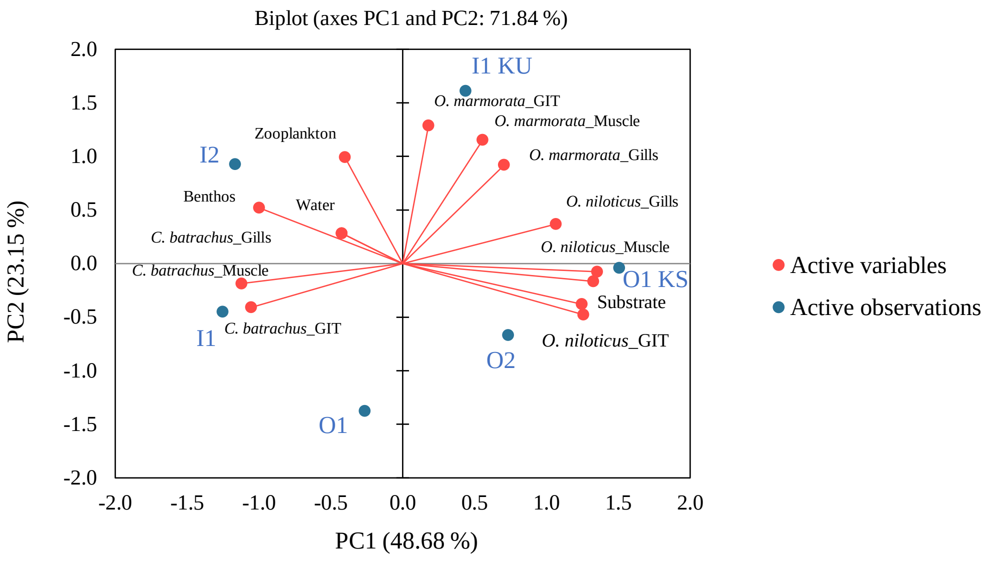

Figure 9. PCA biplot of MPs concentration

water bodies (Asare et al., 2018). Several findings reveal that persistent accumulation of heavy metals in the environment can harm aquatic fauna and possibly interact with MPs (Asare et al., 2018; Naqash et al., 2020). MPs can adsorb heavy metals in the environment. It is known that MPs have a high affinity for heavy metals Pb, Cu, Cd, and Zn, which can transfer to human tissues (Cox et al., 2019; Godoy et al., 2019). Brennecke et al. (2016) showed that MP polystyrene beads and PVC fragments could adsorb heavy metals Cu and Zn.

Additive translocation in MPs can occur along with food webs (Cole et al., 2016). In addition, exposure to MPs is harmful to aquatic organisms and humans in the long term and can cause chronic toxic effects when associated with toxic compounds (Cox et al. 2019; Godoy et al. 2019; Naqash et al. 2020). Unfortunately, the effects of MP consumption on human health are not known for sure, but these findings suggest that when MPs are in the GIT, they can release monomers and can absorb additives and toxins causing physiological damage (Cox et al., 2019; Naqash et al., 2020).

Table 1. Heavy metal concentration in water and sediment at each station

Heavy metal at each station	Heavy metal concentration			
	Water (μg/mL)	MP in Water (μg/g)×10^3	Sediment (μg/g)	MP in sediment (μg/g)×10^3
		Pb		
I1	0.14-0.14*	0.99-24.90	3.25-3.25	1.75-3.62
I2	0.18-0.18*	0.40-0.58	3.25-3.25	0.98-11.02
I1 KU	0.26-0.26*	0.70-14.50	3.25-3.25	0.35-0.64
O1	0.21-0.21*	0.86-6.59	53.38-53.38*	0.46-1.91
O2	0.28-0.28*	1.32-4.60	18.09-18.09	0.14-0.53
O1 KS	0.30-0.30*	0.76-17.20	3.25-3.25	0.18-0.44
		Cu		
I1	0.02-0.02	0.00-0.13	22.64-22.64	0.00-0.24
I2	0.05-0.05	0.00-0.67	26.87-26.87	0.00-0.51
I1 KU	0.05-0.05	0.00-1.13	5.31-5.31	0.00-0.03
O1	0.06-0.06	0.00-0.02	17.80-17.80	0.00-0.17
O2	0.06-0.06	0.00-0.02	13.57-13.57	0.00-0.09
O1 KS	0.06-0.06	0.00-0.14	5.47-5.47	0.00-0.05

*Indicating that the value exceeded the permissible limit by the WHO (2011) and US EPA (2002)

Table 1. Heavy metal concentration in water and sediment at each station (cont.)

Heavy metal at each station	Heavy metal concentration			
	Water (μg/mL)	MP in Water (μg/g)×10^3	Sediment (μg/g)	MP in sediment (μg/g)×10^3
		Cd		
I1	0.03-0.03*	0.00-0.54	0.85-0.85*	0.00-0.78
I2	0.09-0.09*	0.06-0.11	0.85-0.85*	0.00-0.00
I1 KU	0.09-0.09*	0.00-0.10	0.85-0.85*	0.00-0.08
O1	0.10-0.10*	0.00-0.19	0.85-0.85*	0.00-0.05
O2	0.09-0.09*	0.00-0.17	0.85-0.85*	0.00-0.01
O1 KS	0.10-0.10*	0.00-6.35	0.85-0.85*	0.02-0.16
		Zn		
I1	0.00-0.00	0.00-0.42	74.59-74.59	0.00-0.20
I2	0.03-0.03*	1.37-0.15	75.86-75.86	0.33-3.77
I1 KU	0.05-0.05*	0.18-1.28	28.02-28.02	0.07-0.32
O1	0.03-0.03*	0.17-0.58	24.72-24.72	0.21-1.10
O2	0.10-0.10*	0.08-1.22	51.77-51.77	0.12-0.90
O1 KS	0.04-0.04*	0.14-8.20	22.89-22.89	0.00-0.91

*Indicating that the value exceeded the permissible limit by the WHO (2011) and US EPA (2002)

Table 2. Heavy metal concentration in fish muscle and MPs ingested by fish

Heavy metal at each station	Species	Heavy metal concentration							
		Pb		Cu		Cd		Zn	
		Muscle (μg/g)	MP in Muscle (μg/g)×10^3	Muscle (μg/g)	MP in Muscle (μg/g)×10^3	Muscle (μg/g)	MP in Muscle (μg/g)×10^3	Muscle (μg/g)	MP in Muscle (μg/g)×10^3
I1	*C. batrachus*	-	11.95-11.95	0.43-0.43	1.66-1.66	0.02-0.02*	0.00-1.36	0.50-0.50*	0.86-0.86
	O. marmorata								
	O. niloticus								
I2	*C. batrachus*	0.06-0.24*	0-5.80	0-0.06	0-1.83	0-0.30*	0-1.03	0.30-0.37*	0-0.86
	O. marmorata	0-0.26*	0-138.25	-	-	0-1.03*	0-22.25	0.40-0.87*	-
	O. niloticus								
I1 KU	*C. batrachus*	-	-	-	-	-	-	0.24-0.24*	-
	O. marmorata	0.07-0.07*	145-145	-	23.75-23.75	-	23.5-23.5	0.36-0.36*	13.25-13.25
	O. niloticus	0.03-0.06*	0-130	0-0.007	0-23.5	0-0.002	0-28.75	0.26-0.35*	0-20.50
O1	*C. batrachus*	0.07-0.08*	0-56.6	-	0-15.25	0.01-0.13*	-	0.33-0.49*	0-0.70
	O. marmorata								
	O. niloticus	0.05-0.05*	30.38-30.38	-	-	0.14-0.14*	3.69-3.69	0.39-0.39*	0.062
O2	*C. batrachus*								
	O. marmorata								
	O. niloticus	0.05-0.24*	0-118.25	0.03-0.15	0-19	0.22-0.40*	-	0.28-0.77*	0-61.75
O1 KS	*C. batrachus*								
	O. marmorata	0.06-0.25*	0-118.75	0-0.35	-	0-0.35*	0-11.25	0.16-0.43*	0-14.75
	O. niloticus	0.04-0.09*	0-122.25	0-26.25	0-26.25	-	0-3.75	0.33-0.46*	0-166.25

*Indicating that the value exceeded the permissible limit of the WHO (2011) and US EPA (2002).

The SEM/EDX analysis confirmed the presence of heavy metals on the MP surface in fish muscle (Figure 10). These findings validated several studies that stated heavy metals can be adsorbed on the surface of MPs, in which the ability of MPs to increase the concentration of toxic compounds can reach 106 times higher through the adsorption process (Naqash et al., 2020; Wang et al., 2017; Turner and Holmes, 2015).

3.5 Health risk assessment

The health risk assessment was calculated based on the estimated daily intake (EDI) of accumulated heavy metals and MPs in each fish species in the inlet and outlet networks of the Rawa Jombor Reservoir (Table 3). The calculation of the value of MP accumulation in *O. niloticus* showed a higher EDI value than other species. This value was comparable with a previous study which showed that from 300 g of fish consumed, adults generally would consume an average of 2.29 MP particles/day (Barboza et al., 2020). This study also showed that regular consumption in the studied location would not result in health risks. The EDI value of heavy metal levels in each was more than the RfD value. Long-term accumulation of MPs in humans may cause a health hazard, but evidence is still limited.

All species of fish in this study were commercial fish commonly found and consumed by the residents. Therefore, the average trace concentration in fish was used for the calculation of THQ for residents. THQ and TTHQ values of heavy metals Pb, Cu, Cd, and Zn were lower than 1 for each fish species (Table 4). These results indicated that the health risks associated with metal exposure were not significant, and the types of fish at the inlet and outlet of the Rawa Jombor Reservoir were in the safe category for consumption.

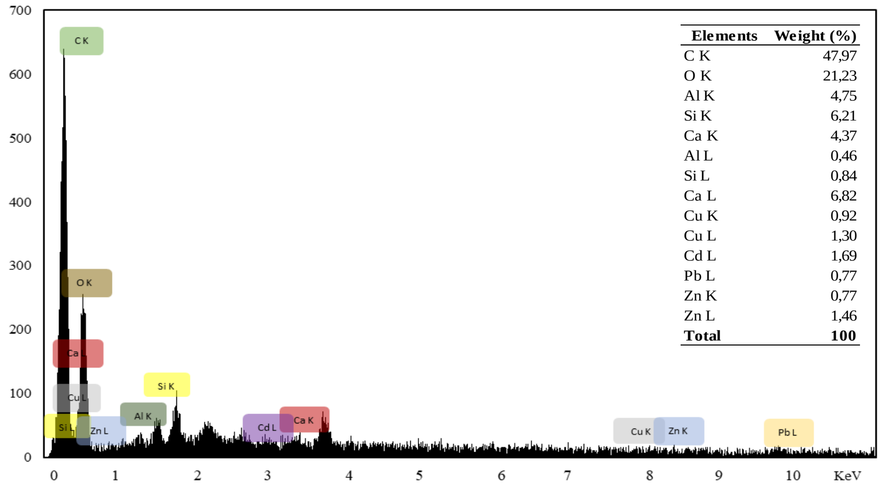

Figure 10. EDX spectra with the surface elemental composition of MPs

Table 3. Estimated daily intake of MPs and heavy metals due to consumption of fish from Rawa Jombor Reservoir

Species	EDI MPs (particles/day)	EDI HM in muscle (µg·kg/day)			
		Pb	Cu	Cd	Zn
C. batrachus	0.95	0.16	0.21	0.16	0.79
O. marmorata	0.79	0.24	0.21	0.14	0.83
O. niloticus	2.14	0.17	0.05	0.24	0.86

Table 4. Target hazard quotient, total target hazard quotient, and target cancer risk of heavy metals due to consumption of fish from Rawa Jombor Reservoir

Species	THQ ($\times10^{-3}$)				TTHQ ($\times10^{-3}$)	TCR (L/kg)	∑TR (L/kg)
	Pb	Cu	Cd	Zn		Cd	
C. bartrachus	0.00	0.18	0.02	0.00	0.20	0.0004	0.0004
O. marmorata	0.00	0.18	0.02	0.00	0.20	0.0004	0.0004
O. niloticus	0.00	0.05	0.03	0.00	0.07	0.0007	0.0007

4. CONCLUSION

MP contamination was found to be at moderate levels in the inlet and outlet networks of the Rawa Jombor Reservoir. Variations in polymer, shape, and color of MPs indicated that water is an important source of secondary MPs that can enter and be distributed to reservoirs with PP and PE as the commonly found polymer types. The most polluted station, Inlet 2, showed high MP accumulation in the aquatic fauna. This finding indicates that the concentration of MPs in the environment is in line with the accumulation of MPs in aquatic fauna. This finding also indicates MPs in aquatic fauna increase through trophic transfer, indicating biomagnification. Furthermore, heavy metals were adsorbed on the surface of microplastics in high concentrations. The adsorption ability of MPs of heavy metals can endanger the health of the ecosystem. It can be dangerous if the accumulation of MPs occurs in trophic transfer and biomagnification. The condition of fish MP contamination in the inlet and outlet of the Rawa Jombor Reservoir was still safe for consumption, but long-term consumption may cause cancer with Cd as the main contributor. However, management and mitigation of MP pollution are important to reduce MP contamination.

ACKNOWLEDGEMENTS

This study was funded by Universitas Gadjah Mada, Final Project Recognition (RTA) program (grant number 3143/UN1.P.III/DIT-LIT/PT/2021). The authors would like to extend special thanks to Aldina Himmarila Muliawati, S.Si., Indradi Octodhiyanto, S.Si., Sufraha Islamia, S.Si., Raditia Nugraha, S.Si., and Rio Hanafi, S.Pd., for helping us during data collection in Rawa Jombor Reservoir.

REFERENCES

Akhbarizadeh R, Moore F, Keshavarzi B. Investigating microplastics bioaccumulation and biomagnification in seafood from the Persian Gulf: A threat to human health? Food Additives and Contaminants: Part A 2019;36(11):1696-708.

Alina AA, Soeprobowati TR, Muhammad F. Water quality of Swamp Jombor Klaten, Central Java based on phytoplankton community. Jurnal Biologi 2015;4(3):41-52. (in Indonesian)

Amelia TS, Khalik WM, Ong MC, Shao YT, Pan HJ, Bhubalan K. Marine microplastics as vectors of major ocean pollutants and its hazards to the marine ecosystem and humans. Progress in Earth and Planetary Science 2021;8(1):1-26.

Amin RM, Sohaimi ES, Anuar ST, Bachok Z. Microplastic ingestion by zooplankton in Terengganu coastal waters, Southern South China Sea. Marine Pollution Bulletin 2020;150:1-8.

Andrady AL. Microplastics in the marine environment. Marine Pollution Bulletin 2011;62(8):1596-605.

Andrady AL. The plastic in microplastics: A review. Marine Pollution Bulletin 2017;119(1):12-22.

Arumsari K. Diversity of Chironomidae Bentonic Larvae and Bacteria in Organic Matter Contaminated Sediments, Jombor Swamp, Central Java [dissertation]. Yogyakarta, Universitas Gadjah Mada; 2019. p. 22. (in Indonesian).

Asare ML, Cobbina SJ, Akpabey FJ, Duwiejuah AB, Abuntori ZN. Heavy metal concentration in water, sediment and fish species in the Bontanga Reservoir, Ghana. Toxicology and Environmental Health Sciences 2018;10(1):49-58.

Atmawati SN. Diversity of Chironomidae Bentonic Larvae and Bacteria in Organic Matter Contaminated Sediments, Jombor Swamp, Central Java [dissertation]. Yogyakarta, Universitas Negri Yogyakarta; 2012. p. 37-45. (in Indonesian).

Baalkhuyur FM, Dohaish EJAB, Elhalwagy MEA, Alikunhi NM, AlSuwailem AM, Røstad A, et al. Microplastic in the gastrointestinal tract of fishes along the Saudi Arabian Red Sea Coast. Marine Pollution Bulletin 2018;131:407-15.

Barboza LGA, Frias JPGL, Booth AM, Vieira LR, Masura J, Baker J, et al. Microplastics Pollution in the Marine Environment. London, United Kingdom: Academic Press (Elsevier); 2019.

Barboza LGA, Lopes C, Oliveira P, Bessa F, Otero V, Henriques B, et al. Microplastics in wild fish from North East Atlantic Ocean and its potential for causing neurotoxic effects, lipid oxidative damage, and human health risks associated with ingestion exposure. Science of the Total Environment 2020;717:1-14.

Barrows AP, Neumann CA, Berger ML, Shaw SD. Grab vs. neuston tow net: A microplastic sampling performance comparison and possible advances in the field. Analytical Methods. 2016;9(9):1446-53.

Bellasi A, Binda G, Pozzi A, Galafassi S, Volta P, Bettinetti R. Microplastic contamination in freshwater environments: A review, focusing on interactions with sediments and benthic organisms. Environments 2020;7(30):1-27.

Bordós G, Urbányi B, Micsinai A, Kriszt B, Palotai Z, Szabó I, et al. Identification of microplastics in fish ponds and natural freshwater environments of the Carpathian Basin, Europe. Chemosphere 2019;216:110-6.

Brennecke D, Duarte B, Paiva F, Caçador I, Canning-Clode J. Microplastics as vector for heavy metal contamination from the marine environment. Estuarine, Coastal and Shelf Science 2016;178:189-95.

Campanale C, Massarelli C, Savino I, Locaputo V, Uricchio VF. A detailed review study on potential effects of microplastics and additives of concern on human health. International Journal of Environmental Research and Public Health 2020;17(1212):1-26.

Chubarenko I, Bagaev A, Zobkov M, Esiukova E. On some physical and dynamical properties of microplastic particles in marine environment. Marine Pollution Bulletin 2016;108(1-2):105-12.

Cole M, Lindeque P, Fileman E, Halsband C, Goodhead R, Moger J, et al. Microplastic ingestion by zooplankton. Environmental Science and Technology 2013;47(12):6646-55.

Cole M, Lindeque PK, Fileman E, Clark J, Lewis C, Halsband C, et al. Microplastics alter the properties and sinking rates of zooplankton faecal pellets. Environmental Science and Technology 2016;50(6):3239-46.

Collard F, Gilbert B, Compère P, Eppe G, Das K, Jauniaux T, et al. Microplastics in livers of European anchovies *(Engraulis encrasicolus*, L.). Environmental Pollution 2017;229:1000-5.

Costa E, Piazza V, Lavorano S, Faimali M, Garaventa F, Gambardella C. Trophic transfer of microplastics from copepods to jellyfish in the marine environment. Frontiers in Environmental Science 2020;8:1-7.

Cox KD, Converton GA, Davies HL, Dower JF, Juanes F, Dudas SE. Human consumption of microplastic. Environmental Science and Technology 2019;53:7068-74.

DeForest DK, Brix KV, Adams WJ. Assessing metal bioaccumulation in aquatic environments: The inverse relationship between bioaccumulation factors, trophic transfer factors and exposure concentration. Aquatic Toxicology 2007;84(2):236-46.

Desforges JP, Galbraith M, Ross PS. Ingestion of microplastics by zooplankton in the Northeast Pacific Ocean. Archives of Environmental Contamination and Toxicology 2015; 69(3):320-30.

Eriksen M, Mason S, Wilson S, Box C, Zellers A, Edwards W, et al. Microplastic pollution in the surface waters of the Laurentian Great Lakes. Marine Pollution Bulletin 2013;77 (1-2):177-82.

Fan Y, Zheng K, Zhu Z, Chen G, Peng X. Distribution, sedimentary record, and persistence of microplastics in the Pearl River catchment, China. Environmental Pollution 2019;251:862-70.

Ferreira M, Thompson J, Paris A, Rohindra D, Rico C. Presence of microplastics in water, sediments and fish species in an urban coastal environment of Fiji, a Pacific small island developing state. Marine Pollution Bulletin 2020;153:1-9.

Firmansyah, Oktavilia S, Prayogi R, Abdulah R. Indonesian fish consumption: an analysis of dynamic panel regression model. Proceedings of the 4th International Conference on Tropical and Coastal Region Eco Development; 2018 Oct 30-31; Semarang: Indonesia; 2019.

Frias JPGL, Otero V, Sobral P. Evidence of microplastics in samples of zooplankton from Portuguese coastal waters. Marine Environmental Research 2014;95:89-95.

Godoy V, Blázquez G, Calero M, Quesada L, Martín-Lara MA. The potential of microplastics as carriers of metals. Environmental Pollution 2019;255:1-12.

He B, Goonetilleke A, Ayoko GA, Rintoul L. Abundance, distribution patterns, and identification of microplastics in Brisbane River sediments, Australia. Science of the Total Environment 2020;700:1-33.

Hidalgo-Ruz V, Gutow L, Thompson RC, Thiel M. Microplastics in the marine environment: A review of the methods used for identification and quantification. Environmental Science and Technology 2012;46(6):3060-75.

Hoellein TJ, McCormick AR, Hittie J, London MG, Scott JW, Kelly JJ. Longitudinal patterns of microplastic concentration and bacterial assemblages in surface and benthic habitats of an urban river. Freshwater Science 2017;36(3):491-507.

Hurley J, Hardege J, Valero KCW, Morley S. In situ microplastics ingestion by Antarctic marine benthic invertebrates. Proceedings of the 23rd EGU General Assembly Conference Abstracts; 2021 Apr 19-31; Online, Vienna, Austria; 2021.

Jabeen K, Li B, Chen Q, Su L, Wu C, Hollert H, et al. Effects of virgin microplastics on goldfish (*Carassius auratus*). Chemosphere 2018;213:323-32.

Jiang C, Yin L, Wen X, Du C, Wu L, Long Y, et al. Microplastics in sediment and surface water of west dongting lake and south dongting lake: Abundance, source and composition. International Journal of Environmental Research and Public Health 2018;15(10):1-15.

Julienne F, Delorme N, Lagarde F. From macroplastics to microplastics: Role of water in the fragmentation of polyethylene. Chemosphere 2019;236:1-8.

Jung MR, Horgen FD, Orski SV, Rodriguez V, Beers KL, Balazs GH, et al. Validation of ATR FT-IR to identify polymers of plastic marine debris, including those ingested by marine organisms. Marine Pollution Bulletin 2018;127:704-16.

Kaposi KL, Mos B, Kelaher BP, Dworjanyn SA. Ingestion of microplastic has limited impact on a marine larva. Environmental Science and Technology 2014;48(3):1638-45.

Khan S, Cao Q, Zheng YM, Huang YZ, Zhu YG. Health risks of heavy metals in contaminated soils and food crops irrigated with wastewater in Beijing, China. Environmental Pollution 2008;152:686-92.

Kumar S, Rajesh M, Rajesh KM, Suyani NK, Rasheeq AA, Pratiksha KS. Impact of microplastics on aquatic organisms and human health: A review. International Journal of Environmental Sciences and Natural Resources 2020;26(2):59-64.

Kusumaningtyas F. Content of Heavy Metal Cadmium (Cd) in Tilapia (*Oreochromis niloticus*), Water, and Sediment and Water Quality in Rowo Jombor, Klaten [dissertation]. Surakarta, Universitas Sebelas Maret; 2015. p. 13. (in Indonesian).

Li J, Qu X, Su L, Zhang W, Yang D, Kolandhasamy P, et al. Microplastics in mussels along the coastal waters of China. Environmental Pollution 2016;214:177-84.

Li J, Huang ZY, Hu Y, Yang H. Potential risk assessment of heavy metals by consuming shellfish collected from Xiamen, China. Environmental Science and Pollution Research 2013;20(5):2937-47.

Li W, Lo HS, Wong HM, Zhou M, Wong CY, Tam NF, et al. Heavy metals contamination of sedimentary microplastics in Hong Kong. Marine Pollution Bulletin 2020;153:1-7.

Liu X, Song Q, Tang Y, Li W, Xu J, Wu J, et al. Human health risk assessment of heavy metals in soilvegetable system: A multi-medium analysis. Science Total Environment 2013;463:530-40.

Lusher AL, Mchugh M, Thompson RC. Occurrence of microplastics in the gastrointestinal tract of pelagic and demersal fish from the English Channel. Marine Pollution Bulletin 2013;67(1-2):94-9.

Mani T, Hauk A, Walter U, Burkhardt-Holm P. Microplastics profile along the Rhine River. Scientific Reports 2015; 5(1):1-7.

McNeish R, Kim L, Barrett H, Mason S, Kelly J, Hoellein T. Microplasticc in riverine fish is connected to species traits. Scientific Reports 2018;8:1-12.

Munier B, Bendell LI. Macro and micro plastics sorb and desorb metals and act as a point source of trace metals to coastal ecosystems. PLoS ONE 2018;13(2):1-13.

Naqash N, Prakash S, Kapoor D, Singh R. Interaction of freshwater microplastics with biota and heavy metals: A review. Environmental Chemistry Letters 2020;18:1813-24.

NCD Risk Factor Collaboration (NCD-RisC). Height and body-mass index trajectories of school-aged children and adolescents from 1985 to 2019 in 200 countries and territories: A pooled analysis of 2181 population-based studies with 65 million participants. The Lancet 2020;396(10261):1511-24.

Ozmen M, Ayas Z, Güngördü A, Ekmekci GF, Yerli S. Ecotoxicological assessment of water pollution in Sariyar Dam Lake, Turkey. Ecotoxicology and Environmental Safety 2008;70(1):163-73.

Park TJ, Lee SH, Lee MS, Lee JK, Lee SH, Zoh KD. Occurrence of microplastics in the Han River and riverine fish in South Korea. Science of the Total Environment 2019;708:1-36.

Payton TG, Beckingham BA, Dustan P. Microplastic exposure to zooplankton at tidal fronts in Charleston Harbor, SC USA. Estuarine, Coastal and Shelf Science 2020;232:1-10.

Pinheiro LM, do Sul JA, Costa MF. Uptake and ingestion are the main pathways for microplastics to enter marine benthos: A review. Food Webs 2020;24:1-11.

Rina TR. Pollution of the Aquatic Environment and Management Strategy for Net Cage Cultivation and Floating Stalls in the Jombor Swamp, Klaten, Central Java [dissertation]. Yogyakarta, Universitas Gadjah Mada; 2020. p. 60-84. (in Indonesian).

Salam MA, Paul SC, Zain RAMM, Bhowmik S, Nath MR, Siddiqua SA, et al. Trace metals contamination potential and health risk assessment of commonly consumed fish of Perak River, Malaysia. PLoS ONE 2020;15(10):1-18.

Shruti VC, Jonathan MP, Rodriguez-Espinosa PF, Rodríguez-González F. Microplastics in freshwater sediments of Atoyac River Basin, Puebla City, Mexico. Science of the Total Environment 2019;654:154-63.

Stolte A, Forster S, Gerdts G, Schubert H. Microplastic concentrations in beach sediments along the German Baltic coast. Marine Pollution Bulletin 2015;99(1-2):216-29.

Sun X, Liang J, Zhu M, Zhao Y, Zhang B. Microplastics in seawater and zooplankton from the Yellow Sea. Environmental Pollution 2018;242:585-95.

Turner A, Holmes LA. Adsorption of trace metals by microplastic pellets in fresh water. Environmental Chemistry 2015; 12(5):600-10.

United States Environmental Protection Agency (US EPA). A Guidance Manual to Support the Assessment of Contaminated Sediments in Freshwater Ecosystems: Volume 3. Chicago, Illinois, USA: US EPA; 2002.

United States Environmental Protection Agency (US EPA). Integrated risk information system (IRIS) [Internet]. 2015 [cited 2021 Sep 19]. Available from: https://www.epa.gov/iris.

United States Environmental Protection Agency (US EPA). Guidance for Assessing Chemical Contaminant Data for Use in Fish Advisories, Volume 2: Risk Assessment and Fish Consumption Limits. 3rd ed. Washington, DC, USA: US EPA; 2000.

Wang J, Peng J, Tan Z, Gao Y, Zhan Z, Chen Q, et al. Microplastics in the surface sediments from the Beijiang River littoral zone: Composition, abundance, surface textures and interaction with heavy metals. Chemosphere 2017; 171:248-58.

Wang J, Wang M, Ru S, Liu X. High levels of microplastic pollution in the sediments and benthic organisms of the South Yellow Sea, China. Science of the Total Environment 2019;651:1661-9.

World Health Organization (WHO). Guidelines for Drinking-Water Quality. Geneva, Switzerland: WHO Press; 2011.

Yan M, Nie H, Xu K, He Y, Hu Y, Huang Y, et al. Microplastic abundance, distribution and composition in the Pearl River along Guangzhou city and Pearl River estuary, China. Chemosphere 2019;217:879-86.

Yuan W, Liu X, Wang W, Di M, Wang J. Microplastic abundance, distribution and composition in water, sediments, and wild fish from Poyang Lake, China. Ecotoxicology and Environmental Safety 2019;170:180-7.

Ziajahromi S, Drapper D, Hornbuckle A, Rintoul L, Leusch FD. Microplastic pollution in a stormwater floating treatment wetland: Detection of tyre particles in sediment. Science of the Total Environment 2020;713:1-8.

Phosphorus Fractions and Arbuscular Mycorrhizal Fungi Communities in a Tropical Coarse-Textured Soil under Natural Forest and Para Rubber Ecosystems

Apinya Saentho[1], Worachart Wisawapipat[2], Weravart Namanusart[3], Tanabhat-Sakorn Sukitprapanon[1], and Phrueksa Lawongsa[1*]

[1]*Department of Soil Science and Environment, Faculty of Agriculture, Khon Kaen University, Khon Kaen 40002, Thailand*
[2]*Department of Soil Science, Faculty of Agriculture, Kasetsart University, Bangkok 10900, Thailand*
[3]*Rajamangala University of Technology Isan, Nakhon Ratchasima 30000, Thailand*

ARTICLE INFO

Received: 27 Sep 2021
Received in revised: 3 Dec 2021
Accepted: 12 Dec 2021
Published online: 26 Jan 2022
DOI: 10.32526/ennrj/20/202100188

Keywords:
AMF/ Phosphorus fractionation/ Rubber tree age/ Sequential extraction

*** Corresponding author:**
E-mail: phrula@kku.ac.th

ABSTRACT

Soil phosphorus (P) plays an essential role in rubber tree plantations that are rapidly and extensively being established in Southeast Asia. However, available information is quite limited on soil P fractions and arbuscular mycorrhizal fungi (AMF) in the tropical region. Herein, we investigated P fractions and AMF community under natural forest and rubber plantations at different ages of 5 years, 11 years, and 22 years in tropical coarse-textured soils from Thailand. The studied loamy sand soils were acidic (pH=5.0-5.7) with low available P concentrations (1.73-6.48 mg/kg). Data on the P fractions data revealed that the labile P (water-extractable P_i and $NaHCO_3$-extractable P_i) and moderately labile P ($NaOH_{0.1}$-extractable P_o and HCl-extractable P_i) pools in rubber-growing soils were higher than those in the natural forest soil. Elevated values of these properties were substantial with increasing stand ages. The rubber monocropping systems declined in the density and diversity of AMF spores compared to the natural forest site. *Glomus badium*, *Rhizophagus fasciculatus*, *Acaulospora Laevis*, and *Ambispora appendiculata* were the most dominant and tolerant AMF species across the rubber stands (>50% of the total species). The P fractions and AMF were correlated with soil labile-P forms. Soil labile and moderately P fractions were the important factors affecting the difference in AMF community. This study highlighted that long-term rubber plantations in tropical ecosystems promoted labile P fraction but demoted AMF density and diversity.

1. INTRODUCTION

Rubber tree plantations have been established more rapidly and extensively than any other tree crops in Southeast Asia, where over 85% of the world's rubber tree plantations are located (IRSG, 2021; WRS, 2021). Thailand has been ranked as the top natural rubber producer, with its expansion lasting for more than a century. In 2021, the rubber plantation area in Thailand covered over 22 million ha, representing the second-largest area of such plantations in the world (FAO, 2019; IRSG, 2021). The expansion of rubber plantations in Thailand formerly replaced natural forests; however, more recently, its expansion has substituted much existing agriculture or intensive annual cash crops such as sugarcane or cassava, because of native forest depletion and protection (Chambon et al., 2016). Studies have reported that monocropping rubber plantation exacerbated soil chemical fertility through acidification and caused a severe decline in P availability, presumably due to the abundant amounts of Fe/Al (hydr)oxides and clay-sized particles that accumulated with increasing rubber stand age (Fox et al., 2014).

Phosphorus (P) is the primary limiting essential plant nutrient for agricultural productivity in tropical regions (Cherubin et al., 2016; Maranguit et al., 2017; Wagg et al., 2014). Highly weathered acidic soils and abundant Fe/Al (hydr)oxides can retain and

Citation: Saentho A, Wisawapipat W, Namanusart W, Sukitprapanon T-S, Lawongsa P. Phosphorus fractions and arbuscular mycorrhizal fungi communities in a tropical coarse-textured soil under natural forest and para rubber ecosystems. Environ. Nat. Resour. J. 2022;20(2):209-220. (https://doi.org/10.32526/ennrj/20/202100188)

chemically fix P, leading to P restrictions in tropical agricultural production (Holford, 1997; Rausch and Bucher, 2002). Parent materials, organic matter decomposition and P fertilizer addition contribute available P to soils; however, different pathways of P resupply may cause different P pool sizes. The P replenishment from diverse P pools with differing solubilities becomes vital when available P is depleted (Henriquez, 2002; Maranguit et al., 2017). Many studies have indicated that the cycling of various P pools is influenced by plant-soil-microbial interactions, which are, in turn, dependent on agricultural practices, stand age, seasonal changes, ecosystem types, and environmental factors (Chen et al., 2008; Liu et al., 2018; Stutter et al., 2015). In addition to soil-based P nutrition, rubber trees could also retranslocate or redistribute a substantial portion of nutrients before senescence of plant parts which could reduce the dependency of rubber trees on soil nutrients (Li et al., 2016). Soil P exists in inorganic and organic forms, such as dissolved inorganic and organic P in aqueous solution or adsorbed P in solid minerals (Negassa and Leinweber, 2009). Inorganic P (P_i) typically includes primary mineral-P (such as apatite: $Ca_5(PO_4)_3(OH,F,Cl)$) and secondary crystalline and amorphous precipitates of Al/Fe (hydr)oxides and P absorbed onto silicate clay minerals (Costa et al., 2016). Organic P (P_o) is primarily associated with microbial biomass and recalcitrant compounds of soil organic matter, such as stabilized inositol phosphates and active orthophosphate diesters (Nash et al., 2014; Steidinger et al., 2015). Various P fractions with different levels of mobility and solubility can be assessed using sequential extractions, which provide information about labile and non-labile P fractions that can act as sources or sinks of available P to plants (Costa et al., 2016; Neufeldt et al., 2000). Non-labile P was the most dominant form of P fractions in tropical acid soils with less contribution from labile and moderately labile P fractions (Lustosa Filho et al., 2020).

Chemical fractions and bioavailability of soil P have been reported to substantially decrease with increasing stand age of rubber tree plantations in the temperate zone of China (Liu et al., 2018). Several microbial organisms can enhance soil P availability (Wagg et al., 2014). Arbuscular mycorrhizal fungi (AMF) are an essential group of soil microorganisms that play a vital role in soil fertility, plant nutrition, and changes in plant physiology and secondary metabolisms (Cervantes-Gámez et al., 2016; Schweiger and Müller, 2015). In addition, AMF can assimilate P from the pools often regarded as unavailable to plants (Cardoso et al., 2006; Liu et al., 2018; Moreira et al., 2013). Rubber monoculture plantations have been shown to harbor lower AMF spore diversity than natural rubber tree stands, possibly due to management practices in the plantations, such as pesticide utilization or extensive weeding (Feldmann et al., 2000). Some studies indicated that the cycling of various P fractions was influenced by plant-soil-microbial interactions and soil management and environmental-related factors (Chen et al., 2015; Stutter et al., 2015). However, information on the effects of rubber tree plantation age on soil P fractionations and AMF diversity remains poorly understood.

The main objectives of this study were to (i) investigate the P fractions and AMF diversity in different ages of rubber plantations from young rubber (5 years old: YR), mature rubber (11 years old: MR), and old rubber (22 years old: OR) compared to a natural forest (FR) and (ii) examine the relationship of the P fractions with AMF diversity in the soils. The result of this study should improve the understanding of soil P forms and the diversity of AMF communities in tropical soil under different ages of rubber tree plantations.

2. METHODOLOGY

2.1 Study sites

The study was carried out in a rubber tree plantation (*Hevea brasiliensis*) compared to the natural forest in the Don Chang Sub-district, Mueang District, Khon Kaen Province, Northeast Thailand (16°21′N, 102°45′E; Figure 1). This area has a tropical savanna environment. Temperature and precipitation data have been monitored for several years in the Khon Kaen Province. Based on the records, the temperature varied between 18 and 35°C throughout the year, with a mean annual temperature of 30°C and average daily low and high temperatures of 22 and 34°C, respectively. The mean annual precipitation was 1,250 mm (Thai Meteorological Department, 2018). The studied sites were covered by natural deciduous dipterocarp forest (FR), young rubber plantation (YR), mature rubber plantation (MR) and old rubber plantation (OR). The rubber sites had been used for cassava monocropping before being converted to rubber ecosystems. The rubber plantations had been tilled between the tree lines (7 m) twice a year at the beginning and the end of the rainy season during the first 5 years of the rubber tree growth. There was no additional control of the undergrowth in rubber plantations after the initial 5 years period. Chemical fertilizer (N:P:K, 20:10:17) and manure had been applied mostly in July during the first 5 years, depending on materials and availability. On average, these farmers used chemical fertilizer at the rates of 44 kg/ha/year for YR plantations, respectively. The fertilizers were applied at a distance of 0.5 m around the tree base. Local grass could be observed in the FR and YR sites, whereas there were no under growths in the MR and OR sites. Some shrubs could also be found in the FR site. The studied soils were Ban Phai (Bpi) series (Marlairotsiri et al., 2004), which was classified as Lixisols or Alfisols based on World Reference Base for Soil Resources or USDA Soil Taxonomy.

Figure 1. Location of four study sites in Don Chang, Khon Kaen District, Thailand

2.2 Soil sampling

Soil samples were collected from three representative blocks on each of the rubber stand sites of each of the three stand ages and in the natural forest in dry season (June 2018). This sampling period was undertaken before the annual fertilization period in July. The experimental design was Randomized Complete Block Design. For each block on each the rubber sites, three soil samples were taken and composited: three at mid-distances between the 7 m inter-rows. For the natural forest site, three samples were collected and composited from the plot diagonal. About 2 kg of the composite sample were obtained from each site. The samples were obtained at the topsoil from 0-15 cm depth, which was expected to have high microbial activity. Each sample replicate was passed through a 2 mm diameter mesh. The soil was divided into two parts. One part was used for the analysis of physicochemical properties and the other for microbial community analysis. A sub-sample was preserved on ice during the sampling procedure and stored at -4°C before microbial analyses. In addition, triplicates of soil cores were collected for bulk density analysis.

2.3 Physical and chemical properties analyses

Soil texture was examined using the pipette method (Gee and Bauder, 1986). Bulk density (BD) was calculated as the ratio of the dry mass of fine soil (<2 mm) to the soil core volume (Blake and Hartge, 1986). The pH was determined in distilled water using a soil-to-water ratio of 1:1. Total nitrogen (TN) was determined using the Kjeldahl method (Bremner, 1965). Organic matter content (OM) was determined using the Walkley and Black method (Walkley and Black, 1934). Available phosphorus (Avail. P) was extracted using the Bray-II method (Bray and Kurtz, 1945). Total phosphorus (TP) was determined using perchloric acid ($HClO_4$) digestion (Kuo, 1996). The available potassium (Avail. K), available magnesium (Avail. Mg), and available calcium (Avail. Ca) of soils 1 mol/L ammonium acetate at pH 7 were measured using atomic absorption spectroscopy (Chapman, 1965). Soil microbial biomass P (MBP) was analyzed the chloroform fumigation extraction method. In brief, aliquots of the fresh soil corresponding to 15 g dry weight equivalent were fumigated for 24 h using $CHCl_3$, and then the amount of inorganic P was extracted using 0.5 mol/L $NaHCO_3$ (pH 8.5). Nonfumigated soil was treated using the same method as the control. The microbial biomass P was calculated based on the difference in available P extracted with 0.5 mol/L $NaHCO_3$ between the fumigated and unfumigated soil divided by a correction factor of 0.4 (Brookes et al., 1982).

2.4 Phosphorus sequential fractions

Soil P fractions were determined using the sequential extraction scheme of Hedley et al. (1982) as modified (Zhang and Kovar, 2009; Liu et al., 2018). Details of the extraction procedures, including extracting solution, target pool, extraction conditions and solid-to-solution ratio, are summarized in Table 1. In each step, 30 mL of the extractant was added to 1 g of soil sample in a 50 mL centrifuge tube (1:30 soil-to-solution ratio), with the centrifuge tubes being shaken end-over-end for 16 h at 25°C. The soil extractions were centrifuged at 2,054 g (3,500 rpm) for 15 min and filtered through a Whatman No. 42 membrane to collect a clear solution for P analysis. The extracted P_i was measured using the molybdate colorimetric method at 882 nm (Tiessen and Moir, 1993). The total P in the extract was determined after digestion using H_2SO_4 and potassium persulfate in a heat block at 121°C (Hedley et al., 1982). The P_o was calculated as the difference between total P and P_i (Zhang and Kovar, 2009). The P_o in the water and HCl-extractable fractions was not excluded from the analysis because several studies have shown that the P concentrations in both extracts were below the method detection limit (Costa et al., 2016; Maranguit et al., 2017). Finally, soil residual P was digested using concentrated H_2SO_4 and 30% H_2O_2 extraction at 225°C for 30 min, with a step of digestion at 360°C for 1 h. To reflect ecological relevance, the P fractions were classified into three groups: labile P (water-P_i+$NaHCO_3$-P_i+$NaHCO_3$-P_o), moderately labile P ($NaOH_{0.1}$-P_i+$NaOH_{0.1}$-P_o+HCl-P_i) and non-labile P ($NaOH_{0.5}$-P_i+$NaOH_{0.5}$-P_o+residual-P_o), according to previous studies (Costa et al., 2016; Crews and Brookes, 2014; Hu et al., 2016; Liu et al., 2018).

Table 1. Summarized six-step sequential extraction of inorganic P and three-steps of organic P procedure and their hypothetical interpretation

P fraction	Extracting solution	Target pool	Extraction condition	SSR (g/mL)
F_i-1[a]	Deionized water	Labile P_i or mobile P	16 h	1:30
F_i-2	0.5 mol/L $NaHCO_3$ (pH 8.5)	Labile P_i and adsorbed onto soil surfaces	16 h	1:30
F_o-2[b]	0.5 mol/L $NaHCO_3$ (pH 8.5)/ $(NH_2)_2S_2O_8$+H_2SO_4	Labile P_o and adsorbed onto soil surfaces	16 h/ 0.5-1 h at 121°C	1:20
F_i-3	0.1 mol/L NaOH	Poorly crystalline Fe and Al (hydr)oxides bound P_i	16 h	1:30
F_o-3[b]	0.1 mol/L NaOH/ $(NH_2)_2S_2O_8$+H_2SO_4	Poorly crystalline Fe and Al (hydr)oxides bound P_o	16 h/ 0.5-1 h at 121°C	1:20
F_i-4	1 mol/L HCl	Insoluble Ca-P and apatite minerals	16 h	1:30
F_i-5[c]	0.5 mol/L NaOH	P_i strongly bound Fe and Al (hydr)oxides	16 h	1:30
F_o-5[b]	0.5 mol/L NaOH/ $(NH_2)_2S_2O_8$+H_2SO_4	P_o strongly bound Fe and Al (hydr)oxides	16 h/0.5-1 h at 121°C	1:20
F-6	(H_2SO_4)+30% (H_2O_2)	Residual fractions	0.5 h at 225°C 1 h at 360°C	1:20

SSR=solid-to-solution ratio; [a]Tiessen and Moir (1993); [b]Zhang and Kovar (2009); [c]Condron et al. (2005)

2.5 Arbuscular mycorrhiza fungi spore extraction and identification

Arbuscular mycorrhiza fungi (AMF) were extracted from 100 g of soil samples using modified wet sieving and the 50% sucrose centrifugation method (Daniels and Skipper, 1982). The retained spores after passing through a 45 µm sieve were collected using a micropipette under a microscope (Primo Star, ZEISS P95-T2,1,6X DSLR 415500-1825). Spore characterization was determined by mounting samples on glass slides in polyvinyl-lactoglycerol (PVLG). Spores were examined microscopically and identified to the species level whenever possible, based on morphological characters using descriptions provided from INVAM (International Culture Collection of (Vesicular) Arbuscular Mycorrhizal Fungi, Morgantown, WV, United States). Relative abundance (RA) was measured based on the following formula:

$$RA=\frac{\text{Spore numbers of a species (genus)}}{\text{Total number of identified spore sample}}\times 100$$

The equations for the Shannon diversity index (H) and Evenness (E) index were:

$$\text{Shannon diversity index (H)} = -\sum (n_i/N)\ \text{In}(n_i/N)$$

$$\text{Evenness index (E)} = \text{H/InS}$$

Where; n_i is the total number of spores of a species, N is the total number of identified spore samples, and S is the total number of identified species per sampling site (Zak et al., 1994).

2.6 Statistical analyses

Differences in the P fractions and in the soil properties between the different ages of rubber tree plantations and the natural forest were tested using analysis of variance and least significant difference (LSD) at p=0.05. The data showed that there was no statistical between each block, which indicated the area homogeneity. All statistical analyses were tested using the SAS statistical analysis software version 10.0.

Principal component analysis (PCA) was performed to identify associations of P fractions and soil properties with the relative abundance of AMF in the rubber tree and forest systems. Only variables with factor loadings lower than 0.70 were excluded from the PCA analysis to identify the importance of P fractions, soil properties and the AMF species (Krailertrattanachai et al., 2019).

3. RESULTS

3.1 Soil physical and chemical properties

Of the selected soil physical properties, the soil textures of FR, YR, MR, and OR were loamy sands and the bulk density increased with increasing stand age (Table 2). The lowest bulk density was in the YR site. The pH of the soils was strongly acidic to moderately acidic, with a significant difference among the sites. The concentrations of plant nutrients, (TP, Avail. P, and Avail. Mg) increased with increasing stand age from 5 years to 11 years to 22 years, respectively. The TP and Avail. P concentrations for the OR site were highest among the locations. The natural forest site had a higher levels of organic matter and Avail. Ca, Avail. K, and TN than the rubber tree plantation sites (Table 3).

Table 2. Physical properties of studied soils from natural forest (FR), young rubber plantation (YR), mature rubber plantation (MR), and old rubber plantation (OR)

Site	Sand (%)	Silt (%)	Clay (%)	Bulk density (g/cm^3)
FR	77^c±0.2	13^b±0.2	10^a±0.3	1.72^b±0.04
YR	81^b±0.8	10^c±0.4	9^a±0.4	1.66^c±0.02
MR	77^c±0.1	18^a±0.3	5^c±0.3	1.76^{ab}±0.04
OR	84^a±0.6	10^c±0.8	7^b±0.2	1.79^a±0.01
p-value	*	*	*	*
CV (%)	0.42	3.23	4.22	1.70

Values (mean±SD) with different lowercase superscripts in each column are significantly (p<0.05) different.
* indicates statistical different based on LSD (p<0.05)

Table 3. Chemical properties of studied soils from natural forest (FR), young rubber plantation (YR), mature rubber plantation (MR) and old rubber plantation (OR)

Site	pH	OM (g/kg)	TN (g/kg)	TP (mg/kg)	Avail. P (mg/kg)	Avail. K (mg/kg)	Avail. Mg (mg/kg)	Avail. Ca (mg/kg)
FR	5.0^{b}	7.93^{a}	0.35^{a}	138.21^{b}	2.96^{c}	74.6^{a}	35.6^{a}	139.2^{a}
	±0.1	±0.8	±0.1	±2.9	±0.7	±7.9	±9.4	±33.2
YR	5.3^{ab}	3.82^{b}	0.19^{b}	122.41^{c}	1.73^{d}	38.5^{c}	21.5^{ab}	50.9^{b}
	±0.1	±0.3	±0.0	±2.0	±0.2	±5.0	±2.3	±12.1
MR	5.4^{ab}	3.30^{b}	0.15^{b}	134.83^{b}	4.94^{b}	59.0^{b}	16.9^{b}	82.6^{b}
	±1.0	±0.6	±0.1	±1.0	±0.6	±3.7	±2.0	±15.6
OR	5.7^{a}	3.87^{b}	0.19^{b}	144.73^{a}	6.48^{a}	52.9^{bc}	32.5^{a}	68.2^{b}
	±0.2	±0.2	±0.0	±1.4	±0.7	±9.5	±10.8	±17.1
p-value	*	*	*	*	*	*	*	*
CV (%)	5.84	7.17	32.6	1.48	15.3	13.1	26.9	27.1

OM=organic matter; TN=Total nitrogen; TP=Total phosphorus; Avail. P=available phosphorus; Avail. K=available potassium; Avail. Mg=available magnesium; Avail. Ca=available calcium
Mean values (±SD) with different lowercase superscripts in each column are significantly different at $p<0.05$ (*).

3.2 Soil phosphorus fractions

The absolute and relative concentrations of P extracted in each sequential extraction step are presented in Figure 2 and Table S1. There were evident effects of rubber age on changes in both inorganic and organic P fractions. The labile P, moderately labile P, and non-labile P pools contributed 13%, 43%, and 44%, respectively, to total soil P for the natural forest, and 16-17%, 32-42%, and 42-52%, respectively for young rubber, mature rubber, and old rubber stands. Of the P fractions within the labile P pool, the water-extractable P_i fraction for the natural forest (1.5% of total soil P) was smaller than for the rubber plantations (1.8-2.4% of total soil P). The $NaHCO_3$-P_i fraction increased from 2.6% to 3.8% to 6.6% of total soil P for the respective rubber tree ages of 5 years, 11 years, and 22 years, respectively. However, the $NaHCO_3$-P_o fraction for the corresponding-aged rubber stands showed a decreasing trend from 12.4% to 10.7% to 6.6% of total soil P, respectively.

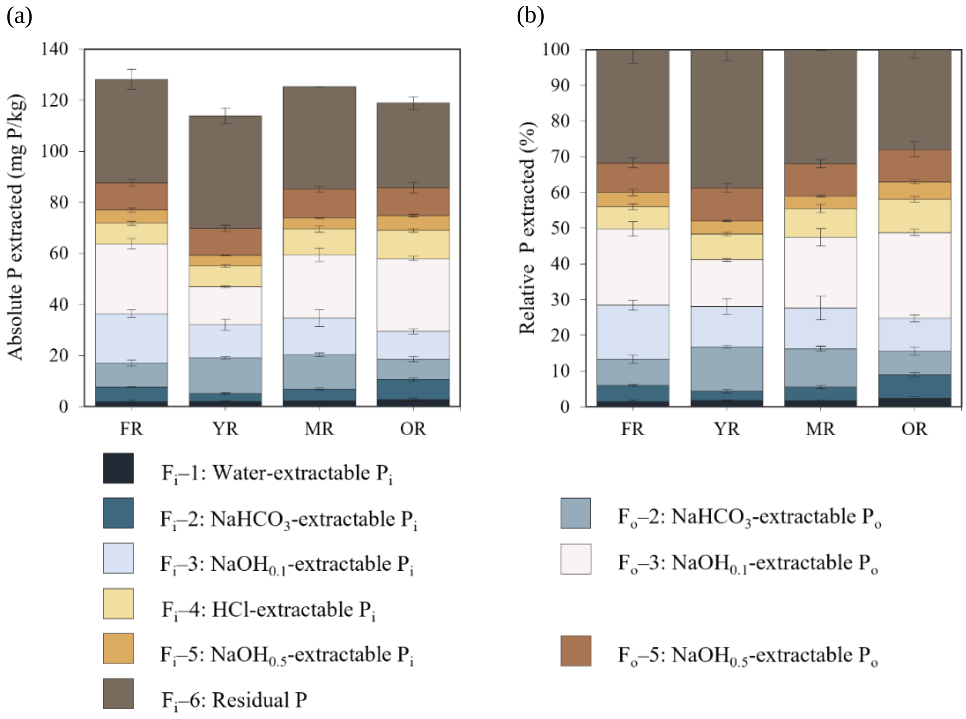

Figure 2. P fractionations in tropical sandy soils under natural forest (FR), young rubber (YR), mature rubber (MR), and old rubber (OR) plantations: (a) absolute P extracted; (b) relative P extracted, where data are means of triplicate with error bars denoting SD and statistical differences between fractions and sites are provided in Table S1.

For the moderately labile P pool, the $NaOH_{0.1}$-P_i fraction (9.2-11.4% of total soil P) was highest in the natural forest. The fractions of $NaOH_{0.1}$-P_o (13.1%, 19.8%, and 24.0% of total soil P) and of HCl-P_i (7.2%, 8.1%, and 9.3% of total soil P) for the stands aged 5 years, 11 years, and 22 years, respectively, increased with the rubber stand age. Both the $NaOH_{0.1}$-P_o and HCl-P_i pools in the natural forest were comparable to those in the rubber ecosystems (21.3% and 6.3% of total soil P, respectively) were comparable to those in the rubber ecosystems.

For the non-labile P pool, the $NaOH_{0.5}$-P_i fraction in the natural forest (4.0% and 3.6-4.8% of total soil P, respectively), was similar to those for the rubber plantations. The $NaOH_{0.5}$-P_o fraction in the natural forest and rubber ecosystems were also similar, corresponding to 8.3% and 9.1-9.3% of total soil P, respectively. However, the residual P pool in the young rubber, mature rubber, and old rubber stands declined with the plantation age to 38.7%, 31.9%, and 27.9% of total soil P, respectively, for ages 5 years, 11 years, and 22 years, while that in the natural forest (31.7%) was similar to the mature rubber.

The organic P pool calculated from the sum of the $NaHCO_3$-, $NaOH_{0.1}$-, and $NaOH_{0.5}$-P_o fractions varied between 35% and 40% of total soil P across the sites, suggesting that the inorganic P pools (60-65% of the total soil P) were the dominant P pool in both the natural forest and rubber plantations. There were no substantial differences between the inorganic and organic P observed for the forest and rubber tree plantations.

3.3 Soil microbial biomass phosphorus and abuscular mycorrhizal fungal spore distribution

The microbial biomass P (MBP) in the natural forest was similar to that for the young rubber and old. However, it was lower in mature rubber plantations (Figure 3(a)). Consequently, this parameter was affected by the rubber stand age.

The levels of AMF spores for the old rubber and natural forest sites ranged from 3.64 to 16.28 spores per g soil collected, respectively (Figure 3(b)). The highest level of spore abundance was recorded in the natural forest and the lowest was in the old rubber stand. In total, 10 species were detected based on morphological spore identification (Table 4), belonging to 2 genera of AMF, namely *Glomus* (64%) and *Acaulospora* (31%) that were the most abundant and were identified in all soils. Figure 4 shows the spores of some important AMF.

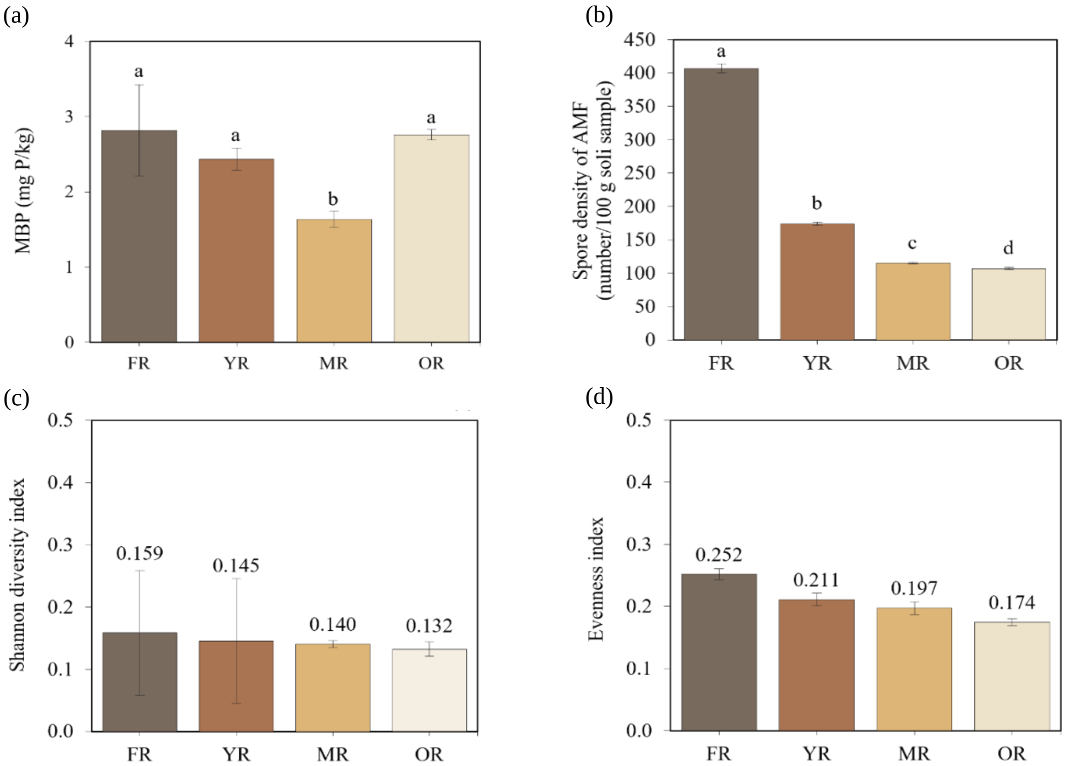

Figure 3. Microbial biomass P (a), AMF spore density (b), Shannon diversity index (c), and Evenness index (d) in natural forest (FR), young rubber (YR), mature rubber (MR), and old rubber (OR) plantations. The data were means of triplicate (±SD) and different lowercase letters indicate significant (p<0.05) difference.

Table 4. Relative abundance of arbuscular mycorrhizal fungi isolated from soil at study sites

Arbuscular mycorrhizal fungi (AMF)	Relative abundance (%)			
	FR	YR	MR	OR
Acaulospora scrobiculata	4.91	4.02	6.96	3.74
Ambispora appendiculata	7.62	2.30	0.87	0.93
Acaulospora laevis	12.78	11.49	6.96	9.35
Acaulospora mellea	3.19	5.17	5.22	4.67
Acaulospora sp.	5.65	5.75	13.91	10.28
Glomus badium	14.99	14.37	12.17	11.21
Rhizophagus fasciculatus	7.86	5.75	7.83	6.54
Claroideoglomus etunicatum	4.18	4.02	5.22	6.54
Rhizophagus manihotis	1.23	1.72	0.87	0.93
Funneliformis verruculosus	3.69	4.60	3.48	2.80
Rhizophagus intraradices	1.97	1.15	1.74	0.93
Glomus sp.	28.50	32.18	34.78	35.51
Unidentified species	3.44	7.47	0.00	6.54

FR=natural forest; YR=young rubber plantation; MR=mature rubber plantation; OR=old rubber plantation

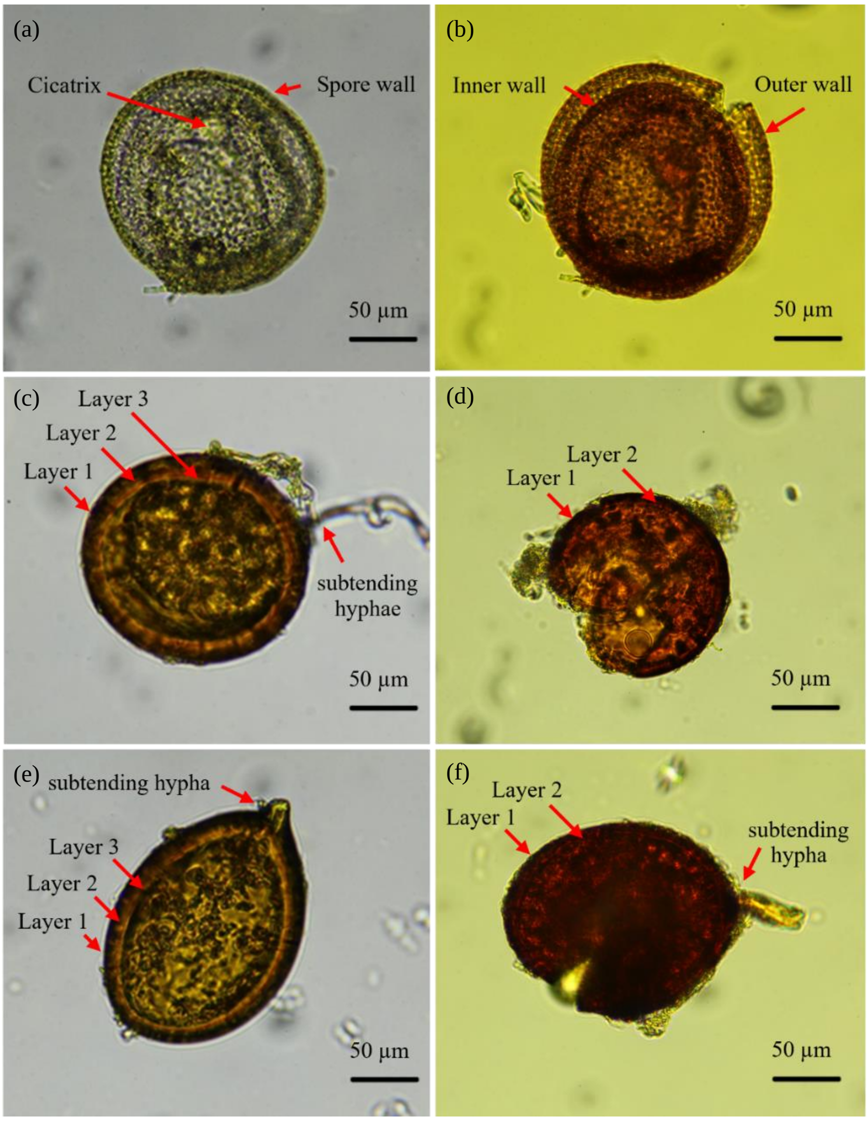

Figure 4. Some arbuscular mycorrhizal fungi spore morphotypes detected in topsoil in study pots for spore characterization in water (a, b, and e) and polyvinyl-lactoglycerol (b, c, and f) for: (a, b) *Acaulospora scrobiculata*; (c, d) *Glomus badium*; (e, f) *Rhizophagus fasciculatus*

3.4 Arbuscular mycorrhizal fungal diversity

The AMF diversity indices differed significantly between natural forest and rubber tree age. Therefore, the Shannon-Wiener diversity index and Evenness index were highest in the natural forest, but they were similar in all rubber plantations (Figure 3(c) and 3(d)). The AMF communities were dominated by *Glomus badium* (14.99-11.21% of total) at all sites, followed by *Acaulospora Laevis* (12.78-9.35% of total), as shown in Table 4.

3.5 Relationships between phosphorus fractions and abuscular mycorrhizal fungal species

PCA of the soils revealed that land-use types (rubber trees with differing stand ages and natural forests) affected soil AMF species, P fractions, and relevant soil properties. The first two axes in the PCA analysis contributed 90% of the variation in soil attributes and microbial communities, indicating substantial diversity in the nature of the studied soils (Figure 5, Figure S1). Four groups were recognized based on the positive and negative values of factor loadings: OM group 1 (OM, TN, F_i-3, *A. scrobiculata*, *A. appendiculata*, and *G. badium*), F-6 group 2 (F-6, F_o-2, *R. manihotis*, and *F. verruculosus* and pH group 3 (pH, F_i-1, F_i-4, Avail. P, F_o-5, *C. etunicatum*, *A. mellea*, *Glomus* sp., and *Acaulospora* sp.) with some in an outlier group 4 (TP, F_i-2, F_i-5, F_o-3, Avail. K, Avail. Ca, and Avail. Mg). The soil properties and AMF species in group 1 and group 2 separated the natural forest from the young rubber, whereas those in group 3 divided the mature and old rubber tree soils. High Avail. K and Avail. Mg contents were present in soils of the natural forest and the old rubber tree stand ecosystems.

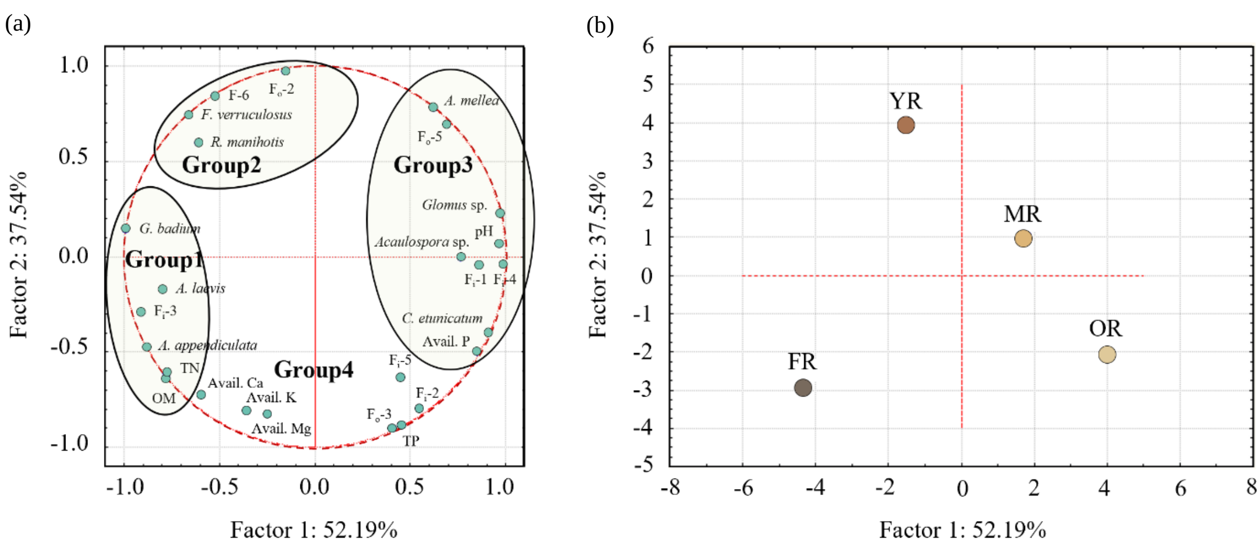

Figure 5. Principal component analysis of P fractions, soil properties, and arbuscular mycorrhizal fungal species in soils under natural forest (FR), young rubber (YR), mature rubber (MR), and old rubber (OR) plantations: (a) distribution of soil parameters (variables); (b) distribution of forest and rubber systems (cases), where only factor loadings with absolute values lower than 0.70 are included and Group abbreviations for P-fractions are provided in Table S1.

4. DISCUSSION

4.1 Changes in P fractions under natural forest and rubber ecosystems

Our data highlighted that rubber stand age had a profound impact on total P, the available P content, and the corresponding P fractionation (Table 1 and Figure 1). The P sequential extraction data also demonstrated the transformation of diverse P pools in the studied soils induced by rubber plantation management. The conversion from natural forest to young rubber plantations decreased the moderately labile P ($NaOH_{0.1}$-P_i and $NaOH_{0.1}$-P_o) and non-labile pools ($NaOH_{0.5}$-P_i) but increased the labile P pools (water-extractable P_i, and $NaHCO_3$-extractable P_o) and the soil pH. This information could reflect the transformation of the P pools associated with poorly crystalline Fe/Al (hydr)oxides ($NaOH_{0.1}$-P_i and P_o) and P associated with crystalline Fe/Al (hydr)oxides ($NaOH_{0.5}$-P_i) to the more labile P pool that is the most relevant for the readily available P fraction for plant utilization (Lustosa Filho et al., 2020). It was also possible that the elevation of the labile P pool could have been enhanced by inorganic P fertilizer freshly used as part of the management of the young rubber plantation (Neufeldt et al., 2000), whereas the effects of inorganic P fertilizers on the labile P were less pronouced as the P fertilization were stoped after about 8 years of the rubber plantation. Several studies have documented consistent data indicating the enhancement of water-extractable P and $NaHCO_3$-P_i fractions in different rubber plantation stands (Henriquez, 2002; Maranguit et al., 2017), attributable to inorganic P fertilizer use and subsequent accumulation of newly adsorbed P on soil constituents that could remain readily available for plant use. The depletion of moderately labile P_o ($NaOH_{0.1}$-P_o) in the young rubber plantation may have been due to the higher rate of organic matter decomposition and reduction of P input from litterfall. Conversely, the incremental increase of labile P_o ($NaHCO_3$-P_o) in the young rubber plantation could not be attributed to a decrease in the moderately labile P_o. In addition, soil microorganisms are an important source of soil organic phosphorus; thus, the decrease in organic phosphorus may have been related to the decrease in microbial biomass phosphorus.

With the increasing age of the rubber plantation stands from 5 years to 22 years, some clear trends were observed in the P fractionation transformation: i) an increase in the total P, Bray-II-extractable P, water-P_i, $NaHCO_3$-P_i, $NaOH_{0.1}$-P_o, and HCl-P_i and ii) a decrease in the $NaHCO_3$-P_o and residual P. The change in soil labile P have been due to the fertilizer quantity and the higher canopy cover in the mature rubber and old rubber plantation, causing a lower degree of leaching by drainage and possibly decreasing basic cation loss and soil acidification (Haynes and Swift, 1986). Progressive P fertilization could build up both the total P content and labile P pools (water-P_i, $NaHCO_3$-P_i) in the studied soils. Moreover, the alleviation of soil acidification in the mature rubber and old rubber could decrease P adsorption onto Fe and Al (hydr)oxides (Arai and Sparks, 2001), resulting in a higher level of labile P pools. These data were consistent with studies in temperate and tropical soils showing that soil acidification caused a rapid transformation of the labile P pool into moderately labile, occluded and recalcitrant P through precipitation of Fe/Al (hydr)oxides with the labile P (Costa et al., 2016; Yang and Post, 2011). Furthermore, the decreases in the residual P and the $NaHCO_3$-P_o fractions with increasing water-P_i and $NaHCO_3$-P_i suggested that these P pools could act as both a source and sink of bioavailable P, which could be manageable by modifying chemical conditions.

4.2 Soil microbial biomass under natural forest and rubber ecosystems

The soil microbial biomass phosphorus was significantly different between natural forest and rubber plantation. The soil MBP significantly decreased in the mature rubber plantations compared to the young and old rubber plantations and natural forest (Figure 3(a)). MBP was highly dependent on the quantity and quality of organic matter and on the plant litter content returned to the soil. Further detailed investigation is required of the functional groups in the organic matter. However, as the rubber trees grew, the soil MBP was significantly increased in the old rubber stand to reach a similar level to that in the natural forest because more carbon and other nutrients released by rhizodeposition from the larger roots of rubber trees would stimulate microbial growth and activity in soils (Moreira et al., 2013).

4.3 Arbuscular mycorrhizal fungal spore distribution under natural forest and rubber ecosystems

PCA showed that the conversion of natural forests to rubber plantations contributed to variations in the AMF diversity and the concentrations of the soil P fractions (Figure 5). The rubber tree plantation chronosequence affected the concentrations of available P and the inorganic and organic P. The AMF diversity was correlated with soil P forms (labile P, moderately labile P, and residue P) involved in P status in the rubber ecosystem. Furthermore, the increased concentrations of available P in the rubber tree plantation chronosequence were related to soil pH, *C. etunicatum*, *A. mellea*, *Glomus* sp., and *Acaulospora* sp. in the old rubber plantation. The results indicated that AMF diversity was likely to be altered by the rubber trees at different ages. In addition, the distribution of AMF species could have been driven by soil P in the natural forests and rubber plantations ecosystems. Rubber ecosystems declined in term of *G. badium* and *A. appendiculata* and were enhanced in *C. etunicatum* compared to the natural forest, which could have been due to the AMF could thriving under the native forest conditions compared to in the tree plantations. Overall, the old rubber stand had a negatively impact on AMF diversity the most. In addition, AMF revealed the colonization, communities and diversity of AMF associated with tree species having different functions to hosts and AMF species being slightly sensitive to fertilization are important influences on the distribution, diversity and regeneration of plant communities (van der Heijden et al., 1998; Bhadalung et al., 2005; Wang et al., 2019).

5. CONCLUSION

Our study showed that rubber plantation increased total P, available P, and available magnesium in tropical sandy soils. Furthermore, these soil properties were more substantially affected with increasing stand age. The P fractions data demonstrated that labile pools, P_o adsorbed to Fe/Al (hydr)oxides and P_i associated with Ca compounds were enhanced with increasing stand age, suggesting the possible transformation of these fractions from the residual P, P_i adsorbed to Fe/Al (hydr)oxides, and exchangeable P_o. The AMF diversity tended to decrease in rubber plantations compared to the natural forest. The diverse P fractions were variously associated with different AMF species. Based on the current study, natural forest conversion to rubber plantation could improve soil P availability but it could deteriorate AMF diversity. The data suggested that ecological-based management should also be undertaken to improve both P availability and microbial diversity for the sustainability of rubber plantation in tropical sandy soil environments.

ACKNOWLEDGMENTS

The authors are thankful to ERASMUS+ Participatory and Integrative Support for Agricultural Initiative (PISAI) (Project No. 586157-EPP-1-2017-1-TH-EPPKA2-CBHE-JP) for providing support. The Graduate School of KKU provided the first author with a M.S. scholarship (Grant No. 611JT101). Research and Graduate Studies, the Knowledge Development for Rubber Tree in Northeast (KDRN-KKU) Research Group and the Soil Organic Matter Management Research Group of Khon Kaen University (KKU) provided financial support.

CONFLICT OF INTEREST

The authors declare that there are no conflicts of interest.

REFERENCES

Arai Y, Sparks DL. ATR-FTIR Spectroscopic investigation on phosphate adsorption mechanisms at the ferrihydrite-water interface. Journal of Colloid and Interface Science 2001; 241:317-26.

Bhadalung NN, Suwanarit A, Dell B, Nopamornbodi O, Thamchaipenet A, Rungchuang J. Effects of long-term NP-fertilization on abundance and diversity of arbuscular mycorrhizal fungi under a maize cropping system. Plant and Soil 2005;270(1):371-82.

Blake GR, Hartge KH. Bulk density. In: Klute A, editor. Methods of Soil Analysis. Madison, WI, USA: American Society of Agronomy; 1986. p. 363-82.

Bray RH, Kurtz LT. Determination of total, organic, and available forms of phosphorus in soils. Soil Science 1945;59:39-46.

Bremner JM. Total nitrogen. In: Black CA, editor. Methods of Soil Analysis. Madison, WI, USA: American Society of Agronomy; 1965. p. 1049-178.

Brookes PC, Powlson DS, Jenkinson DS. Measurement of microbial biomass phosphorus in soil. Soil Biology and Biochemistry 1982;14:319-29.

Cardoso I, Boddington C, Janssen B, Oenema O, Kuyper T. Differential access to phosphorus pools of an oxisol by mycorrhizal and nonmycorrhizal maize. Communications in Soil Science and Plant Analysis 2006;37:1537-51.

Cervantes-Gámez R, Bueno-Ibarra MA, Cruz-Mendívil A, Calderón-Vázquez CL, Ramírez-Douriet CM, Maldonado-Mendoza IE, et al. Arbuscular mycorrhizal symbiosis-induced expression changes in *Solanum lycopersicum* leaves revealed by RNA-seq analysis. Plant Molecular Biology Reporter 2016;34:89-102.

Chambon B, Ruf F, Kongmanee C, Angthong S. Can the cocoa cycle model explain the continuous growth of the rubber (*Hevea brasiliensis*) sector for more than a century in Thailand? Journal of Rural Studies 2016;44,187-97.

Chapman HD. Cation-exchange capacity. In: Norman AG, editor. Methods of Soil Analysis. Madison, WI, USA: American Society of Agronomy; 1965. p. 891-901.

Chen CR, Condron LM, Xu ZH. Impacts of grassland afforestation with coniferous trees on soil phosphorus dynamics and associated microbial processes: A review. Forest Ecology and Management 2008;255:396-409.

Chen CR, Hou EQ, Condron LM, Bacon G, Esfandbod M, Olley J, et al. Soil phosphorus fractionation and nutrient dynamics along the Cooloola coastal dune chronosequence, Southern Queensland Australia. Geoderma 2015;(257-258):4-13.

Cherubin MR, Franco ALC, Cerri CEP, Karlen DL, Pavinato PS, Rodrigues M, et al. Phosphorus pools responses to land-use change for sugarcane expansion in weathered Brazilian soils. Geoderma 2016;265:27-38.

Condron LM, Turner BL, Cade-Menun BJ. Chemistry and dynamics of soil organic phosphorus. In: Sims JT, Sharpley AN, editors. Phosphorus: Agriculture and the Environment. Kimberly, ID, USA: American Society of Agronomy; 2005. p. 87-121.

Costa MG, Gama-Rodrigues AC, Gonçalves JL, de M Gama-Rodrigues EF, Sales MV, et al. Labile and non-labile fractions of phosphorus and its transformations in soil under eucalyptus plantations Brazil. Forests 2016;7:1-15.

Crews TE, Brookes PC. Changes in soil phosphorus forms through time in perennial versus annual agroecosystems. Agriculture, Ecosystems and Environment 2014;184:168-81.

Daniels BA, Skipper HA. Methods for the recovery and quantitative estimation of propagules from soil. In: Schenck, NC, editor. Methods and Principles of Mycorrhizal Research. St. Paul, MN, USA: American Phytopathological Society; 1982; p. 29-35.

Food and Agriculture Organization (FAO). FAOSTAT [Internet]. 2019 [cited 2020 Aug 1]. Available from: http:// www.fao.org /go/to/home/E.

Feldmann F, da Silva Jr JP, Idczak E, Lieberei R. AMF spore community composition at natural and agricultural sites in Central Amazonia-a long term study. Proceedings of German-Brazilian Workshop on Neotropical Ecosystems-Achievements and Prospects of Cooperative Research; 2000 Sep 3-8; Hamburg: Germany; 2000.

Fox J, Castella JC, Ziegler AD, Westley SB. Rubber plantations expand in mountainous Southeast Asia: What are the consequences for the environment? Asia Pacific Issues 2014; 114:1-8.

Gee GW, Bauder JW. Particle-size analysis. In: Klute A, editor. Methods of Soil Analysis. Madison, WI, USA: American Society of Agronomy; 1986. p. 383-411.

Haynes RJ, Swift RS. Effects of soil acidification and subsequent leaching on levels of extractable nutrients in a soil. Plant Soil 1986;95:327-36.

Hedley MJ, Stewart JWB, Chauhan BS. Changes in inorganic and organic soil phosphorus fractions induced by cultivation practices and by laboratory incubations. Soil Science Society of America Journal 1982;46:970-6.

Henriquez C. Assessing Soil Phosphorus Status Under Different Agronomic Land Use [dissertation]. Iowa State University; 2002.

Holford ICR. Soil phosphorus: Its measurement, and its uptake by plants. Australian Journal of Soil Research 1997;35:227-39.

Hu B, Yang B, Pang X, Bao W, Tian G. Responses of soil phosphorus fractions to gap size in a reforested spruce forest. Geoderma 2016;279:61-9.

International Rubber Study Group (IRSG). Rubber statistical bulletin, database [Internet]. 2021 [cited 2021 Aug 1]. Available from: https://www.rubberstudy.org/welcome.

Krailertrattanachai N, Ketrot D, Wisawapipat W. The distribution of trace metals in roadside agricultural soils Thailand. International Journal of Environmental Research and Public Health 2019;16(5):Article No. 714.

Kuo S. Phosphorus. In: Sparks DL, Page AL, Helmke PA, Loeppert RH, Soltanpour PN, Tabatabai MA, Johnston CT, Sumner ME, editors. Methods of Soil Analysis. Madison, Wisconsin, USA: Soil Science Society of America; 1996. p. 869-919.

Li Y, Lan G, Xia Y. Rubber trees demonstrate a clear retranslocation under seasonal drought and cold stresses. Frontiers in Plant Science 2016;7:Article No. 1907.

Liu C, Jin Y, Liu C, Tang J, Wang Q, Xu M. Phosphorous fractions in soils of rubber-based agroforestry systems: Influence of season, management and stand age. Science of the Total Environment 2018;(616-617):1576-88.

Lustosa Filho JF, de Silva Carneiro JS, Barbosa CF, de Lima KP, do Amaral Leite A, Melo LCA. Aging of biochar-based fertilizers in soil: Effects on phosphorus pools and availability to *Urochloa brizantha* grass. Science of the Total Environment 2020;709:Article No. 136028.

Maranguit D, Guillaume T, Kuzyakov Y. Land-use change affects phosphorus fractions in highly weathered tropical soils. Catena 2017;149:385-93.

Marlairotsiri K, Suchinai A, Hoontakul K. Characterization of Established Soil Series in the Northeast Region of Thailand Reclassified According to Soil Taxonomy 2003. Bangkok, Thailand: Land Development Department; 2004. p. 6-7.

Moreira A, Moraes LAC, Zaninetti RA, Canizella BT. Phosphorus dynamics in the conversion of a secondary forest into a rubber tree plantation in the amazon rainforest. Soil Science 2013; 178:618-25.

Nash DA, Friedman JW, Mathu-Muju KR, Robinson PG, Satur J, Moffat S, et al. A review of the global literature on dental therapists. Community Dentistry and Oral Epidemiology 2014;42:1-10.

Negassa W, Leinweber P. How does the Hedley sequential phosphorus fractionation reflect impacts of land use and management on soil phosphorus: A review. Journal of Plant Nutrition and Soil Science 2009;172:305-25.

Neufeldt H, da Silva JE, Ayarza MA, Zech W. Land-use effects on phosphorus fractions in Cerrado oxisols. Biology and Fertility of Soils 2000;31:30-7.

Rausch C, Bucher M. Molecular mechanisms of phosphate transport in plants. Planta 2002;216:23-37.

Schweiger R, Müller C. Leaf metabolome in arbuscular mycorrhizal symbiosis. Current Opinion in Plant Biology 2015;26:120-6.

Steidinger BS, Turner BL, Corrales A, Dalling JW. Variability in potential to exploit different soil organic phosphorus compounds among tropical montane tree species. Functional Ecology 2015;29:121-30.

Stutter MI, Shand CA, George TS, Blackwell MSA, Dixon L, Bol R, et al. Land use and soil factors affecting accumulation of phosphorus species in temperate soils. Geoderma 2015;(257-258):29-39.

Thai Meteorological Department. Climate data [Internet]. 2018 [cited 2021 Dec 7]. Available from: https://www.tmd.go.th/programs/uploads/tempstat/max_stat_latest_en.pdf.

Tiessen H, Moir JO. Characterization of available P by sequential extraction. In: Carter MR, editor. Soil Sampling and Methods of Analysis. Canadian Society of Soil Science; 1993. p. 75-86.

van der Heijden MGA, Klironomos JN, Ursic M, Moutoglis P, Strietwolf Engel R, Boller T, et al. Mycorrhizal fungal diversity determines plant biodiversity, ecosystem variability and productivity. Nature 1998;74:69-72.

Wagg C, Bender SF, Widmer F, van der Heijden MGA. Soil biodiversity and soil community composition determine ecosystem multifunctionality. Proceedings of the National Academy of Sciences of the United States of America 2014;111:5266-70.

Walkley A, Black IA. An examination of the Degtjareff method for determining soil organic matter, and a proposed modification of the chromic acid titration method. Soil Science 1934;37:29-38.

Wang J, Wang GG, Zhang B, Yuan Z, Fu Z, Yuan Y, et al. Arbuscular mycorrhizal fungi associated with tree species in a planted forest of Eastern China. Forests 2019;10:1-14.

World Rubber Summit (WRS). Facing the future: Inclusiveness, sustainability and growth for the next normal [Internet]. 2021 [cited 2021 Aug 1]. Available from: https://www.wrs 2021. rubberstudy.org/.

Yang X, Post WM. Phosphorus transformations as a function of pedogenesis: A synthesis of soil phosphorus data using Hedley fractionation method. Biogeosciences 2011;8:2907-16.

Zak JC, Willig MR, Moorhead DL, Wildman HG. Functional diversity of microbial communities: A quantitative approach. Soil Biology and Biochemistry 1994;26:1101-8.

Zhang H, Kovar JL. Fractionation of soil phosphorus. In: Kovar JL, Pierzynski GM, editors. Methods for Phosphorus Analysis for Soils, Sediments, Residuals, and Waters. Southern Cooperative Series Bulletin; 2009. p. 50-60.

M^{2+}(Ni, Cu, Zn)/Al-LDH Composites with Hydrochar from Rambutan Peel and Study the Adsorption Efficiency for Organic Dyes

Risfidian Mohadi[1], Normah[2], Neza Rahayu Palapa[3], and Aldes Lesbani[1,3*]

[1]*Graduate School of Faculty Mathematics and Natural Sciences, Sriwijaya University, Palembang-South Sumatera, Indonesia*
[2]*Magister Programme Graduate School of Mathematics and Natural Sciences, Sriwijaya University, Palembang-South Sumatera, Indonesia*
[3]*Research Center of Inorganic Materials and Coordination Complexes, Faculty of Mathematics and Natural Sciences, Sriwijaya University, Palembang-South Sumatera, Indonesia*

ARTICLE INFO

Received: 5 Nov 2021
Received in revised: 26 Dec 2021
Accepted: 9 Jan 2022
Published online: 1 Feb 2022
DOI: 10.32526/ennrj/20/202100218

Keywords:
LDH-Hc composite/ Rambutan peel/ Selectivity/ Recyclable/ Adsorption

*** Corresponding author:**
E-mail:
aldeslesbani@pps.unsri.ac.id

ABSTRACT

Ni/Al LDH, Cu/Al LDH, and Zn/Al LDH were composed with rambutan peel hydrochar (Hc) and the materials were applied as adsorbent for the removal of methylene blue from aqueous solution, measured using UV-Vis Spectrophotometric method. The preparation of the LDH-Hc composites were proven by XRD, FT-IR, and SEM analysis which showed similar characteristics of the LDH-Hc composites with pure LDH and hydrochar. The methylene blue removal efficiency was optimized by various parameters including adsorption selectivity, adsorption regeneration, pH, contact time, adsorption concentration, and temperature. The adsorption study analysis proved that LDH composited with rambutan peel hydrochar had a selective ability for methylene blue. Zn/Al-hydrochar had the most stable adsorption regeneration ability and adsorbed MB easily after seven regeneration cycles using water solvents and ultrasonic devices. Ni/Al-hydrochar and Cu/Al-hydrochar were effective up to five regeneration cycles for MB removal. The adsorption results showed that the optimal pH for MB adsorption was at pH 6 with an equilibrium adsorption contact time of 100 min and a tendency to follow the pseudo second order kinetic model. Parameter data of concentration and temperature of adsorption was determined using Langmuir and Freundlich equations. The results showed that the adsorption matched the Freundlich isotherm model with the adsorption capacity (q_m) of Ni/Al-Hc, Cu/Al-Hc, and Zn/Al-Hc adsorbents reaching 144.928, 175.439, 217.391 mg/g, respectively, with the adsorption process taking place continuously, spontaneously, and endothermically.

1. INTRODUCTION

Methylene blue (MB) is the most widely used dye in industry (Xu et al., 2020) such as pharmaceutical, paper, textile, paint, and plastic industries (Ahmad et al., 2020; Dang et al., 2020; Mantasha et al., 2020; Wang et al., 2016). Dyestuff waste is one of the environmental pollution problems that must be overcome to ensure sustainable industrial production (Nakhli et al., 2020). Methylene blue is a cationic dye that is classified as a toxic dye with mutagenic and carcinogenic properties that will significantly affect human health which can cause neuronal apoptosis, increased heart rate, inflammation of the leptomeninges, nausea, and vomiting and harm aquatic ecosystems (Alver et al., 2020; Liao et al., 2020; Nakhli et al., 2020).

Therefore, industrial waste treatment needs to be carried out to reduce the concentration of waste before being discharged into the environment. To overcome pollution in wastewater, various methods can be used such as adsorption, photocatalytic separation (Karagöz et al., 2008), membrane processes, coagulation, biodegradation (Li et al., 2020a), flocculation (Li et al., 2020b), aerobic and anaerobic treatment, ion exchange and electrochemistry (Ebadollahzadeh and Zabihi, 2020). Among them, the simplest, cheapest, and most effective wastewater treatment process is adsorption

Citation: Mohadi R, Normah, Palapa NR, Lesbani A. M^{2+}(Ni, Cu, Zn)/Al-LDH composites with hydrochar from rambutan peel and study the adsorption efficiency for organic dyes. Environ. Nat. Resour. J. 2022;20(2):221-233. (https://doi.org/10.32526/ennrj/20/202100218)

(Badri et al., 2020), one of the main industrial wastewater treatment methods for effluent purification. Adsorption is a method of transferring pollutant molecules to solid materials that can selectively remove pollutants from liquid waste by attracting pollutant molecules to the surface of the adsorbent (Alver et al., 2020). However, to reduce processing costs, efforts can be made to use alternative adsorbents that are cheap, abundant and easy to find. Recently, many studies have developed inexpensive and effective adsorbents to remove dyes in industrial waste made from agricultural wastes (Alinezhad et al., 2020). In the literature, a number of adsorbents have been investigated such as clay (Adeyemo et al., 2017), duku peel (Juleanti et al., 2021), wood waste (Stjepanović et al., 2021), orange peel (Chopra et al., 2012), plant biomass (Yeow et al., 2021), pineapple (Mahmuda et al., 2021), rice husk (Palapa et al., 2020a), coconut husk, bamboo dust (Rafatullah et al., 2010), and rambutan peel (Normah et al., 2021a).

Rambutan peel has been reported to have main chemical components containing cellulose, lignin, hemicellulose and phenolic compounds. This research conducted by Castro and das Virgens (2019) supports the effective application of rambutan skin as an adsorbent. Some of the advantages of rambutan peel as an adsorbent include having a good adsorption capacity, selective adsorption and can be regenerated (Mahmuda et al., 2021; Alrozi et al., 2012; Setiawan et al., 2018). Therefore, the conversion of rambutan peel into an adsorbent will provide an alternative that has the potential to be modified with layered double hydroxide to form a composite.

Layered double hydroxide or LDH is an anionic clay material that has a two-dimensional (2D) structure and contains anions in the interlayer, LDH is the same as hydrotalcite which is composed of divalent (M^{2+}) and trivalent (M^{3+}) metals which have the general formula $[M^{2+}_{1-x}M^{3+}_{x}(OH)_2]\ [A^{n-}_{x/n}]\cdot mH_2O$, A^{n-}: interlayer anions as charge balance (Lu et al., 2020; Xu et al., 2021). LDH has the advantage of producing a material that has a large adsorption capacity and is flexible (Lesbani et al., 2020; Normah et al., 2021b). However, LDH cannot be recycled and cannot be used in a regeneration process. Therefore, a method is needed to produce a stronger structure so that it can be used repeatedly by being composited with a supporting material (Wijaya et al., 2021).

Based on several investigations, LDH can be composited with biochar, zeolite, graphite, and chitosan (Bezerra et al., 2021; Fang et al., 2021). Zubair et al. (2018) reported that Ni/Fe LDH was composited with starch and applied to remove methyl orange in the liquid phase with a maximum adsorption capacity of 387.59 mg/g and a stable regeneration cycle reaching four cycles for the starch composite adsorbent NiFe-LDH. Alagha et al. (2020) reported Mg-Fe/LDH magnetic composite with activated carbon was applied to remove nitrate and phosphate in wastewater with reusability performance results with five regeneration cycles.

This study aimed to modify the LDH in the form of Ni/Al, Cu/Al, and Zn/Al composites with hydrochar rambutan peel, characterized using XRD, FT-IR, and SEM analysis. The adsorbent was applied for the selectivity of organic dyes in the form of methylene blue (MB), Rhodamine-B (Rh-B), methyl orange (MO), methyl red (MR), then the adsorbent would be tested for effectiveness in studies of regeneration, adsorption isotherms, and adsorption thermodynamics with the most selective dyes with adsorbents.

2. METHODOLOGY

2.1 Materials

The chemicals used to synthesize materials are nickel(II) nitrate ($Ni(NO_3)_2\cdot3H_2O$, 99% purity) by Sigma Aldrich, copper(II) nitrate ($Cu(NO_3)_2\cdot3H_2O$, 98% purity) by LOBA Chemie, zinc(II) nitrate ($Zn(NO_3)_2\cdot3H_2O$, 98.9% purity) by Merck, aluminum(III) nitrate, ($Al(NO_3)_3.9H_2O$, MW=375.13 g/mol, 98% purity) by Sigma Aldrich, hydrochloric acid (HCl, MW=36.458 g/mol, 37%), sodium hydroxide (NaOH, MW=40.00 g/mol by Merck, and the basic ingredient for making hydrochar is rambutan peel. Adsorbate used dye methylene blue (MB), Rhodamine-B (Rh-B), methyl orange (MO), and methyl red (MR).

2.2 Methods

2.2.1 Rambutan peel preparation

Rambutan peel powder was prepared using rambutan peel that had been cleaned and then dried in the sun. The dried rambutan peel was cut into small pieces and then baked at 110°C for 8 h. Then, the peel was mashed and passed through a 50 mesh sieve.

2.2.2 Hydrochar (Hc) preparation

Hydrochar was prepared using the hydrothermal carbonization (HTC) method (Li et al., 2020c) using a stainless steel autoclave hydrothermal device with 2.5 g of rambutan peel powder and 50 mL of distilled water tightly closed in the oven at 200°C for 10 h. In the final process, the autoclave was cooled to room temperature and the product in the autoclave was filtered. The resulting solid (hydrochar) was dried at a temperature of 105°C. Hydrochar was analyzed by characterization with XRD, FT-IR, and SEM.

2.2.3 Composite LDH-Hc preparation

The preparation of LDHs into LDH-Hc composites was carried out by the coprecipitation method by preparing 30 mL of a solution of M^{2+} (Ni, Cu, and Zn) (0.75 M) mixed with 30 mL (0.25 M) aluminum (III) nitrate and stirred. A 2 M NaOH solution was added dropwise to the mixture until it reached pH 10 and was maintained for 1 h until a precipitate was formed. To the LDH-Hc composite precipitate mixture was added as much as 3 g of hydrochar powder from rambutan peel, then stirred and kept at 80°C for 72 h. The product from the process was filtered using a vacuum and rinsed with distilled water, and the resulting product was then dried at 60°C to dryness. The preparation results in the form of Ni/Al-Hc, Cu/Al-Hc, and Zn/Al-Hc were analyzed by XRD, FT-IR, and SEM.

2.2.4 Adsorption experiment procedure

Adsorption selectivity is done by mixing several dyes using the same concentration and the same volume of dye. The dyes were methylene blue (MB), rhodamine-B (Rh-B), methyl orange (MO), and methyl red (MR) with a concentration of 8 mg/L each of 50 mL, then the mixture was added to 0.05 g (rambutan peel, Hc, Ni/Al-Hc, Cu/Al-Hc, and Zn/Al-Hc) and stirred using a shaker with time variations of 0, 15, 30, 60, to 120 min. After the expiration of each time, the mixture is separated by centrifugation to obtain the filtrate and residue, the filtrate is then analyzed for wavelength using a UV-Vis spectrophotometer in the range of 400-700 nm.

After obtaining the most selective dye, methylene blue (MB), adsorption studies using MB were done on each adsorbent.

The adsorption process of MB was studied through the influence of adsorption time. Various of the adsorption times were carried out with the concentration of MB 60 mg/L, then 20 mL was taken and added as much as 0.02 g of adsorbent and stirred for 0-150 min.

The kinetics adsorption was calculated using kinetic adsorption model such as pseudo first-order (PFO) and pseudo second-order (PSO). The formula should be written by:

$$\text{Pseudo first-order (PFO): } \log\left(q_e\text{-}q_t\right) = \log q_e - \left(\frac{k_1}{2,303}\right) t \quad (1)$$

$$\text{Pseudo first-order (PFO): } \frac{t}{q_t} = \frac{1}{k2qe^2} + \frac{1}{q_e} t \quad (2)$$

Where; q_e is adsorption capacity at equilibrium (mg/g); q_t is adsorption capacity at t (mg/g); t is adsorption time (min); k_1 is adsorption kinetic rate at pseudo first-order (/min); k_2 is adsorption kinetic rate at pseudo second-order (g/mg/min).

The adsorption isotherm model in the form of Langmuir and Freundlich models was used to determine the equilibrium adsorption capacity data and analyze the adsorption mechanism.

Langmuir and Freundlich isotherm equations are as follows:

$$\text{Langmuir: } \frac{C}{m} = \frac{1}{bK} + \frac{C}{b}\frac{C}{m} = \frac{1}{bK_{ML}} + \frac{C}{b} \quad (3)$$

Where; C is a saturated concentration of adsorbate; m is the amount of adsorbate; b is the maximum adsorption capacity (mg/g); K_{ML} is the Langmuir constant (mg/L).

$$\text{Freundlich: } \text{Log } q_e = \log K_F + \frac{1}{n}\log C \quad (4)$$

Where; q_e is adsorption capacity at equilibrium (mg/g); C_e is a concentration of adsorbate at equilibrium (mg/L); K_F is Freundlich constant.

The experimental adsorption isotherm was carried out with various initial concentrations of methylene blue (MB) (60, 70, 80, 90, and 100 mg/L) As much as 20 mL of MB solution was added to 0.02 g of adsorbent (rambutan peel, Hc, Ni/Al-Hc, Cu/Al-Hc and Zn/Al-Hc) and stirred for 2 h with temperature variations of 30, 40, 50, and 60°C. The last process was the separation of solutions and solids using centrifugation, then the solution was measured using a UV-Vis Spectrophotometer.

Adsorption thermodynamics used to calculate the Gibbs free energy change data (ΔG), enthalpy (ΔH), and entropy (ΔS) calculated by Equation (5-6):

$$\Delta G = -RT\ln(K_d) \quad (5)$$

$$\ln K_d = \frac{\Delta S}{R} - \frac{\Delta H}{RT} \quad (6)$$

K_d is the solute distribution coefficient (L/g); R is the universal gas constant (8.314 mol/K); T is temperature (K); Gibbs free energy (ΔG, kJ/mol); entropy (ΔS, kJ/mol); and enthalpy (ΔH, J/mol/K).

The regeneration process was carried out to test the effectiveness of the adsorbent in reusing the adsorbent. In this study, the regeneration process was carried out by adding 50 mL of adsorbate solution and 0.5 g of adsorbent (rambutan peel, Hc, Ni/Al-Hc, Cu/Al-Hc, and Zn/Al-Hc). The mixture of adsorbent and adsorbate was stirred for 3 h then separated between the solution and residual adsorbent, the solution was taken and measured using a UV-Vis spectrophotometer, while the remaining adsorbent was dried at 40°C and reused through the desorption process. The desorption process was carried out by adding 50 mL of water to the residual adsorbent and then desorption using an ultrasonic device for 2 h. The adsorbent that has gone through the desorption process is dried and then reused for the next adsorption process for seven repetitions of the same procedure.

3. RESULTS AND DISCUSSION

The successful preparation of LDH-Hc composite materials in the form of Ni/Al-Hc, Cu/Al-Hc, and Zn/Al-Hc was proven by the results of XRD, FT-IR, and SEM characterization analysis. The data characterization results are shown in Figure 1. Figure 1(a) shows an XRD diffractogram of rambutan peel with the appearance of two distinctive peaks at diffraction angles of 16° and 23.3° which describe that the rambutan peel contains cellulose compounds (Oliveira et al., 2016). Figure 1(b) shows the diffractogram of Hc material from the preparation of rambutan peel through the hydrothermal carbonization (HTC) process and shows a diffraction pattern similar to Figure 1(a). In the Hc diffractogram there was an increase in crystallinity, this was due to changes in amorphous cellulose compounds. The results of XRD characterization of composite materials were confirmed through the JCPDS (Joint Committee on Powder Diffraction Standard) data corresponding to each LDH. Typical diffraction peaks of Ni/Al LDH according to JCPDS data No.15-0087 (Wang et al., 2018), Cu/Al LDH with JCPDS No. 30-0630 (Palapa et al., 2020b) and Zn/Al LDH with JCPDS No. 48.2023 (Shin et al., 2020). The diffraction patterns of the Mg/Al-Hc, Ca/Al-Hc, and Zn/Al-Hc composites are presented in Figure 1.

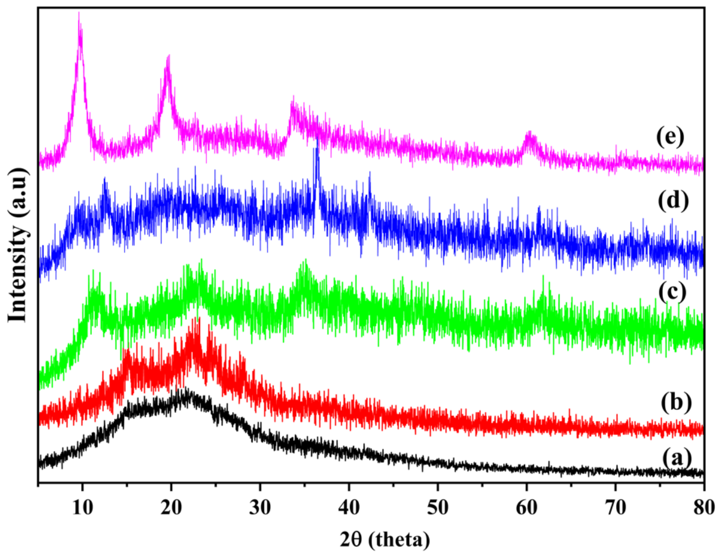

Figure 1. X-ray Powder diffraction patterns of rambutan peel (a), Hc (b), Ni/Al-Hc (c), Cu/Al-Hc (d), and Zn/Al-Hc (e)

Based on Figure 1, the diffraction peaks in Figure 1(c) which show the Ni/Al-Hc diffractogram at 2 θ angles 11.38°(003), 22.9°(002), 35.2°(012), 61.6°(110). The peaks that emerge are described as typical peaks of the layered structure. The diffraction peaks of Ni/Al-Hc composite materials were in accordance with JCPDS No. 15-0087 with diffraction of 2θ 10.9°(003), 34.5°(012), and 61.6°(110). The diffraction peaks of the Cu/Al-Hc composite material shown in Figure 1(d) have diffraction peaks at 12.75°(003), 18.9°(002), 36.44°(012), and 61.5°(110) was identified as a layered structure according to JCPDS No.30-0630. Figure 1(e) shows the Zn/Al-Hc difactogram with peaks at 2 θ angles around 9.78°(003), 19.66°(002), 33.80°(012), and 60.24°(110) according to JCPDS No. 48.2023. In addition, Figure 1 shows a typical diffraction peak of Hc around 19° to 22.9° with a reflection plane (002) identified as a cellulose compound from rambutan peel. Based on the results of the analysis, the preparation of composite materials in the form of Ni/Al-Hc, Cu/Al-Hc, and Zn/Al-Hc has been successfully prepared as evidenced by the appearance of diffraction peaks for pure LDH and Hc as the base material.

The successful preparation of the LDH-Hc composite material is supported by the FT-IR characterization presented in Figure 2. The spectra of the Ni/Al-Hc, Cu/Al-Hc, and Zn/Al-Hc composites have the characteristics of pure LDH and Hc, which appear about 3,424 cm^{-1} which corresponds to the vibration of the -OH group on the surface of the LDH layer, the peak of 1,635 cm^{-1} indicates the vibration of water molecules between the LDH layer, the vibration at the peak of about <1,000 cm^{-1} indicates the presence of metal molecules bound to oxygen in the LDH layer. LDHs (M-O, M-O-M, O-M-O) are characteristics of LDH (Hu et al., 2019). In addition, the vibrations that appear in 2953 cm^{-1} are associated with the C-H group, the 1,683 cm^{-1} peak associated with the C-O group and the 1,013 cm^{-1} peak associated with the C=C group which is characteristic of cellulose compounds in Hc materials (Castro and das Virgens, 2019). The LDH-Hc composite material has a vibration similar to that of pure LDH and Hc. FT-IR data confirm the successful modification of LDH with Hc.

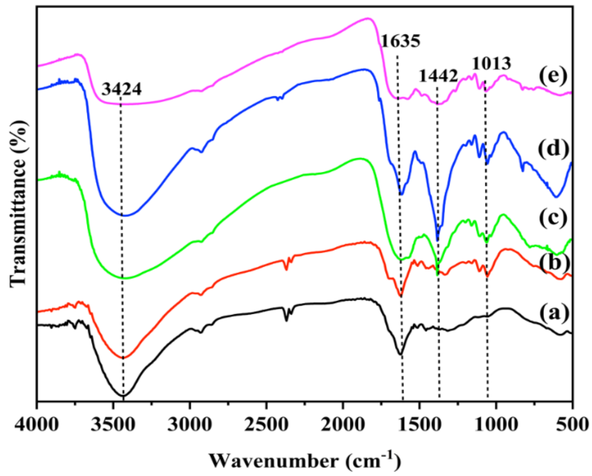

Figure 2. Spectrum FT-IR of Rambutan peel (a), Hc (b), Ni/Al-Hc (c), Cu/Al-Hc (d), and Zn/Al-Hc (e)

SEM analysis is used to see the surface morphology of the material. The results of the SEM analysis of the material are presented in Figure 3. The rambutan peel shown in Figure 3(a) has a surface morphology with flat-shaped particles but heterogeneous in size and rough surface texture, while the Hc shown in Figure 3(b) has a surface morphology with particles shaped like round like a ball and more homogeneous in size. This is caused by the degradation of lignin and cellulose compounds in rambutan peels during the carbonization process. LDH-Hc in the form of Ni/Al-Hc (c), Cu/Al-Hc (d) and Zn/Al-Hc (e) has a rough, uneven surface texture and irregular pores and has a pore size of large pores with high aggregates.

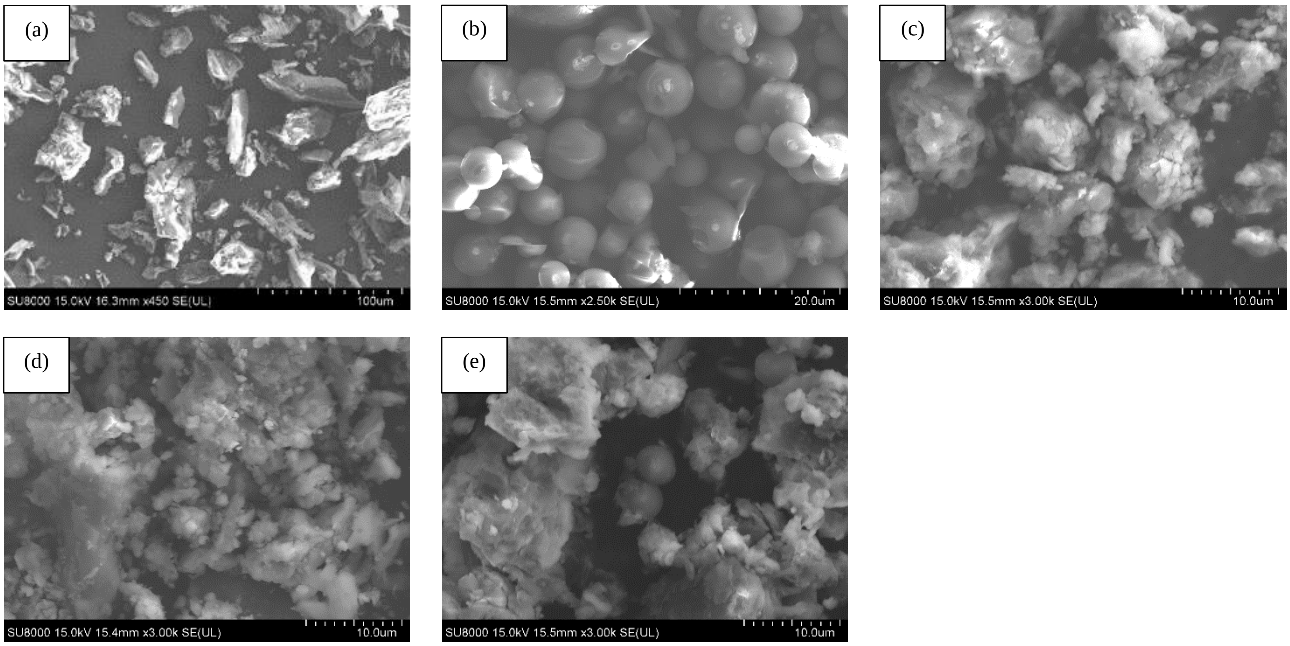

Figure 3. SEM image of Rambutan peel (a), Hc (b), Ni/Al-Hc (c), Cu/Al-Hc (d), and Zn/Al-Hc (e)

The adsorption selectivity was carried out by mixing four dyes in the form of methylene blue (MB), rhodamine-B (Rh-B), methyl red (MR), and methyl orange (MO) with a concentration of 8 mg/L added to each of the peel adsorbents. rambutan, Hc, Ni/Al-Hc, Cu/Al-Hc, and Zn/Al-Hc, and the wavelength at the maximum absorbance of the mixed dye solution was measured using a UV-Vis spectrophotometer. The results of these measurements are presented in Figure 4. The adsorption selectivity of the mixed dye was analyzed from changes in the adsorbed concentration which progressively increased during the adsorption process from 0, 15, 30, 60, to 120 min. Figure 4 shows the results of the adsorption selectivity on MB dye at first 8.33 mg/g, rambutan peel to 4.11 mg/g, Hc to 2.56 mg/g, Ni/Al-Hc to 0.2 mg/g, Cu/Al-Hc to 1.68 mg/g, and Zn/Al-Hc to 0.26 mg/g. Rh-B dye was initially 8.26 mg/g, rambutan peel was 6.01 mg/g, Hc to 2.45 mg/g, Ni/Al-Hc to 1.04 mg/g, Cu/Al-Hc to 3.98 mg/g, Zn/Al-Hc to 0.71 mg/g, for MR dyes initially at first of 8.13 mg/g, rambutan peel of 6.01 mg/g, Hc to 6.53 mg/g, Ni/Al-Hc to 2.64 mg/g, Cu/Al-Hc to 5.13 mg/g, and Zn/Al-Hc to 2.8 mg/g. MO at first was 8.24 mg/g, rambutan peel was 8.18 mg/g, Hc to 5.87 mg/g, Ni/Al-Hc to 3.49 mg/g, Cu/Al-Hc to 4.12 mg/g, and Zn/Al-Hc to 3.83 mg/g. A drastic decrease occurred at minute 120 with each adsorbent adsorbent. It can be concluded that the dye is selective for the adsorbent of rambutan peel, Hc, Ni/Al-Hc, Cu/Al-Hc, and Zn/Al-Hc are MB dye. After knowing

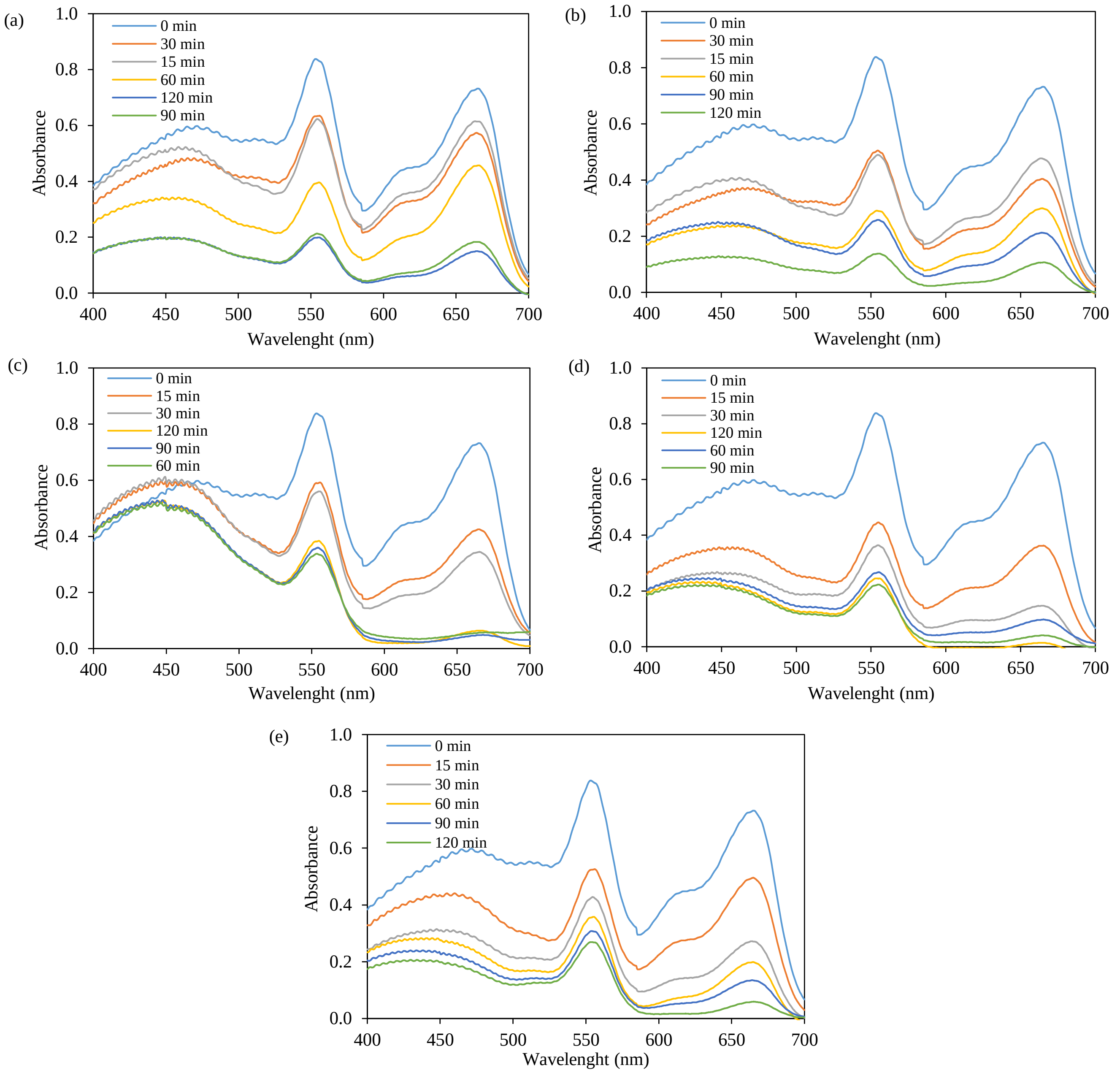

Figure 4. UV-Visible spectra of mixture MB, Rh-B, MR, and MO on Rambutan peel (a), Hc (b), Ni/Al-Hc (c), Cu/Al-Hc (d), and Zn/Al-Hc (e)

the most selective dye was MB, then MB was continued for the adsorption process using regeneration studies and adsorption isotherms and thermodynamic adsorption processes to determine the effectiveness of the adsorbent in removing MB.

Furthermore, conducting a regeneration study to determine the effectiveness of each adsorbent for repeated use. The results of the study regeneration of rambutan peel, Hc, Ni/Al-Hc, Cu/Al-Hc, and Zn/Al-Hc are shown in Figure 5.

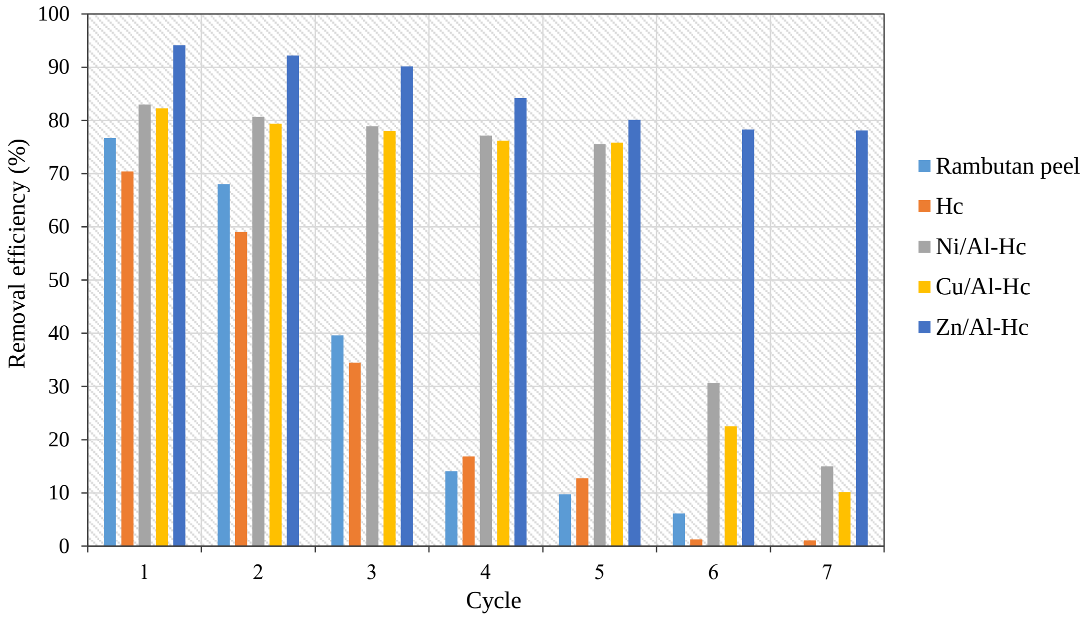

Figure 5. Rambutan peel, Hc, Ni/Al-Hc, Cu/Al-Hc, and Zn/Al-Hc adsorbent regeneration ability

Rambutan peel, Hc, Ni/Al-Hc, and Cu/Al-Hc composites showed a decrease in adsorption ability. Rambutan peel had an adsorption capacity of 76.65% in the first cycle and decreased to 0.12% in the last cycle. Hc has a cycle I of 70.43%, and its ability also decreased to 1.09% in the last cycle. The results of the regeneration of Zn/Al-Hc composites showed a stable adsorption ability compared to Ni/Al-Hc and Cu/Al-Hc. Ni/Al-Hc reached 83.02% in the first cycle and decreased to 14.98% for the last cycle, while Cu/Al-Hc in the first cycle was 82.29% and the last cycle decreased to 10.13%. Zn/Al-Hc reached the first cycle of 94.13%, the second was 92.19%, the third was 90.13%, the fourth was 84.21%, the fifth was 80.12%, the sixth was 78.33% and the last one was 78.11%. Rambutan peel, Hc, Ni/Al-Hc, and Cu/Al-Hc experienced a very significant decrease while the Zn/Al-Hc composite material decreased but not significantly. Based on these data, Zn/Al-Hc has the best regeneration ability compared to rambutan peel, Hc, Ni/Al-Hc, and Cu/Al-Hc.

The variation of pH adsorption of methylene blue using rambutan peel adsorbents, Hc, Ni/Al-Hc, and Cu/Al-Hc is shown in Figure 6.

On rambutan peel Hc, Ni/Al-Hc, Cu/Al-Hc, and Zn/Al-Hc the maximum adsorption of MB occurred at the optimum pH which was pH 6. Experiments with pH variations were generally carried out to determine the optimum pH for MB adsorption. Based on Mantasha et al. (2020), the OH^- ion from the adsorbent at acidic pH of blue will maintain the N group in the methylene dye, so that the interaction between methylene blue and the adsorbent will increase and the attractive force that occurs is also getting bigger. Meanwhile, at alkaline pH, methylene blue forms a salt that ionizes the negatively charged Cl^- group and at the same time OH^- ions from the adsorbent will inhibit the absorption process caused by the formation of repulsion by the same charge around the surface of the adsorbent with a charge of methylene blue dye. Which causes the methylene blue dye to be difficult to apply to the adsorbent surface.

The adsorption ability on the adsorption kinetics parameters can be seen in Figure 7. Find the adsorption kinetics model using Equations 1 and 2 in the form of Pseudo First Order (PFO) and Pseudo Second Order (PSO) equations. Adsorbents Hc, Ni/Al-Hc, Cu/Al-Hc and Zn/Al-Hc composites on the MB adsorption kinetics process showed that the absorption time occurred at 100 min. The parameters calculated from Equations 1 and 2 are shown in Table 1.

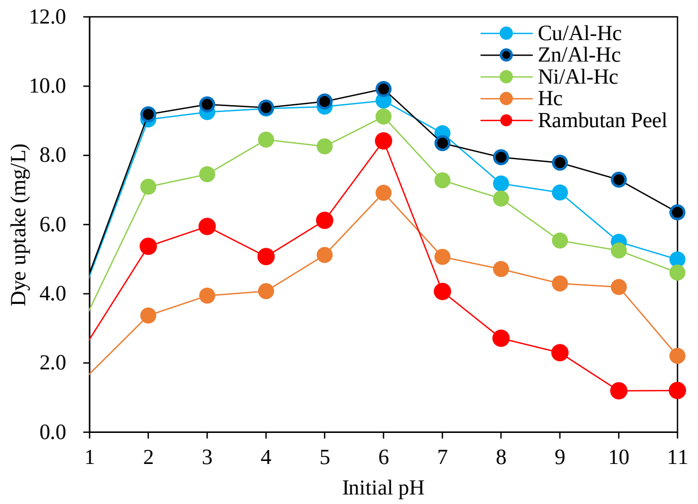

Figure 6. The effect of pH on adsorption capacity of adsorbent (rambutan peel, Hc, Ni/Al-Hc, Cu/Al-Hc, Zn/Al-Hc) and removal of MB

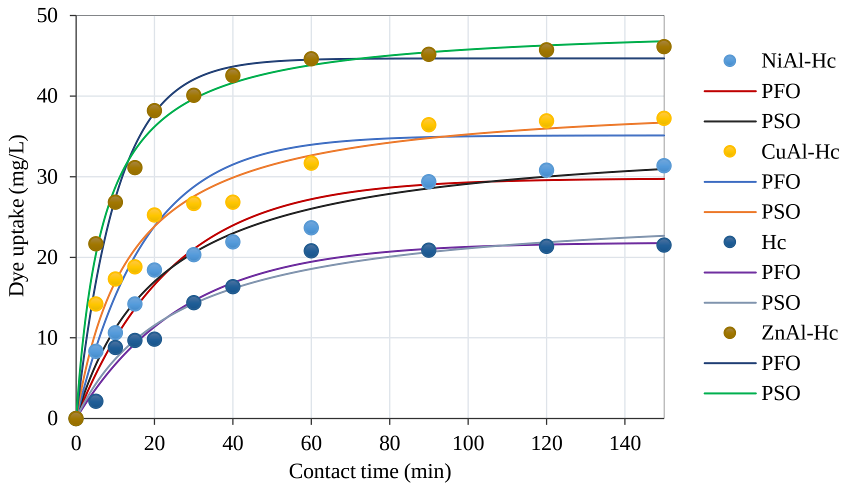

Figure 7. Adsorption kinetics model of MB using Hc, Ni/Al-Hc, Cu/Al-Hc, and Zn/Al-Hc

Table 1. Kinetic parameters of dyes adsorption onto Hc, Zn/Al-Hc, Cu/Al-Hc, and Ni/Al-Hc

Adsorbent	$Qe_{experiment}$ (mg/g)	PFO			PSO		
		Qe_{Calc} (mg/g)	R^2	k_1	Qe_{Calc} (mg/g)	R^2	k_2
Hc	46.143	24.400	0.938	0.037	47.619	0.998	0.097
Zn/Al-Hc	44.705	41.763	0.974	0.038	49.261	0.995	0.007
Cu/Al-Hc	31.381	29.356	0.970	0.030	35.971	0.993	0.022
Ni/Al-Hc	21.450	24.160	0.965	0.047	27.173	0.952	0.016

One of the most important characteristics in the adsorption process is kinetics. To clarify the adsorption kinetics of MB using the Hc, Ni/Al-Hc, Cu/Al-Hc, and Zn/Al-Hc composites adsorbent, the kinetic models, PFO and PSO were used. For the study of adsorption kinetics, the concentration of MB used was 50 mg/L with varying times ranging from 0 to 180 min and 0.02 g of adsorbent was added at the optimum condition of pH 6. The PSO model as the equation was assumed to be ideal on the adsorption surface of MB. The constant values of K1 and q_e were calculated from the slope and intercept log (q_e-q_t) versus t (Equations 1-2).

Table 1 shows that the adsorption kinetics tend to follow the PSO model with a linear regression value that is closer to 1 (R^2>0.952). Each adsorbent reached the optimal q_e value with the adsorption equilibrium time at 100 minutes. The largest value of q_e It can be seen that the PSO model is almost right for the first step. However, the PSO kinetic model seen from the highest linear regression R^2 (Table 1) and seen from the adsorption capacity value calculated from the pseudo model is close to the experimental value, which shows that the dominant kinetic phenomenon of PSO for MB adsorption by the adsorbent Hc, Ni/Al-Hc, Cu/Al-Hc, and Zn/Al-Hc composites with the dominant adsorption process occurring chemical interactions between the adsorbent and the adsorbate.

Furthermore, the adsorption ability is determined through the isotherm parameters which can be presented in Figure 8. Determination of the adsorption isotherm is determined through the Langmuir and Freundlich equations based on Equations 3 and 4.

Figure 8 shows the Langmuir and Freundlich isotherm model pattern. Figure 8 shows that the Zn/Al-Hc composite material has a higher adsorbed concentration (q_e) than rambutan peel, Hc, Ni/Al-Hc, and Cu/Al-Hc. Figure 6 on rambutan peel, Hc, Ni/Al-Hc, Cu/Al-Hc looks lower for MB adsorption. Determination of the adsorption isotherm model through the linear regression value of R^2 which is close to 1. The calculated data are presented in Table 2.

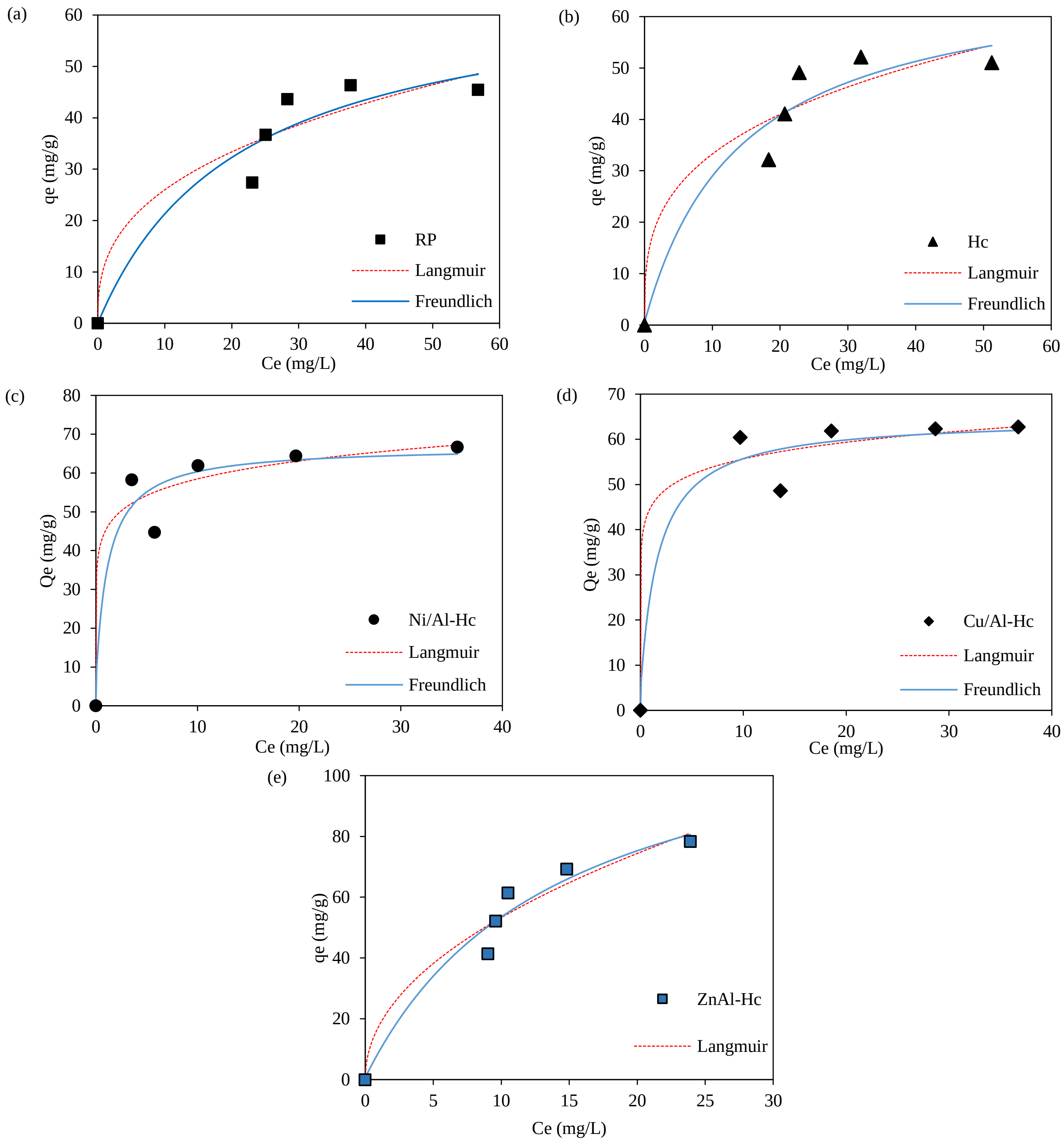

Figure 8. Adsorption isotherm model of MB using Rambutan peel (a), Hc (b), Ni/Al-Hc (c), Cu/Al-Hc (d), and Zn/Al-Hc (e)

Table 2 shows the Langmuir and Freundlich isotherm data in the form of Langmuir constant (kL), maximum adsorption capacity (q_m), adsorption intensity (n), and Freundlich constant (kF). Table 1 shows the Langmuir data at the Langmuir constant value (kL) of 0.070, 0.080, 0.025, 0.074, 0.040 and is in the range of 0 and 1 which identifies a suitable system for the adsorption process (Mishra et al., 2020; Zhao et al., 2020). The q_m data shows the value of large adsorption capacity on the adsorbent of LDH-Hc composite materials (Ni/Al-Hc, Cu/Al-Hc, Zn/Al-Hc) reaching 144.928 mg/g, 175.439 mg/g, 217.910 mg/g while rambutan peel precursors and Hc had lower adsorption capacities of 43.860 mg/g and 49.286 mg/g, respectively. Furthermore, Table 2 is equipped with data on the Freundlich isotherm with the value of the Freundlich constant (kF) and the value of n where the kF value reaches 0.921 to 20.029 which is related to the binding energy between the adsorbate and the adsorbent, while the adsorption intensity (n) with a value of n reaches 0.285 to 10.560 related according to the adsorption process.

Based on Table 2, the adsorption process tends to follow the Freundlich isotherm according to the linear coefficient value (R^2) which is closer to 1. Freundlich isotherm is an adsorption process following adsorption by multilayer adsorption and Freundlich can also describe physical adsorption (Wang et al., 2020) is supported by a value of 1/n<1 (Table 2) as the intensity of multilayer adsorption of adsorbate molecules on the surface of a heterogeneous material (Binh and Nguyen, 2020).

Table 2. Isotherm model of MB adsorption on Rambutan peel, Hc, Ni/Al-Hc, Cu/Al-Hc, and Zn/Al-Hc

Materials	Langmuir			Freundlich		
	q_m (mg/g)	kL	R^2	n	kF	R^2
Rambutan peel	43.860	0.070	0.995	0.285	20.029	0.999
Hc	49.286	0.080	0.999	4.651	4.870	0.999
Ni/Al-Hc	144.928	0.025	0.991	2.699	10.737	0.999
Cu/Al-Hc	175.439	0.074	0.936	10.560	0.921	0.999
Zn/Al-Hc	217.391	0.040	0.989	1.863	15.153	0.994

The comparison of MB adsorption for several adsorbents is presented in Table 3. Table 3 shows the adsorption capacity of several adsorbents for MB dye. Comparison between the performance of the adsorbent and various adsorbents that have a value (q_m) which is associated with the maximum adsorption capacity of the adsorbent for the removal of the adsorbent in the form of MB. It can be seen that Ni/Al-Hc, Cu/Al-Hc, and Zn/Al-Hc have a larger adsorption capacity in MB removal, this is due to the large surface area and more active sites of LDH and Hc. so that the interaction of the adsorbate with the adsorbent is more so that the adsorption capacity is large. The adsorbents prepared in this study have higher adsorption capacities when compared with the ones on Table 3.

Furthermore, the thermodynamic parameters provide data on the Gibbs free energy (ΔG), enthalpy (ΔH), and entropy (ΔS) which are calculated according to Equations 3 and 4. The adsorption thermodynamic data are shown in Table 4.

Table 4 shows the results of the calculation of negative adsorption values for ΔG on each adsorbent. ΔG values increase with increasing adsorption temperature from 30°C to 60°C. A negative value ΔG indicates that the MB adsorption process takes place spontaneously (Normah et al., 2021b). In this study, the ΔH value showed a range of 10.851 kJ/mol to 42.150 kJ/mol which was related to the tendency of MB adsorption to occur by physical adsorption and a positive ΔH value indicated that MB adsorption was endothermic (Wijaya et al., 2021). The value of S° is positive and is in the range of 0.037 J/mol·K to 0.144 J/mol·K. This is related to the irregularity of the particles during the adsorption process which increases due to the interaction between solid in the form of adsorbent-liquid in the form of MB adsorbate.

Table 3. Comparison of several adsorbents to removal MB

Adsorbent	Adsorption capacity (mg/g)	Reference
Cellulosic olice stones biomass	22.4	Al-Ghouti and Al-Absi (2020)
Fe_3O_4@C_{60}@MA	7.51	Xu et al. (2020)
Scenedesmus microalgae	55.26	Rathee et al. (2019)

Table 3. Comparison of several adsorbents to removal MB (cont.)

Adsorbent	Adsorption capacity (mg/g)	Reference
Bio-adsorbent of Pleurotus eryngii	18.45	Wu et al. (2019)
PDOPA-f-Mg/Al LDH	132	Zhao et al. (2017)
MnMgFe	20	Khuluk et al. (2019)
Ni/Fe/Ti LDH	29.940	Rathee et al. (2019)
Mg3AlDBS	10.864	Abdellaoui et al. (2019)
Rambutan peel	57.803	In this study
Hc	49.286	In this study
Ni/Al-Hc	144.928	In this study
Cu/Al-Hc	175.439	In this study
Zn/Al-Hc	217.391	In this study

Table 4. Thermodynamic parameters of MB adsorption on Rambutan peel, Hc, Ni/Al-Hc, Cu/Al-Hc, and Zn/Al-Hc

Parameters	T (K)	Materials				
		Rambutan peel	Hc	Ni/Al-Hc	Cu/Al-Hc	Zn/Al-Hc
ΔG	303	-0.210	-0.430	-1.479	-0.368	-1.373
	313	-0.566	-0.956	-2.076	-0.739	-2.809
	323	-1.011	-1.481	-2.672	-1.109	-4.246
	333	-1.807	-2.007	-3.269	-1.479	-5.682
ΔS		0.053	0.053	0.060	0.037	0.144
ΔH		15.503	15.503	16.593	10.851	42.150

4. CONCLUSION

In this study, LDH in the form of Ni/Al, Cu/Al, and Zn/Al were synthesized using the coprecipitation method and modified with hydrochar from rambutan peel which was prepared using the hydrothermal carbonization method. The material was applied as an adsorbent for the removal of methylene blue in aqueous solution using UV-Vis spectrophotometric method. The manufacture of LDH-Hc composites was proven by XRD, FT-IR, and SEM analysis. The results of adsorption selectivity showed that LDH with rambutan peel hydrochar showed good selective ability for methylene blue d and regeneration studies showed that the LDH-Hc composite showed a more stable adsorption regeneration ability reaching seven regeneration cycles for Zn/Al-Hc, while Ni/Al-Hc and Cu/Al-Hc achieved five regeneration cycles compared to LDH without modification, which only achieved three regeneration cycles using water solvent. The optimum pH of MB was found at pH 6. The study of adsorption kinetics was carried out using pseudo first order and pseudo second order equations and the removal of conformity MB followed the pseudo second order kinetic model. Parameter data of concentration and temperature of adsorption using Langmuir and Freundlich equation was determined. The results showed that the adsorption matched the Freundlich isotherm model with adsorption capacity (q_m) using Ni/Al-Hc, Cu/Al-Hc, and Zn/Al-Hc adsorbents reaching 144.928, 175.439, and 217.391 mg/g, respectively, with the adsorption process taking place continuously, spontaneously, and endothermically. The performance of the LDH-Hc composite using the adsorption method is superior to many other materials that have been used for dye absorption in the literature.

ACKNOWLEDGEMENTS

Authors thank Research Center of Inorganic Materials and Complexes, FMIPA Sriwijaya University for support this research.

REFERENCES

Abdellaoui K, Pavlovic I, Barriga C. Nanohybrid layered double hydroxides used to remove several dyes from water. ChemEngineering 2015;3(2):Article No. 41.

Adeyemo AA, Adeoye IO, Bello OS. Adsorption of dyes using different types of clay: A review. Applied Water Science 2017;7(2):543-68.

Ahmad A, Jini D, Aravind M, Parvathiraja C, Ali R, Kiyani MZ, et al. A novel study on synthesis of egg shell based activated carbon for degradation of methylene blue via photocatalysis. Arabian Journal of Chemistry 2020;13(12):8717-22.

Al-Ghouti MA, Al-Absi RS. Mechanistic understanding of the adsorption and thermodynamic aspects of cationic methylene blue dye onto cellulosic olive stones biomass from wastewater. Scientific Reports 2020;10(1):Article No. 15928.

Alagha O, Manzar MS, Zubair M, Anil I, Mu'azu ND, Qureshi A. Magnetic Mg-Fe/LDH intercalated activated carbon composites for nitrate and phosphate removal from wastewater: Insight into behavior and mechanisms. Nanomaterials 2020;10(7):Article No. 1361

Alinezhad H, Zabihi M, Kahfroushan D. Design and fabrication the novel polymeric magnetic boehmite nanocomposite (boehmite@ Fe_3O_4@PLA@SiO_2) for the remarkable competitive adsorption of methylene blue and mercury ions. Journal of Physics and Chemistry of Solids 2020;144:Article No. 109515.

Alrozi R, Zamanhuri NA, Osman MS. Removal of methylene blue from aqueous solution by adsorption onto NaOH-treated rambutan peel. 2012 IEEE Business, Engineering and Industrial Applications Colloquium (BEIAC) 2012;5:92-7.

Alver E, Metin AÜ, Brouers F. Methylene blue adsorption on magnetic alginate/rice husk bio-composite. International Journal of Biological Macromolecules 2020;154:104-13.

Badri A, Alvarez-Serrano I, Luisa López M, Ben Amara M. Sol-gel synthesis, magnetic and methylene blue adsorption properties of lamellar iron monophosphate $KMgFe(PO_4)_2$. Inorganic Chemistry Communications 2020;121:Article No. 108217.

Bezerra BGP, Bieseki L, de Mello MIS, da Silva DR, Rodella CB, Pergher S. Memory effect on a LDH/zeolite a composite: An XRD in situ study. Materials 2021;14(9):Article No. 2102.

Binh QA, Nguyen HH. Investigation the isotherm and kinetics of adsorption mechanism of herbicide 2,4-dichlorophenoxyacetic acid (2,4-D) on corn cob biochar. Bioresource Technology Reports 2020;11:Article No. 100520.

Castro JDS, das Virgens CF. Thermal decomposition of *Nephelium lappaceum* L. peel: Influence of chemical pretreatment and evaluation of pseudo-components by Fraser-Suzuki function. Journal of Thermal Analysis and Calorimetry 2019;138(5):3541-9.

Chopra M, Drivjot, Amita. Adsorption of dyes from aqueous solution using orange peels: Kinetics and equilibrium. Journal of Advanced Laboratory Research in Biology 2012;3(1):1-8.

Dang W, Zhang J, Nie H, Wang F, Tang X, Wu N, et al. Isotherms, thermodynamics and kinetics of methane-shale adsorption pair under supercritical condition: Implications for understanding the nature of shale gas adsorption process. Chemical Engineering Journal 2020;383:Article No. 123191.

Ebadollahzadeh H, Zabihi M. Competitive adsorption of methylene blue and Pb (II) ions on the nano-magnetic activated carbon and alumina. Materials Chemistry and Physics 2020;248:Article No. 122893.

Fang Q, Ye S, Yang H, Yang K, Zhou J, Gao Y, et al. Application of layered double hydroxide-biochar composites in wastewater treatment: Recent trends, modification strategies, and outlook. Journal of Hazardous Materials 2021;420:Article No. 126569.

Hu X, Li P, Zhang X, Yu B, Lv C, Zeng N, et al. Ni-based catalyst derived from NiAl layered double hydroxide for vapor phase catalytic exchange between hydrogen and water. Nanomaterials 2019;9(12):Article No. 1688.

Juleanti N, Palapa NR, Taher T, Hidayati N, Putri BI, Lesbani A. The capability of biochar-based CaAl and MgAl composite materials as adsorbent for removal Cr (VI) in aqueous solution. Science and Technology Indonesia 2021;6(3):156-65.

Karagöz S, Tay T, Ucar S, Erdem M. Activated carbons from waste biomass by sulfuric acid activation and their use on methylene blue adsorption. Bioresource Technology 2008; 99(14):6214-22.

Khuluk RH, Rahmat A, Buhani, Suharso. Removal of methylene blue by adsorption onto activated carbon from coconut shell (*Cocous nucifera* L.). Indonesian Journal of Science and Technology 2019;4(2):229-40.

Lesbani A, Asri F, Palapa NR, Taher T, Rachmat A. Efficient removal of methylene blue by adsorption using composite based Ca/Al layered double hydroxide-biochar. Global NEST Journal 2020;22(2):250-7.

Li J, Zhao P, Li T, Lei M, Yan W, Ge S. Pyrolysis behavior of hydrochar from hydrothermal carbonization of pinewood sawdust. Journal of Analytical and Applied Pyrolysis 2020c;146(12):Article No. 104771.

Li Y, Peng L, Li W. Adsorption behaviors on trace Pb^{2+} from water of biochar adsorbents from konjac starch. Adsorption Science and Technology 2020b;38(9-10):344-56.

Li Z, Sellaoui L, Gueddida S, Dotto GL, Ben Lamine A, Bonilla-Petriciolet A, et al. Adsorption of methylene blue on silica nanoparticles: Modelling analysis of the adsorption mechanism via a double layer model. Journal of Molecular Liquids 2020a;319:Article No. 114348.

Liao W, Wang H, Li HQ, Yang P. Fe(II) Removal from aqueous solution by layered double hydroxide/graphene composites: Adsorption coupled with surface oxidation. Environmental Engineering Science 2020;37(1):43-52.

Lu Y, Chen J, Zhao L, Zhou Z, Qiu C, Li Q. Adsorption of rhodamine b from aqueous solution by goat manure biochar: Kinetics, isotherms, and thermodynamic studies. Polish Journal of Environmental Studies 2020;29(4):2721-30.

Mahmuda KN, Wen TH, Zakaria ZA. Activated carbon and biochar from pineapple waste biomass for the removal ofmethylene blue. Environmental and Toxicology Management 2021;1(1):30-6.

Mantasha I, Saleh HAM, Qasem KMA, Shahid M, Mehtab M, Ahmad M. Efficient and selective adsorption and separation of methylene blue (MB) from mixture of dyes in aqueous environment employing a Cu(II) based metal organic framework. Inorganica Chimica Acta 2020;511:Article No. 119787.

Mishra S, Sahoo SS, Debnath AK, Muthe KP, Das N, Parhi P. Cobalt ferrite nanoparticles prepared by microwave hydrothermal synthesis and adsorption efficiency for organic dyes: Isotherms, thermodynamics and kinetic studies. Advanced Powder Technology 2020;31(11):4552-62.

Nakhli A, Bergaoui M, Toumi KH, Khalfaoui M, Benguerba Y, Balsamo M, et al. Molecular insights through computational modeling of methylene blue adsorption onto low-cost adsorbents derived from natural materials: A multi-model's approach. Computers and Chemical Engineering 2020; 140:Article No. 106965.

Normah N, Juleanti N, Siregar PMSBN, Wijaya A, Palapa NR, Taher T, et al. Size selectivity of anionic and cationic dyes using LDH modified adsorbent with low-cost rambutan peel to hydrochar. Bulletin of Chemical Reaction Engineering and Catalysis 2021a;16(4):869-80.

Normah, Palapa NR, Taher T, Mohadi R, Utami HP, Lesbani A. The ability of composite Ni/Al-carbon based material toward readsorption of iron(II) in aqueous solution. Science and Technology Indonesia 2021b;6(3):156-65.

Oliveira EIS, Santos JB, Gonçalves APB, Mattedi S, José NM. Characterization of the rambutan peel fiber (*Nephelium lappaceum*) as a lignocellulosic material for technological applications. Chemical Engineering Transactions 2016; 50:391-6.

Palapa NR, Taher T, Mohadi R, Rachmat A, Lesbani A. Preparation of copper aluminum-biochar composite as adsorbent of malachite green in aqueous solution. Research Square 2020a;524:1-24.

Palapa NR, Taher T, Rahayu BR, Mohadi R, Rachmat A, Lesbani A. CuAl LDH/Rice husk biochar composite for enhanced adsorptive removal of cationic dye from aqueous solution. Bulletin of Chemical Reaction Engineering and Catalysis 2020b;15(2):525-37.

Rafatullah M, Sulaiman O, Hashim R, Ahmad A. Adsorption of methylene blue on low-cost adsorbents: A review. Journal of Hazardous Materials 2010;177(1-3):70-80.

Rathee G, Awasthi A, Sood D, Tomar R, Tomar V, Chandra R. A new biocompatible ternary layered double hydroxide adsorbent for ultrafast removal of anionic organic dyes. Scientific Reports 2019;9(1):Article No. 16225.

Setiawan IKA, Napitupulu M, Walanda DK. Biocharcoal dari Kulit Rambutan (*Nephelium lappaceum* L.) sebagai Adsorben Zink dan Tembaga. Jurnal Akademika Kimia 2018; 7(4):Article No. 193.

Shin J, Kim K, Hong J. Zn-Al layered double hydroxide thin film. Coating 2020;10(669):1-7.

Stjepanović M, Velić N, Galić A, Kosović I, Jakovljević T, Habuda-Stanić M. From waste to biosorbent: Removal of congo red from water by waste wood biomass. Water 2021:13(3):Article No. 279.

Wang S, Gao B, Li Y, Zimmerman AR, Cao X. Sorption of arsenic onto Ni/Fe layered double hydroxide (LDH)-biochar composites. RSC Advances 2016;6:17792-9.

Wang W, Zhang N, Shi Z, Ye Z, Gao Q, Zhi M, et al. Preparation of Ni-Al layered double hydroxide hollow microspheres for supercapacitor electrode. Chemical Engineering Journal 2018;338:55-61.

Wang Z, Zhang L, Fang P, Wang L, Wang W. Study on simultaneous removal of dye and heavy metal Ions by NiAl-layered double hydroxide films. ACS Omega 2020; 5(34):21805-14.

Wijaya A, Siregar PNBSM, Priambodo A, Palapa NR, Taher T, Lesbani A. Innovative modified of Cu-Al/C (C=Biochar, Graphite) composites for removal of procion red from aqueous solution. Science Technology Indonesia 2021;6(4):228-34.

Wu J, Xia A, Chen C, Feng L, Su X, Wang X. Adsorption thermodynamics and dynamics of three typical dyes onto bio-adsorbent spent substrate of *Pleurotus eryngii*. International Journal of Environmental Research and Public Health 2019;16(5):Article No. 679.

Xu H, Zhang P, Zhou SY, Jia Q. Fullerene functionalized magnetic molecularly imprinted polymer: Synthesis, characterization and application for efficient adsorption of methylene blue. Chinese Journal of Analytical Chemistry 2020;48(9):e20107-e20113.

Xu H, Zhu S, Xia M, Wang F. Rapid and efficient removal of diclofenac sodium from aqueous solution via ternary core-shell CS@PANI@LDH composite: Experimental and adsorption mechanism study. Journal of Hazardous Materials 2021;402:Article No. 123815.

Yeow PK, Wong SW, Hadibarata T. Removal of azo and anthraquinone dye by plant biomass as adsorbent: A review. Biointerface Research in Applied Chemistry 2021;11(1): 8218-32.

Zhao J, Huang Q, Liu M, Dai Y, Chen J, Huang H, et al. Synthesis of functionalized MgAl-layered double hydroxides via modified mussel inspired chemistry and their application in organic dye adsorption. Journal of Colloid and Interface Science 2017;505:168-77.

Zhao Y, Zhan L, Xue Z, Yusef KK, Hu H, Wu M. Adsorption of Cu (II) and Cd (II) from wastewater by sodium alginate modified materials. Journal of Chemistry 2020;2020:Article No. 5496712.

Zubair M, Jarrah N, Ihsanullah KA, Manzar MS, Kazeem TS, Al-Harthi MA. Starch-NiFe-layered double hydroxide composites: Efficient removal of methyl orange from aqueous phase. Journal of Molecular Liquids 2018;249:254-64.

INSTRUCTION FOR AUTHORS

Publication and Peer-reviewing processes of Environment and Natural Resources Journal

Environment and Natural Resources Journal is a peer reviewed and open access journal that is published twice a year (January-June and July-December). Manuscripts should be submitted online at https://ph02.tci-thaijo.org/ index.php/ennrj/about/submissions by registering and logging into this website. Submitted manuscripts should not have been published previously, nor be under consideration for publication elsewhere (except conference proceedings papers). A guide for authors and relevant information for the submission of manuscripts are provided in this section and also online at: https://ph02.tci-thaijo.org/index.php/ennrj/author. All manuscripts are refereed through a **double-blind peer-review** process.

Submitted manuscripts are reviewed by outside experts or editorial board members of **Environment and Natural Resources Journal**. This journal uses double-blind review, which means that both the reviewer and author identities are concealed from the reviewers, and vice versa, throughout the review process. Steps in the process are as follows:

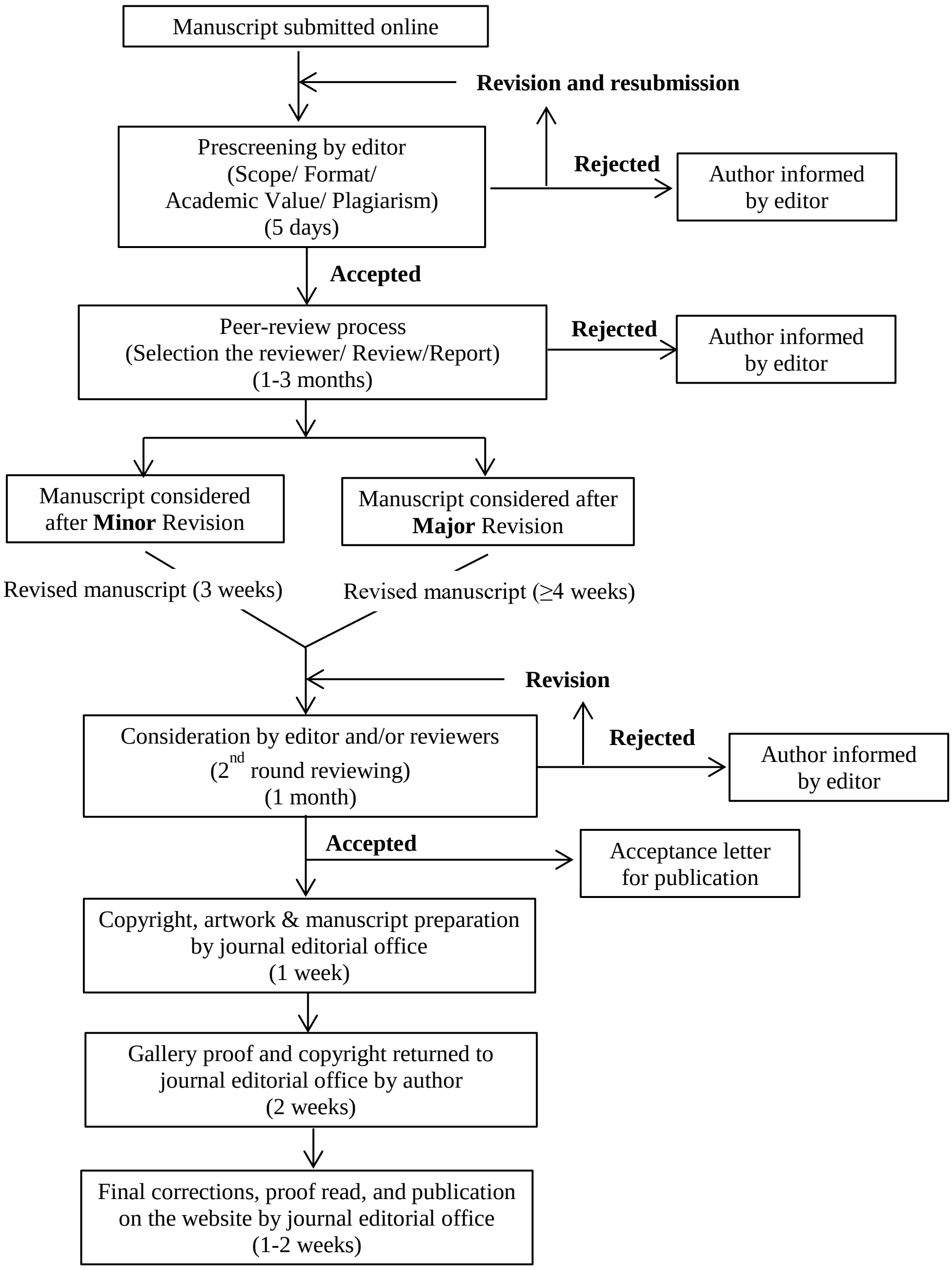

The Environment and Natural Resources Journal (EnNRJ) accepts 2 types of articles for consideration of publication as follows:

- *Original Research Article:* Manuscripts should not exceed 3,500 words (excluding references).
- *Review Article (by invitation):* This type of article focuses on the in-depth critical review of a special aspect in the environment and also provides a synthesis and critical evaluation of the state of the knowledge of the subject. Manuscripts should not exceed 6,000 words (excluding references).

Submission of Manuscript

Cover letter: Key points to include:

- Statement that your paper has not been previously published and is not currently under consideration by another journal
- Brief description of the research you are reporting in your paper, why it is important, and why you think the readers of the journal would be interested in it
- Contact information for you and any co-authors
- Confirmation that you have no competing interests to disclose

Manuscript-full: Manuscript (A4) must be submitted in Microsoft Word Files (.doc or .docx). Please make any identifying information of name(s) of the author(s), affiliation(s) of the author(s). Each affiliation should be indicated with superscripted Arabic numerals immediately after an author's name and before the appropriate address. Specify the Department/School/Faculty, University, Province/State, and Country of each affiliation.

Manuscript-anonymized: Manuscript (A4) must be submitted in Microsoft Word Files (.doc or .docx). Please remove any identifying information, such as authors' names or affiliations, from your manuscript before submission and give all information about authors at title page section.

Reviewers suggestion *(mandatory)*: Please provide the names of 3 potential reviewers with the information about their affiliations and email addresses. *The recommended reviewers should not have any conflict of interest with the authors. Each of the reviewers must come from a different affiliation and must not have the same nationality as the authors.* Please note that the editorial board retains the sole right to decide whether or not the recommended potential reviewers will be selected.

Preparation of Manuscript

Manuscript should be prepared strictly as per guidelines given below. The manuscript (A4 size page) must be submitted in Microsoft Word (.doc or .docx) with Times New Roman 12 point font and a line spacing of 1.5. *The manuscript that is not in the correct format will be returned and the corresponding author may have to resubmit*. The submitted manuscript must have the following parts:

Title should be concise and no longer than necessary. Capitalize first letters of all important words, in Times New Roman 12 point bold.

Author(s) name and affiliation must be given, especially the first and last names of all authors, in Times New Roman 11 point bold.

Affiliation of all author(s) must be given in Times New Roman 11 point italic.

Abstract should indicate the significant findings with data. A good abstract should have only one paragraph and be limited to 250 words. Do not include a table, figure or reference.

Keywords should adequately index the subject matter and up to six keywords are allowed.

Text body normally includes the following sections: 1. Introduction 2. Methodology 3. Results and Discussion 4. Conclusions 5. Acknowledgements 6. References

Reference style must be given in Vancouver style. Please follow the format of the sample references and citations as shown in this Guide below.

Unit: The use of abbreviation must be in accordance with the SI Unit.

Format and Style

Paper Margins must be 2.54 cm on the left and the right. The bottom and the top margin of each page must be 1.9 cm.

Introduction is critically important. It should include precisely the aims of the study. It should be as concise as possible with no sub headings. The significance of problem and the essential background should be given.

Methodology should be sufficiently detailed to enable the experiments to be reproduced. The techniques and methodology adopted should be supported with standard references.

Headings in Methodology section and Results and Discussion section, no more than three levels of headings should be used. Main headings should be typed (in bold letters) and secondary headings (in bold and italic letters). Third level headings should be typed in normal and no bold, for example;

2. Methodology
2.1 Sub-heading
2.1.1 Sub-sub-heading

Results and Discussion can be either combined or separated. This section is simply to present the key points of your findings in figures and tables, and explain additional findings in the text; no interpretation of findings is required. The results section is purely descriptive.
Tables Tables look best if all the cells are not bordered; place horizontal borders only under the legend, the column headings and the bottom.
Figures should be submitted in color; make sure that they are clear and understandable. Please adjust the font size to 9-10, no bold letters needed, and the border width of the graphs must be 0.75 pt. *(Do not directly cut and paste them from MS Excel.)* Regardless of the application used, when your electronic artwork is finalized, please 'save as' or convert the images to TIFF (or JPG) and separately send them to EnNRJ. The images require a resolution of at least 300 dpi (dots per inch). If a label needed in a figure, its font must be "Times New Roman" and its size needs to be adjusted to fit the figure without borderlines.

All Figure(s) and Table(s) should be embedded in the text file.

Conclusions should include the summary of the key findings, and key take-home message. This should not be too long or repetitive, but is worth having so that your argument is not left unfinished. Importantly, don't start any new thoughts in your conclusion.

Acknowledgements should include the names of those who contributed substantially to the work described in the manuscript but do not fulfill the requirements for authorship. It should also include any sponsor or funding agency that supported the work.

References should be cited in the text by the surname of the author(s), and the year. This journal uses the author-date method of citation: the last name of the author and date of publication are inserted in the text in the appropriate place. If there are more than two authors, "et al." after the first author' name must be added. Examples: (Frits, 1976; Pandey and Shukla, 2003; Kungsuwas et al., 1996). If the author's name is part of the sentence, only the date is placed in parentheses: "Frits (1976) argued that . . ."

Please be ensured that every reference cited in the text is also present in the reference list (and vice versa).

In the list of references at the end of the manuscript, full and complete references must be given in the following style and punctuation, arranged alphabetically by first author's surname. Examples of references as listed in the References section are given below.

Book
Tyree MT, Zimmermann MH. Xylem Structure and the Ascent of Sap. Heidelberg, Germany: Springer; 2002.

Chapter in a book
Kungsuwan A, Ittipong B, Chandrkrachang S. Preservative effect of chitosan on fish products. In: Steven WF, Rao MS, Chandrkachang S, editors. Chitin and Chitosan: Environmental and Friendly and Versatile Biomaterials. Bangkok: Asian Institute of Technology; 1996. p. 193-9.

Journal article
Muenmee S, Chiemchaisri W, Chiemchaisri C. Microbial consortium involving biological methane oxidation in relation to the biodegradation of waste plastics in a solid waste disposal open dump site. International Biodeterioration and Biodegradation 2015;102:172-81.

Published in conference proceedings
Wiwattanakantang P, To-im J. Tourist satisfaction on sustainable tourism development, amphawa floating marketSamut songkhram, Thailand. Proceedings of the 1st Environment and Natural Resources International Conference; 2014 Nov 6-7; The Sukosol hotel, Bangkok: Thailand; 2014.

Ph.D./Master thesis

Shrestha MK. Relative Ungulate Abundance in a Fragmented Landscape: Implications for Tiger Conservation [dissertation]. Saint Paul, University of Minnesota; 2004.

Website

Orzel C. Wind and temperature: why doesn't windy equal hot? [Internet]. 2010 [cited 2016 Jun 20]. Available from: http://scienceblogs.com/principles/2010/08/17/wind-and-temperature-why-doesn/.

Report organization:

Intergovernmental Panel on Climate Change (IPCC). IPCC Guidelines for National Greenhouse Gas Inventories: Volume 1-5. Hayama, Japan: Institute for Global Environmental Strategies; 2006.

Remark

** Please be note that manuscripts should usually contain at least 15 references and some of them must be up-to-date research articles.*

** Please strictly check all references cited in text, they should be added in the list of references. Our Journal does not publish papers with incomplete citations.*

Copyright transfer

The copyright to the published article is transferred to Environment and Natural Resources Journal (EnNRJ) which is organized by Faculty of Environment and Resource Studies, Mahidol University. The accepted article cannot be published until the Journal Editorial Officer has received the appropriate signed copyright transfer.

Online First Articles

The article will be published online after receipt of the corrected proofs. This is the official first publication citable with the Digital Object Identifier (DOI). After release of the printed version, the paper can also be cited by issue and page numbers. DOI may be used to cite and link to electronic documents. The DOI consists of a unique alpha-numeric character string which is assigned to a document by the publisher upon the initial electronic publication. The assigned DOI never changes.

Mahidol University

Wisdom of the Land

Research and Academic Service Section, Faculty of Environment and Resource Studies, Mahidol University
999 Phutthamonthon 4 Rd, Salaya, Nakhon Pathom 73170, Phone +662 441-5000 ext. 2108 Fax. +662 441 9509-10
E-mail: ennrjournal@gmail.com Website: https://www.tci-thaijo.org/index.php/ennrj